ANOMALOUS PROTEIN AGGREGATION ON NANOTUBULAR TITANIUM DIOXIDE

Jacob Hershel Forstater

A dissertation submitted to the faculty of the University of North Carolina at Chapel Hill in partial fulfillment of the requirements for the degree of Doctor of Philosophy in the Department of Physics and Astronomy

Chapel Hill
2013

Approved by:

Yue Wu

Max Berkowitz

Reyco Henning

Alfred Kleinhammes

Amy Oldenburg

Richard Superfine

ABSTRACT

JACOB FORSTATER: Anomalous Protein Aggregation on Nanotubular Titanium Dioxide
(Under the direction of Yue Wu)

Immobilized enzymes are widely used as catalysts in industrial chemical production, diagnostic devices, and biosensors. Immobilization improves an enzyme's stability and creates an insoluble enzyme-based material that is easier to manipulate and recover. This is typically achieved by either covalently immobilizing enzymes to the surface of an inorganic carrier or by confining them within an inorganic scaffold. Both of these strategies are problematic – surface adsorption limits immobilization to a monolayer, while confinement prevents access to the enzymatically active site. The desired approach would be to assemble enzymes, without chemical modification, into solid enzyme-based materials with an accessible microstructure.

In this dissertation, I detail the discovery and development of an inorganic nanomaterial, titania nanotubes, that can initiate and template the non-covalent, self-assembly of enzymes into stable, micron-sized, enzyme-based superstructures which retain their native enzymatic activity.

On the basis of quantitative adsorption measurements, dynamic light scattering, and microcalorimetry, I demonstrate that this process occurs in two stages – at low enzyme concentrations, enzyme multilayers form around the nanotube; above a critical enzyme concentration the enzyme-coated nanomaterial and any additional free enzyme self-assemble into micron-sized ellipsoidal structures. The resulting enzyme-based material has enhanced enzymatic activity and contains more than 99.9% enzyme by weight.

Using solid-state nuclear magnetic resonance (NMR), x-ray diffraction (XRD), and

thermogravimetric analysis (TGA), I investigate the interfacial properties of the nanotube and similar materials and I show that this phenomenon is uniquely associated with the active anatase-(001) like surface of titania nanotubes, which contain a high density of stable, coordinatively undersaturated Ti sites on its surface.

These findings present a nanotechnology-enabled mechanism for creating stable protein-based materials and present a new route for creating such materials without covalent modification. In this dissertation I detail the assembly of these structures, the role of the nanomaterial's surface chemistry, and the design rules suggested by these findings for creating other nanomaterial templates for biomolecule assembly.

To Sarah

and

In memory of my grandparents Sidney Forstater, שמולקא בן יצחק וחנה ז"ל, and Louise Fradkin, לאה בת הערש ושרה מלכה ז"ל, who instilled in me both a love of learning and a sense of identity and taught me to take pride in what I do.

ACKNOWLEDGEMENTS

"If I have ever made any valuable discoveries, it has been owing more to patient attention, than to any other talent."

— *Isaac Newton*

Over the past six years, I have received support and encouragement from many individuals. I am indebted to my advisor, Prof. Yue Wu, for the independence and intellectual freedom he allotted me, for expecting more from me than I knew I was capable, and for patiently teaching me the value of seeing the forest for the trees. I would like to thank the different members of my preliminary oral exam and dissertation committees – Profs. Max Berkowitz, Reyco Henning, Alfred Kleinhammes, Amy Oldenburg, Gary Pielak, and Rich Superfine – for challenging me to be a better scientist and for their support and advice as I moved from an idea to a completed study. Drs. Pabitra Sen and Tim O'Brien provided critical intellectual feedback, mentorship, and support and I am very grateful for their contributions.

I am particularly thankful of Dr. Alfred Kleinhammes's feedback, collaboration, and mentorship during my graduate career. His sense of humor, friendship, and appreciation of good coffee have been invaluable. Thank you to Maggie Sandor who, in addition to enjoying hundreds, maybe thousands, of cups of coffee with me, has always been a supportive friend and coworker. Her dedication, tireless efforts, and perseverance have always inspired me.

I performed many measurements for this dissertation using equipment in the laboratories of Profs. Joe DeSimone and Rich Superfine, and I am especially grateful to them for opening up their labs and to their students and colleagues who graciously assisted and accommodated me. I'm very thankful to Kellie Machlus and Jeff Damrauer, who in addition to being good friends, graciously and patiently assisted this physicist as he ventured into biology. I also

thank Amar Kumbhar and Wallace Ambrose of CHANL for performing much of the TEM imaging.

I would like to acknowledge TA Instruments, which generously lent me the microcalorimetry and thermal analysis instrumentation for this research; in particular, I'm grateful to Neil Demarse for making the arrangements and for introducing me to microcalorimetry.

Many wonderful graduate students and postdocs passed through Prof. Wu's lab during my time, I grateful for their contributions and feedback. In particular, I greatly benefited from the advice and expertise of Qiang Chen, Shaun Gidcumb, Greg Mogilevsky, and Haijing Wang.

I am especially grateful to my family and friends – you know who you are. Your love, encouragement, and occasional harassment have sustained me.

And of course, to my wife Sarah, words cannot express my thanks. This work is a testament to your love, support, and remarkable patience.

TABLE OF CONTENTS

LIST OF TABLES

LIST OF FIGURES

LIST OF ABBREVIATIONS AND SYMBOLS

$\langle \Delta H \rangle$	Average excess enthalpy
P_i	Population of ith state
α	Symbol for a generic measurable property
ΔG_i	Gibb's free energy of state i
ΔH_{cal}	Change in calorimetric enthalpy
ΔH_{VH}	Change in van't Hoff enthalpy
κ^{-1}	Debye Length
$\langle \Delta C_p^{N \rightarrow U} \rangle$	Heat capacity difference between native and unfolded protein
$\langle \Delta C_p^{trans} \rangle$	Heat capacity due to thermal transition
$\langle C_p \rangle$	Average heat capacity
$\langle C_p \rangle_{1/2}$	Heat capacity at midpoint of thermal unfolding curve, relative to pre-transition baseline
$\langle \Delta G \rangle$	Average excess Gibb's free energy
$\langle \Delta S \rangle$	Average excess entropy
ϕ_p	Porosity
τ	Characteristic timescale of enzymatic reaction
θ	Surface coverage
A_w	Scaling factor for two-state unfolding model
$C_{p,n}$	Heat capacity of native protein
$C_{p,u}$	Heat capacity of unfolded protein
D_e	Effective diffusivity
$K_{L,U}$	Binding affinity of of unfolded protein for ligand
T	Tortuosity
T_m	Unfolding temperature
Z	Canonical partition function

AA	Antibiotic-antimitotic solution
CM-TiNT	Cryomilled Titania Nanotubes
CU	Cooperativity unit
DLS	Dynamic Light Scattering
DPBS	Dulbecco's Phosphate Buffered Saline
DSC	Differential scanning (micro)calorimetry
FBS	Fetal bovine serum
H_{excess}	Excess enthalpy
HEPES	2-[4-(2-hydroxyethyl)piperazin-1-yl]ethanesulfonic acid
HWHM	Half Width at Half Max
k_b	Boltzmann's constant
K_{eq}	Equilibrium constant
MAS	Magic-angle spinning
MD	Molecular dynamics
N	Native state of protein
NMR	Nuclear magnetic resonance
NTile	Anatase Nanotile
PES	Polyethersulfone
pI	Isoelectric point
PID	Proportional, integral, derivative
R	Gas constant
RFU	Relative fluorescence units
RH	Relative humidity
RNaseA	Bovine pancreatic ribonuclease a
SAED	Selected Area Electron Diffraction
SDS-PAGE	Denaturing Gel Electrophoresis

SEM	Scanning Electron Microscopy
T	Temperature
$T_{m_{1/2}}$	Midpoint of thermogram
TEM	Transmission Electron Microscopy
TGA	Thermogravimetric Analysis
TiNP	Titania Nanoparticle
TiNT	Titania Nanotube
U	Unfolded state of protein
XRD	X-ray Diffraction

CHAPTER 1
INTRODUCTION

1.1 Introduction

Many proteins have evolved to self-assemble into stable, large, and remarkably complex hierarchical materials which are structurally robust, functional, and biocompatible[5, 6]. For example, in eukaryotic cells, most enzymes, which are catalytic proteins, are either spatially confined within subcellular organelles or co-localized into larger complexes with enzymes that function in tandem[7–11]. Many biochemical processes require a series of different enzymes that perform a cascade of consecutive reactions. Assembling them into larger structures has two major benefits - it improves the reaction efficiency by minimizing the diffusion of intermediate reaction products amongst the different enzymes and allows potentially toxic intermediates to be confined with the complex[11–13].

Although this strategy is useful in nature, it has been very hard to replicate. Naturally existing protein assemblies result from either confinement in a larger structure, such as the subcellular organelles, or by programmed assembly, resulting from specific structural motifs which have evolved over billions of years[14]. So far we have only been able to create structural assemblies containing proteins with specially engineered proteins[14], or by chemically crosslinking proteins with polymers that self-assemble[15] or polymerize[12, 16]. It has remained a key challenge to assemble large, stable, and functional protein structures without relying on chemical modification.

It is possible to form protein assemblies by altering the solution conditions or by in-

troducing specific ligands. For example, proteins can form larger aggregates or assemble at elevated salt concentrations[17], under macromolecular crowding conditions[18, 19], or in the presence of a small molecule or ligand which alters the protein's self-association properties[20–23].

Given the variety of different conditions and environments in which protein assemblies might be utilized, the desired approach would be to assemble solid protein-only materials with an accessible microstructure by utilizing specific ligands or by exploiting interfacial interactions between the protein and a engineered substrate. In fact, in recent years there has been incredible interest in understanding how material interfaces can direct protein assembly and in developing insoluble protein-based materials[24]. Such materials offer novel opportunities as biocatalysts[25], biomaterials[26], and for stabilizing and delivering biopharmaceuticals[27].

For instance, the creation of insoluble, stable, enzyme-based materials is a promising strategy for creating robust and highly selective biocatalysts[28]. Current strategies either immobilize enzymes as surface adsorbates on inorganic carriers or confine them within an inorganic scaffold. However, adsorption gives rise to very low enzyme loading capacities, limited by the monolayer coverage[29], and requires structurally modifying covalent linkages to prevent desorption[16, 30–36], while confinement often makes the enzyme inaccessible to the external molecules it is supposed to react with[12, 15, 16, 37–39]. Thus far, it has proven exceptionally difficult to assemble enzyme-based materials while preserving the near-native structure of the enzyme and the accessibility of the catalytic site.

1.2 Protein Adsorption and Interactions at an Interface

Protein adsorption at solid, liquid, and air interfaces is ubiquitous in nature[31, 40–44] and has widespread implications in a wide variety of areas including biopharmaceutical production, biocatalysis[38], and medicine, including diseases linked to protein-aggregation[36, 45–48]. It is the first step in many biological processes such as transmembrane signaling and is responsible for initiating the blood coagulation cascade[31, 49, 50]. It also plays a critical role in many modern biomedical applications, such as ensuring adequate vascularization of artificial tissue scaffolds[40].

However, despite its ubiquity, protein adsorption is a far more complicated process than typically encountered with rigid small molecules. A variety of differences exist between proteins and small molecules. For instance, proteins have a complicated and delicately balanced structural arrangement, with varying degrees of freedom, which is largely held together by non-covalent bonds[31]. Owing to multiple amphoteric surface groups they have an external charge distribution. Proteins do not simply adsorb to an interface, rather structural rearrangements can occur, which in turn, can alter surface affinities, induce surface aggregation, and alter the adsorption behavior over time[31, 40, 51].

However, experimentalists and theorists alike can take comfort that the delicate balance of interactions that occur during protein adsorption can also lead to a rich variety of undiscovered novel phenomena. This notion is appropriately exemplified by one prominent researcher[52], who referred to protein adsorption as: "...a common but very complicated phenomenon."

In this dissertation I examine globular proteins, which are an important class of widely prevalent structural and functional proteins that are ellipsoidal-shaped and typically quite compact. Examples include insulin[53], hemoglobin[54], immonoglobulins[31], and structural protein monomers such as actin and tublin[55]. Structurally, this compactness occurs

by burying the the majority of hydrophobic (apolar) residues within the folded protein and exposing the hydrophilic (polar) residues on the external hydrated surface[31, 56, 57]. This makes them highly soluble in aqueous environments, but the dense packing decreases the conformational entropy.

Globular proteins typically have a highly ordered secondary structure. Frequently the secondary structure is dominated by α-helix and β-sheet structures, which are stabilized by significant intramolecular hydrogen bonding between peptide units within the polypeptide backbone[31, 57]. The significant hydrogen bonding restricts the rotational mobility of the bonds in the polypeptide chains and further reduces the conformational entropy.

Hydration of apolar residues is both enthalpically and entropically unfavorable[4, 43, 58, 59]; this energetic barrier makes it particularly favorable for the protein to assume a structure which limits the hydrophobic residue exposure to water. However, approximately 40% of the hydrophobic residues will still be located on the external surface of the protein[60–62]. Thus there is a spatially dependent structure of hydrophobic and hydrophilic patches on the external surface of a protein and the interaction of a protein with a solid sorbent will critically depend on the hydrophobicity of the interface it comes into contact with[63].

1.3 Driving Forces for Adsorption

Typically, protein adsorption to a solid interface involves three primary phases - the transport of protein from the bulk solution to the interface[31], initial contact of the protein to the surface[44], and conformational changes and structural relaxation at the interface[61].

Strong protein-surface interactions can dramatically influence protein stability[64], moreover, it is possible for the protein to unfold into either a non-equilibrium or meta-stable state, resulting in irreversible protein adsorption or kinetically trapped arrangements[61].

There are numerous driving forces for protein adsorption at a solid-liquid interface. For spontaneous adsorption to occur, the Gibb's free energy of the protein-sorbent system must be reduced by adsorption. The enthalpic contributions are primarily due to hydrogen-bonding[63] and electrostatic interactions[31], while entropic increases will arise from the release or rearrangement of interfacial water and counterions[58] as well as conformational changes to the adsorbed protein.

Before proceeding, it is useful to examine the basic fundamentals of how a protein might interact with a material interface and to explore the parameter space available to control or modify these interactions.

1.3.1 Solution Conditions

Proteins contain amphoteric groups on the surface with different pKa values. Thus changing the pH will alter the protein charge distribution and net charge; in turn, the proteins electrostatic attraction to or repulsion from the substrate will vary with pH[65, 66].

Along these lines, the ionic strength of the solution will tune the effective length scale of electrostatic interactions. With increasing ionic strength the charge on the protein and substrate are increasingly screened[31, 55, 67]. This typically increases the adsorption of proteins to similarly charged substrates and decreases the adsorption to oppositely charged interfaces[31]. Additionally, increased ionic strength will reduce the lateral repulsion between adjacent adsorbed proteins. This increases the packing density of proteins on the interface[43, 68]. For example, lysozyme adsorption on SiO_2 nanoparticles is decreased as the pH is lowered[40, 69, 70].

The specific ion will also affect the interaction. Chaotropic ions will destabilize the protein structure, which will typically result in increased protein adsorption[40], while kos-

motropic ions will typically stabilize the protein but can produce protein aggregates[40, 41]. However these trends are but guidelines; experiments show that the specific ion effects does not always follow the Hoffmeister series[40].

1.3.2 Protein Structure

Generally speaking, the protein's composition, structure, and size broadly impact its adsorption properties. If hydrophobic residues are exposed on the protein surface, there is an energetic driving force to dehydrate these residues or prevent their exposure[57]. The exact structural motifs and cohesive structure will determine its stability and thus propensity to unfold on an interface[56]. In particular, proteins with extensive disulfide bonds will undergo less conformational change at an interface and the extent of hydrophobic dehydration will be reduced. Because hydrophobic dehydration is one of the primary driving forces for adsorption, adsorption is typically reduced for proteins containing disulfide bonds[71].

Similarly, the protein's exact composition and structure determines which amino acids are exposed on the surface, the hydrophobicity, and the charge on the surface[17]. Larger proteins typically are more strongly adsorbed to an interface due to the increase contact area between the protein and interface[30, 31, 64].

1.3.3 Substrate Properties

The interaction between proteins and nanoparticles has been widely studied[33, 45, 72–76], and protein monolayers have been previously immobilized or adsorbed on nanomaterials such as carbon nanotubes[39], gold nanoparticles[38, 77, 78], and on metal oxide nanomaterials such as SiO_2[30, 79], TiO_2[80, 81], and ZnO[82, 83]. Here I review some of the fundamental materials properties which affect protein adsorption and briefly review

some important trends observed in recent studies.

1.3.3.1 Morphology

The size[34], curvature[32], rigidity[84], shape[31, 61], and roughness[64] of a material will impact protein adsorption. These properties are largely coupled for non-planar interfaces and isolating their individual effects is difficult. For instance, increasing the size of a spherical microparticle will decrease the surface curvature, making the surface appear more planar to an adsorbing protein. The amount of protein adsorbed per unit area is frequently increased on high-curvature surfaces, due to the reduced steric repulsion between charged, adsorbed proteins[30, 34, 85, 86].

However increasing the curvature can alter the adhesion properties of a polymer, surfactant, or protein at an interface. For example, in theoretical studies[87] of poly(3-hexylthiophene) adsorption on rutile (110), which is electrostatically attracted[88] to the interface, the polymer's adhesion strength was significantly reduced on highly curved surfaces.

Changing the curvature can also alter the morphology of the adsorbed layers. Investigations of phosphatidylcholine lipid adsorption on SiO_2 particles showed that on highly curved surfaces, lipids will form bilayers with widely separated outer polar heads, which then interdigitate to compensate for the increased outer head group spacing and high free volume[89].

The roughness of the substrate is particularly important for utilizing materials as biomedical scaffolds. Studies of collagen, which can self-assemble in solution, showed that the morphology of the adsorbed protein, but not total coverage, depends on the roughness of substrate[90]. On smooth surfaces the collagen formed supermolecular assemblies, while on rough surfaces it did not, potentially due to differences in the protein's surface mobility.

Deposition of nanometer-sized grains of hydroxyapatite on titanium orthopedic implants improved the adhesion of bone-forming cells (osteoblasts) and osseointegration[91].

There are differing opinions and contrasting results as to the the effect of curvature on protein stability. For instance, the native structure of lysozyme[34] and human carbonic anhydrase[32] was more retained when adsorbed to SiO_2 nanoparticles with higher curvatures (smaller particles). However, Ribonuclease A was found to be destabilized on high curvature surfaces and the extent of unfolding was observed to increase with surface curvature[30].

1.3.3.2 Surface Coordination, Polarity, and Interfacial Properties

Recent studies also highlight the effect of size and curvature on nanomaterial surface chemistry and exposed functional groups. As an illustration, as the size of TiO_2 anatase nanoparticles was progressively increased from 6 nm to 104 nm the isoelectric point (pI) progressively decreased from pH 6.0 to pH 3.0[92]. As will be discussed later, the change in the surface acidity results from changes in surface coordination resulting from defects or structural changes[93]. It is well known that increasing the presence of surface defects or undercoordinated ions, or dangling bonds can have cytotoxic effects[94, 95]. Molecular water or hydroxyl groups (resulting from dissociative adsorption) will generally replace sites where structural ligands have been lost or surface atoms removed due to defects or undercoordination[96]. These changes drastically alter the effective biological identity of the interface[10, 72].

Changes to surface hydrophobicity will impact protein affinity and interactions at the interface[31, 33, 47, 66, 71, 97–100]. Proteins typically adsorb to highly polar interfaces and studies suggest that this may facilitate protein conformational changes that increase the number of interprotein or protein-surface contacts.[31]. In particularl, glycoproteins

and membrane proteins are extensively adsorbed on hydrophilic surfaces, as hydrophilic objects prefer to be oriented in a polar or ionic environment[44, 61, 84]. Significant protein unfolding typically occurs at hydrophilic interfaces. In addition to the entropic gain, this improves the ability of the protein to form ion pairs with oppositely charged surface groups at the interface and is enthalpically favored[43].

Recent work has suggested that undercoordinated transition metal ions could modify protein-protein interactions and promote protein self assembly[101–103]. This is a topic I will return to shortly.

1.4 Parameter Space

There are many possible ways to customize either a (nanomaterial) interface or protein to assemble into larger structures. In figure 1.1, I broadly classify techniques to achieve supramolecular or hierarchical structures of proteins either on their own, or by including a nanomaterial interface. Although a variety of techniques exist to assemble hierarchical protein structures, they remain limited in their scope, stability, and specificity. Moreover, techniques which rely on protein-engineering or modification are extremely limited[14] and frequently alter the structure and function of the protein of interest[12].

Clearly the least laborious and powerful route is to utilize an engineered material template or interface which can promote assembly by a gentle, non-covalent mechanism. Although non-covalent mechanisms are known[5, 77, 104], they have so far not been utilized to create large hierarchical protein-structures which are functional and in the case of enzymes, retain their catalytic activity and accessibility.

It is clear that there are a vast number of properties which one can explore. Nanomaterials are particularly useful for enzyme immobilization due to their high surface-to-volume ratios,

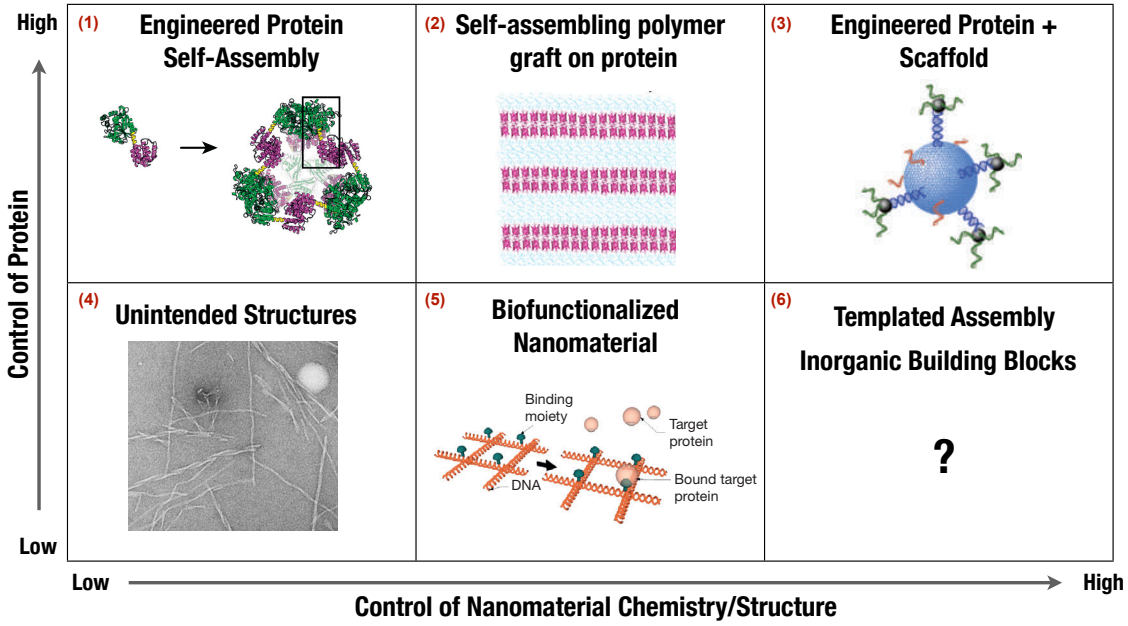

Figure 1.1: Examples of self-assembled or templated structures that can be achieved and the level of control or customization needed of either the material interface or the protein. **(1)** Proteins can be engineered with specific structural motifs and programmed to self-assemble[14] **(2)** Proteins are chemically grafted with block copolymers which will self-assemble into a globular protein-diblock copolymer, upon solvent evaporation[15] **(3)** Engineered gold nanoparticles and synthesized DNA linkers can be used to create complicated structures based on sequence specific interactions and annealing[105] **(4)** Amyloid fibrils of β2-microglobulin peptides induced by polymer nanoparticles[106] **(5)** A target protein can be captured onto an interface by chemical grafting of its binding partner (for instance Avidin-Biotin) onto a material interface[84] **(6)** Idealization of what is needed, maximum control of nanomaterial, minimum customization of the protein needed. *Portions of illustration excerpted from sources indicated above[14, 15, 84, 105, 106]*

varied hydrophilicity, porosity, unique surface chemistries, and electrical properties[77, 95, 105, 107, 108]. Furthermore, they can be easily integrated into electrical devices which exploit their chemical, optical, or electrical properties for biosensing or other detection applications[34, 80, 109].

Recent work has suggested that undercoordinated transition metal ions could modify protein-protein interactions and promote protein self assembly[101–103]. A material with a high density of undercoordinated transition metal ions could be useful for enzyme immobilization or templating the assembly of larger structures. Significant progress has been made

in the synthesis of nanomaterials with unique structures and morphologies[110] which expose and stabilize undercoordinated transition metals on the surface[107, 111–113]. These surfaces could provide a high surface area and high density of undercoordinated transition metal sites needed for such applications.

In this dissertation I report the first successful non-covalent assembly of enzymes into an insoluble solid that contains over 99% enzymes by weight and has enhanced catalytic activity. This is achieved by a novel enzyme assembly mechanism enabled by the unique, undercoordinated, surface chemistry of the TiO_2 anatase (001) surface. After introducing an extremely low concentration of TiO_2 nanotubes, which have an active anatase-(001)-like surface, into an enzyme solution, I first observe the growth of multilayer enzyme coatings on the nanotubes, followed by assembly of such enzyme-coated objects into large micron-sized structures. I demonstrate that the nanotube's stable undercoordinated Ti sites are required for this phenomenon. Evidence indicates that an enzyme monolayer adsorbs to the nanotube surface, interacting with the undercoordinated Ti sites of the anatase (001) surface. This monolayer acts as a seed for the further adsorption, with coverages equivalent to more than 50 layers of enzyme. Finally these enzyme-coated nanotubes reach a critical size, and self-assemble along with additional free enzyme, forming larger micron-sized structures.

This, I believe, is the first report of non-covalent immobilization of extensive protein multilayers on a nanomaterial and the first report of the emergence of a self-assembled mesophase of protein-nanotube conjugates. These findings present a nanotechnology-enabled mechanism of biomaterial growth and open a new route for creating stable protein-based materials, in particular, enzyme-based biocatalysts.

1.5 Overview of Dissertation and Organization of Chapters

In this dissertation, I explore the use of inorganic materials as templates to assemble functional biomolecule assembles and I report and characterize a novel phenomenon - the self-assembly of micron-sized, catalytically active, enzyme-based materials, initiated by the surface chemistry of the anatase (001)-like surface of titania nanotubes. Here I primarily utilize a stable globular protein, Ribonuclease A, to demonstrate and characterize this phenomenon, which occurs through a process of multilayer adsorption of the protein onto the nanotube surface, forming multilayer coated enzyme-structures which subsequently self-assemble.

To the best of my knowledge, I have detailed a series of phenomena which have never been previously reported with any material, including the titania nanotube. These phenomena include extensive non-covalent multilayer adsorption of protein onto a surface, self-assembly of protein-nanotube conjugates into catalytically active biomaterials, and the non-covalent assembly of enzymes into an insoluble solid containing in excess of 99% enzyme by weight with enhanced catalytic activity.

This dissertation is guided by a series of fundamental questions and is organized as follows:

In **chapter 2** I detail the the synthesis of novel titanium dioxide nanomaterials, used in this dissertation, and characterize the surface chemistry and structure of these materials through detailed measurements with x-ray diffraction, solid state nuclear magnetic resonance, thermogravimetric analysis and electron microscopies. I further detail ways to tailor the morphology and dispersion properties of the nanotubes, examine their colloidal stability, and detail their role in creating particle-stabilized emulsions.

In **chapters 3 and 4**, I investigate how a material with unique structural and surface prop-

erties can influence and control the orientation, structure, and morphology of biomolecules.

In **chapter 3** I characterize the adsorption of Ribonuclease A on the surface of Titania nanotubes and demonstrate that the amount of adsorbed protein vastly exceeds monolayer loading capacities. I develop a model of concentric multilayer adsorption to account for the surface coverage and examine the role of protein structure, charge, and conformation on this phenomena.

This is continued in **chapter 4**. In this chapter, I investigate the overall structure, size, and the assembly process of RNaseA-TiNT structures. Using dynamic light scattering and adsorption measurements, I show that assembly proceeds in two steps. First protein adsorbs onto the nanotube in concentric multilayers. Above a critical concentration, these protein-nanotube conjugates self-assemble with addition of free protein, forming micron-sized protein-nanotube structures. I then present a thermodynamic model of assembly and use this to understand the process of assembly. Finally, I reexamine the surface characteristics of the nanotube and how they might contribute to this phenomenon. I investigate whether these interactions occur on other materials, detailed in **chapter 2**, and detail how these findings inform the creation of other useful substrates for protein immobilization or creating hierarchical assemblies.

In **chapters 5 to 7**, I examine how the structure and function of adsorbed or assembled protein is affected by the surface geometry and coordination of the nanotube and whether functional, active, and stable non-covalent assemblies can be created.

In **chapter 5** I examine whether the significant protein adsorption or the formation of protein-nanotube aggregates is due to protein oligomerization. I also investigate the enzymatic activity of the resulting protein-nanotube hybrids and demonstrate that the self-assembled RNaseA-TiNT structures either retain or have enhanced enzymatic activity. I use this to understand the microstructure of the nanotubes. As an aside, I also examine the

cytotoxicity of the nanotubes.

In **chapters 6 and 7** I review the thermodynamic basis for performing differential scanning calorimetry to investigate protein structure, stability, and interactions and subsequently use this to investigate multilayer adsorption of Ribonuclease A on titania nanotubes and the process of self-assembly. I examine the enthalpic and entropic contributions to this process and the potential implications of these findings for customizing and directing the assembly of hierarchical structures.

Finally, in **chapter 8**, I briefly examine this research as an entirety, assembling the understanding I have gained from previous chapters. Furthermore, I detail gaps I perceive in my current understanding of this phenomenon and suggest experiments and theory that would help to resolve these remaining questions. I further detail possible commercial and scientific applications for these findings.

CHAPTER 2
TITANIA NANOMATERIALS - STRUCTURE, SYNTHESIS, AND SURFACE CHEMISTRY

2.1 Introduction

Water is a typical solvent for both colloidal and biological systems. An understanding of the structural and dynamic properties of water at the interfaces of these materials is critical to understanding a wide variety of biophysical, materials, and interfacial phenomena. Fundamentally, interfacial water is critical to macromolecule and ion solubility[58] and biomolecule stability[10, 114–116]. The structure of interfacial water also impacts the interparticle and intermolecular forces which govern colloidal stability[117, 118] and adsorption[58, 63].

The interaction between immobilized transition metals and amino acids is a well known phenomenon[119] and non-covalent interactions between transition metal ions and protein surface residues can modify protein-protein interfacial interactions. Recent work has suggested that undercoordinated transition metal ions could modify protein-protein interactions and promote protein self assembly[101–103].

In this chapter, I characterize the structure of titania nanotubes and other anatase nanomaterials. Furthermore, using a variety of instrumental techniques, I examine the surface chemistry, morphology, and structure of these materials in an attempt to understand how we can create a material which has a high density of undercoordinated surface groups. Finally, I briefly discuss some of the unique interfacial properties of the nanotube and techniques

I have developed to modify the surface chemistry and form stable suspensions in aqueous solution.

2.2 Materials and Methods

2.2.1 Chemicals

Chromatographically purified lyopholized Bovine Pancreatic Ribonuclease A (RNaseA), titanium(IV) n-butoxide (TNBT; 97%) and Hydrofluoric Acid (HF, 48 wt% in H_2O) were purchased from Sigma Aldrich (St. Louis, MO). 1 M 2-[4-(2-hydroxyethyl)piperazin-1-yl]ethanesulfonic acid (HEPES) buffer (pH 7.2) and NaOH were purchased from Fisher Scientific (Hampton, NH). 32 nm anatase TiO_2 nanoparticles were purchased from Alfa Aesar (Ward Hill, MA). All chemicals were used without further purification.

2.2.2 Nanomaterial Synthesis and Processing

I created three types of anatase nanomaterial's were create in the the laboratory. As detailed below, using commercially available anatase nanoparticles, I synthesized titania nanotubes using a hydrothermal alkaline method. The resulting nanotubes are referred to as long titania nanotubes. Subsequently, I developed two different techniques to shorten these nanotubes and improve the suspension of these nanotubes, these methods, shortening and cryomilling, are described below.

2.2.2.1 Long Titania Nanotube Synthesis

Titania Nanotubes were hydrothermally synthesized and shortened as previously described[111, 113]. Briefly, 32 nm anatase nanoparticles (4 g) were added to freshly prepared 10 M NaOH (400 mL). The mixture was then sealed in a custom made PTFE-lined stainless steel vessel and maintained at 135 °C for 72 hr. The resulting material was repeatedly washed with distilled water or HCl (0.1 M) until the supernatant reached a pH of 5 - 6. The full synthesis protocol is detailed in the appendix of this chapter.

2.2.2.2 Shortened Nanotube Production

The nanotubes were shortened by wet ball milling in a laboratory ball mill (Glen-Mills, Clifton, NJ). Approximately 50 mL of the nanotube suspension mixed with 30 g of 100 µm diameter ZrO_2 beads (Glen-Mills) in a grinding vessel and ground for 30 minutes. The grinding vessel was surrounded by a cooling bath which kept the grinding vessel temperature below 100 °C. Following ball milling, the supernatant, which contains only shortened nanotubes, was decanted and centrifuged to remove any excess grinding media. The resulting suspension was filtered through a 0.2 µm polyethersulfone membrane (PES) membrane filter (Millipore, Billerica, MA). The nanotube concentration was determined by TGA on a Q5000IR TGA or a Discovery TGA (TA Instruments, New Castle, DE).

2.2.2.3 Cryomilled Nanotube Production

"Cryomilled" nanotubes were also produced by wet ball milling in a laboratory ball mill (Glen-Mills, Clifton, NJ). Here either the nanotubes were used in the suspended form previously described or the suspension of long-nanotubes was further concentrated by pelleting the nanotubes in a centrifuge and removing the clear supernatant solution. Typically, ap-

proximately 50 mL of the concentrated nanotube suspension was mixed with 30 g of 100 µm diameter ZrO_2 beads (Glen-Mills) and was placed in a grinding vessel. The grinding vessel was surrounded with a cooling ice bath and placed inside a refrigerated room held at 4 °C and the suspension was then ground for up to 45 minutes. Following ball milling, the supernatant, which contains only shortened nanotubes, was decanted and centrifuged to remove any excess grinding media. The resulting suspension was filtered through a 0.2 µm PES membrane filter (Millipore, Billerica, MA). The nanotube concentration was determined by thermogravimetric analysis on a Discovery TGA (TA Instruments, New Castle, DE).

2.2.2.4 Anatase Nanotiles Synthesis

Anatase nanotiles were synthesized similarly to previous publications[120]. Typically, titanium(IV) n-butoxide (21 mL, 0.579 mol) and Hydrofluoric Acid (1.6 mL, 0.005 mol) were combined in a PTFE-lined stainless steel autoclave and maintained at 180 °C for 24 hours. The resulting precipitate was repeatedly washed with ethanol and distilled water. Subsequently it was dried under vacuum and calcinated in air at 400 °C for 1 hour. The resulting precipitate was dispersed in water and dialyzed against a 500-fold excess of 25 mM HEPES for 72 hours; the dialysate was exchanged every 24 hours.

2.2.3 Experimental Measurements

2.2.3.1 Dynamic Light Scattering and Zeta Potential Measurements

Dynamic light scattering (DLS) measurements were performed at $\theta = 173^\circ$ on a Malvern Zetasizer Nano ZS (Malvern Instruments Ltd., Worcestershire, UK) using either a disposable folded capillary cell (Malvern) or a disposable low-volume sizing cuvette (Brandtech). Measurements were performed in triplicate at 25.0 °C and allowed to equilibrate for a mini-

mum of120 s prior to measurement. Measurements were analyzed in software provided with the instrument using cumulant analysis, as outlined in chapter 3. Zeta potential measurements were performed in triplicate using the disposable folded capillary cell (Malvern) on a Malvern Zetasizer Nano ZS equipped with a MPT-2 Autotitrator (Malvern), vacuum degasser, and liquid filled glass combination electrode. Prior to the experiments, the electrode was calibrated with three pH buffer standards (Fisher Scientific). Automated pH titration was employed for isoelectric point measurements. Standardized HCl and NaOH solutions (Sigma Aldrich) were used as titrants.

2.2.3.2 Electron Microscopy

To prepare TEM samples, the samples were drop deposited onto a 300 Mesh lacey carbon grid (Ted Pella, Redding, CA) and allowed to dry in air. High-resolution TEM imaging was performed at either 180kV or 200kV on a JEOL 2010F-FasTEM. Images were acquired using a 2k x 2k Gatan CCD bottom mount camera. SEM imaging was performed on a Hitachi S-4700 field emission SEM at 5kV and a FEI 600 Helios NanoLab DualBeam at 15 kV. Where indicated, prior to imaging at 15 kV, a 2.5 nm thick layer of Au/Pd was sputtered onto the sample in an Argon plasma (Cressington Scientific Instruments Ltd, Watford, England).

2.2.3.3 Thermogravimetric Analysis

Anatase nanomaterials were dried in a vacuum oven (Yamato ADP-21, Yamato Scientific America Inc., Santa Clara, CA) at 50 °C overnight and equilibrated under ambient conditions (RH $\approx$40%) for a minimum of 30 days. TGA was performed with a Discovery TGA (TA Instruments, New Castle, DE) in platinum pans.

Except where indicated, measurements were performed at 10 °C min^{-1} from 45 °C to

600 °C using a dry nitrogen atmosphere with a constant flow rate of 10 mL min^{-1}

2.2.3.4 X-Ray Diffraction

Samples were dried in a vacuum oven (Yamato ADP-21, Yamato Sciencific America Inc., Santa Clara, CA) at 50 °C and the dry pellet was gently broken up using a mortar and pestle. XRD was performed on powder samples using a Rigaku Multiflex XRD with a monochromatic Cu 40 kV/40mA beam source (λ=0.154 05 nm). Acquisitions were taken at 0.25 ° min^{-1} with a resolution of 0.02°.

2.2.3.5 Solid-State NMR

^{1}H solid-state nuclear magnetic resonance (NMR) measurements were performed on a 9.4 T (400 MHz) 89 mm magnet (Agilent, Wilmington, DE) with an 18 channel shim (Magnex, Oxford, UK), which was used to remove significant magnetic field inhomogeneities. Shimming was performed at the field center on a 10% H_2O/90% D_2O sample until the 4.9 ppm water peak was symmetric and had a FWHM < 0.5 ppm. Spectra were acquired using either a 2.0 mm or 2.5 mm double-resonance magic angle spinning (MAS) probe (Revolution NMR, Fort Collins Co.) using either a 2.0 mm or 2.5 mm diameter Zirconia spinners with a nominal volume of 11 µL with either Kel-F or Torlon caps and spacers, and Torlon drive caps (Revolution, NMR). The probe was interfaced with a Tecmag Apollo Spectrometer (Tecmag, Houston, TX) and SU-24 shim power supply unit (Tecmag) and a 500 W broadband power amplifier (CPC Inc, Hauppauge, NY).

MAS was driven by compressed dried air which was fed from the building's air handling supply. The air was desiccated and filtered down to 0.1 µm to remove any dust particulates, moisture, or oil. It was then fed into a 120 gallon air ballast, held at 90 PSI. This air was supplied to a high-flow rate non-relieving regulator, across which the pressure was dropped

65 PSI and fed into the individual regulators controlling the MAS gases. This was used to ensure adequate supply of dry air for the MAS and to minimize pressure fluctuations resulting from changes in the buildings air supply.

The MAS speed was first manually set by adjusting the pressure of the drive and bearing gases and monitored by a fiber optic tachometer (Revolution NMR). Subsequently, the speed was automatically controlled by varying the flow rate of the drive gas using a mass flow controller (MassTrak 810, Sierra Instruments, Monterey, CA) coupled with a computer-controlled feedback circuit (MAS Spin-Speed Controller, Revolution NMR). The proportional, integral, and derivative (PID) parameters for the controller were set using a powder-filled spinner prior to the start of experiments. In a typical experiment, the mean spinning speed was within 0.2 Hz of the set point (typically 26 kHz) and had a standard deviation of less than 2 Hz.

The sample rotation angle was set to the magic angle, θ_M=54.74° by spinning a rotor filled with KBr (Sigma Aldrich) and examining the ^{79}Br resonance. The deviation from the magic angle was set to extend the rotor echos beyond 8 ms and was quantified in the frequency domain by the ratio of the height of central peak to the second spinning sideband. The angle was adjusted until the ratio was less than 20, which corresponds to an approximate deviation of 0.1° from the magic angle, 54.74°.

The resonant frequency, power levels, and pulse widths were calibrated prior to experiments using the proton resonance from 10% H_2O/90% D_2O and optimized under MAS using either Hexamethylbenzene or Adamantane (Sigma Aldrich). The exact parameters for specific experiments and measurement methods are detailed within the chapter.

2.3 Titanium Dioxide

Titanium(IV) dioxide (TiO_2 or titania) is a naturally occurring metal oxide which forms three major crystal polymorphs under natural conditions: rutile, anatase, and brookite[121]. Both rutile and anatase are widely used in consumer products — as opacifier or white pigment in paint, cosmetics, food coloring, and as a thickener[122].

TiO_2's modern prevalence is largely related to its high refractive index and high UV-absorbance. These properties have contributed to its widespread use as a sunscreen and as a UV-blocking additive for polymers. Furthermore, titania, especially anatase, is an excellent photocatalyst[123] and is widely used in solar cells and for other photocatalytic applications[107]. Among the three different crystal polymorphs, commercially available titania nanoparticles are most commonly anatase[111].

Anatase has a tetragonal unit cell of dimensions a=b=3.782 Å and c=9.502 Å, with a bulk structure shown in Figure 2.1, and belongs to symmetry group D_{4h}^{19}-$I4_1/amd$. The unit cell is essentially formed by a distorted octahedral configuration consisting of a titanium surrounded by six oxygen atoms. The equatorial bond between the oxygen and titanium is 1.94 Å, while both of the apical bonds, which form along the [001] direction are elongated to 1.98 Å[124]. The corner-sharing octahedra form the (001) planes. The edges formed by these octahedra are connected to the octahedra below; this stacking results in purely threefold coordinated oxygen[121].

2.4 Structure of Titania Nanotubes

The titania nanotube is formed from a delaminated anatase basis, exposing a surface which is dominantly made up of stable undercoordinated titanium sites. Its unique surface

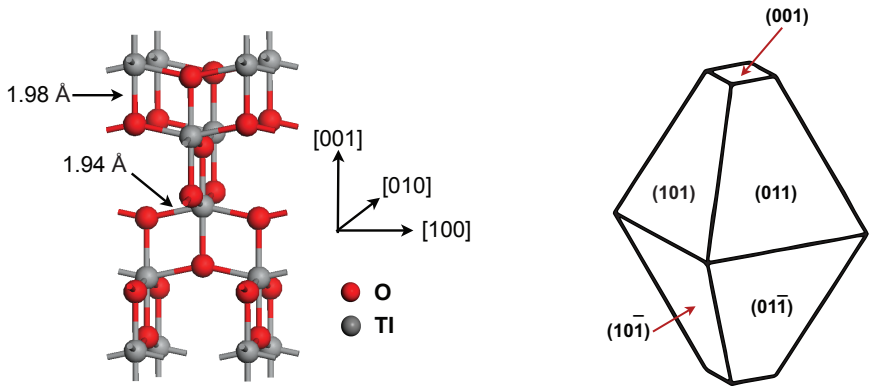

Figure 2.1: *(Left)* The bulk structure of anatase is formed by a distorted octahedral configuration of titanium and oxygen. The structural anisotropy is highlighted by the differing apical and equatorial bond lengths. *(Right)* The Wulff construction of anatase approximates the equilibrium crystal shape and crystal plane exposure. The minority surface of anatase the (001) plane is shown at the top, figure after Vittadini *et. al.*[125].

chemistry has been well documented[111, 112]. As illustrated in figure 2.2, this is formed by cleaving the anatase unit cell through the apical bonds, along the [001] direction, at 0.65 of the unit cell height. As seen in figure 2.3A, this unit is then stacked along the [001] direction with an interlayer spacing of 8.7 Å, with each layer shifted by half a unit cell in the [100] and [010] directions to account for the glide shift between layers observed in previous TEM studies[111]. Curving the delaminated anatase (001) surface around the [010] axis (figure 2.3B), results in a loss of registry between adjacent layers, which agrees with the experimentally observed glide shift. The resulting nanotube has an approximate inner diameter of 6 nm. It is typically 3-4 layers thick, and has an approximate outer diameter of 12 nm.

The surface coordination of the delaminated anatase unit differs from the clean anatase-(001) surface. The exact implications of this will be discussed later in this chapter. On the clean anatase-(001), the surface Ti groups are all five-fold coordinated and bonded to 2-fold coordinated bridging oxygens[125]. As seen in figure 2.3C, similarly to the clean anatase-(001) surface, all of the exposed Ti on the nanotube surface are 5-fold coordinated, however here half of the surface oxygen groups are now 3-fold coordinated, while half remain 2-fold

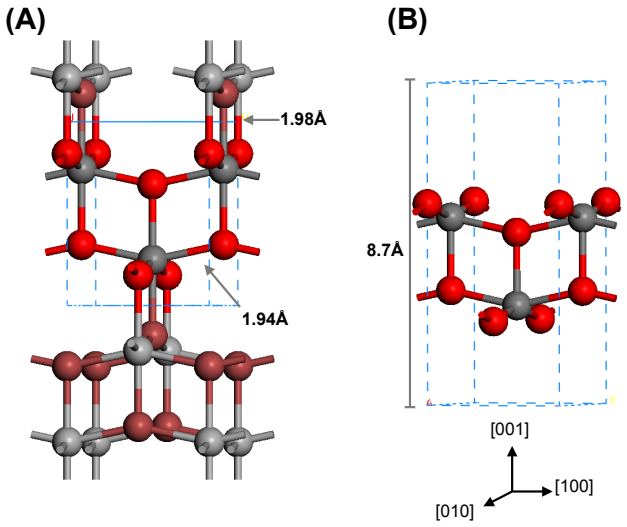

Figure 2.2: Structure of bulk anatase and delaminated anatase vacuum slab used in simulations, where titanium is represented by grey balls and oxygen by red balls. The different shades of red and grey are only used to visually highlight the region which is cleaved. (A) Structure of bulk anatase, the equatorial bond length (1.94 Å) and apical bond length (1.98 Å) are indicated. The dashed blue bounding box indicates bonds cleaved to form delaminated anatase unit used in simulations. Bulk anatase is cleaved through the apical bonds, along the [001] direction at 0.65 of the unit cell height. (B) a vacuum slab of the delaminated anatase unit used in simulations. The vacuum size height was fixed at 8.7 Å and centered around the cleaved slab to match the experimentally observed interlayer spacing.

coordinated.

This model is in agreement with experimentally observed TEM imaging. As seen in figure 2.4, TEM imaging shows elongated structures with 3-4 walls with an interlayer spacing of 8.7 Å; the nanotubes are open at the ends. Typically, the inner diameter measured by TEM ranges between 4 nm to 5 nm.

In figure 2.5, I show the experimental XRD pattern of the nanotubes along with simulated XRD patterns the delaminated anatase unit cell, (shown in figure 2.5A), and the nanotube model constructed from this (shown in figure 2.5C). I performed the simulations in Accelrys Materials Studio using the Reflex Powder Diffraction module at a step size of 0.2°. Without applying constraints, the simulation is performed by assuming that the unit cell repeats infinitely in all directions. For the nanotubes, this would physically equate to an

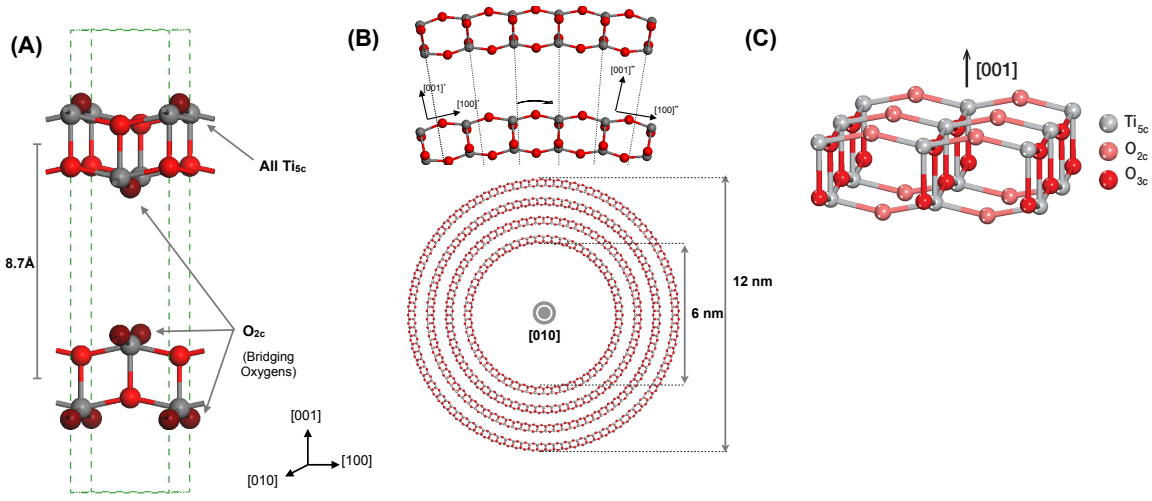

Figure 2.3: Structure of delaminated anatase unit cell and construction of nanotube. (A) DA unit cell is (B) curved around the anatase [010] axis, resulting in a loss of registry between adjacent layers, as indicated by the dashed lines which show the distortion of the crystal planes parallel to the nanotube axis. The glide shift between layers is 78°. (C) The exposed surface contains both 2-fold and 3-fold coordinated oxygen on the surface.

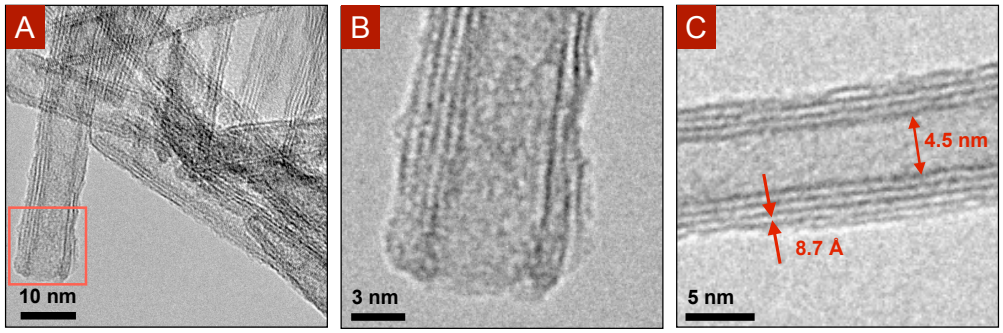

Figure 2.4: TEM imaging of long nanotubes. (A) the open end of nanotube is outlined in red and shown in (B) Measurements of the interlayer spacing and inner diameter are shown in (C).

infinitely large array of aligned, oriented nanotubes and would generate peaks associated with the spacing between the nanotubes. The nanotubes were never observed in TEM or SEM to align in an oriented manner.

Effectively this equates to the difference between examining a single crystal with XRD versus a polycrystalline sample. Therefore, I performed the simulations by imposing constraints to approximate the physical size of the crystallite ”grains” observed[111]. The

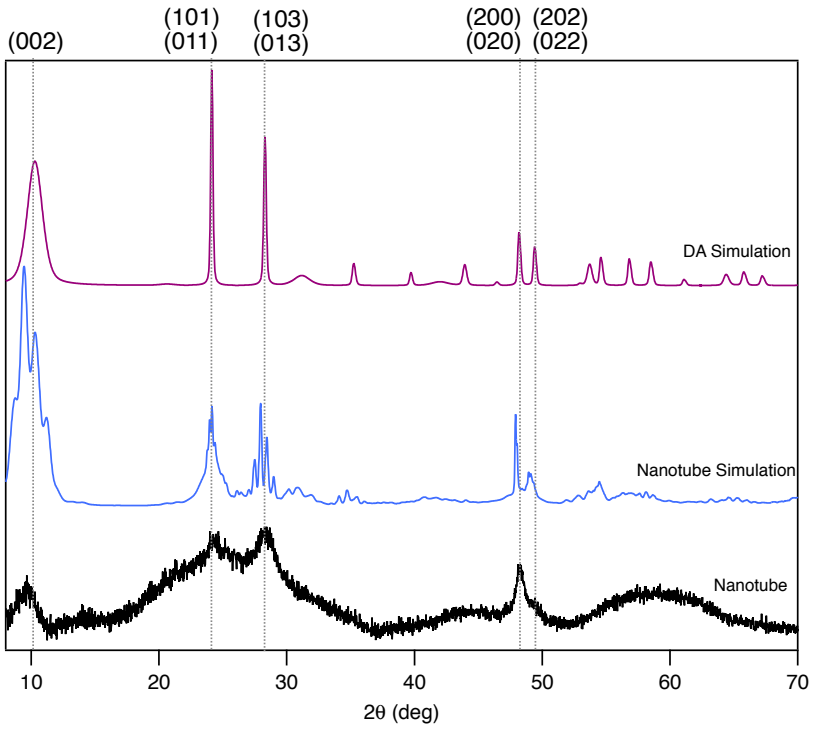

Figure 2.5: XRD of titania nanotubes. Simulated XRD pattern of delaminated anatase structure, and nanotube made out of delaminated anatase. The experimental XRD of the nanotube is shown at the bottom. The large peak centered around 60° is a result of the amorphous silicon sample holder used in diffractometer. The corresponding crystal planes based on the structural model are indicated at the top.

crystallite size of the delaminated anatase unit was constrained to the typical width of the 4 layers (5 nm) in the [001] direction, while the crystallite size of the nanotubular model was constrained to match the diameter of the tubular unit cell (14 nm) and typical length observed in TEM (500 nm). Despite this the simulated XRD peaks are significantly narrower than the experimentally observed peaks. This occurs due to the finite size and polydispersity of the nanotubes examined with XRD as well as the instrument resolution (FWHM=2.1°).

The low angle XRD peak at 2θ=10.2° corresponds to the observed interlayer spacing of 8.7Å. The (010) peak is absent due to the structure factor selection rules for anatase, which cancel the (010) reflection[112]. In the DA model, the peaks at 2θ=24° and 2θ=28° correspond to (101)/(011) and (103)/(013) planes, respectively. However, curvature removes the registry between parallel layers along the circumference. This distorts or eliminates the

peaks associated with these atomic planes. Specifically this is manifested by the elimination of the (101) and (103) peaks, whose registry occurs across layers in the [100] directions in the DA unit cell. The (011) and (013) planes remain in the tubular model, but the registry now occurs along the axis of the tube. The resulting parallel, but curved planes contribute to the broad reflections seen at 2θ=24° and 2θ=28°. Similarly, the (200) planes, which are parallel to the curvature, lose their coherence in the tubular model, while the (020) planes, which are perpendicular to the curvature, are unaffected.

2.5 Controlling the morphology and dispersion of Titania Nanotubes

There has been significant interest in developing a facile route to control the aspect ratio of titania nanotubes[83, 111, 112, 126–129]. Although the use of structure-directing agents[107, 128] or alternative synthesis routes[130] can yield alternative morphologies or structures, they have been unable to replicate the unique surface chemistry of the titania nanotube[120, 131]. Therefore, it is useful to develop and characterize post-synthesis processing techniques which can modify the morphology, aspect ratio, or dispersibility of the nanotubes. Furthermore, it would be highly desirable to do so without chemical modification or the addition of surfactants, as is needed with many other nanomaterials[132].

2.5.1 Shortened Titania Nanotubes

Many possible applications demand uniform stable suspensions of the nanotubes under aqueous conditions. The synthesized nanotubes have a typical length between 1 μm to 3 μm and in an aqueous environment they rapidly sediment to the bottom of the sample container. In SEM imaging of the sediment, I observe large intertwined aggregates of nanotubes, suggesting that the formation of larger aggregates may cause the nanotubes to sediment.

To improve the dispersion and create a more uniform solution of the nanotubes, I utilized wet mechanical ball milling, as detailed in the experimental section. An aqueous suspension of the nanotubes and large Zirconia beads were loaded into a modified blender, which was kept below 100 °C to prevent unraveling of the nanotubes or other structural phase transitions which occur at elevated temperatures[133]. The impact between the relatively fragile nanotubes with each other and the large Zirconia beads leads to mechanical attrition of the nanotubes and yields a good dispersion of nanotubes with a typical length of approximately 100 nm, shown in figure 2.6 and figure 2.7. As seen in figure 2.8. the shortened nanotube retains the characteristic XRD peaks of the longer nanotube, however the peaks here are broadened due to the decreased crystallite size.

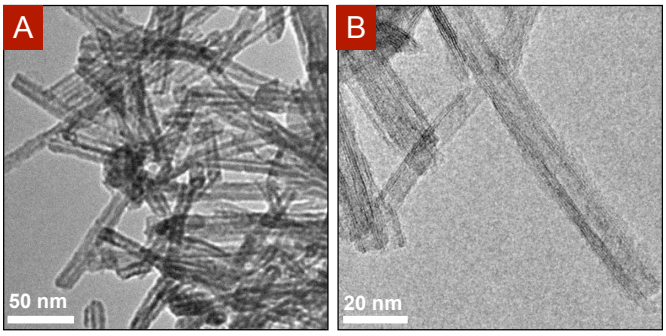

Figure 2.6: TEM imaging of shortened titania nanotubes.

The resulting dispersion appears polydisperse. A monodisperse dilute nanotube solution, of lengths L < 120 nm, would not appear polydisperse (optically polydisperse). Optical polydispersity would result from collective diffusion effects which occur at higher concentrations (*c.f.* Buitenhuis *et al*[134]). Therefore, to improve the dispersion and remove any remaining aggregates, I filtered the resulting solution of shortened nanotubes through a 0.2 µm membrane filter. Dynamic light scattering of the suspension before and after filtering, as seen figure 2.9, shows that filtering the suspension significantly reduces the polydispersity and also results in a highly stable dispersion. For example, the inset of figure 2.9 shows a filtered suspension which was allowed to sit untouched for over 6 months, the picture clearly shows no detectable sediment.

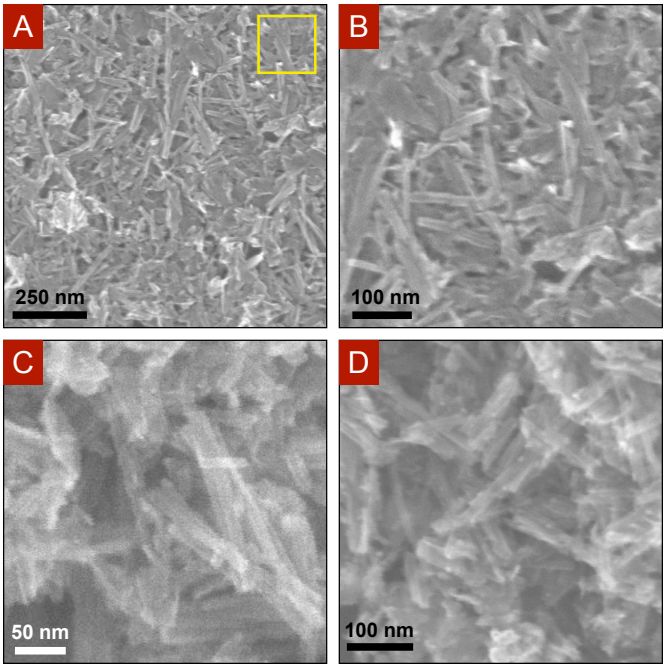

Figure 2.7: SEM imaging of short nanotubes. The yellow box in (A) indicates the approximate region shown in (B)

2.5.2 Cryomilling

The shortened nanotube suspensions typically had a concentration of TiNT in the range of 1 mg mL^{-1} to 2 mg mL^{-1}. For studying this interaction between the nanotube and biomolecules this far exceeds the needed concentrations. However for other applications of the nanotubes investigated in our group significantly higher concentrations are needed. Therefore, I developed a new method for improving the dispersion of higher concentrations of nanotubes. Hereafter this will be referred to as ”cryomilling.”

It is critical that the temperature of nanotube suspension during ball milling not exceed approximately 100 °C. Above this temperature, the nanotubes unravel into planar sheets of hydroxylated anatase-(001)[111]. Significant heat is generated by the collisions between the nanotubes, grinding media, and the sample container wall, as well as by motor used to turn the blade. Without cooling, the chamber temperature raises approximately 10 °C min^{-1}. Due to the low thermal conductivity of the polymer grinding chamber, adding an ice cooling

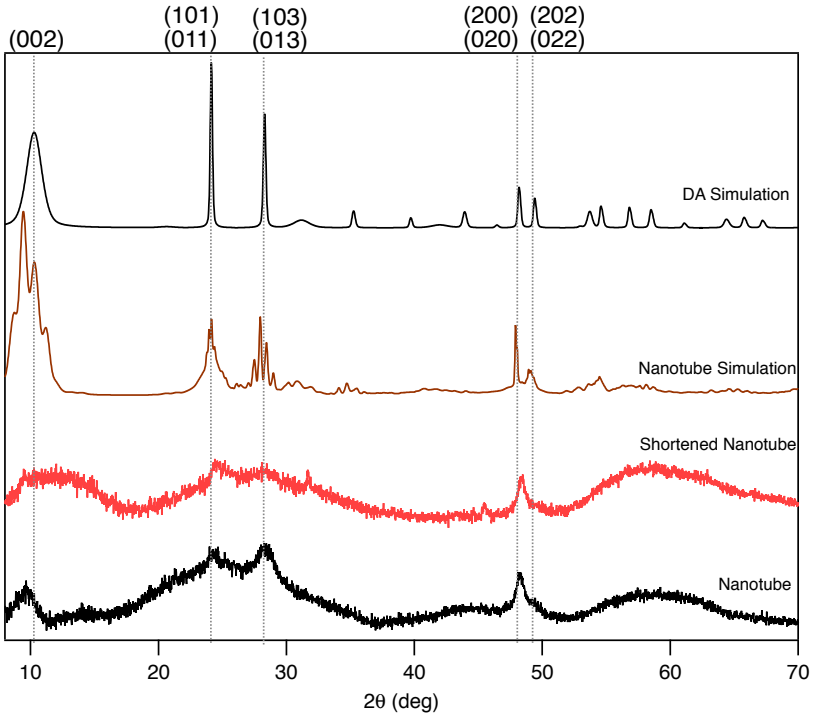

Figure 2.8: XRD of shortened titania nanotubes. The XRD spectrum of the shortened nanotube retains the primary peaks found in the nanotube. For comparison, the long (unshortened) nanotube spectrum is shown as well as the simulated XRD pattern of delaminated anatase structure and the nanotube made out of delaminated anatase. Again, the large peak centered around 60° is a result of the amorphous silicon sample holder used in diffractometer. The corresponding crystal plane assignment based on the structural model is indicated at the top.

bath around the sample container is only able to reduce the heating rate slightly, to approximately 4 °C min^{-1} to 8 °C min^{-1}. This required that the temperature and ice bath constantly monitored and frequently changed out. Furthermore, the motor on the blender apparatus frequently overheated, forcing me to halt the grinding.

Increasing the nanotube concentration within the ball milling chamber increases the number of nanotube-nanotube collisions and significantly improves the efficiency of shortening[135]. Although this improves the yield the necessary ball-milling time was not noticeably reduced. Therefore to ensure that the temperature of the motor and chamber did not overheat, I placed the sample container within a walk-in refrigerated room (4 °C). Optimizing this protocol both improved the apparent size dispersion of the nanotubes and

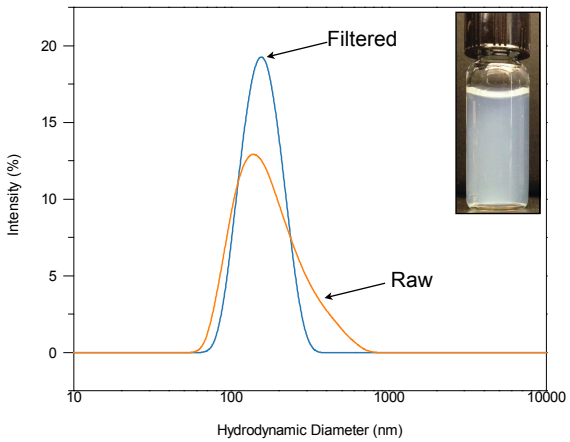

Figure 2.9: Dynamic light scattering of shortened nanotubes after ball milling (orange) and after filtering the suspension through a 0.2 µm PES filter. (Inset) Picture of filtered shortened nanotube dispersion after sitting untouched for over 6 months.

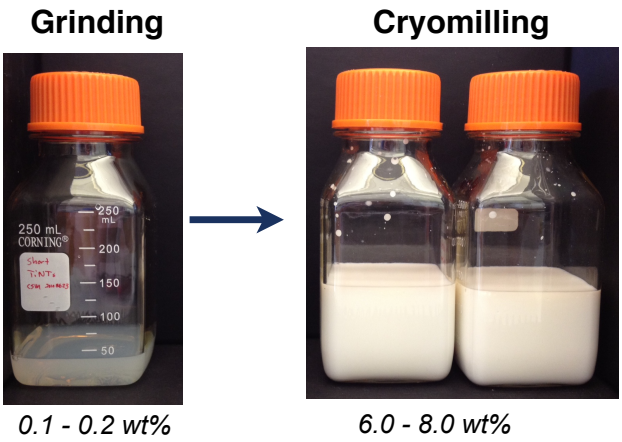

Figure 2.10: Images of the solution formed by traditional shortening (grinding) versus improved cryomilling process.

yield as compared to the previous shortening process, resulting in nanotube concentrations upwards of 60 mg mL^{-1} to 80 mg mL^{-1}, as seen in figure 2.10. Furthermore, it facilitated the use of larger 350 mL grinding containers, which improved the overall production rate.

TEM imaging of the cryomilled nanotubes (CM-TiNT) , as seen in figure 2.11, does not reveal any significant structural or morphological differences between the shortened nanotubes and the cryomilled nanotubes. Due to the increased concentration the density of nanotubes on the TEM grids was significantly higher. In the TEM imaging, I have

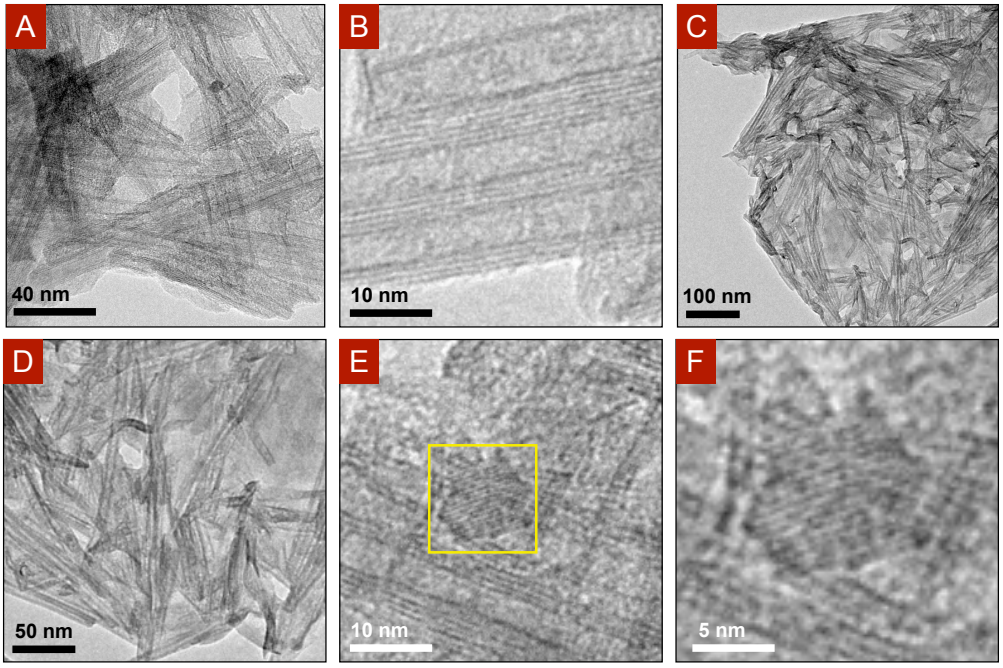

Figure 2.11: TEM imaging of cryomilled nanotubes. Box in (E) shows region examined in (F).

highlighted one region where a potential change is observed. Figure 2.11F shows a region with a large number of parallel lines. The lines here have the same interlayer spacing as the nanotube's walls, however the inner diameter of the nanotube, which would appear as a 5 nm gap, is clearly absent. Comparing the images in figures 2.11B and 2.11F, this image suggests that the increasing collision rate may produce some nanosheets, which typically are produced only at elevated temperatures[111].

2.6 ζ-Potential and Origin of Surface Charge on Titania Nanotubes

In aqueous media, metal oxides can obtain a surface charge by ionization of amphoteric surface groups or by the preferential adsorption of ions in solution[136]. The ionization of amphoteric surface groups is pH dependent. Dissociatable surface groups will release or take up a proton (H^+ ion) depending on the solution pH, or can interact with immersed

H^+ or OH^- ions. For a typical metal oxide, charging is typically caused by binding or dissociation of H^+ according to:

$$-M - OH_2^+ \underset{K_+}{\overset{H^+}{\longleftarrow}} \mathrm{M{-}OH} \underset{K_-}{\overset{OH^-}{\longrightarrow}} \mathrm{M{-}O^-} + \mathrm{H_2O} \tag{2.1}$$

In an electrolyte solution, the surface charge resulting from this process is compensated for by a counterion layer that forms around the surface. This layer, called the electric double layer (EDL), consists of a compact interfacial layer of charge and diffuse ion layer surrounding this. While a variety of models exist to approximate the potential distribution and dynamics at the interface, it is instructive to follow the approach of Stern[137]. In Stern theory, the double layer is divided into two parts – an inner layer consisting of immobilized ions which are directly adsorbed to the surface of the material, called the Stern layer, and an outer diffuse layer called the Guoy-Chapman layer, which consists of mobile ions that obey the Poisson-Boltzman equation.

Experimentally, measurement of the charge on the surface is quite challenging[136], however a variety of methods exist to measure the electric potential at the interface between the immobile Stern layer and the mobile diffuse layer. This potential is defined at the ζ potential.[138]. The point at which the ζ-potential is zero is defined as the isoelectric point (pI) . The concentration of potential-determining ions here provides an instructive way to compare materials and broadly examine the charge of the interface in solution[1].

I determined the zeta potential using phase-analysis light scattering[118]. Briefly, this technique determines the electrophoretic mobility of the nanotubes by examining the phase of light scattered off the nanotubes under a known applied field. Although on a primitive level the zeta potential can be determined from these measurements with the Smoluchowski equation[139] more advanced theory has been developed to provide a general relationship between the electrophoretic mobility and the zeta potential[118, 136, 139, 140]. These

models are implemented into measurement software.

In figure 2.12, I show measurements of the ζ-potential as a function of pH of two different batches of shortened titania nanotubes. The approximate isoelectric point is determined from a linear fit of the points adjacent to ζ=0 mV. These measurements reveal that the nanotube has an isoelectric point of approximately pH 2.7 - 2.8. This value is significantly lower than most previously published reports on anatase microparticles and nanoparticles. No concensus exists for the isoelectric point of anatase in general and it does appear to vary significantly with the history and preparation of the particle. For comparison, in figure 2.13, I plot a histogram of 72 different published measurements[1]. The isoelectric point occured at a mean pH of 6.0 ± 0.7.

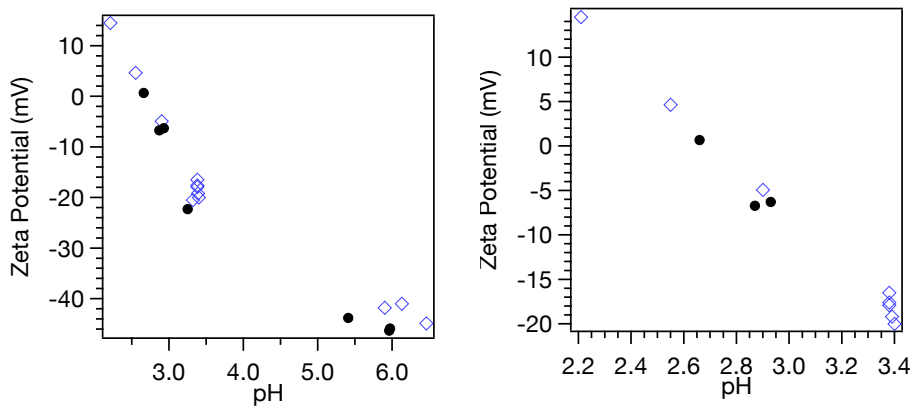

Figure 2.12: Zeta potential of two different batches of shortened titania nanotubes as a function of pH. The isoelectric point (pI) is approximately pH 2.7 to 2.8. (Left) Measurements over entire range of pH values examined (Right) Plot of the same data over a narrower pH region.

The low isoelectric point exhibited by the nanotube could result from increased lattice defects[140, 141] or the result of an increased number of acidic surface groups. This will be examined more in depth later in this chapter through NMR measurements.

In figure 2.14, I show zeta potential measurements of two different batches of cryomilled nanotubes and compare this with one of the short nanotube batches. All three exhibit similar zeta-potential as a function of pH. Furthermore, the cryomilled and shortened nanotubes

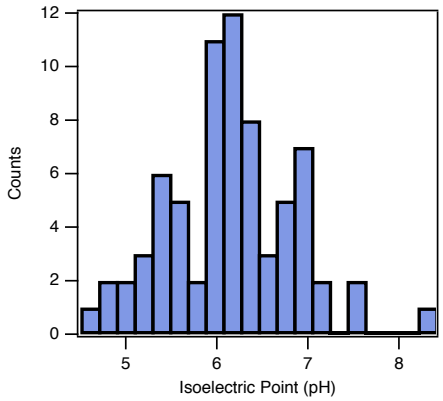

Figure 2.13: Histogram of different published isoelectric points for anatase (N=72). The average pI was 6.0 $\pm$ 0.7. Published values were accumulated from[1].

both have similar isoelectric points, varying between pH = 2.7 - 2.9, suggesting that the surface groups which contribute to the acid-base properties of the nanotubes remain intact. This is illustrated by the stability of the suspension as a function of pH, as seen in figure 2.15. The zeta potential is a good indicator of the colloidal stability of a particulate suspension[136]. At zeta potentials with a magnitude greater than 30 mV, suspensions are typically resistant to flocculation or aggregation due to the strong Coulombic repulsion between the particles. In figure 2.15, this is illustrated by increasing sediment formation below pH 5.2.

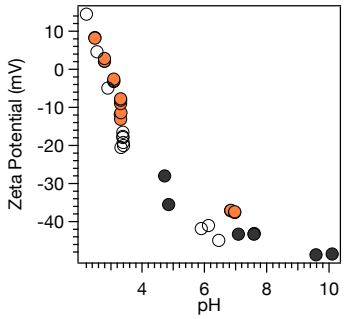

Figure 2.14: Zeta potential of two different cryomilled batches (filled circles) shown with shortened nanotubes (open circle) as a function of pH. Figure highlights similar behavior and isoelectric point occuring at approximately pH 2.7-2.9.

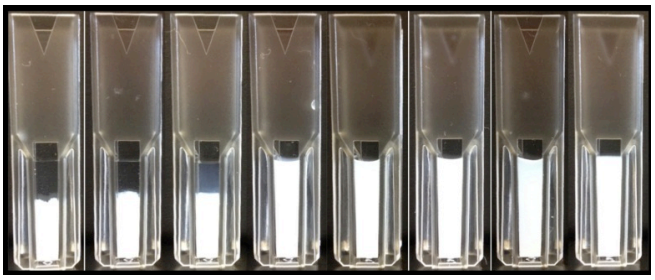

Figure 2.15: Photographs of the cryomilled nanotubes, at identical volume fractions, and different pH.

2.7 Pickering Emulsions of Cryomilled Nanotubes

Titanium dioxide nanotubes have numerous applications in petrophysical applications, including use as a dielectric contrast agent. In investigating some of possible applications, most of which is not detailed in this dissertation, I examined whether the cryomilled nanotubes would migrate to or aggregate at the oil-water interface.

I added kerosene or toluene to a dilute suspension of cryomilled nanotubes, as illustrated in figure 2.16. After briefly agitating the solution, I discovered that a large amount of nanotubes appeared to transfer to the oil phase. This was not observed in control samples. A stable water-in-oil (w/o) emulsion formed in the oil phase and contained 50 μm to 70 μm wide water droplets in the oil phase, as seen in figure 2.17 . Deemulsification occurred slowly and after 1 year a majority of the emulsion remained intact. The large droplet size (> 1 μm), high volume fraction of the disperse phase, and metastability are characteristic of macromelusions[138].

Oil and water are immiscible due to the high surface tension difference between them. Agitation can briefly form a dispersion, but once agitation is removed, the oil and water individually coalesce to reduce their total interfacial area and leads to complete phase separation[136]. In figure 2.17, I observe a continuous oil phase with a disperse water

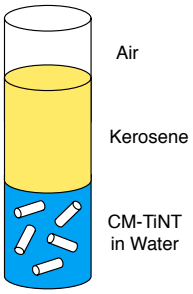

Figure 2.16: Illustration of sample composition used in investigations of oil-water interfacial aggregates.

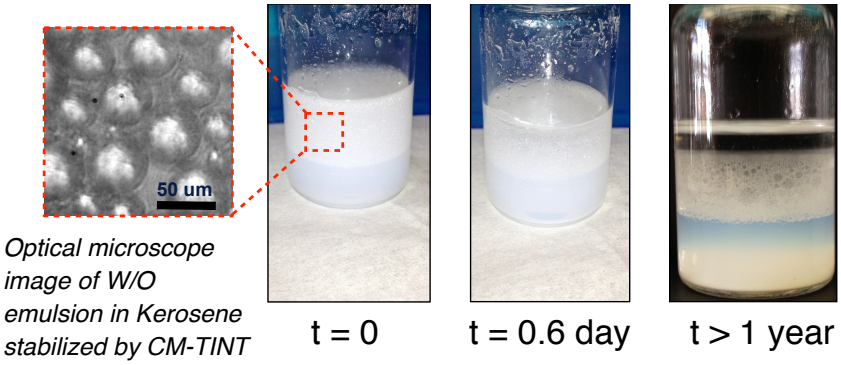

Figure 2.17: The adsorption of cryomilled nanotubes at the oil-water interface forms a highly stable water-in-oil emulsion. Shown at right, the emulsion is still intact after sitting for over 1 year.

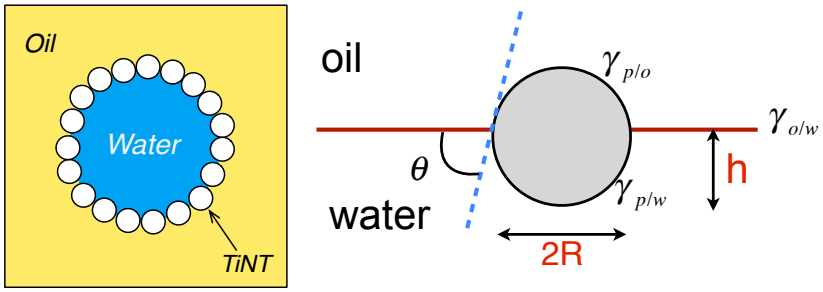

Figure 2.18: (Left) Illustration of a TiNT-stabilized water-in-oil Pickering emulsion. (Right) Illustration of a particle of radius R, at the oil-water interface. Labels refer to interfacial tension, γ, between the p(article), o(il), and w(ater) phases.

phase. These emulsions only formed in the presence of the cryomilled nanotubes. Particle stabilized emulsions, called Pickering emulsions, can form when interfacial tension between the particle and each of the individual immiscible liquid phases is smaller than the interfacial tension between the two different liquid phases[142], as illustrated in figure 2.18

Adsorption of the nanotube to the oil-water interface eliminates an area of the interface between immiscible phases[142, 143]. This is clearly seen by a back of the envelope derivation. Consider a particle of radius, R, which is adsorbed at the oil-water interface. In terms of the contact angle, θ, between particle/water and particle/oil interfaces, the planar area of the oil-water interface that is eliminated by the presence of the particle is:

$$A_e = \pi R^2 sin^2(\theta) = \pi R^2 (1 - cos^2(\theta)) \tag{2.2}$$

Let us assume that R is small enough such that we can neglect gravity and assume that the oil-water interface is planar and designate the surface tension between the different interfaces, γ, with subscripts **o**(il), **w**(ater) , and **p**(article).

Therefore the energy required to remove a particle from the interface into the oil phase will be:

$$E = 2\pi R^2 (1 + cos(\theta)) \left(\gamma_{p/o} - \gamma_{p/w}\right) + \pi R^2 (1 - cos^2(\theta)) \gamma_{o/w} \tag{2.3}$$

Relating the surface tensions by the Young-Laplace equation[144]:

$$\gamma_{p/o} - \gamma_{p/w} = \gamma_{o/w} cos(\theta) \tag{2.4}$$

The energy change simplifies to:

$$E = \pi R^2 \gamma_{o/w} \left(1 + cos(\theta)\right)^2 = \frac{\pi R^2}{\gamma_{o/w}} \left(\gamma_{o/w} - \left(\gamma_{p/w} - \gamma_{p/o}\right)\right)^2 \tag{2.5}$$

It is clear from this back fo the envelope calculation that if the $\gamma_{p/w} - \gamma_{p/o} > \gamma_{o/w}$, it will be favorable for the particle to be held at the interface. As an aside the cryomilled nanotubes form stable w/o pickering emulsions over a wide range of pH values, as seen in figure 2.19 .

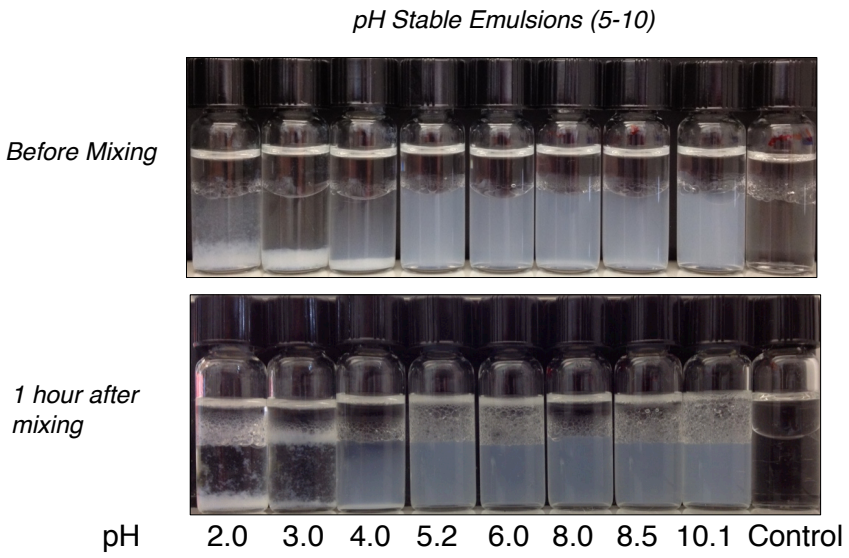

Figure 2.19: pH stability of water/kerosene pickering emulsions formed with cryomilled nanotubes. (Top) prior to agitation (bottom) 1 hour after agitation.

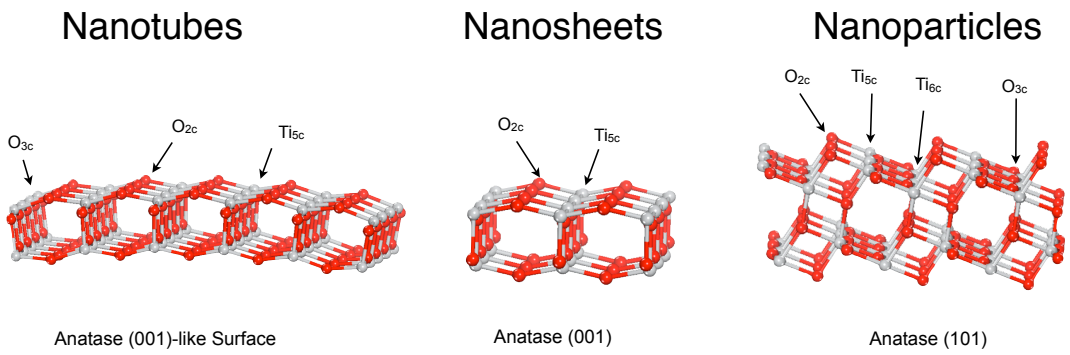

Figure 2.20: Illustration of the surface structure and chemistry of the anatase surfaces exposed on the nanotubes, nanosheets, and nanoparticles and the degree coordinative saturation of the exposed Ti and O groups.

2.8 Other Anatase Nanomaterials

2.8.1 Anatase Nanoparticles

Anatase nanoparticles are used at the precursor material for synthesizing the nanotubes. The nanoparticle surface is largely made up of the highly stable and inactive (101)

surface[145], as illustrated in figure 2.20. The nanoparticles have an average particle size of 32 nm, but are quite polydisperse, as seen in figure 2.21A . The regular atomic pattern observed in TEM (figure 2.21B) highlights the crystalline nature of the nanoparticles. The nanocrystalline structure of the nanoparticles is further evidenced by the clear diffraction peaks observed in selected area electron diffraction (SAED) measurements, which would appear as broad diffuse rings if the nanoparticles were amorphous[146]. XRD of the nanoparticles, shown in figure 2.22, agrees well with the indexed pattern and intensities of anatase[2].

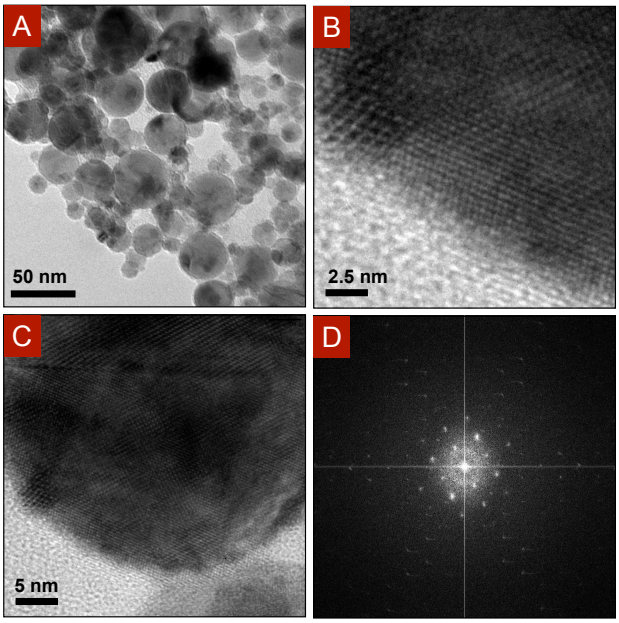

Figure 2.21: TEM imaging of anatase nanoparticles. The region shown in (C) was used to obtain the electron diffraction pattern shown in (D).

2.8.2 Anatase Nanotiles

Anatase nanotiles were synthesized by a solvothermal method, as detailed in the experimental section. Hydrofluoric acid is used as a capping agent and stabilizes thermodynamically unstable {001} facets during growth[120, 147]. This produces thin planar tiles of anatase with a fluorinated surface. The fluorine groups can be removed and re-

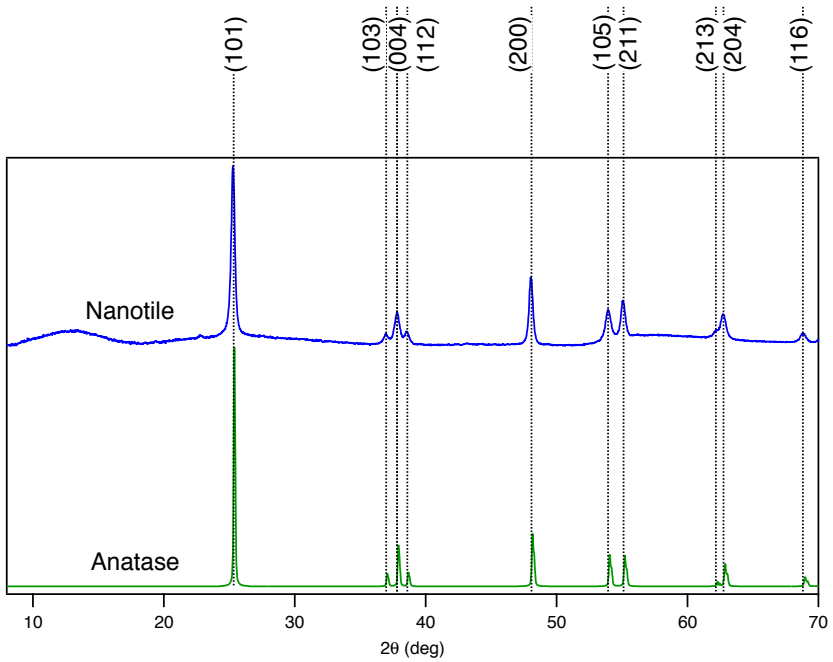

Figure 2.22: XRD of anatase nanoparticles and nanotiles. The corresponding crystal plane assignment based on the structural model is indicated at the top. Assignments based on Horn et. al[2].

placed with hydroxyl groups by calcinating the surface in air. The size and aspect ratio of the resulting material is altered by changing either the reaction temperature or the ratio of the reactants[120, 148], however the surface chemistry is unaltered. In figure 2.23, TEM imaging of nanotiles reveals approximately 80 nm x 80 nm rectangular sheets with a lattice spacing of 2.34 Å. The XRD spectrum, shown in figure 2.22, contains ten well-resolved peaks which are indexed to the crystal structure of anatase. Noticeably absent are the characteristic diffraction peaks of rutile occuring at 27° and 31°. The resulting material is unambiguously pure anatase.

2.9 Surface Chemistry and Hydration of Anatase Nanomaterials

The interaction between a metal oxide surface and water molecules is crucial to understanding the surface chemistry of metal oxide. When water molecules come into contact

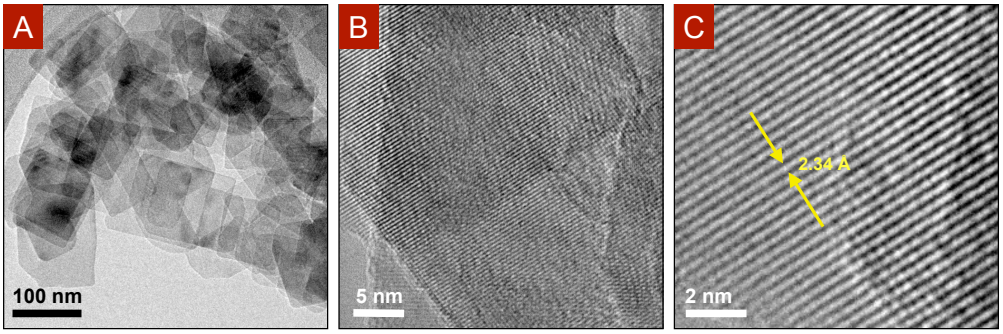

Figure 2.23: TEM images of nanotiles at different magnifications. Arrows drawn in (C) show the lattice spacing, 2.34 Å, which corresponds to the spacing between different (001) planes in the anatase crystal.

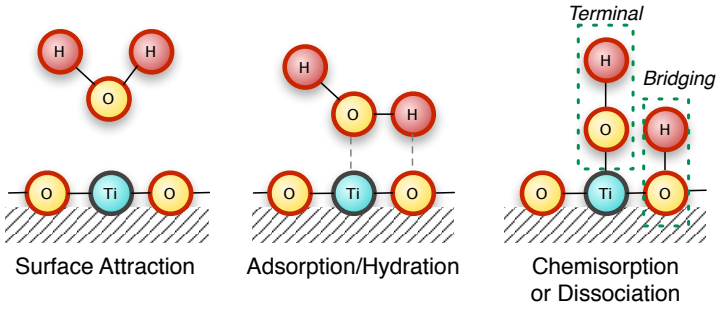

Figure 2.24: Illustration of the different mechanisms by which water can interact with a metal oxide surface.

with the surface, they adsorb, forming a hydration layer. Subsequently, hydrogen present on the water will orient towards the surface oxygens, and physadsorb, forming a weak hydroxyl group without dissociation, as seen in figure 2.24

Hydroxyl groups formed by this process can be coordinated to one or more metal groups on the surface. Multiple types of hydroxyl groups can form on the metal-oxide surface, depending on the different numbers of metal atoms nearby. Bridging hydroxyl groups where the hydroxyl is coordinated with two metal atoms are more acidic than a terminal hydroxyl, which is only coordinated by one metal atom, as illustrated in figure 2.24.

The types of surface hydroxyl groups present on the surface will depend on the acid-base properties of the surface sites, their density, and the ion exchange properties of the surface[93, 140, 145, 149–153]. There have been many detailed theoretical studies of

the behavior of water on different anatase crystal surfaces[125, 126, 145, 150, 151, 154–165]. These models have considered the effect of different levels of coverage[125], surface reconstruction[150, 166], and different possible morphologies of the anatase (001) surface[126, 150].

On the clean anatase (001) surface, the surface Ti groups are all five-fold coordinated. This coordinative undersaturation makes them highly reactive, resulting in a very high surface energy. On the clean anatase (001) surface, water spontaneously dissociates and adsorbs up to half of the Ti groups. This dissociative adsorption hydroxylates the undercoordinated Ti groups and reduces the surface energy. Above half-monolayer coverage, water molecularly adsorbs by hydrogen bonding with surface hydroxyl groups[125]. On the other hand, the anatase (101) surface, which is found on anatase nanoparticles consists of octahedral 6-coordinated Ti groups exposed on the surface. A limited number of 5-coordinated Ti sites can exist on the surface of the nanoparticle as defect sites, resulting from lattice disorder and corner defects[151]. Except at defect sites, water is found to molecularly adsorb on the anatase (101) surface[125, 145].

The distinct water adsorption behavior of the different anatase surfaces and morphologies provides a unique route to examine the surface chemistry of the different nanomaterial morphologies I have previously discussed. Previous studies by my colleagues on the hydration of the nanotubes[111] unambigously showed that the titania nanotube surface is in fact anatase - (001) like, following the predicted surface hydration behavior[125]. In follow up studies with my colleagues, I examined the chemisorption of methanol[113], another probe molecule for which there are significant predictions[162]. Here I further confirmed that the surface of the titania nanotube contains stable undercoordinated five-fold coordinated Ti sites which contribute to its remarkable catalytic activity.

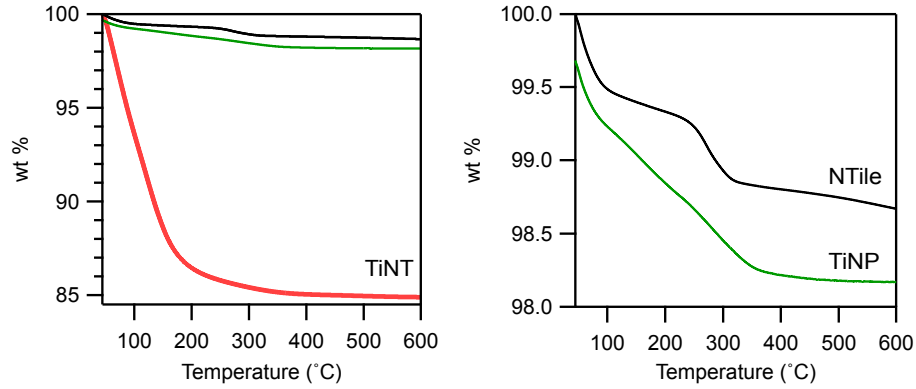

Figure 2.25: TGA of different anatase nanomaterials which were equilibrated under ambient conditions. (Left) Nanotubes, nanotiles (Black), and nanoparticles (Green) (Right) Plot of the TGA curves of the nanotiles and nanoparticles only.

2.9.1 Thermogravimetric Analysis

Thermogravimetric analysis (TGA) of the nanoparticles, nanotiles, and nanotubes, following their exposure to ambient conditions, clearly highlights their different hydration properties. As seen in figures 2.25 and 2.26, the nanotubes exhibit only a single weight loss between 50 °C to 150 °C, corresponding to the loss of molecularly adsorbed water[111]. On the other hand the nanotiles have two different distinct weight losses, one occurring between 50 °C and 100 °C, corresponding to the evaporation of bulk water, and an additional weight loss near 275 °C, due to the removal of the surface hydroxyl groups[158, 163], clearly seen in the derivative curves in figure 2.26.

The extensive weight loss observed in nanotube's may be a result of slightly differing sample preparation techniques, the nanotubes were dried at in an oven at 105 °C rather than under vacuum at 50 °C. However, it is more likely a result of the nanotube's significantly larger water-accessible surface area. The nanotube's water-accessible surface area (for a 4-layered nanotube) is approximately 500 $m^2\ g^{-1}$, while the nanoparticle and nanotile have accessible areas of 45 $m^2\ g^{-1}$ and 80 $m^2\ g^{-1}$, respectively.

In contrast, the nanoparticle weight linearly decreases between 50 °C and 300 °C.

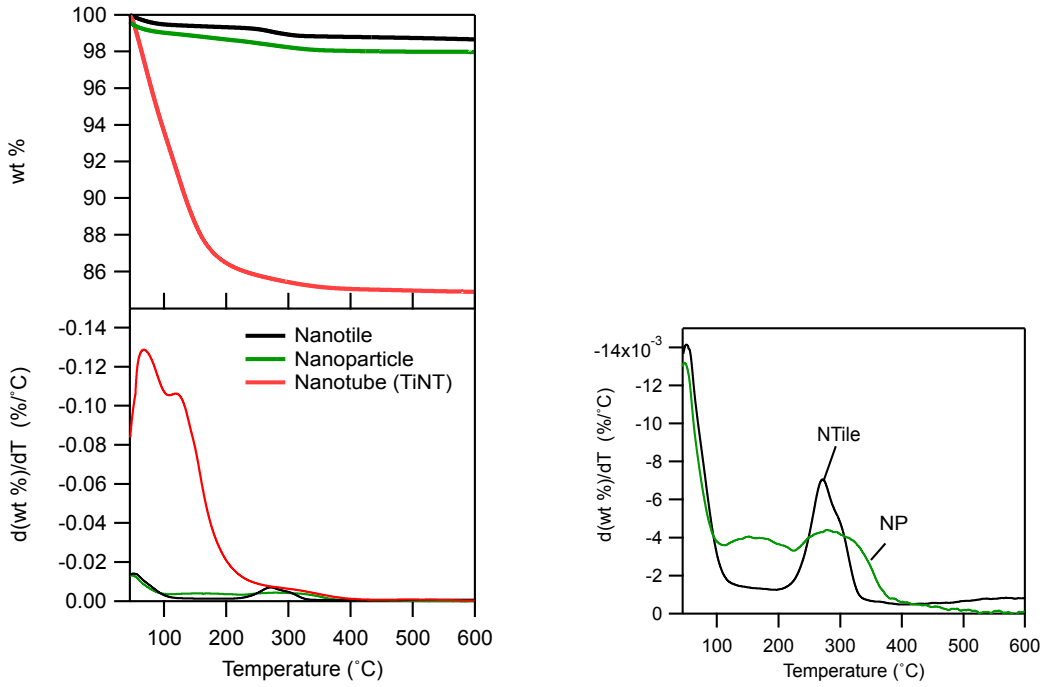

Figure 2.26: (Left) TGA (top) and DTA (bottom) curves of different anatase nanomaterials which were equilibrated under ambient conditions. (Right) DTA Curves of nanotiles and nanoparticles.

Anatase nanoparticles typically contain a large number of defect sites on the low-energy (101) surface and frequently expose a variety of additional crystal facets[147]. The continuous loss is consistent with the large number of energetic environments on the nanoparticle surface and the removal of molecularly adsorbed water with different hydrogen bonding configurations.

2.9.2 Solid State NMR

High-resolution ^{1}H solid-state NMR is an extremely useful technique for examining the surface hydroxylation of the different nanomaterials. It is well known that the acidic surface sites that donate protons to adsorbed molecules are critical to heterogenous catalyst function. NMR has been widely used to detect the presence of accessible hydroxyl groups,

their specific acidity, and to elucidate the structure and composition of zeolites and other porous materials[153, 167].

In solution-state NMR, the rapid diffusion of molecules in solution effectively averages any orientational dependence of the shielding or dipolar coupling tensors with respect to the applied magnetic field over the NMR timescale. However in most solids these tensors are not sufficiently averaged over the timescale of a measurement and the spectra are significant broadened. Furthermore, the typical linewidth frequently exceeds the chemical shift differences between individual lines and effectively masks individual resonances.

However to first order, the anisotropic components of the chemical shift and dipolar coupling have the same orientational dependence. For instance, for a spin-$\frac{1}{2}$ multispin system consisting of homonuclear-coupled spins, I and S, connected by internuclear vector $\mathbf{r_{ij}}$, the dipolar coupling Hamiltonian is:

$$\hat{H}_{dd}^{homo} = -\sum_{i>j} d_{ij} \cdot \frac{1}{2}\left(3\cos^2\theta_{ij} - 1\right)\left[3\hat{I}_z^i\hat{S}_z^j - \hat{\mathbf{I}}^i \cdot \hat{\mathbf{S}}^j\right] \tag{2.6}$$

where $d_{ij} = \frac{\mu_0}{4\pi}\frac{\gamma_i\gamma_j\hbar}{r_{ij}^3}$ is the dipolar coupling constant of spins, i, and j, θ_{ij} is the angle between the $i-j$ internuclear vector with the applied field, $\mathbf{B_0}$.

The dipolar coupling depends on $\frac{1}{2}\left(3\cos^2\theta_{ij} - 1\right)$. At θ_M = 54.74° with respect to the applied field this value vanishes. It's practically impossible to align all the crystallites in a powdered sample to the magic angle, but it is practical to achieve a similar effect by rapidly rotating the sample at the magic angle. If the rotation is done rapidly enough such that the average orientation of the crystals are the same, the anisotropic component of the dipolar coupling and chemical shift will be removed[168].

For a crystal with orientation β, which is spun at an orientation χ, $(3\cos^2\theta - 1)$ is averaged to:

$$\langle \frac{1}{2}\left(3\cos^2\theta - 1\right)\rangle = \frac{1}{2}\left(3\cos^2\chi - 1\right) \times \frac{1}{2}\left(3\cos^2\beta - 1\right) \tag{2.7}$$

and at $\chi = \theta_M$, $(3\cos^2\chi - 1)$ vanishes. This technique is called magic-angle spinning (MAS). Full elimination of this anisotropy requires that sample be spun significantly faster than the linewidth due to the dipolar coupling, typically about three to four times faster[169]. However practically speaking slower spinning speeds will reduce the linewidth but will produce sharp extra peaks, centered around the isotropic chemical shift, which are spaced at integer multiples of the spinning speed.

The linewidth of the resulting signal may still be broadened by a number of other factors such as heteronuclear dipolar interactions with quadrupolar nuclei[167], magnetic field inhomogeneities[170], deviations of the MAS rotor from the magic angle[171], motional processes, or exchange[169]. However in the systems I examine here, the residual linewidth is primarily the result of homonuclear dipolar coupling of spin-1/2 atoms and motional processes and I will further restrict my discussions to these issues.

To investigate the surface hydration of the different nanomaterials, I obtained ^{1}H NMR spectra of the nanomaterials at different levels of hydration. In a typical experiment the nanomaterial was first allowed to equilibrate under ambient conditions in excess of 30 days. In the following discussion this is referred to as "as received" and abbreviated as "as rcv'd." The equilibrated nanomaterial was then loaded into a clean 2.5 mm Zirconia spinner with a Torlon drive cap and tip; the spinner is airtight when sealed. The mass of the sample was determined from the difference between the mass of the empty spinner and the full spinner. After obtaining a high resolution spectra of this sample, the cap of the sample was removed and the sample was placed into a water-vapor saturated atmosphere and allowed to equilibrate for 24 hours. I did not observe any change to the spectra in samples hydrated longer than 24 hours. The samples were then removed from the humid chamber, quickly capped, and examined again using NMR. Subsequently, the samples were uncapped and

placed into a desiccator filled with a desiccant powder at the bottom to dry. After a given amount of time the samples were removed, recapped, and spectra acquired as previously described. I repeated this process at regular intervals for periods in excess of 30 days.

2.9.2.1 MAS Spinner Background Contribution

The MAS spinner consists of a Zirconia sleeve as well as a polymer top cap, spacer, and bottom drive tip. The drive tip is typically polyimide (Torlon). The top cap and spacer can be made of either a fluoropolymer, typically polychlorotrifluoroethylene (Kel-F) or polyimide (Torlon). The fluoropolymer does not contain any H atoms and thus it is preferable to use it for ^{1}H experiments. However the fluoropolymer compressive strength is insufficient for spinning speeds above about 15-18 kHz and only Torlon parts can be used.

To sufficiently average the dipolar coupling, I performed experiments with an MAS spinning speed of 26 kHz. In figure 2.27, I compare the background contribution to the NMR spectra, at 14 kHz MAS, of a spinner containing Kel-F parts and Torlon parts. The Torlon contains a wide and significant background contribution; the small contribution seen for the spinner with Kel-F is due to the Torlon drive tip, which is used in all samples. To understand the magnitude of these contributions I loaded titania nanotubes into the different spinners. It is evident that the nanotubes' spectra significantly overlaps with the proton spectra of the Torlon components.

Another complication arises from my experimental protocol. Each hydration experiment consists of spectra of the same sample taken at different drying times; between trials I had to remove the top cap to allow the sample to either be hydrated or desiccated. The contribution of the top cap to the NMR spectra is very sensitive to the position of the top cap in the RF coil - changes in the sample mass, spinning, as well as removal and replacement of the top cap all cause the exact position of the top cap to vary from trial to trial. For a given sample,

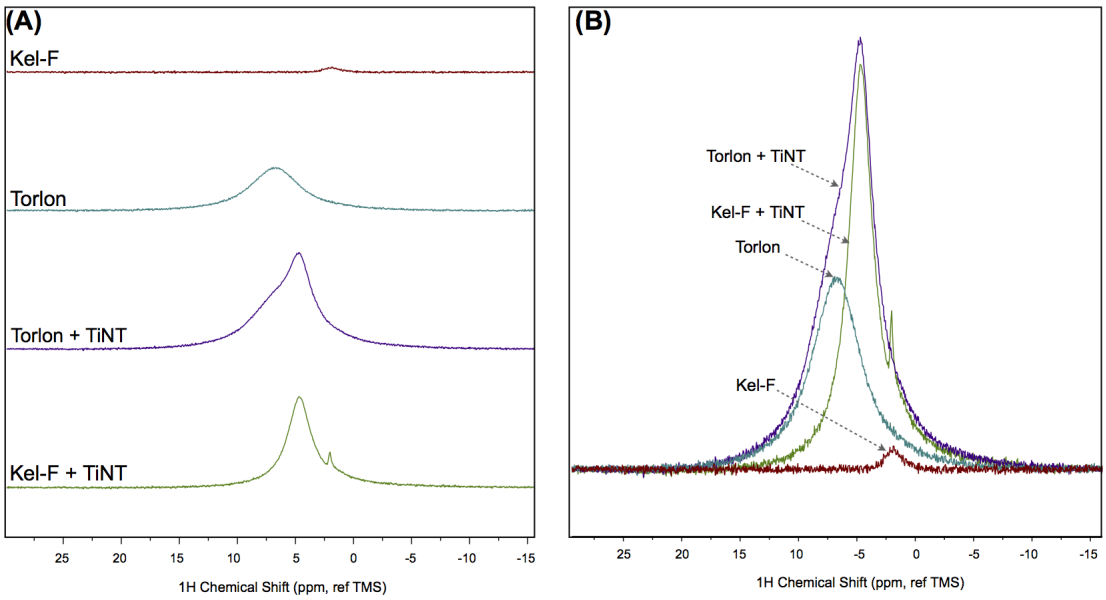

Figure 2.27: The Torlon drive tip, spacer, and cap used on the MAS spinner significantly overlaps with the signal from the nanotube. (A) Stacked spectra of (from top) empty spinner containing fluoropolymer (Kel-F) parts, same spinner containing polyimide (Torlon) parts, spinner containing Torlon and nanotube sample, spinner containing Kel-F and nanotube sample. (B) Same spectra shown overlayed.

this meant that although the background had the same chemical shift, its contribution to the signal and its width and height would change based on where it was in relation to the coil. Therefore to accommodate these constraints I had to fit all of my spectra to remove the sample background contribution. This will be shown at length below.

An additional complicating factor is that the Torlon parts used in the spinners appear to have different chemical shifts, typically centered between 5-8 ppm. After speaking with the manufacturer it was revealed that the Torlon formulation and provider had been changed at different times and that the Torlon parts we had accumulated over the years would have different molecular weights, additives, and formulations. Much of this was unfortunately realized in retrospect after considerable problems arose with the background contribution of the probe, therefore in each section below I have to identify the chemical shift of the Torlon background associated with each spinner's components.

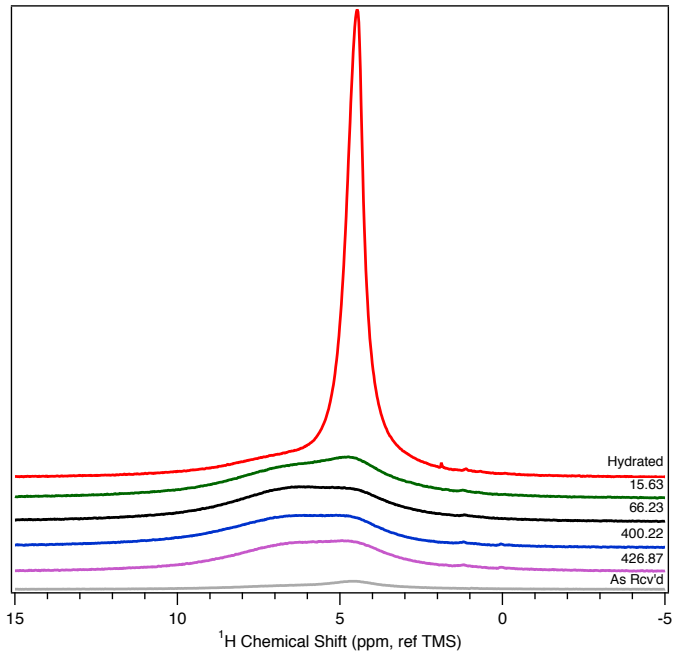

Figure 2.28: Proton NMR of titania nanotubes. ^{1}H solid-state NMR of TiNT equilibrated under ambient conditions (TiNT As Rcv'd), hydrated for 24 hours in a water-vapor saturated atmosphere (TiNT Hydrated) and then dried. The time listed above each curve is the number of total hours the sample has been dried. Spectra have been offset for clarity and normalized to mass, scan numbers, and probe tuning. All samples were acquired under identical conditions at an MAS speed of 26 kHz.

2.9.2.2 Titania Nanotubes

In figure 2.28, I examine the ^{1}H NMR spectra of the nanotubes at different levels of hydration. The spectra have been offset, but have been normalized by the sample mass, number of acquisitions, and adjusted for differences in the Q-factor of the NMR probe's resonant circuit.

Prior to equilibrating it in atmosphere, the "as received" sample was first dried in an oven at 105 °C. The spectrum has two major overlapping resonances which are clearly seen by deconvoluting the spectra into two components. Examples of this are shown in figure 2.29A. The nanotubes have a broad peak at 6.1 ppm and a narrow peak centered near 4.7 ppm. The peak near 6.1 ppm is dominantly due to the Torlon components of the MAS spinner, as

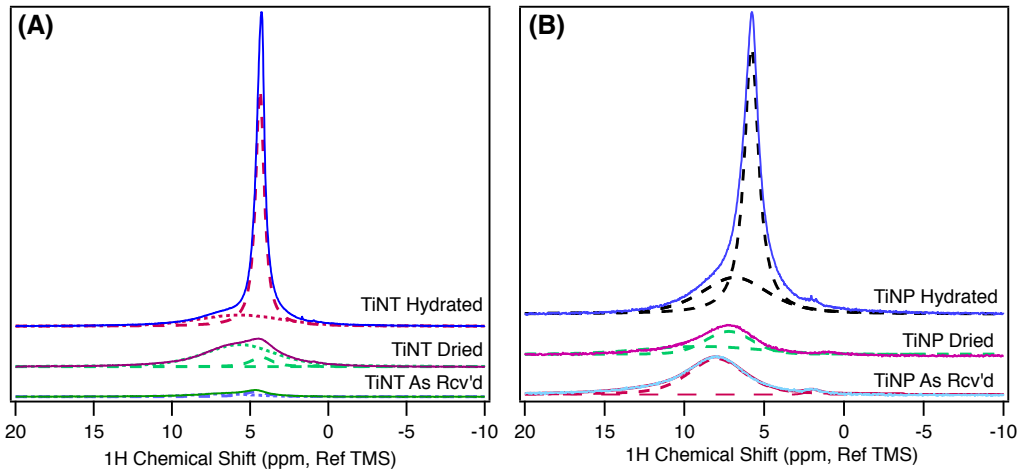

Figure 2.29: Proton NMR of nanotubes and nanoparticles. ^{1}H solid-state NMR spectra (solid lines) and deconvolution (dashed) of (A) TiNT equilibrated under ambient conditions (TiNT As Rcv'd), hydrated for 24 hours in a water-vapor saturated atmosphere (TiNT Hydrated) and dried for 16 hours in a desiccator (TiNT Dried). (B) TiNP equilibrated under ambient conditions (TiNT As Rcv'd), hydrated for 24 hours in a water-vapor saturated atmosphere (TiNT Hydrated) and dried for 24 hours in a desiccator (TiNT Dried). All samples were acquired under identical conditions at an MAS speed of 26 kHz.

demonstrated in figure 2.27. The broad resonance of the Torlon is largely due to both strong dipolar coupling and inhomogenous broadening due to the magnetic field gradients across the Torlon present in different parts of the spinner[171].

The peak at 4.7 ppm corresponds to bulk and interfacial water. The peak is narrow (FWHM $\approx$ 0.6 ppm to 1.6 ppm) but wider than that of pure bulk water (FWHM $<$ 0.2 ppm) and slightly upfield (4.7 ppm versus 4.9 ppm for bulk water). The increase in width suggests that the 4.7 ppm peak corresponds to water molecules with a shorter spin-spin relaxation time (T2) than the bulk water. The upfield shift suggest that this peak corresponds to interfacial water and water near the surface that is hydrogen bonded either to the interface or other surrounding water molecules[172]. The deconvoluted peak at 4.7 ppm is shown in figure 2.30.

The peak at 4.7 ppm is present in the nanotube sample prior to placing it in the humid chamber and has a FWHM of 1.67 ppm. Since the sample has been exposed to atmosphere

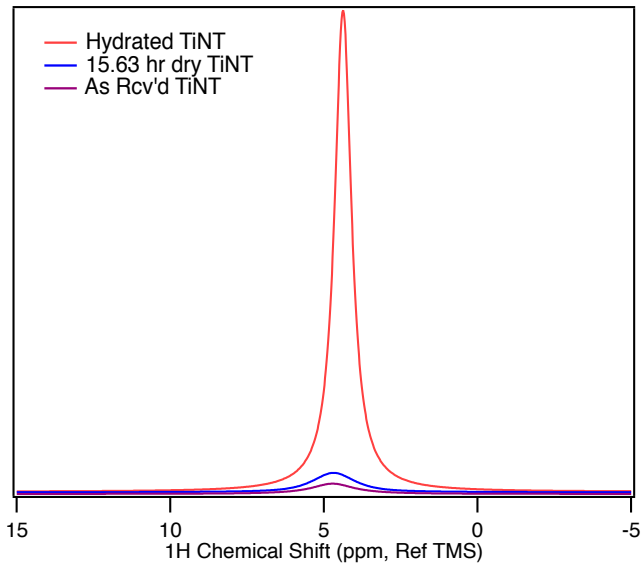

Figure 2.30: Proton NMR of titania nanotubes. Deconvoluted peak of ^{1}H solid-state NMR TiNT equilibrated under ambient conditions (TiNT As Rcv'd), hydrated for 24 hours in a water-vapor saturated atmosphere (TiNT Hydrated) and then dried for 15.63 hr. All samples were acquired under identical conditions at an MAS speed of 26 kHz. The spectra were fit to two peaks defined by the Voigt function (Lorentzian-Gaussian combination), the peak resulting from the signal is shown above, the other resulted from the MAS spinner background.

($\approx$30-40$\%$ relative humidity (RH)) bulk and interfacial water is nominally present on the sample. The intensity of this peak dramatically increases after placing the sample in water-vapor saturated atmosphere for 24 hours and narrows to 0.65 ppm. This narrowing and intensity increase suggest that the water in the humid atmosphere has physadsorbed onto interfacial water already present on the nanotubes. After 15.6 hr of drying, the intensity of this peak significantly decreases and broadens to to 1.61 ppm. The area under the curves is directly proportional to the number of protons present. The ratio of the peak area at 15.6hr drying to the peak prior to hydrating (as received) is 2.08:1. Although much of the hydrated water has been removed, there are still about twice many protons present than before hydrating. The slightly decreased FWHM (1.61 ppm vs. 1.67 ppm) suggests that the increased proton population contains some more mobile proton species, possibly bulk water.

Reexamining figure 2.28 , it is evident that even after over 400 hours of drying the proton population does not significantly change from the initially dried state and is still larger than the "as received" sample. Prior to equilibrating it in atmosphere, the "as received" sample was first dried in an oven at 105 °C. This temperature provides sufficient energy to remove all the bulk and interfacial water, leaving only structural hydroxyl groups that might exist either at defect sites or due to possible dissociative adsorption on the surface[111, 163]. This suggests that the additional protons on the interface of the nanotube after drying in a desiccator are likely strongly hydrogen bonded interfacial water. The rate of water desorption, r_d, varies exponentially with temperature, $r_d(T) \propto \exp\left(-E/(k_B T)\right)$, where E is the desorption energy, typically roughly 0.5 eV for water[173]. Increasing the temperature from 25 °C to 105 °C will increase the desorption rate by roughly 62 times.

In agreement with my TGA data, I do not observe any clear resonances from surface hydroxyl groups. These findings agree with previous studies showing that the nanotube surface was stable against permanent hydroxylation[111–113]. Furthermore, the existence of the mobile, hydrogen-bonded interfacial water is consistent with FTIR[152], NMR[174] and theoretical models[126], which have found that up to three layers of hydrogen bonded interfacial water may exist on the anatase surface.

2.9.2.3 Anatase Nanoparticles

In figure 2.29B I compare the ^{1}H NMR spectra of Titania Nanoparticles (TiNP) at three different levels of hydration. Again, the spectra have been offset and normalized by the sample mass, number of acquisitions, and adjusted for differences in the Q-factor of the NMR probe's resonant circuit. The nanoparticle surface is dominantly anatase-(101) and is expected to contain primarily physadsorbed water in a variety of hydrogen bonding environment and limited hydroxyl groups at defect sites. The hydrated TiNP spectra is deconvoluted into two peaks, a broad peak centered at approximately 7 ppm due to Torlon

background and a dominant peak at 5.8 ppm which has a 1.08 ppm FWHM. The 5.8 ppm peak corresponds to hydrogen bonded water or more rigid configurations of physadsorbed water. A small shoulder is visible but could not be reasonably fit. In both the "as received" spectra and the spectra taken after drying for 24 hours, three peaks are clearly visible. To demonstrate this the deconvoluted spectra after 24 hours of drying is shown in detail in figure 2.31. The Torlon background is dominantly present at 7.2 ppm.

Both spectra contain a wide downfield peak corresponding to the wide variety of hydrogen bonding configurations of interfacial water. After 24 hours drying this peak occurs at 8.8 ppm (FWHM = 8.9 ppm), while in the "as received" sample, it occurs at 9.0 ppm is is similarly wide (8.3 ppm). The similar chemical shift and width suggest that the peak corresponds to either structural water contained at defect sites or extremely rigidly attached water that has hydrogen bonded to acidic surface sites[174]. Notably, both spectra also contain a sharp upfield shoulder. The sample, as received, has a shoulder at 1.98 ppm (FWHM = 1.05 ppm) likely corresponding to basic hydroxyl groups present on the surface. Although this should appear on the hydrated sample, any contribution is near the noise floor and I have avoided over-fitting the spectra by introducing an unnecessary number of peaks. After 24 hours of drying this shoulder is not clearly resolved, however a shoulder appears at 0.88 ppm (FWHM 1.66 ppm), which may contain portions of the previously observed peak (as evidenced in the residuals of the fit shown in figure 2.31. This peak likely correspond also to more protons but the wide peak suggests that the protons are weakly bound and highly mobile, while the upfield shift suggests a more basic bonding environment[172]. These findings are consistent with the diverse variety of hydrogen bonding environments frequently observed in anatase nanoparticles and the presence of a dominantly anatase (101) surface.

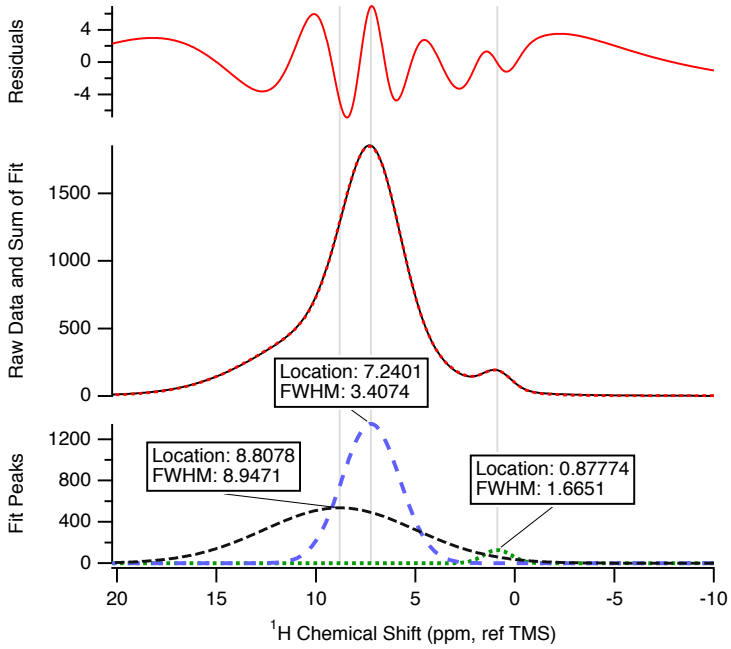

Figure 2.31: Proton NMR of titania nanoparticles. A closer examination of the TiNP sample after 24 hours drying shows two individual peaks, a broad peak at 8.8 ppm and a narrow peak at 0.88 ppm. Spectra were deconvoluted into 3 separate Gaussian peaks. The spinner background is at 7.24 ppm.

2.9.2.4 Anatase Nanotiles

In figure 2.32 I compare the ^{1}H NMR spectra of calicinated Titania Nanotiles (NTiles) at three different levels of hydration. These spectra were normalized to the sample mass, number of adquisitions, and adjusted for differences in the Q-factor of the NMR probe's resonant circuit. The nanotiles expose the anatase-(001) surface and the undercoordinated surface groups on the nanotiles are stabilized by terminal hydroxyl groups[157, 172]. As with other samples, the hydrated nanotiles contain a contribution from the Torlon background at 6.6 ppm and a FWHM $\approx$ 3.4 ppm linewidth, clearly seen in figure 2.32B. The hydrated sample contains an extremely sharp peak (FWHM 0.26 ppm) at 4.4 ppm. Despite the minor upfield shift, the extremely narrow peak suggests we may be examining bulk water.

This sample was provided to me in a hydrated form and I believe it may have contained

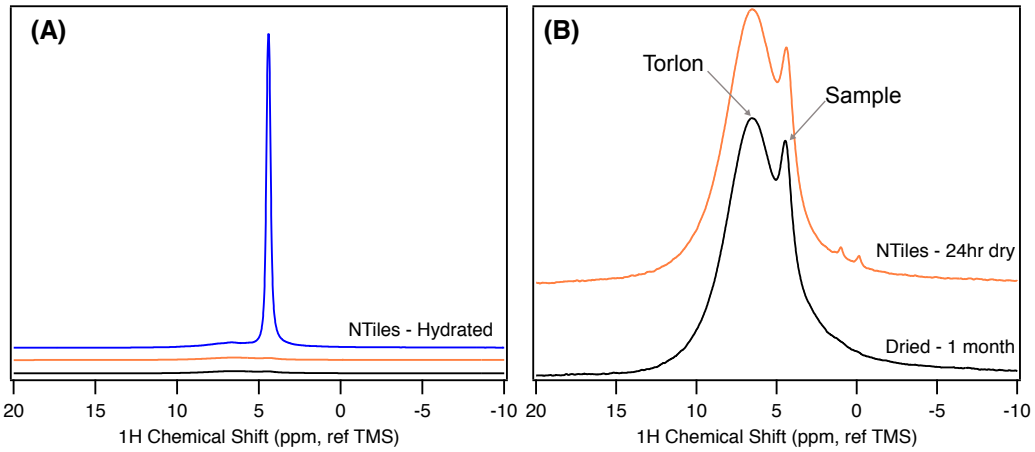

Figure 2.32: Proton NMR of nanotiles. Examination of the surface hydroxyl groups on Batch 4 Nanotiles using solid-state ^{1}H NMR. (A) From top to bottom the spectra are - nanotiles equilibrated in saturated water vapor atmosphere for 24 hours (blue), dried for 24 hours in desiccator (orange), and nanotiles dried for 1 month in dessicator (black). The intensity of the hydrated (blue) peak has been scaled by 0.5. (B) Zoomed in view showing only the 24 hour dried and 1 month dried spectra. Arrows drawn to indicate the peak due to the Torlon background and the peak due to sample.

extraneous amounts of water. Furthermore I was not informed of the sample's hydration history prior to my measurements. However after 24 hours of drying the sample the peak at 4.4 ppm vanishes and a peak at 3.6 ppm appears (FWHM $\approx$ 1.2 ppm). Two additional sharp peaks are visible at 0.8 ppm and -0.8 ppm, however they are nearly at the noise floor and it is unclear whether they are real or artifacts. After 1 month of drying the sample still contains the peak at 3.6 ppm, however the FWHM has reduced to 0.93 ppm, as seen in deconvoluted spectra in figure 2.33. After 1 month of drying 77% of the protons present at 1 day of drying remain. These protons are clearly strongly bound to the surface of the nanotiles. The upfield shift is typical of terminal hydroxyl groups associated with more basic surface sites[111, 171, 172].

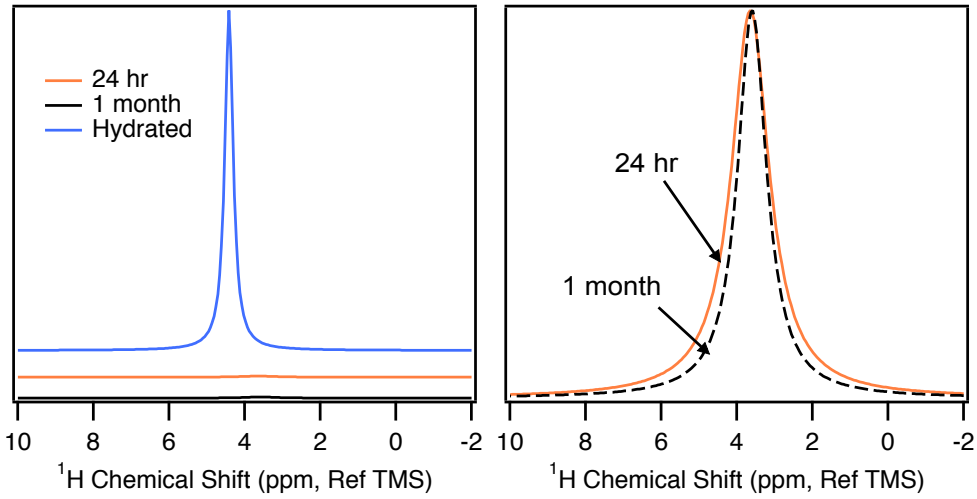

Figure 2.33: Examination of the surface hydroxyl groups on nanotiles using solid-state ^{1}H NMR. Spectra were deconvoluted into two components - one containing the proton peak observed above and the other the broad background resulting from the spinner drive tip and cap. The deconvoluted fit of the sample is shown here. (A) From top to bottom the spectra are - nanotiles equilibrated in saturated water vapor atmosphere for 24 hours, dried for 24 hours in desiccator, and nanotiles dried for 1 month in desiccator. (B) Zoomed in view showing only the 24 hour dried and 1 month dried spectra. The ratio of the area under the 24 hour dried peak to the 1 month dried peak is 1.00:0.77.

2.9.3 Comparing different materials

Based on the TGA and NMR it is evident that the three different nanomaterials have differing hydration properties, schematically illustrated in figure 2.34. While the nanotubes may contain surface hydroxyl groups at defect sites the majority of the surface remains stable against hydroxylation and is instead hydrated by interfacial water with varying hydrogen bonding configurations. Here the stability against hydroxylation appears to derive from bond strain induced by the nanotube's curvature. Whereas removing the curvature produces the nanotiles which are entirely anatase-(001). Without the curvature the undercoordinated sites are immediately hydroxylated to lower the surface energy. Finally, the nanoparticles are primarily composed of anatase-{101} surfaces which contain only molecularly adsorbed water. However due to the high presence of defects in the nanoparticles limited hydroxylation may occur at corner defects where Ti-5C sites can exist[125, 156].

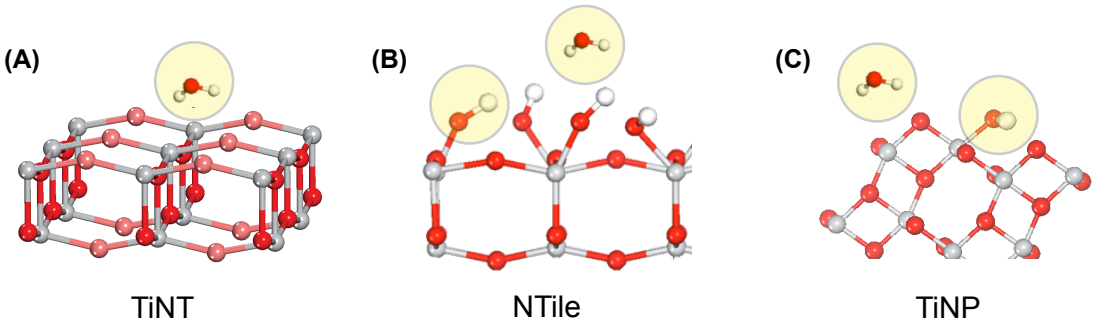

Figure 2.34: llustration of the possible identities of the proton moieties (circled in yellow). observed in the NMR and TGA of nanomaterial. (A) Titania nanotube contains primarily bulk and interfacial water. (B) Nanotile contains strongly bound surface hydroxyl groups and bulk/interfacial water. (C) Nanoparticle contains bulk/interfacial water, shown is one possible model by which adsorb.

The difference between the fully hydroxylated nanotiles and the undercoordined nanotube suggest that they may interact differently with the protein molecules. Previous studies of the nanotubes have shown that up to 40% of the atoms in the nanotubes are undercoordinated[93, 175]. Bidentate ligands have the optimal geometry for chelating Ti-5c sites and restoring 6-fold coordination[165, 176]. In particular, the Ti-5c sites have a very high affinity for oxygen-containing ligands[93, 175]. Investigations of amino acid adsorption on TiO_2 has been widely investigated[64, 76, 165, 177], however no conclusive experimental studies of the anatase (001) surface have been possible as it is hydroxylated except under ultra high vacuum or as part of a nanotube.

2.10 Conclusions

In this chapter I characterized the structure and chemistry of three different anatase nanomaterials, the multilayered titania nanotube, anatase nanotiles, and anatase nanoparticles. The structure and chemistry of the nanotube has been a contentious issue of debate for many years[111, 113, 129, 131, 133, 150, 178]. However, only the delaminated anatase model of the nanotube has been able to replicate the experimental XRD patterns[111, 112].

On the basis of NMR and TGA measurements I clearly distinguished the surface chemistry of these materials. Here I showed that only the nanotubes expose an anatase-(001) like surface which is stable against hydroxylation. Similarly to studies examining the unraveled surface of the nanotubes[111], I find that nanotiles also contain a hydroxylated anatase-(001) surface. This prevents undercoordinated Ti-5C sites from being exposed.

Here I have restricted my discussion to the structure and chemistry of nanotubes which have been water-washed and as such may contain excess sodium ions within the interlayers, even after excessive washing[127, 129, 133, 150]. Recent studies[127] have suggested that the Na-ions may play a structural role in the nanotube's stability. On the basis of NMR measurements, Bavykin[127] suggested that the nanotubes may contain two different types of structural hydroxyl groups. Invoking a titanate-like model, he suggested that both water-washed and acid-washed nanotubes contained structural OH groups containing ion-exchangable protons as well as crystallographic water. However in the water washed nanotubes, he observed a decrease in the number of ion-exchangable protons and an increase in the content of crystallographic water, suggesting that some of the structural protons may in fact be replaced by Na ions.

Attempts to employ Bavykin's model to refute the delaminated anatase model are flawed for a number of reasons. Bavykin synthesized his material using an alkaline hydrothermal synthesis, however he employed a lower-temperature, reflux-based synthesis, which utilized a mixture of NaOH and KOH. On the basis of his own previous publications, it is well known that the structure and morphology of the nanotubes is highly sensitive to the synthesis temperature, ionic species, and ionic strength[129]. Although his NMR measurements were performed at a slightly higher MAS speed (28 kHz) he observed a significantly wider (nearly 10-15 ppm) spectrum containing a variety of complicated overlapping features which were fitted with a very large number of different Lorentzian peaks. The sharp, almost powder-like pattern results from significant chemical shift anisotropy and strong residual dipolar

coupling which are not present in any samples I have examined. This suggests that while Bavykin's structural characterization may be correct, the methods use have produced and characterized a very different material.

One additional factor which has not yet been considered is the introduction of defects or structural alteration induced by shortening the nanotubes or other mechanical processing. Although I have not detailed it in this dissertation, I performed additional XRD and NMR on cryomilled nanotubes and also examined the effect of different processing conditions and techniques such as sonication. Briefly, these studies did not show any significant deviations in the XRD patterns, but did show additional new NMR peaks corresponding to mobile basic hydroxyl groups when samples were cryomilled or sonicated for longer periods of time than discussed in this dissertation. These findings suggest that a careful balance must be struck between reducing the aspect ratio of the nanotubes or improving the colloidal stability with the need to maintain the original surface chemistry. However it also suggests that additional processing may be able to alter the hydrophilicity of the resulting nanomaterial by increasing the concentration of surface hydroxyl groups, leading to tailorable intermediates with potentially different protein adsorption properties.

CHAPTER 3

GLOBULAR PROTEIN ADSORPTION ON TITANIA NANOTUBES

3.1 Introduction

A unique combination of physics, biology, and chemistry is needed to gain a fundamental understanding of the molecular-level events which govern protein interactions with inorganic materials. Although this has been an area of significant interest, there is still a real need to fundamentally understand how a material's structural and chemical properties affect biomolecule interactions and how the structure and functions of proteins adsorbed onto an interface are affected by these parameters. As discussed in chapter 1, the properties of the substrate, protein, and solution will determine the resulting interaction. Among a number of factors which affect protein adsorption include ionic strength and salt concentration[32, 35, 40, 43–45, 50, 65, 68, 86, 143, 179–187], protein charge[32, 34, 35, 40, 43–45, 50, 63, 65, 68, 79, 83, 86, 94, 143, 179–198], substrate surface charge[32, 34, 35, 43, 45, 65, 79, 83, 86, 94, 143, 183–185, 187, 189, 194, 197], protein and substrate hydrophobicity[35, 43, 45, 50, 63, 65, 79, 83, 94, 143, 183, 184, 188, 189, 193, 194, 196, 197], and protein structural properties such as the isothermal compressibility[42–44, 46, 51, 98, 193, 199].

In this chapter, I investigate how a material with unique structural and surface properties can influence and control the orientation, structure, morphology of biomolecules. I characterize the adsorption of three globular proteins, Ribonuclease A, Lysozyme, and Ubiquitin on the surface of titania nanotubes. The nanotubes contain a high density of stable, undercoordinated Ti surface groups. All of the protein's adsorbed to the nanotube at coverages much

larger than the monolayer adsorption capacity. This chapter serves as the start of our journey to explore how the nanotube's unique undercoordinated surface chemistry and distinct crystalline structure influence protein behavior and assembly on the nanotube surface.

3.2 Experimental

3.2.1 Production of Titania Nanotubes

I produced shortened titania nanotubes (TiNT), by a hydrothermal synthesis. The details of this synthesis are detailed in chapter 2[111, 112], and dispersed the nanotubes in 25 mM HEPES buffer (pH 7.2) at a final concentration of 75 $\mu g\, mL^{-1}$. I then filtered the nanotube dispersion through a 200 nm membrane filter to remove any preexisting aggregates. Nanotube aggregates were not detected with dynamic light scattering.

The resulting nanotubes typically consist of 4 layers of anatase (001) rolled around the anatase [010] axis and have a typical outer diameter and length of 12 nm and 100 nm, respectively[112]. The nanotubes have an isoelectric point of pH 2.7 and form a stable dispersion at physiological pH.

3.2.2 Quantitative Adsorption Measurements

Lyophilized, chromatographically-purified Bovine Pancreatic Ribonuclease A (RNaseA, Product: R6513), Bovine serum albumin (BSA, Product: A2058), and Hen's Egg White Lysozyme (HEWL) were purchased from Sigma Aldrich, Recombinant Human Ubiquitin (Ubq, Product: BML-UW8795, Lot: X08313B) was purchased from Enzo Life Sciences, 1 M HEPES buffer (pH 7.2) was purchased from Fisher Scientific. For a given set of exper-

iments, I freshly prepared 25 mM HEPES buffer from the 1 M stock using clean volumetric flasks, I then passed the buffer through a 0.10 µm PES membrane filter (Millipore) to remove any possible microbial contaminants or dust that could interfere with my experiments. Immediately prior to my experiments I weighed out lyophilized protein on a calibrated Denver Instruments TP-114 analytical balance ($\pm$ 0.1 mg) within a low protein-binding Eppendorf microcentrifuge tube and subsequently added a known volume of the 25 mM HEPES buffer with a micropipette. I filtered the protein solution through a 100 nm PES syringe filter to remove any possible preexisting aggregates. In a typical experiment with RNaseA, the stock concentration was 2.5 ± 0.2 mg mL^{-1}. I performed sodium dodecyl sulfate polyacrylamide gel electrophoresis (SDS-PAGE) on each protein lot prior prior to using it; no protein oligomers were detected with SDS-PAGE.

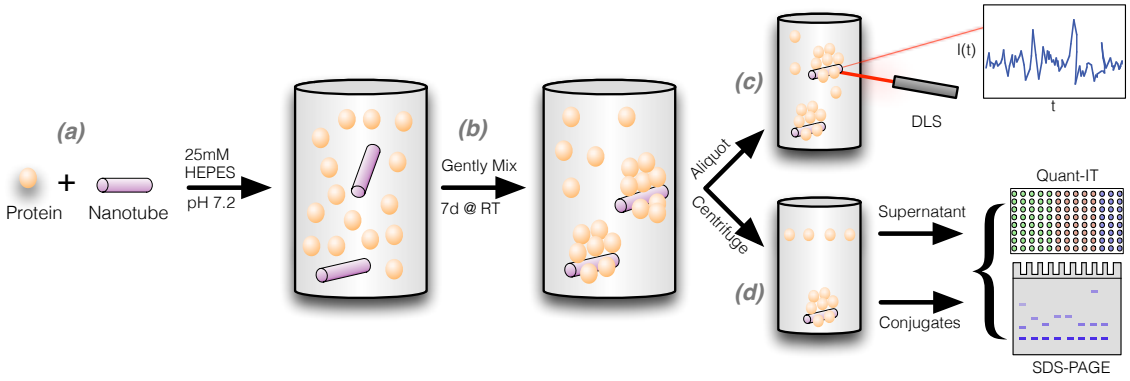

Figure 3.1: Schematic overview of adsorption experiments and measurements detailed in the text. Briefly, in a typical experiment (a) Protein and nanotube stock solutions were individually prepared in 25 mM HEPES buffer (pH 7.2) at room temperature. Subsequently, a series of individual experiments with varying protein and nanotube concentrations were prepared in either a 96-well microplate or microtube suspension. The trials were then gently mixed on a rotisserie rack or microplate shaker, typically for 7 days. (c) An aliquot of the mixed solution was taken and dynamic light scattering measurements were performed to determine the hydrodynamic size of the samples (d) The remaining sample was centrifuged to separate the protein bound to the nanotube from the free protein in solution. The free protein concentration was measured with a fluorometric assay in a microplate reader. SDS-PAGE was performed on the sedimented protein-nanotube conjugates to determine if protein oligomers formed.

I prepared the samples for quantitative adsorption experiments, an overview of which is

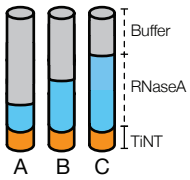

Figure 3.2: Illustration showing how sample composition was varied among trials in adsorption experiments

illustrated in figure 3.1, by combining a fixed amount of nanotube with a varying amount of protein and buffer in low protein-binding centrifuge tubes or a deep well microplate; the total sample volume was held constant, as depicted in figure 3.2. The samples were subsequently mixed on a rotisserie rack or microplate mixer for 7 days at room temperature.

A depletion method was used to determine the amount of protein bound to the nanotubes. The nanotubes and protein-nanotube conjugates were first pelleted by centrifugation, leaving the unbound protein in the supernatant. The protein concentration in the supernatant was assayed with the Quant-IT Protein Assay (Invitrogen, Carlsbad, CA), in triplicate, at 23.6 °C on a SpectraMax384 Microplate Reader (Molecular Devices, Sunnyvale, CA) in a black 96 well microplate (Brandtech, Essex, CT), and analyzed using SoftMax Pro (Molecular Devices) following the manufacturers instructions.

3.2.3 Dynamic Light Scattering and Zeta Potential Measurements

Dynamic light scattering (DLS) measurements were performed in a backscattering geometry, at 173° on a Malvern Zetasizer Nano ZS (Malvern Instruments Ltd., Worcestershire, UK) using either a disposable folded capillary cell (Malvern) or a disposable low-volume sizing cuvette (Brandtech). Measurements were performed in triplicate at 25.0 °C and allowed to equilibrate for a minimum 120 s prior to measurement. Measurements were analyzed in software provided with the instrument using a cumulant analysis. Zeta potential measurements were performed in triplicate using the disposable folded capillary cell

(Malvern) on a Malvern Zetasizer Nano ZS equipped with a MPT-2 Autotitrator (Malvern), vacuum degasser, and liquid filled glass combination electrode. Automated pH titration was employed for isoelectric point measurements. Standardized HCl and NaOH solutions (Sigma Aldrich) were used as titrants.

3.3 Results and Discussion

3.3.1 Ribonuclease A Adsorption

3.3.1.1 Adsorption Isotherm

I used Ribonuclease A (RNaseA) as a model protein to examine the interaction between proteins and the nanotube surface. RNaseA is a 13.7 kDa, globular protein which is highly stable under my experimental conditions and is not prone to aggregate. [200]

I first characterized the interaction between RNaseA and TiNT by performing quantitative adsorption measurements at room temperature. Here, I varied the concentration of RNaseA while holding the nanotube concentration and the total volume constant, as illustrated in figure 3.2.

The samples were gently mixed for 7 d on a rotisserie rack to ensure they had reached equilibrium. Subsequently, I pelleted the protein-nanotube conjugates in a laboratory centrifuge and measured the amount of protein remaining in the supernatant using a fluorescent assay. I used low protein binding centrifuge tubes in all steps of the experiment to minimize non-specific protein adsorption on the sample walls. In protein-only controls, the amount of protein loss due to adsorption on the sample container walls or during centrifugation was not statistically significant.

The amount of RNaseA adsorbed was determined by subtracting the amount present in the supernatant, measured by the fluorescent assay, from the initial amount of protein in each sample, as illustrated in figure 3.1. This was then normalized by the total surface area of nanotube present in solution. This is a reasonable approximation to the total binding area available to RNaseA for monolayer adsorption. The RNaseA is too large to intercalate within the TiNT interlayers. Therefore the external surface area of the TiNT, 119.3 $m^2\ g^{-1}$, was used to calculate the adsorption isotherm of RNaseA per unit surface area of TiNT[111, 112]. The amount of RNaseA adsorbed per unit area of nanotube versus the concentration of unbound RNaseA, present in solution at equilibrium, is plotted in figure 3.3.

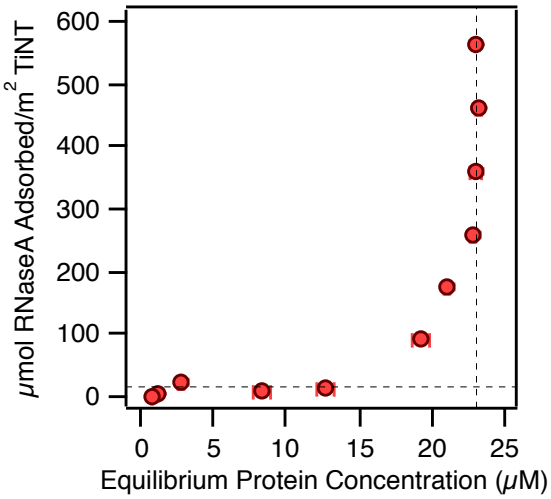

Figure 3.3: Equilibrium adsorption isotherm of Ribonuclease A per unit surface area of TiNT. The dashed lines are drawn to guide the eye. Error bars represent uncertainty based on replicate measurements (n=3) and propagation of systematic uncertainties associated with the measurement.

As seen in figure 3.3, RNaseA adsorbs onto TiNT in two distinct regimes. At low equilibrium protein concentrations, c, the surface coverage increases in a step-like or sigmoidal manner. When the equilibrium concentration reaches about 2.5 µM the surface coverage saturates at a surface coverage of $\approx$ 10 µmol RNaseA/m^2 TiNT. Then the surface coverage does not increase until c > 13 µM, after which the surface coverage increases with the equilibrium protein.

The adsorption behavior changes dramatically when the equilibrium protein concentration exceeds a critical concentration, c* = 23 μM. Above c*, as additional protein is added to the system, the equilibrium protein concentration remains fixed, while the surface coverage rapidly increases from $\approx$ 190 μmol RNaseA/m^2 TiNT to as high as 563.3 $\pm$ 0.9 μmol RNaseA/m^2 TiNT.

The maximum coverage measured, 563.3 $\pm$ 0.9 μmol RNaseA/m^2 TiNT, is over 1000 times the expected value of a closed-packed RnaseA monolayer on the nanotube surface, which is 0.48 μmol RNaseA/m^2 TiNT. The observed capacity cannot be accounted for by confinement of the protein in the nanotube's interlayers, which are only 8.0 Å wide, or inside the nanotube's inner diameter, which could only fit a single-file row of RNaseA.

At c*, the equilibrium protein concentration remains fixed even as additional protein is added. This could occur if the protein concentration had exceeded the solubility limit. However the solubility limit of RNaseA is more than 1000 times larger, $\approx$ 30 mM[201], than the concentrations in my experiment. Furthermore, no protein aggregates or crystallization was detected optically or with dynamic light scattering. Therefore this observed behavior is likely to correspond to a change in the interaction between the protein and the nanotube rather than emergence of a new protein-only phase.

This adsorption capacity as well as the observed isotherm are strikingly different from other studies of similar systems. At the solid-liquid interface, protein adsorption equilibrium isotherms are typically described by Freundlich[173, 202] or Langmuir[31] isotherms. Langmuir's model of adsorption makes two critical assumptions. First, the adsorption affinity, or heat of adsorption, is independent of the coverage, or more simply, it assumes that molecules do not interact with one another. Secondly, it assumes that a unimolecular (monolayer) layer is the upper limit of adsorption[173].

The Langmuir isotherm is valid for clean, smooth, and non-porous surfaces, with

uniform and fully reversible adsorption; however protein adsorption is typically irreversible[202]. For heterogenous surfaces, an empirical fit can be fit with the Freudenlich isotherm described by: $\theta = a(\theta_{eq})^m$, where a, and m are functions describing the interaction. Although this accounts for a distribution of binding sites, it assumes that each population of binding sites follows Langmuir-like behavior.

3.3.1.2 Concentric Multilayer Model

To contextualize the surface coverage, I developed a model to determine the theoretical surface coverage associated with forming of concentric protein layers on the nanotube surface, as illustrated in figure 3.4. I estimated the geometric surface coverage of RNaseA on the nanotube by modeling the protein as a hard sphere of diameter, a, and the nanotube as an open cylinder with an outer radius, r_0, and length, l. This model neglects conformational change of the protein and steric effects, thus allowing for a greater number of proteins on the surface than would be physically realized. I have also have neglected the ellipsoidal shape of the protein, assuming it to be a slightly larger sphere with a length equivalent to the largest diameter of RNase. These assumptions will over predict the number of protein predicted to reside per layer, as the minor difference in size does not adequately compensate for the significant steric effects that experimentally limit the monolayer capacity[43]. Therefore this model will actually predict the coverage at maximum packing density, which is unlikely to physically occur, and thus will predict fewer layers than actually would be realized, but provides a straightforward model to calculate the approximate number of layers.

To compute the number of protein molecules in n layers, I calculate the total surface area available for the protein to adsorb, assuming a buildup of concentric protein multilayers, and use the projected area occupied by the spherical protein to determine the binding capacity.

Assuming each layer to be densely packed: a nanotube of length l and radius r_0 has an

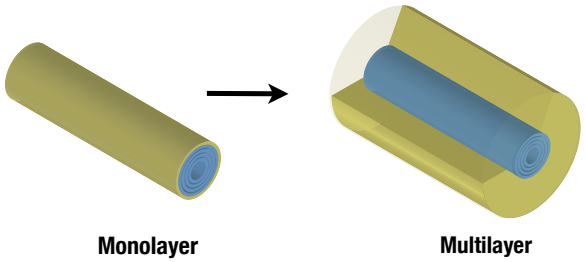

Figure 3.4: Isometric illustration of monolayer and multilayer coated nanotubes. The protein is colored yellow and nanotube is colored blue.

external surface area of $2\pi r_0 l$. Following the adsorption of a single protein layer the new surface area available for binding will be $2\pi(r_0 + a)l$, where a is the diameter of the protein. Extending this for n layers:

$$\text{Total Surface Area} = \sum_{i=1}^{n} 2\pi(r_0 + (i-1)a)l = nl\pi(2r_0 + (n-1)a) \tag{3.1}$$

In previous experiments, I found that most nanotubes are four layers thick, but the process of shortening nanotubes produces nanotubes with lengths varying from $\approx$ 75 nm to 100 nm[111–113, 203]. To remove the length dependence in my calculation nanotubes, I normalized the surface area by the nanotube weight. The simplest unit, which the delaminated anatase nanotube structure[112] can be constructed from, is from four concentric layers of TiO_2 contains 954 TiO_2 molecules. This unit has a mass of $\approx$ 1.25×10^{-19} g , a length $l \approx 0.380$ nm, and a radius, $r_0 \approx 6.25$ nm. I therefore find that surface area per gram nanotube in units of $m^2\ g^{-1}$ is:

$$m^2/(g\ \text{TiNT}) = 9.55\ m^2\ g^{-1}\ nm^{-2}(12.5\,\text{nm} + (n-1)a)a \tag{3.2}$$

Defining the protein surface density, σ, with units protein/m^2 and converting to µmol g^{-1}:, I find:

$$\frac{\mu mol \text{ Protein}}{g \text{ nanotube}} = \left(1.59 \times 10^{-17} \frac{m^2 \centerdot \mu mol}{g \centerdot nm^2 \centerdot (\text{molecules protein})}\right) \sigma \left(12.5nm + (n-1)a\right) a \tag{3.3}$$

Assuming the diameter of RNaseA to be 4.4 nm[43, 62], the projected surface area will be

$$\pi\left(\frac{4.4 \times 10^{-9} m}{2}\right)^2 = 1.52 \times 10^{-17} m^2 \tag{3.4}$$

and the resulting surface density will be:

$$\sigma = \frac{\text{molecule RNaseA}}{1.52 \times 10^{-17} m^2} \tag{3.5}$$

The resulting monolayer coverage (n=1) is therefore: 57.5 µmol RNaseA/g TiNT. From the external surface area of the nanotube, 119.3 $m^2\ g^{-1}$, I determine the surface coverage corresponding to monolayer coverage is: 0.48 µmol RNaseA/m^2 TiNT

In figure 3.5, I use this model and plot the theoretical number of concentric RNaseA layers versus the associated surface coverage, I have also marked the points corresponding to surface coverages shown in figure 3.3. From this, it is evident that the adsorption capacities I measured vastly exceed monolayer coverage exceeding the equivalent of over 4000 layers. While the model may not capture the exact physical reality of the system, it does provide an essential context to my measurements.

3.3.2 Adsorption of Other Model Proteins

I performed similar adsorption experiments with two additional globular proteins, Hen's Egg White Lysozyme (Lysozyme) and Human Ubiquitin (Ubq). As detailed in table 3.1,

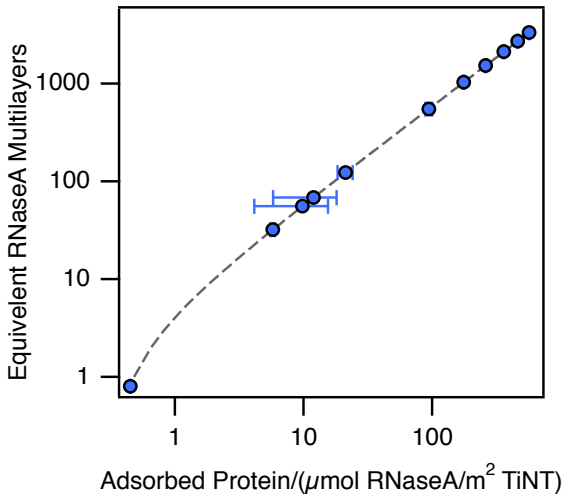

Figure 3.5: Theoretical number of concentric RNaseA layers versus the surface coverage from my model. Blue dots highlight the surface coverages measured in my experiment and theoretical number of concentric multilayers coverage would correspond to. Error bars correspond to coverage uncertainty based on replicate measurements and propagation of systematic uncertainty.

Property	**Ribonuclease A**	**Lysozyme**	**Ubiquitin**
Molar Mass (Da)	13686.63	14313.14	8564.84
Number of Residues	124	129	76
Specific Volume at 25 °C	.704	.702	.743
Dimensions ($Å^3$)	38 x 28 x 22	45 x 30 x 30	51 x 43 x 29
Isoelectric Point (pH)	9.4	11	6.79
Charge at pH 7.2 (+e)	6.29	8.97	0.96
Isothermal Compressibility ($m^2\,N^{-1}$)	.112	.467	???
Structure - $\%\alpha$-helix	11.5	29	16
Structure - $\%\beta$-sheet	33	6	37
Monolayer Coverage (theory) ($\mu mol\,m^{-2}$)	0.48	0.47	0.68

Table 3.1: Various physical properties of Ribonuclease A[43, 200], Lysozyme[43, 50, 204], and Ubiquitin[205]. Charge calculated from protein sequence as described in the text.

Lysozyme and RNaseA both have comparable sizes and masses, while Ubiquitin is $\approx 35\%$ lighter.

A protein's isoelectric point (pI) is defined by the pH at which it has no net charge; above the pI the protein will carry a positive charge, below it it will carry a negative charge. The amino acid (AA) composition of the protein and the acid-base properties (pKa) of

the AA groups are well known. From this I can reasonably approximate the net charge on the proteins as a function of pH. Experimentally, Lysozyme and Ubiquitin both have significantly different isoelectric points than RNaseA. Ubiquitin has an experimental isoelectric point of pH 6.79[200] and will have a slightly negative surface charge at pH 7.2. Lysozyme's isoelectric point is significantly higher, occuring at pH 11[44], and will have a larger positive surface charge than RNaseA at pH 7.2.

This allows us to examine the role of charge in adsorption. From the amino acid composition and known pKa of the amino acid groups in each protein, I calculated the net charge as a function of pH, utilizing software which automated the calculation when I provided it with the AA sequence, which I obtained from the protein data bank.

In figure 3.6, I plot the net charge on all three proteins as a function of pH. It is evident that at pH 7.2, Lysozyme has a more significant positive charge (+8.97e) than RNaseA (+6.29e), while Ubiquitin has a near-unity charge (+0.96e). It should be noted that these differ slightly from the experimentally observed properties. It does not account for which residues are exposed or for post-translational modifications that would also modify the charge. These estimates provide a rough idea of the charge. This is evident from the calculated properties of Ubiquitin, which experimentally has an isoelectric point of 6.89 and should thus be negatively charged at pH 7.2, while the calculated pH titration shows it has a slightly positive charge.

In figure 3.7, I show the equilibrium adsorption isotherms for RNaseA, Lysozyme, and Ubiquitin at pH 7.2. Although the behavior of RNaseA at c*=23 μM was not exhibited by the other two proteins, the adsorption capacity of all three proteins significantly exceeded monolayer coverage (indicated in table 3.1). As seen in figure 3.7, before c* the amount of protein adsorbed was largest for Ubiqituin, which has nearly neutral charge at pH 7.2, and was smallest for Lysozyme, which has the largest charge. This is consistent with experimental observations that protein adsorption on a substrate is maximized near the protein's

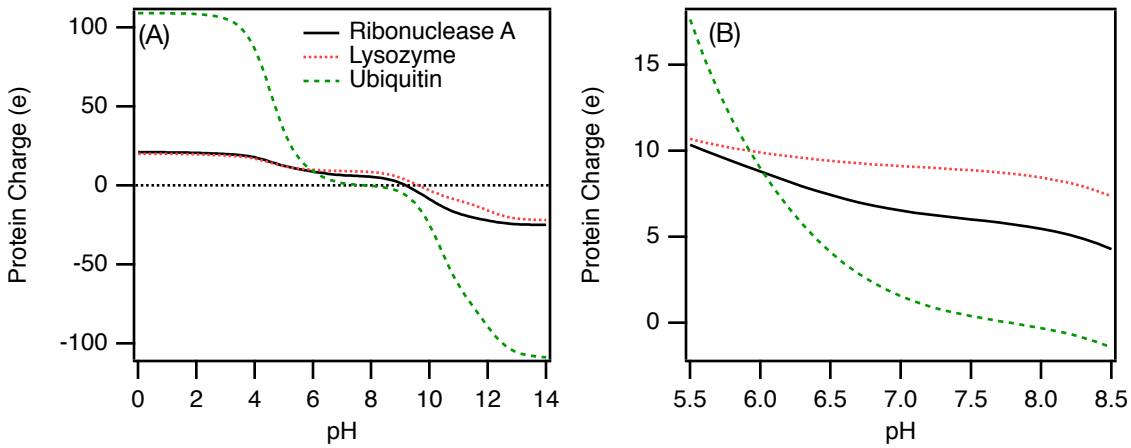

Figure 3.6: Calculated net charge on Ribonuclease A, Lysozyme, and Ubiquitin as a function of pH, determined from protein sequence (using CLC Bio). (A) Charge plotted from pH 0 to 14 (B) Charge between 5.5 and 8.5 highlights the differences between the proteins. Near our experiments at pH 7.2, the proteins all have a slight net positive charge. These measurements are not purely indicative of the surface charge - noting that Ubiquitin's experimental isoelectric point is actually 6.89.

isoelectric point[31] due to the decreased protein-protein repulsion.

The differences between the RNaseA and Lysozyme adsorption isotherms may also be due to their differing dipole moments – RNaseA has a large dipole moment, while Lysozyme's is quite small[206]. Due to RNaseA's large dipole it is likely to adsorb in a preferred orientation, while Lysozyme will be more likely to approach the surface of the nanotube with a near-random orientation with a significantly less efficient packing density.

3.3.3 Effect of Ionic Strength

The nanotube and RNaseA are oppositely charged at pH 7.2 and experience a net Coulombic attraction to each other. Therefore, to investigate the role of electrostatic interactions between the protein and nanotube, I performed a series of trials with a fixed concentration of nanotubes and RNaseA and varying amounts of NaCl and examined the mean aggregate size using dynamic light scattering (DLS), as detailed in equation (B.23).

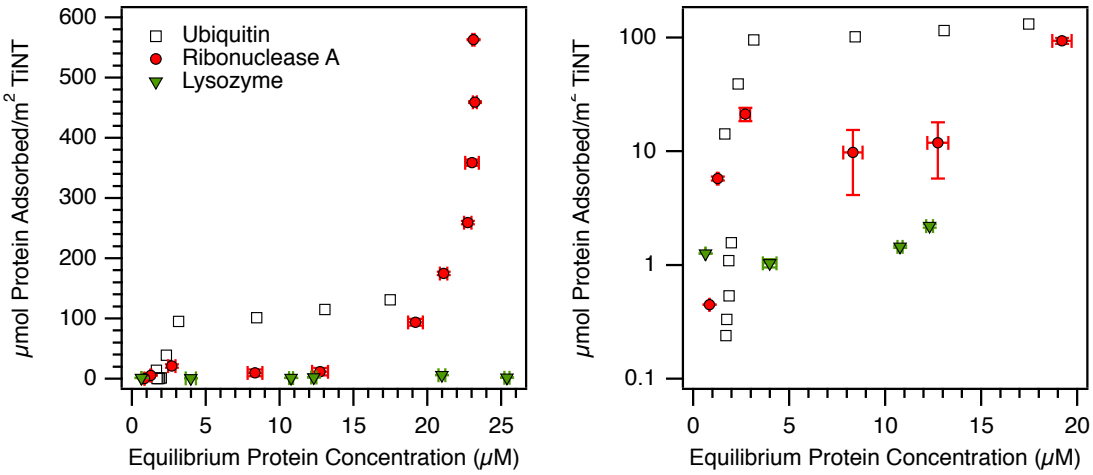

Figure 3.7: Equilibrium adsorption isotherm Ribonuclease A, Lysozyme, and Ubiquitin on TiNT, as determined by a fluorometric assay. *(Left)* The surface coverage (y-axis) is expressed in terms of the number of protein adsorbed per unit area nanotube, the equilibrium concentration (x-axis) of each protein is expressed in in μmol. *(Right)* Log-lin plot of lower equilibrium concentrations highlights the drastically different adsorption isotherms.

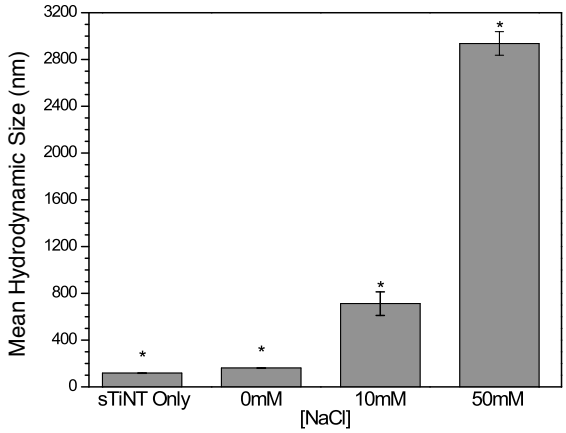

Figure 3.8: Increasing ionic strength increases mean aggregate size. All samples had identical amounts of TiNT and RNaseA and were incubated in 25 mM HEPES Buffer (pH 7.2) with different concentrations of NaCl. The apparent mean hydrodynamic size was determined by DLS, using equation (B.23). Results are mean ± s.e.m., n=3. Asterisk indicates $p<0.05$ as determined by analysis of variance (ANOVA).

Further details of the measurement and theory behind it are in Appendix B.

Increasing the ionic strength increases the charge screening length (reflected by decreasing Debye length) and effectively diminishes the Coulombic attraction between the protein and nanotube as well as the protein and nanotube's self-repulsion.

As seen in figure 3.8, the mean aggregate size increased significantly with increasing ionic strength, while the hydrodynamic radius of the nanotube and protein in control experiments was unchanged.

At 25 °C the Debye length for NaCl is, κ^{-1} = 0.304 nm([NaCl])$^{-1/2}$, where [NaCl] is the ionic strength expressed in molar units. At 10 mM NaCl the Debye length is 3.04 nm, while at 50 mM NaCl the Debye length reduces to 1.36 nm. At elevated ionic strengths the adsorption of charged proteins to an oppositely charged substrate will be reduced, while adsorption to a like-charged interface will be increased. Therefore these findings suggest that the observed size increase with ionic strength may be due to decreased repulsion between the adsorbed protein and free protein[40].

To contextualize these findings it is important to understand how the average distance between the proteins compares with the Debye length. The average center-to-center distance between the proteins is $d \approx \left(\frac{3}{4}\pi n\right)^{-1/3}$, where n is the number density of protein. In these experiments, the RNaseA concentration was fixed at 25.5 µM or 1.535 $\times$ 10^{16} RNaseA/cm^3, and therefore $d \approx 3.02 \times 10^6$ cm $\approx$ 30 nm. RNaseA is a prolate ellipsoid. However it can be well approximated by its approximate (spherical) hydrodynamic diameter of 3.4 nm[207]. As such, the closest approach between the residues of two seperate RNaseA molecules will be 30 nm - 2$\times$1.7 nm = 26.6 nm.

At 10 mM NaCl, the Debye length is an order of magnitude smaller than the average separation distance between the proteins and the protein-protein Coulombic repulsion will be significantly reduced. The significant size increase, as observed in figure 3.8, suggests that the protein-protein Coulomb repulsion hinders the growth of larger aggregates. At elevated ionic strength, the decrease in protein-protein repulsion allows the protein to come closer, where attractive forces between individual protein residues can dominate. Further increasing the ionic strength results in a significantly larger size.

These observations are atypical for globular protein adsorption[31]. Increasing the ionic strength reduces the lateral interactions between adsorbed proteins and allows for increased packing density on the nanotube surface or cooperative adsorption[31, 40, 67] — this should result in a measurable size decrease. An additional consequence of increasing the salt is that it screens the Coulombic interaction between the protein and the nanotube surface. If this were the primary driving force for protein adsorption to the nanotube interface, increasing the salt concentration should decrease the amount of protein adsorbed and decrease the size. This suggests that the Coulombic attraction between the nanotube and free protein is not the primary source of the observed adsorption behavior.

The measured increase in aggregate size suggests that the interaction between bound and free protein may play an important role in multilayer aggregate formation. Furthermore, these findings suggest that while the nanotube does effectively reduce the energetic barrier to protein-protein association, it does provide a sufficiently large driving force to hide the effects of repulsion between proteins.

The absence of aggregation except when both nanotube and protein are present further highlights the important role of the nanotube as the source of this phenomenon. At pH 7.2, the nanotube has a ζ-potential of $\zeta \approx$–50 mV, while RNaseA has a ζ-potential of $\zeta \approx$4.1 mV. This suggests that to first order, aggregation of the nanotube-only control and protein-only control are prevented over experimental timescales by an energetic barrier of $\approx 2k_B\text{T}/e$ and $\approx 0.16\ k_B\text{T}/e$, respectively[208].

3.3.4 Hypothesis for Adsorption Isotherm

At first glance, there are four possible basic phenomena which could theoretically result in the observed adsorption capacities:

1. Oligomerization of the protein in solution or on the nanotube surface[34, 40, 209, 210].
2. The formation of equilibrium protein clusters[19, 211], entropically driven association[18], or aggregates as a result of the interaction with the nanotube[211].
3. The formation of concentric protein multilayers or other extended geometries emanating from the nanotube surface[33, 98].
4. Self-assembly of protein structures or protein-nanotube structures[15, 212, 213].

While the first two options are possible, neither are supported by my measurements in subsequent chapters. As will be detailed in chapters 4 and 7, I did not observe any oligomers or other covalent aggregates with denaturing gel-electrophoresis, differential scanning calorimetry, or dynamic light scattering. Furthermore, RNaseA is a highly stable globular protein[200, 214] and is not expected to significantly denature, aggregate, or oligomerize under my experimental conditions[31, 40].

Previous predictions, and recent experimental measurements, have shown that equilibrium clusters of globular proteins can exist at low ionic strengths as a result of the competition between long-range Coulomb repulsion and short range attractive forces[211, 215, 216]. Here cluster growth would occur as the charged proteins attempt to maximize their average interparticle separation, d. Therefore, the size of the clusters should exhibit a strong dependence on the protein volume fraction, ϕ, scaling roughly as $R_c \sim \phi^{1/3}$. However as seen in chapter 4, in my measurements I find that the mean cluster size scales as $R_c \sim \phi^{3.3\pm0.1}$ and only in the presence of the nanotubes. The observation of equilibrium clusters is only associated with significantly higher protein volume fractions. In experiments equilibrium protein clusters[211] were only observed in concentrated protein solutions with $\phi > 1.85 \times 10^{-1}$, whereas the maximum protein volume fraction I employed was 1.54×10^{-3}.

On the other hand, the final two hypotheses could both explain portions of the isotherm. For c<c*, the initial, steplike or sigmoidal behavior, is indicative of cooperative effects and such positive cooperativity has been closely linked surface aggregation mechanisms[40]. Previous studies have shown that protein multilayers can form under conditions which promote protein aggregation or reduce interprotein repulsion[98, 217–219]. Here, the packing density at each layer will depend on the electrostatic repulsion between the proteins with each other and the electrostatic interaction with the substrate on which they are adsorbed.

Self-assembly would explain the behavior for c>c*. The rapid increase of adsorbed protein, observed when the unbound protein concentration is increased above c*, is typical of systems undergoing self assembly or macromolecular condensation[136, 220] — this will be discussed at length in chapter 4 .

3.4 Conclusions

Protein adsorption is a ubiquitous phenomenon. In this chapter, I have examined the adsorption of three different globular proteins, Ribonuclease A, Lysozyme, and Ubiquitin on titania nanotubes at physiological pH. All three of these proteins exist as monomers under physiological conditions. RNaseA and Lysozyme have long been used as standard proteins to examine the protein adsorption properties of macroscopic surfaces and colloidal materials[42–44, 46, 49–52, 60, 62, 63, 68, 80, 98, 119, 181, 191, 193, 195, 199, 218, 219, 221–225] and increasingly on nanoscale substrates[16, 30, 33, 34, 36, 43, 45, 69, 70, 79, 82, 85, 86, 95, 97, 185, 194, 197, 226–243]. These proteins are rigid (characterized by a low adiabatic compressibility) and do not undergo significant conformational change when in contact with hydrophilic substrates such as the nanotube.

Yet protein adsorption is also an exceedingly complicated phenomenon. The complex

composition of proteins means that most proteins do not simply desorb and adsorb to a substrate a small molecule or rigid particle would. Although adsorption is frequently modeled as a simple equilibrium process, it typically is far from it. Rather, over the course of an experiment proteins often undergo very slow structural rearrangements[40]. At low bulk protein concentrations where adsorption kinetics are slower, these conformational changes are particularly slow and allow the proteins to effectively explore their energetic landscape through a cascade of angular rotations[40, 207]. The impact of this is highly undervalued - as structural changes occur the protein affinity for the substrate can also change, creating a dynamic system with a wealth of interesting behaviors - including clustering[40, 79, 244, 245] and aggregation on a substrate[217, 246].

Over long timescales, multilayer adsorption can occur[202] and in this chapter, I examined the adsorption of RNaseA, Lysozyme, and Ubiquitin that had equilibrated for over seven days. In fact, in control experiments, I've let this interaction run months. I find that all three proteins adsorb at supramonolayer capacities. On the basis of a concentric multilayer model I have qualitatively examined the coverage of these proteins. The RNaseA adsorption isotherm exhibited two different adsorption regimes. First RNaseA adsorbs up to a 55 layers of coverage. The coverage then remains constant until a critical protein concentration is reached. Upon reaching this critical concentration (c*=23 μM), any subsequently added RNaseA is adsorbed. On the basis of the adsorption isotherm, I evaluated a series of potential hypotheses that could explain these observations. I suggest that this corresponds to two different phenomena: multilayer adsorption and some type of macromolecular condensation or self-assembly, which I explore in depth in the subsequent chapter.

Multilayer adsorption of Lysozyme and Ribonuclease A have been previously observed[42, 44, 60, 61, 98] , however no more than three layers have ever been reported. Furthermore, the secondary and tertiary layers were particularly sparse. The significant adsorption I observe could be the result of cooperative adsorption, which is closely related to

surface aggregation mechanism of proteins[40]. However up until now, it is unclear what the role of the nanotube surface is in the process, which I explore throughout the remainder of this dissertation.

CHAPTER 4

SELF ASSEMBLY OF GLOBULAR PROTEINS WITH TITANIA NANOTUBES

4.1 Introduction

In chapter 3 I examined the adsorption isotherm of RNaseA, Lysozyme, and Ubiquitin on titania nanotubes. Each protein adsorbed onto the nanotube at coverages that significantly exceeded the monolayer capacity.

The isotherm for RNaseA is particularly intriguing. Adsorption occurred in two stages. Below a critical concentration c*, the coverage rapidly increases and saturates. Once the equilibrium protein concentration exceeds c*, the coverage rapidly increases while the equilibrium concentration remains fixed at c*. This behavior is typical for systems undergoing self assembly or macromolecular condensation and could explain the observed isotherm.

In this chapter I investigate this hypothesis. Using dynamic light scattering, adsorption measurements, and microscopy, I show that this transition at c* likely corresponds to self-assembly of the multilayer-coated nanotubes with additional free protein. I discuss the thermodynamic implications for this observation and present a model to describe the growth of enzyme multilayers on the nanotube and the self-assembly of enzyme-nanotube superstructures.

4.2 Experimental

4.2.1 Preparation of Proteins and Related Solutions

Lyophilized, chromatographically-purified Bovine Pancreatic Ribonuclease A (RNaseA, Product: R6513), and Hen's Egg White Lysozyme (HEWL) were purchased from Sigma Aldrich, Recombinant Human Ubiquitin (Ubq, Product: BML-UW8795, Lot: X08313B) was purchased from Enzo Life Sciences, 1 M HEPES buffer (pH 7.2) was purchased from Fisher Scientific, both were used without further purification. For a given set of experiments, I freshly prepared 25 mM HEPES buffer from the 1 M stock using clean volumetric flasks, I then passed the buffer through a 0.10 µm PES membrane filter (Millipore) to remove any possible microbial contaminants or dust that could interfere with my experiments. Immediately prior to my experiments I weighed out lyophilized protein on a calibrated Denver Instruments TP-114 analytical balance ($\pm$ 0.1 mg) within a low protein-binding Eppendorf microcentrifuge tube and subsequently added a known volume of the 25 mM HEPES buffer with a micropipette. I filtered the protein solution through a 100 nm PES syringe filter to remove any possible preexisting aggregates. In a typical experiment with RNaseA, the stock concentration was $2.5 \pm 0.2\,\mathrm{mg\,mL^{-1}}$. I performed denaturing gel electrophoresis (SDS-PAGE) on each protein lot prior prior to using it; no protein oligomers were detected with SDS-PAGE.

4.2.2 Dynamic Light Scattering and Zeta Potential Measurements

Dynamic light scattering (DLS) measurements were performed in a backscattering geometry, at 173° on a Malvern Zetasizer Nano ZS (Malvern Instruments Ltd., Worcestershire, UK) using either a disposable folded capillary cell (Malvern) or a disposable low-

volume sizing cuvette (Brandtech). Measurements were performed in triplicate at 25.0 °C and allowed to equilibrate for a minimum 120 s prior to measurement. Measurements were analyzed in software provided with the instrument using a cumulant analysis. Zeta potential measurements were performed in triplicate using the disposable folded capillary cell (Malvern) on a Malvern Zetasizer Nano ZS equipped with a MPT-2 Autotitrator (Malvern), vacuum degasser, and liquid filled glass combination electrode. Automated pH titration was employed for isoelectric point measurements. Standardized HCl and NaOH solutions (Sigma Aldrich) were used as titrants.

4.2.3 TEM/SEM Imaging

To prepare TEM samples, the reaction mixture was drop deposited onto a 300 Mesh lacey carbon grid (Ted Pella, Redding, CA) and allowed to dry in air. High resolution TEM imaging was performed at 200 kV on a JEOL 2010F-FasTEM. Images were acquired using a 2k x 2k Gatan CCD bottom mount camera. When indicated, pre-deposited samples were stained for 3 min in a 2% aqueous solution of Uranyl Acetate. The grid was subsequently washed to remove excess Uranyl Acetate and reimaged. Samples for SEM were drop deposited onto a clean Silicon square (Ted Pella). SEM imaging was performed on a Hitachi S-4700 field emission SEM at 5kV and a FEI 600 Helios NanoLab DualBeam at 15 kV. Prior to imaging at 15 kV, a 2.5 nm thick layer of Au/Pd was sputtered onto the sample in an Argon plasma (Cressington Scientific Instruments Ltd, Watford, England).

4.3 Results and Discussion

4.3.1 Growth of Protein-TiNT Aggregates

4.3.1.1 Hydrodynamic Diameter of Protein-TiNT Clusters

I used dynamic light scattering (DLS) to examine the effect of protein charge, employing Ubiquitin and RNase, and the effect of protein:nanotube stoichiometry and compare it with the adsorption measurements in the previous chapter.

In the subsequent discussion, I use the molar ratio of protein-to-TiO_2, which I designate ξ, to compare and contrast different proteins and stoichiometries. In these experiments, the volume fraction of ubiquitin, ϕ_U, was varied from 7.47×10^{-6} to 1.87×10^{-4}. The nanotube concentration was 9.39 µM for all ubiquitin samples, except for the data point at ξ=0.3, here the nanotube was 281 µM. This allowed me to obtain a lower ξ data point, while keeping the protein concentration within the detection limit of the DLS. Furthermore, it was only possible to obtain a small range of data points for the ubiquitin due to its prohibitive cost. The RNaseA volume fraction, ϕ_R, was varied between 8.87×10^{-7} to 1.54×10^{-3}. The nanotube concentration was also held at 9.39 µM, corresponding to a volume fraction $\phi_T \approx 3.8 \times 10^{-7}$, except for the two lowest ξ data points, where the nanotube concentration was increased to 18.78 µM. All samples had a volume of 1000 µL and were contained in 25 mM HEPES buffer at pH 7.2.

With DLS I obtain a mean hydrodynamic size which is characteristic of the size distribution of the resulting aggregates[247, 248], rather than the exact size. It is not safe to assume that the clusters formed are isotropic spheres, rather, as I will show in subsequent imaging, the resulting structures are prolate ellipsoid-like. This anisotropy results in orientationally-dependent diffusion coefficient[247, 249, 250] and scattering cross-section, manifested in

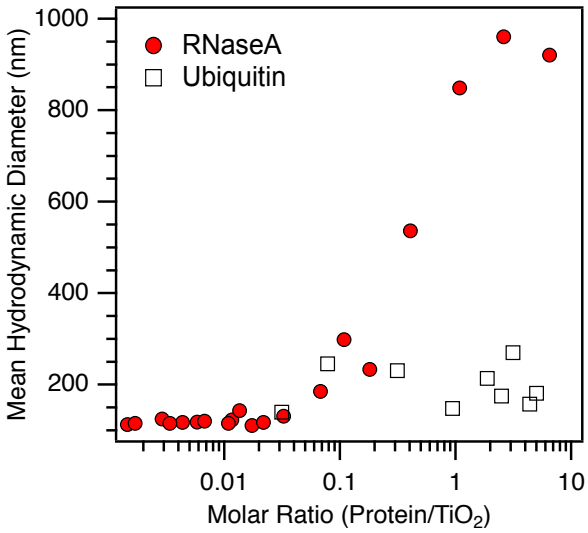

Figure 4.1: Semi-logarithmic plot of mean hydrodynamic size of TiNT conjugates formed with RNaseA (pI = 9.4) and Ubiquitin (pI = 6.79) at pH 7.2 samples versus the molar ratio of protein-to-TiO_2.

the structure factor, $S(q)$. For values of $qL < 3$, where L is the length of the nanotube, the correlation time determined with DLS represents an effective diffusion coefficient which has been isotropically averaged over the object's different rotational axes, and the size reported is that of an diffusionally-equivalent sphere[249, 251].

In figure 4.1, I show DLS measurements of the mean hydrodynamic diameter of non-sedimented clusters of RNaseA and Ubiquitin formed in the presence of TiNT as a function of ξ. From these measurements I obtain an effective mean hydrodynamic diameter which is characteristic of the size distribution of the resulting protein-nanotube aggregates or clusters[248]. Here, RNaseA and Ubiquitin display distinctly different behaviors.

As the RNaseA concentration was increased (reflected by increasing ξ) the mean hydrodynamic size of RNaseA-TiNT clusters increased significantly above that of RNaseA (4.8 nm) or the nanotube (113 nm). The addition of protein results in the formation of RNaseA-TiNT conjugates whose size is strongly dependent on ξ. In agreement with my adsorption measurements, DLS reveals two distinct growth regimes for RNaseA-TiNT con-

jugates as the protein concentration is increased. Below ξ=0.05, the hydrodynamic size remains nearly constant at ≈125 nm while above ξ=0.05, the size grows exponentially until saturating near ξ=2 at ≈1000 nm.

At $\xi \approx 6.3$ the measured size decreases by ≈ 50 nm. While such a decrease could result if protein desorbed, my adsorption measurements show increased adsorption at higher protein concentrations, not decreased. As I will demonstrate later with Lysozyme, the measured decrease is likely the result sedimentation due to an *increase* in size. It is possible that aggregates above 1 μm sedimented prior to the measurement, in which case, my measurement would be skewed towards the smaller, suspended aggregates remaining in solution. Alternatively, the apparent size I measure would be decreased if the aggregates still in solution are sedimenting over the timescale of my measurement. In this case, the apparent diffusion coefficient I measure would be increased due to the contribution of the sedimentation velocity and it is incorrect to apply the Stokes-Einstein equation, which only applies for freely diffusing particles. In such a case, this increased apparent diffusion rate would lead me to "measure" an erroneously smaller size.

On their own, neither the nanotube nor the protein formed any detectable aggregates over the timescale of the experiment. But when combined, the apparent size significantly increased, as seen in figure 4.1. In conjunction with the multilayer loading capacities indicated by my adsorption measurements, these findings suggest that the size increase may be due to the formation of much larger structures containing multiple nanotubes, forming either through interaggregate interactions or self assembly.

In contrast, the apparent size of ubiquitin-TiNT clusters, shown in figure 4.1 does not exhibit any clear dependence on ξ. However, the apparent size aggregates formed do significantly exceed the hydrodynamic size of either ubiquitin (2.5 nm) or the nanotube (113 nm). Although ubiquitin and RNaseA both exhibit similar initial adsorption behaviors and capacities, these measurements highlight a distinct difference in the structure or formation of

higher-order assemblies. While aggregates of Ubiquitin-TiNT do form, they do not exhibit demonstrate the significant apparent size increase found with RNaseA-TiNT.

For specific, well-defined geometries and low polydispersity, it is possible to extract an objects different dimensions from these measurements[209, 247, 250–252]. However, as is made clear in the appendix of chapter 3, the coupling of translational and rotational diffusion as the aggregate size increases complicates this situation. Despite my best efforts, I was not able to extract useful information about my objects shape from existing analytical or computational models[253–258] due to the polydispersity and highly anisotropic nature of the clusters formed. Performing light scattering at a range of q could yield significant information about the structure which would enable me to extract further dimensional information, however, q was fixed on the instrument I had access to.

4.3.1.2 Evidence of Lysozyme-TiNT Aggregate Growth

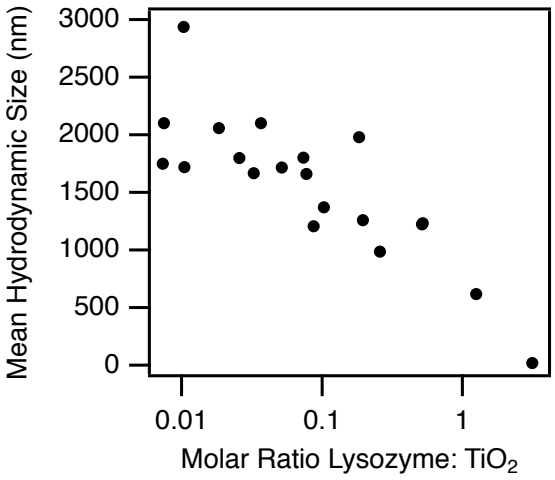

Figure 4.2: Semi-log plot of mean hydrodynamic size of Lysozyme-TiNT samples as a function of increasing molar ratio of Lysozyme-to-TiO_2.

I also examined the hydrodynamic size of Lysozyme-TiNT aggregates as a function of ξ. As seen in figure 4.2, at extremely low concentrations of Lysozyme very large aggregates are observed. However the mean size appears to decrease as the molar ratio of Lysozyme

to TiO_2 increases. In many Lysozyme samples, a white sediment was observed at higher ξ, as seen in figure 4.3. The lysozyme-TiNT aggregates grow so large that they begin to sediment. The observation of this sediment suggests that the decrease in size with ξ observed in figure 4.2 is due to sedimentation of the sample during my measurement. The increased apparent diffusion rate leads to the observed trend.

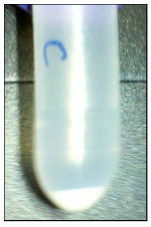

Figure 4.3: Photograph of sample containing lysozyme and TiNT after 3 days of mixing. The Lysozyme-TiNT aggregates grow so large that they form a white sediment at the bottom of the microtube.

4.3.2 Critical Assembly Concentration of RNaseA-TiNT

Self assembly is a structural phase transition that occurs when, upon reaching a critical concentration, ξ^*, it becomes more energetically favorable for any additional solute to aggregate rather than remain free in solution[6, 117, 136].

If the nanotube and protein self-assemble, then I would expect to observe a transition near a critical molar ratio, ξ^*, in both the adsorption and dynamic light scattering data. In figure 4.4 I plot the the amount of the unbound protein as well as the amount of adsorbed protein versus ξ, as shown in figure 4.4A and above it, the DLS data I showed for RNaseA. At low values of ξ, the amount of unbound RNaseA increases steadily while the amount of adsorbed RNaseA remains at a relatively low fixed value. This behavior continues until ξ reaches a critical aggregation concentration (CAC), ξ^*, at ξ^*=2. Above ξ^* the amount of adsorbed RNaseA increases linearly while the amount of unbound RNaseA reaches a steady value. This adsorption behavior and the clear CAC are both consistent with the

system undergoing self assembly starting at around ξ^*. For $\xi < 2$, the measured increase in size is consistent with the approximate increase in size predicted by the adsorbed coverage. However above $\xi > 2$ the expected hydrodynamic size increase is significantly smaller than anticipated by the measured coverages. As discussed in appendix of chapter 3, this could be due to the strong coupling of translational and rotational diffusion at values of qL > 3. This behavior could also occur if self-assembly occurred above $xi > 2$, in which the increased coverage would not correspond to our estimates with the multilayer adsorption model.

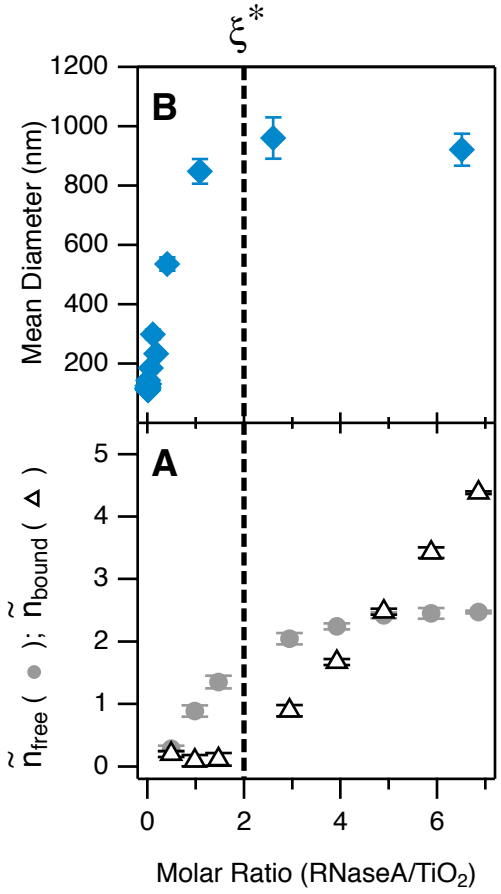

Figure 4.4: Self assembly of RNaseA-TiNT aggregates as a function of the RNaseA:TiO_2 molar ratio, ξ. (A) Adsorption isotherm showing the relative number of nanotube-bound ($\triangle$) and unbound (free) ($\bullet$) protein, units are moles protein normalized by total moles TiO_2 (B) DLS measurement showing that the mean aggregate diameter increases with ξ. The dashed line is drawn to indicate the critical aggregation concentration, ξ^*.

4.3.3 TEM/SEM Imaging

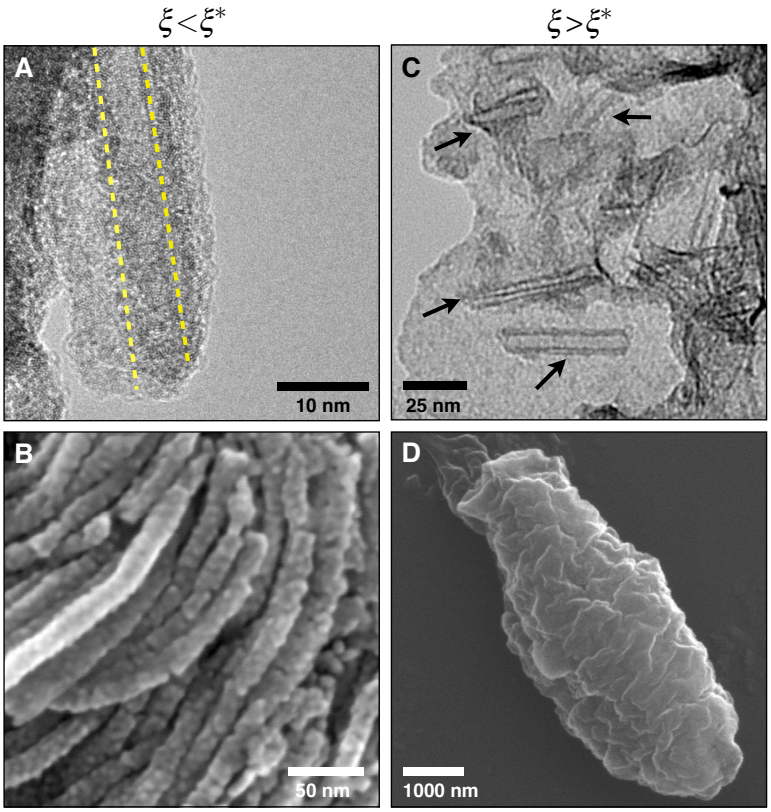

Figure 4.5: (A) TEM image of RNaseA-TiNT at ξ=0.06 shows a 6 nm to 8 nm thick protein layer surrounding the nanotube. Yellow lines are drawn to indicate the outer diameter of nanotube. (B) SEM image at $\xi < \xi^*$ shows individual nanotubes coated with 6 nm to 8 nm of protein, indicating two to three layers of adsorbed protein. (C) TEM image at $\xi > \xi^*$ shows multiple nanotubes embedded in a large plaque suggesting the formation of large aggregates of multiple nanotubes. Arrows are drawn to point out nanotubes. (D) SEM image at $\xi > \xi^*$ shows a large aggregate containing multiple protein-coated nanotubes.

TEM and SEM imaging of the aggregates further support a scenario of multilayer adsorption at low ξ, followed by the formation of larger aggregates at higher ξ. As shown in figures 4.5A and 4.5B , TEM and SEM images of the protein-nanotube conjugates formed at ξ=0.06 clearly show a 6 nm to 8 nm thick adsorbed layer of RNaseA on the nanotube surface. This thickness is nearly twice the diameter of the protein and is consistent with the formation of protein multilayers on the nanotube. Figures 4.5C and 4.5D show TEM and SEM images of aggregates formed just above the critical transition, at $\xi \approx$ 2.1. The TEM image, shown in figure 4.5C, reveals the presence of a large aggregate cluster consisting

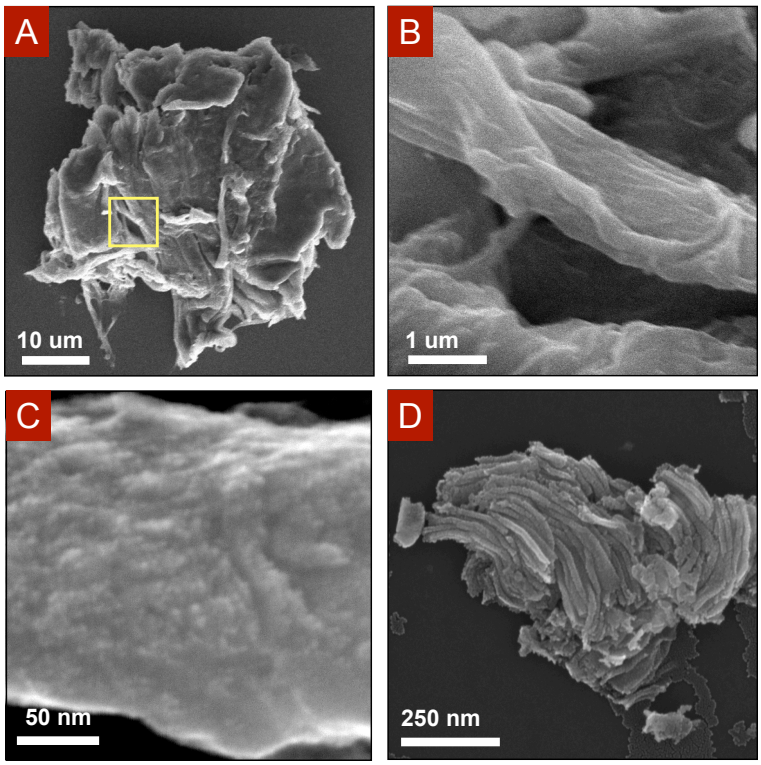

Figure 4.6: (A-C) Additional SEM imaging of RNaseA-TiNT aggregates (A-C) and (D) multilayer coated nanotubes. Yellow box in (A) indicates the approximate region where (A) was taken.

of multiple nanotubes embedded in a large protein plaque, while the SEM image, shown in figure 4.5D, reveals a prolate ellipsoidal aggregate that is approximately 2 µm wide and 6 µm long. These images also show that that protein multilayers form around the entire nanotube, including the open ends, where there is no accessible nanotube surface for adsorption. Here the proteins must adsorb by associating with adjacent, previously adsorbed protein, and would require a driving force to overcome the significant interprotein Coulomb repulsion[60].

Additional SEM imaging, shown in figure 4.6, highlights the morphology of the large structures. In figure 4.6B and figure 4.6C the larger prolate structures have a smooth appearance and no individual nanotubes are clearly seen. However in figure 4.6D, which was taken below ξ^*, individual coated nanotubes are clearly seen.

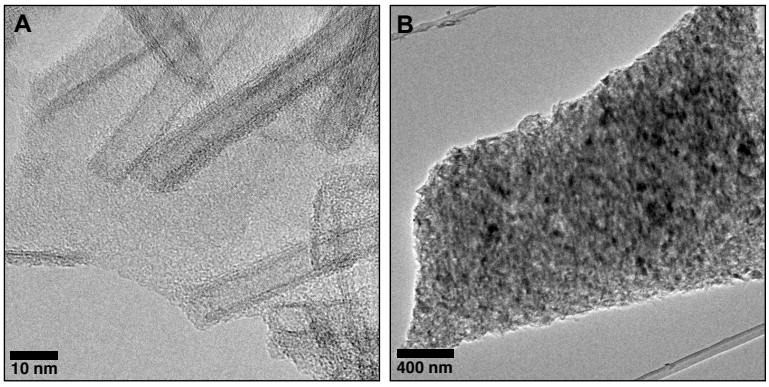

Figure 4.7: Similarly to RNaseA, Lysozyme also forms self-assembled aggregates with TiNT. TEM imagingin reveals a similar microstructure consisting of (A) multiple TiNT surrounded by a larger protein plaque (B) which form micron-sized aggregates.

As seen in figure 4.7, Lysozyme forms similar micron-sized self-assembled aggregates with TiNT. High resolution TEM, shown in figure 4.7A, reveals multiple nanotubes embedded in a thick lysozyme plaque, while figure 4.7B shows the formation of micron-sized aggregates of TiNT and lysozyme similar to those found in my experiments with RNaseA-TiNT. Although I performed TEM on the ubiquitin samples, I was unable to observe any notable Ubiqituin-TiNT structures.

4.3.4 Thermodynamics of Self Assembly of RNaseA-TiNT Structures

The adsorption and growth behavior, shown in my imaging and adsorption measurements in chapter 3 and in figure 4.4A, are both a hallmark signature of self assembly[6, 117, 259, 260]. In particular, the existence of a critical concentration above which the equilibrium protein concentration remains fixed, is indicative of self-assembly. A similar phenomenon involving the emergence of an aggregate mesophase is observed in the formation of supramolecular assemblies and in other self-assembling systems such as liposomes or giant vesicles[6, 117].

Thermodynamically, the structural transition between the dispersed and self-assembled

state is favorable only if assembly reduces the Gibb's free energy of the system. The theoretical underpinnings of self-assembly can be easily formulated by considering a system of solute molecules, of total volume fraction, ϕ, which have a propensity to form aggregates of *N* solute molecules occupying volume fraction, X_N. The total volume fraction of the system is therefore the sum over all possible aggregate states:

$$\phi = \sum_{N=1}^{\infty} X_N \tag{4.1}$$

In equilibrium, the chemical potential, μ, of the solute and coexisting aggregates must be the same:

$$\mu = \epsilon_N + \frac{1}{\beta N} \log\left(\frac{X_N}{N}\right) \tag{4.2}$$

Here ϵ_N is the free energy change associated with transferring a solute monomer from the bulk phase to an aggregate of *N* molecules, while the second term results from the translational entropy of the aggregates[261]. I have used the convention $\beta^{-1} \equiv k_B T$, where T is the temperature of the system and k_B is Boltzmann's constant. Equation (4.2) can be rearranged in terms of X_N:

$$X_N = N \exp\left(\beta N(\mu - \epsilon_1)\right) \tag{4.3}$$

noting that $X_1 = \exp\left((\beta(\mu - \epsilon_N)\right)$, this can be rewritten as:

$$X_N = N\{X_1 \exp(\beta\left(\epsilon_1 - \epsilon_N\right))\}^N \tag{4.4}$$

This equation suggests two possible scenarios depending on whether ϵ_N is greater or less than ϵ_1. When $\epsilon_N \geq \epsilon_1$ it is energetically unfavorable to form aggregates, as it increases the system's Gibb's free energy, and solute will primarily be found as monomer. However, when when $\epsilon_N < \epsilon_1$, aggregate formation will decrease the system's free energy and it becomes favorable for the solute to aggregate rather than to remain monomeric[117].

The transition between these two states will depend directly on the free energy per molecule in the aggregated state, which is a direct function of the aggregate geometry and

the strength of the intermolecular forces. The free energy per molecule in the aggregates will be of the form:

$$\epsilon_N = \epsilon_\infty + \frac{\alpha}{\beta N^P} \tag{4.5}$$

where ϵ_∞ is the energy of a molecule in an infinitely large aggregate, α is a number which depends on the strength of the intermolecular interactions, and P is a constant which depends on the aggregate geometry and dimensionality. Combining equations (4.4) and (4.5) we find:

$$X_N = N\{X_1 \exp\left(\alpha(1 - N^{-P})\right)\}^N \tag{4.6}$$

It is evident from equation (4.1) that any given volume fraction, X_N, cannot exceed unity. Therefore when $X_1 \approx e^{-\alpha}$, any additional solute added must join an aggregate. The critical volume fraction at which this occurs is called the critical aggregation concentration (CAC), or in the case of micelles, the critical micelle concentration (CMC). Additional solute added above this transition will join the aggregates, while the concentration of monomer, X_1, will remain fixed. For spherical particles, this transition occurs at approximately:

$$X_1 \approx \exp\left(-\beta(\epsilon_1 - \epsilon_N)\right) \tag{4.7}$$

An extension of this theory can be applied to systems containing multiple coexisting phases. This is frequently encountered in the formation of liposomes or vesicle superaggregates[6]. In both of these systems, a monomeric species assembles into a primary aggregate, the micelle or vesicle, which later assembles into a mesophase or secondary aggregate, the liposomes or vesicle-superaggregates. At the emergence of the secondary aggregate with M monomers, the monomer, primary, and secondary aggregate chemical potentials must be equivalent:

$$\epsilon_1 + \frac{1}{\beta}\log X_1 = \epsilon_N + \frac{1}{\beta N}\log\left(\frac{X_N}{N}\right) = \epsilon_M + \frac{1}{\beta M}\log\left(\frac{X_M}{M}\right) \tag{4.8}$$

We can similarly solve for the condition at which the mesophase emerges by equating the chemical potentials of any two phases.

From equation (4.7) it is evident that the critical aggregation concentration of this transition I observe in figure 4.4 is determined by the chemical potential difference between any two phases in the system. This allows me to write the CAC in terms of the chemical potential of the protein monomer, ϵ_1, and the aggregates, ϵ_N:

$$\text{CAC} \approx \exp\left(-\beta(\epsilon_1 - \epsilon_N)\right) \tag{4.9}$$

It is worthwhile to remark that the chemical potential difference, $\epsilon_1 - \epsilon_N$, is the Gibb's free energy change associated with the emergence of the aggregate mesophase, ΔG.

From the adsorption data and DLS data in figure 4.4, I can estimate the critical molar ratio at which the mesophase emergences by fitting $_{free}$, shown in figure 4.4, to a Hill equation, $\xi^* \approx 2$, and thus can approximate the Gibb's free energy change associated with self-assembly.

At mesophase emergence, there are 0.35 mol RNaseA adsorbed per mole TiO_2. This corresponds to a surface coverage of 36.7 µmol RNaseA/m^2 TiO_2. This is nearly 100 times the capacity of a monolayer. In my experiments, the CAC corresponds to a concentration of 15.3 µM of monomeric RNaseA, as determined from the data shown in figure 4.4. From this, I can determine that the emergence of the mesophase results in Gibb's free energy reduction of approximately:

$$\Delta G = -\beta \ln(\text{CAC}) \approx 15 k_B T \tag{4.10}$$

At the critical transition, the packing limits for the protein on the nanotube surface have

been reached. This forces the system to rearrange and reassemble through interaggregate interactions[6, 262] which reduce the Gibbs free energy by $15k_B$T. The inhomogeneous microstructure and prolate shape of the observed aggregates are characteristic of binary supraself-assembled systems[6]. The packing of the multilayer-coated nanotubes observed with TEM, as seen in figures 4.5C and 4.7B, allows for a higher packing volume fraction, while the prolate shape decreases the Gaussian curvature and reduces the interfacial tension[6, 117, 261]

Although I am unable to extract the exact parameters in equation (4.6) from my data, it does provide us with some insight. It is clear that by tailoring the intermolecular interactions the exact position of the CAC can be modified. Furthermore, the CAC also depends on the structure of the assembly. As will be discussed in chapter 7, modification of the volume fraction at a constant ξ appears to produce differing structures. Such findings suggest the possibility of a rate-limiting step in the process of assembly. The exact implications of this will be discussed at length in chapter 7.

4.3.5 Model of RNaseA-TiNT Aggregate Formation and Growth

As seen in the TEM images in figure 4.5, I find that protein multilayers form around the entire TiNT, including the open ends, where there is no accessible nanotube surface for adsorption. Here the proteins must adsorb by associating with adjacent, previously adsorbed protein, and would require a driving force to overcome the significant interprotein Coulomb repulsion[60].

Based on my findings, I suggest a plausible model that accounts for the observed RNaseA-TiNT interactions, illustrated in figure 4.8. Initially, the system consists of monomeric protein and individual nanotubes coated with RNaseA. At extremely low protein concentrations ($\xi \ll \xi^*$), protein should adsorb as monolayers, as seen in figure 4.8A. As

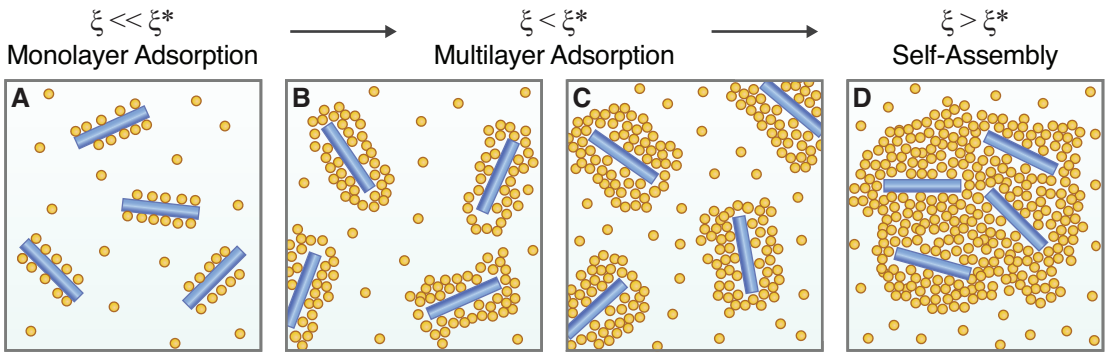

Figure 4.8: Illustration showing proposed process of multilayer adsorption and self assembly of RNaseA (yellow circle) onto TiNT (blue rod) for a fixed TiNT concentration. (A) Protein first adsorbs as a monolayer on the TiNT surface (B) subsequently, protein multilayers form and (C) increase in size as additional protein is added. (D) Finally upon exceeding a critical protein-to-nanotube ratio, the system self assembles into micron sized aggregates.

the protein concentration is increased, extensive protein multilayers form on the nanotubes, as seen in figures 4.8B and 4.8C, continuing until a critical concentration of free protein is reached. Above the critical concentration excess protein and the dispersed individual protein-nanotube conjugates assemble into an aggregate mesophase consisting of large, prolate ellipsoidal structures that contain multiple nanotubes and proteins, as illustrated in figure 4.8D.

4.4 Examining the Interaction of RNaseA With Other Anatase Nanomaterials

To understand if the unique surface chemistry of TiNT could contribute to the protein assembly and aggregation phenomena observed in here, I ran additional experiments to examine the interaction between RNaseA with additional anatase nanomaterials: anatase nanotiles – which contain a hydroxylated anatase (001) surface[120], and commercial anatase nanoparticles, which primarily have an anatase (101) surface, as discussed in chapter 2. As

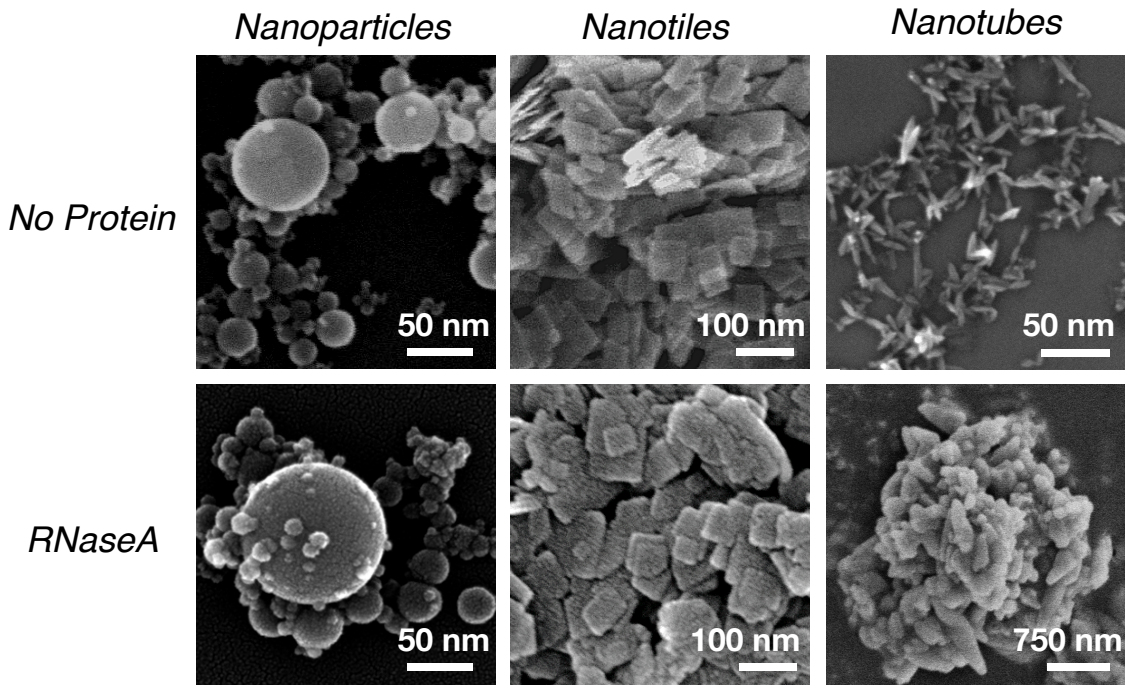

Figure 4.9: SEM images of different TiO_2 nanomaterials (top half) and structures formed after interacting with RNaseA (bottom half). Shown are anatase nanoparticles (TiNP) with a 32 nm average particle size, anatase (001) nanotiles, and titania nanotubes (TiNT). The assembly of larger aggregates formation only occurred with the nanotubes. Bottom samples were sputter coated with 2.5 nm Au/Pd prior to imaging to reduce charging.

seen in figure 4.9, with the exception of the nanotubes, the interaction between RNaseA and other anatase nanomaterials did not increase the size by more than 3-5 nm, suggesting that the unique surface chemistry of the nanotube may be crucial to the production of these functional protein-based materials.

These findings can be understood in the context of the differing surface chemistries. As seen in figures 2.3 and 2.20, the surface Ti sites on clean bulk (001) surface are all fivefold coordinated, the coordinative undersaturation makes these groups highly reactive and contributes to a very high surface energy. As such, under ambient conditions these sites are instantly hydroxylated by dissociative water adsorption[111, 125]. However, in contrast, water is only molecularly adsorbed on the surface of the nanotube, which also contains only fivefold coordinated Ti sites (figure 2.20C). The stability of these groups

against hydroxylation leaves these groups open to react and is crucial to its reactivity. Commercial anatase nanoparticles, which primarily have an anatase (101) surface, also do not contain significant exposed undercoordinated sites.

Although both the nanotubes and nanotiles expose the anatase (001) surface[111, 113, 120], aggregation was only observed on the nanotube. This suggests that this phenomenon requires more than just the presence of the anatase (001) surface. The difference between these two materials lies in the stability of the surface Ti groups against hydroxylation – while both expose the anatase (001) surface, only the nanotube contains exposed and stable undercoordinated Ti surface sites[111–113].

The bond strain induced by the nanotube's curvature is essential for preventing hydroxylation of the nanotube surface. When this is removed, the undercoordinated Ti groups are instantly hydroxylated and no longer available to react[113]. These findings suggest that the exposed, stable, undercoordinated Ti sites on the nanotube surface are crucial to initiating the self association of the free and bound protein.

The mechanistic details of how the nanotube modifies protein-protein interactions remains to be determined. Molecular dynamics (MD) simulations might yield information about the initial steps in assembly. For instance, in MD studies examining protein adsorption on hydroxylated and non-hydroxylated rutile (110) surfaces[263], the protein-surface electrostatic interaction was found to be the dominant driving force for adsorption. In these simulations, the protein Human Serum Albumin (HSA) exhibited a higher affinity for the hydroxylated rutile surface. This is reflected by significantly stronger Coulombic interaction between the HSA and the hydroxylated surface and a larger number of residues adsorbed. On the basis of these simulations, the increased affinity was attributed to to the presence of terminal hydroxyl groups on the rutile surface, whose ordered nature prevented interfacial water from forming a strong hydrogen bonding network. In turn, this enabled protein residues to form hydrogen bonds with the interfacial water and enabled protein residues

to more easily replace the interfacial water and directly hydrogen bond with the interface. These findings highlight the important role of interfacial water on protein adsorption. These findings however also may shed some insight into the observed behavior. For instance, the increased protein-surface affinity on the hydroxylated surface may limit the ability of adsorbed protein to relax or reorient on the surface and effectively fixes the protein in a specific position that may not be ideal for promoting further protein-protein association.

4.5 Conclusions

In conjunction with the findings in the previous chapters, my work reveals that titania nanotubes are able to immobilize extraordinarily large quantities of biomolecules, over 1000 times above monolayer coverage. To the best of my knowledge, this phenomenon has not been reported previously with any other nanomaterial. I show that biomolecule immobilization and assembly on titania nanotubes occurs in two different stages. First, at low biomolecule-to-TiO_2 molar ratios, biomolecule immobilization takes place up to approximately 55 layers of coverage. The coverage then remains constant until a critical biomolecule-to-TiO_2 molar ratio is reached. Upon reaching this critical ratio, the system self assembles into large aggregates, above which any subsequently added biomolecules incorporate into the existing self-assembled aggregates. For RNaseA, self assembly occurs at an RNaseA-to-TiO_2 molar ratio of 2 and was observed in independent experiments employing dynamic light scattering, adsorption measurements, and electron microscopy. The self-assembled product is micron-sized, immobilizing as much as 920 g/g RNaseA/TiO_2.

The sigmoidal relationship between the hydrodynamic size and ξ is a remarkable signature of a self-assembly processes in which proteins (or protein-nanotube conjugates) are added to preexisting aggregates[40, 209, 264, 265]. The sigmoidal dependence suggests two possibilities. First, the fundamental "monomer" for self-assembly is not the nanotube,

but rather, individual nanotubes with multilayer protein coatings. The formation of a critical concentration of these fundamental units is required before it is energetically favorable for assembly to occur. Second, it is possible that in fact the assembly is cooperative and requires a critical protein concentration as well as a critical protein-nanotube concentration to occur. One possible experiment that could examine this would be the hold the protein-to-nanotube molar ratio constant but increase or decrease the volume fraction. If the self-assembly was dependent on the formation of subunits then it should occur at the same point. I examine this in chapter 7.

Multilayer protein adsorption and the formation of larger protein-nanotube aggregates only occurred on the nanotube surface. The significance and unique nature of this surface is highlighted by the lack of any detectable multilayer adsorption or aggregation on the nanotile, where the Ti-5C sites have been hydroxylated. This suggests that the phenomena observed are due to the presence of the high density of stable undercoordinated Ti groups on the nanotube surface.

This study highlights the importance of nanomaterial surface chemistry. Specifically, the surface of the titania nanotube contains a very high density of unterminated undercoordinated Ti sites, which are stable against hydroxylation due to the bond strain imposed by nanotube's curvature. When the nanotube's curvature is removed, such as in the case of nanosheets or nanotiles, the high energy undercoordinated surface Ti sites are instantly terminated by hydroxylation, restoring sixfold coordination. These materials can only immobilize biomolecules up to monolayer coverage.

Here I have demonstrated that undercoordinated transition metal sites could play a critical role in biomolecule immobilization or the templating of larger biomolecule structures. Maintaining enzymatic activity and achieving high immobilization capacities have both been major obstacles for enzyme immobilization. My results suggest that increasing the density of unterminated undercoordinated transition metal surface sites, either synthetically

or by careful control of defect chemistry, could prove to be a fruitful strategy for creating novel enzyme immobilization substrates and may act as an enabling technology for creating protein-based biomaterials or enzyme biocatalysts.

CHAPTER 5
BIOPHYSICAL CHARACTERIZATION OF PROTEIN-NANOTUBE CONJUGATES

5.1 Introduction

Nanomaterials play an increasing role in our daily life. From targeted drug delivery to novel surface coatings, the highly controlled morphology, tailorable surface chemistry, and large surface to volume ratios, make nanomaterials a promising tool for improving daily life. While the use of nanomaterials in consumer products has grown, our understanding of the consequences of human exposure to nanomaterials is only in its infancy[10, 36, 45].

It is now understood that upon exposure to a biological fluid, most nanomaterials will quickly be coated by a biomolecule monolayer which has a loosely associated "protein corona"[66, 100, 106, 266]. The complex series of interactions that govern the formation of this monolayer and the potentially hazardous impact its formation might have on protein-protein interactions are still not fully understood, but many researchers and pharmaceutical products employ a hydrophilic material or surface coating to mitigate protein adsorption[64]. Recent studies have demonstrated that a number of factors determine the nature of the interaction between a given nanomaterial and biomolecules. Among these, particle size[32, 97, 99] and chemical reactivity[10, 229, 240] have proven to be important factors in determining potential toxicity. Despite this, our ability to predict particle-cellular and particle-protein interactions from fundamental principles has thus far been

limited[267, 268]. The interactions occurring at the nanomaterial-biological interface are quite complicated[45] and a number of deleterious effects due to these interactions have previously been reported. These effects include inflammation response due to protein unfolding[240], protein fibrillation, protein aggregation[246], and the modifications of enzymatic activity[34]. Significant evidence also links protein aggregation to the pathology and progression of most protein misfolding diseases[269], including sickle cell anemia and neurodegenerative diseases such as Creutzfeldt-Jakob, Huntington's, Alzheimer's, and Parkinson's diseases[106, 222]. Protein aggregation is also a significant problem for the safe and cost-effective production of therapeutic proteins. Aggregates form during different stages of production, ranging from purification to storage and can reduce the pharmacological benefit of therapeutic proteins[270]. The high adsorption capacity and self-assembly of RNaseA-TiNT hybrids in chapters 3 and 4 suggest that the TiNT could act as a template for creating enzyme-based materials. However, it is essential that the enzyme's structure be sufficiently maintained and that the enzymatically active site remains accessible. Oligomerization or modifications to the site accessibility could be detrimental to any potential applications of this phenomenon. In this chapter, I investigate whether the free or bound protein forms oligomers, whether the immobilized enzymes are active, and free of significant diffusional hinderance, and finally I examine the cytotoxicity of the nanotubes.

5.2 Materials and Methods

5.2.1 Denaturing Gel Electrophoresis

SDS-PAGE measurements were performed on a NuPAGE 8-16% Bis-Tris Gradient Mini Gel (Invitrogen) with an MES running buffer. Samples were pelleted by centrifuge, resus-

pended in 1X NuPage LDS Sample Buffer, and subsequently denatured at 70 °C for 10 min. The volume of sample loaded into the gel varied from 15 µL to 30 µL depending on the trial and anticipated concentration. A seven-protein molecular weight marker (GE High-Range Molecular Weight Marker, GE Healthcare Life Sciences, Piscataway, NJ) was run in one or more lane on each gel to calibrate the molecular weight migration pattern. Gels were run on a XCell SureLock Mini-Cell (Invitrogen) at 200 V for 35 min. Following electrophoresis, gels were stained with colloidal Coomassie G-250 (SimplyBlue Safestain, Invitrogen) per the manufacturers directions for high-sensitivity staining. The gels were subsequently scanned at 600 dpi using a desktop flatbed digital scanner (HP ScanJet, Hewlett-Packard, Palo Alto, CA) and dried between cellulose film for storage (Pierce Gel Drying Kit, Thermo Scientific, Rockford, IL). The scanned images were cropped and the brightness and contrast were uniformly adjusted to increase clarity for the reader. No other image adjustments were performed.

5.2.2 Enzymatic Activity Assay

Samples of RNaseA-TiNT conjugates at different molar ratios of RNaseA-to-TiNT, ξ, were prepared similarly to my adsorption experiments, except in these experiments, the concentration of RNaseA was fixed and the TiNT concentration varied. Serial dilutions of the samples were prepared and assayed with a fluorescence assay (RNaseAlert, Integrated DNA Technologies Inc., Coralville, ID) per the manufactures directions. Measurements were performed in triplicate at 37 °C in a Spectramax384 microplate reader (Molecular Devices). Measurements were taken every 60 seconds.

5.2.3 Cytotoxicity Assay

The cytotoxicity of titania nanotubes (TiNT) and 32 nm anatase nanoparticles (TiNP) to HeLa cells was examined using a fluorometric assay (LiveDead Assay, Invitrogen). HeLa cells were a generous gift of the Superfine group. HeLa cells were grown in a sterile flask in supplemented culture medium (DMEM-F12 supplemented with 10% Fetal Bovine Serum (FBS) and 1% Antibiotic-Antimitotic Solution (AA) and incubated at 37 °C in 4.5 % CO_2 until approximately 80% confluent. The cells were then harvested with Trypsin-EDTA, for 5 minutes at 37 °C; the reaction was neutralized by addition of the supplemented culture medium; the cell density was then determined with a hemocytometer. The detached HeLa cells were subsequently plated in a 96-well sterile microplate at approximately 4×10^4 cells/well, 2.64×10^4 cells/well, 1.32×10^4 cells/well, or 0 cells/well. All wells were filled with supplemented culture medium and incubated overnight at 37 °C in 4.5 % CO_2.

The following morning, the cells were dosed with varying amount of TiNP or TiNT which were suspended in Dulbecco's Phosphate Buffered Saline (DPBS) . All wells were filled to the same volume with DPBS and returned to the incubator for 24 hours. Subsequently, the wells were aspirated, washed with 100 µL DPBS and then filled with 100 µL clean DPBS to cover the bottom of the well. Control wells containing only dead cells were created by treating these with a DPBS solution containing 0.1% v/v Triton-X, which permeabilizes the cell membranes. A fresh 2X solution of the Live/Dead assay was created in DPBS and contained 8 µM Ethidium Homodimer-1, a red fluorescent indicator of cell death, and 8 µM Calcein-AM, a green fluorescent indicator of cell viability. Individual 2X solutions containing either Ethidium Homodimer-1 or Calcein-AM were also created. 100 µL of a given Live/Dead, Live, or Dead solution was added to the appropriate wells and incubated per the manufacturers instructions. All wells were prepared in triplicate and subsequently assayed in at 37 °C in a Molecular Devices SpectraMax microplate reader.

5.3 Results and Discussion

5.3.1 Denaturing Gel Electrophoresis

Protein adsorption on nanoparticles has also been shown to cause protein fibrillation[106, 271] and anomalous aggregation[246]. Therefore, I performed denaturing gel electrophoresis (SDS-PAGE) on the pelleted protein-nanotube conjugate to investigate whether protein oligomers were formed in the process of assembly. As shown in figure 5.1, only a single band, corresponding to the RNaseA monomer mass of 13.7 kDa is visible in the sample lanes, demonstrating that the bound protein does not oligomerize. The bands are shown in order of increasing ξ, for the same nanotube concentration and volume fractions shown in my adsorption measurements and assembly isotherm in chapters chapters 3 and 4. The intensity of the bands appearing in figure 5.1 corresponds to the amount of protein bound. I find that the amount of protein bound increases with ξ. This agrees qualitatively with my DLS and adsorption measurements. Extensive washing of the pellet did not affect the band pattern or intensity, indicating that the protein is strongly bound to the nanotube and confirming that the bands observed do not correspond to residual unbound protein. SDS-PAGE of the supernatant (not shown) also only contained monomers, indicating that the nanotube does not act as a nucleant for oligomerization of the unbound.

Similarly, the Ubiquitin-TiNT samples only contained monomeric Ubiqituin, as seen in figure 5.2. As before, the band intensity is proportional to the amount of protein and the intensity pattern qualitatively agrees with my adsorption measurements. The gaps between lanes present in the gels was due to pipetting error. The series of extra bands on the first sample lane in the bound gel is due to nominal bleed-through of the molecular weight standard during pipetting.

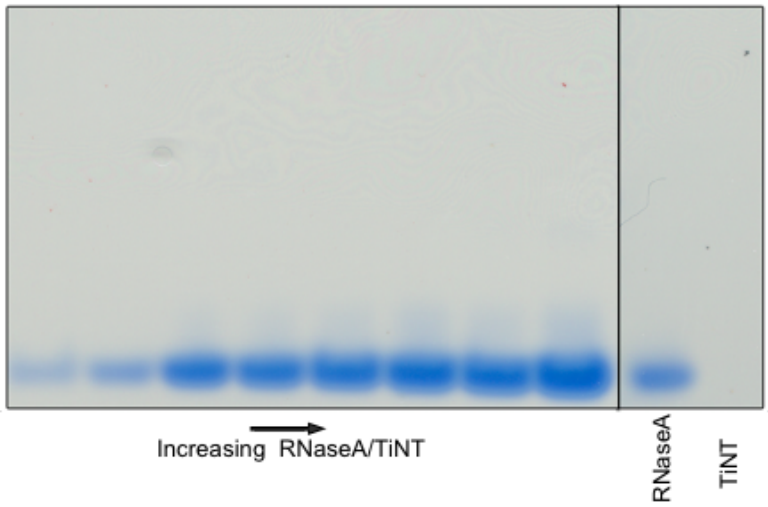

Figure 5.1: SDS-PAGE of RNaseA adsorbed on TiNT. All trials had the same TiNT concentration.

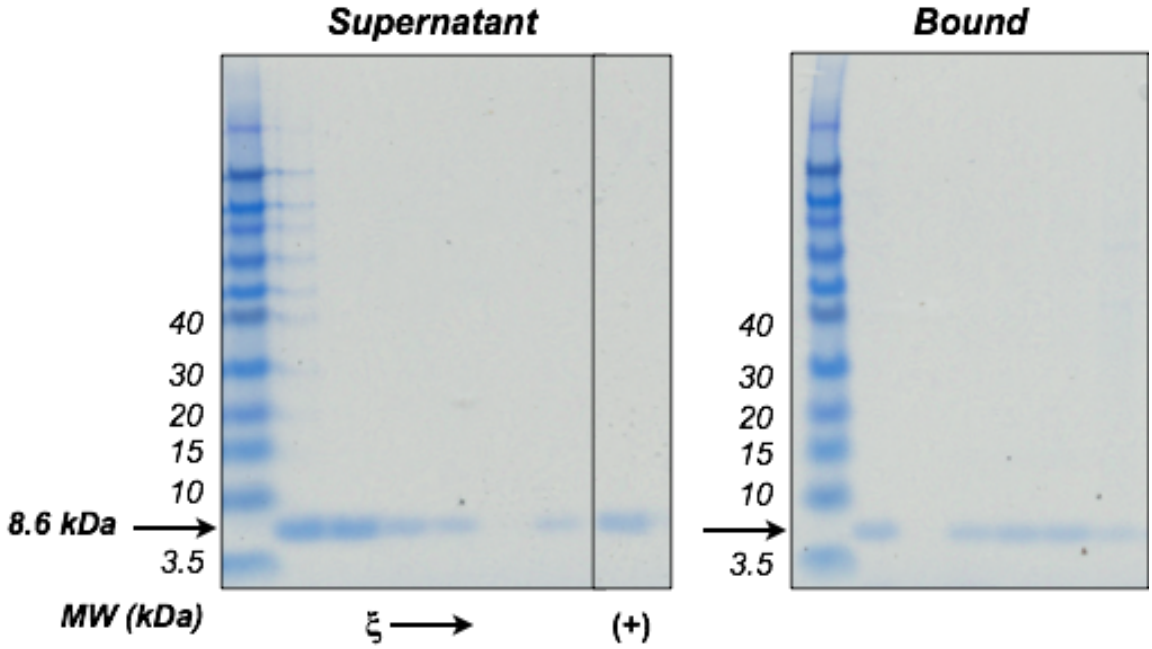

Figure 5.2: SDS-PAGE of the free supernatant (free ubiquitin) and nanotube-bound ubiquitin, shown in order of increasing Ubiquitin:TiO_2 molar ratio. Ubiquitin-only control is indicated by (+). The weight of the MW standard ladder is indicated up to 40 kDa. The molecular weight of the ubiquitin monomer is also indicated on both gels.

These results also shed insight onto the mechanism by which the proteins and the nanotube associate. SDS or LDS, the surfactants used in the denaturing gel electrophoresis, are only able to denature protein structures formed by non-covalent bonds, yet it was able to solubilize the nanotube-associated protein in both the multilayer and self-assembled aggregate states. This suggests that the immobilization, at least past the first layer, is non-covalent in nature.

5.3.2 Assay of Enzymatic Activity of RNaseA Associated With TiNT

5.3.2.1 Relative Enzymatic Activity

Proteins unfold on many nanomaterial surfaces[30, 240, 241] and can result in significant loss of enzymatic activity[30]. For the high loading capacity of TiNT to be useful, it is important that TiNT does not significantly alter the enzymatic activity. Therefore, I measured the enzymatic activity of the multilayer and self-assembled RNaseA-nanotube conjugates with a quantitative assay (RnaseAlert, IDT Inc.). The assay consists of an oligonucleotide substrate which has a fluorescent reporter and dark quencher attached at opposite ends. Enzymatically active RNaseA catalyzes the cleavage of the phosphodiester bond between the 3'-PO_4 end of pyridine and the 5'-OH of the adjacent nucleotide[200], separating the fluorescent reporter from the quencher and restoring fluorescence.

I created a series of samples containing identical RNaseA concentrations and different TiNT concentrations. After they had equilibrated, I transferred them in triplicate to an RNase-free 96-well black microplate. Prior to running the experiment I did not know if the fluorescent intensity would be too small or would saturate the photomultiplier tube in the

microplate reader. Therefore, in addition to the original (1X) concentration of my sample, I also serially diluted the samples up to 8000x v/v and assayed these in parallel. This allowed me to run the trials concurrently and determine the appropriate concentration range after the trials were completed. From this I determined that the fluorescent signal from the 1000x dilution was most appropriate for the photomultiplier tube I employed.

In the microplate, I also included serial dilutions of my controls - nanotube only, buffer only, and protein only. I subsequently incubated all of the samples and controls, at 37 °C, with an identical and excess amount of the oligonucleotide substrate and monitored the fluorescent intensity of the wells once per minute for 60 min.

In figure 5.3 I compare the fluorescent intensity (shown in relative fluorescence units (RFU)), which is directly proportional to the amount of cleaved substrate, after incubating the samples and substrate for 1 h at 37 °C. At $\xi = 1.1$ RNaseA is adsorbed as multilayers on TiNT and here the enzymatic activity is 88.7% of the protein control. This reduction, typical for carrier-bound enzymes, could be due to incorrect orientation of the active site, His-119, or structural modifications resulting from immobilization[12].

In contrast, the activity of self-assembled samples was greater than or equal to that of the native enzyme's activity. For instance at $\xi = 8.6$, I observe an enhanced activity of 107.4%. The differing activity of the multilayer and self-assembled states suggests that the orientation or packing of RNaseA in these two states may also differ.

The measurements contain a contribution from both the free protein in solution and bound enzyme in solution. As such, the measured activity is actually a weighted average of the individual activities of both populations. Therefore, the enhanced activity of the bound protein may actually be larger than the 107.4%. Similarly, it is possible that the

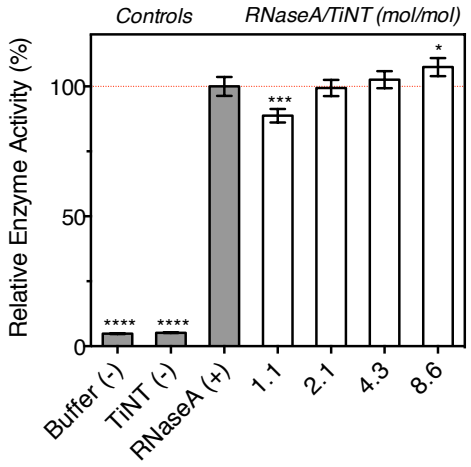

Figure 5.3: Bar plot of enzymatic activity of RNaseA-TiNT samples normalized by the activity of the RNaseA control, red line drawn at 100%. Error bars show S.E; asterisks indicate statistical significance of relative enzymatic activities as compared to RNaseA control (*, p<0.05; ***, p<0.005; ****, p<0.0001).

multilayer-adsorbed enzyme may have a larger reduction in activity than indicated by the measurements.

In my adsorption measurements in chapter 3, I found that the amount of protein bound scaled with ξ. Similarly, the enzymatic activity also appears to increase with ξ, suggesting self assembly may act to increase the active lifetime of adsorbed enzymes or increase the accessibility of adsorbed RNaseA by forming a more ordered or less tortuous assembly. This notion will be discussed further below.

5.3.2.2 Nuclease Contamination Not Evident

Before proceeding, it is important to address the possible issue of nuclease contamination on my results. Nucleases are prevalent in the environment and any contamination would significantly alter my results and contribute to faster degradation rates or higher enzymatic activities. Therefore, to minimize contamination, I implemented a stringent nuclease

decontamination protocol throughout the experiment. Prior to each stage of the experiment, I extensively cleaned my entire workspace with a nuclease decontaminating cleaning solution (RNaseZAP, Invitrogen Inc.). I also used this solution to clean all possible equipment, consumables, or surfaces that I or the sample could come into contact with during the preparation of the experiment. Subsequently, I washed the entire workspace and all equipment down with certified DEPC-treated RNaseA-free water (IDT Inc. and Invitrogen, Inc.) and dried them with fresh nuclease-free lab wipes. I performed this cleaning protocol at every stage of the experiment and created my RNaseA stock solution for the experiments in a different room. Furthermore, only disposable, sterile, RNase-free consumables and lab coats were used during the experiment. The external packaging of all consumables were decontaminated prior to use and were only unsealed unsealed immediately prior to use. Immediately after donning fresh gloves, I washed my gloves in the nuclease-decontaminating solution. The lack of contamination is quite evident in the time course of my controls, as seen in figure 5.4. Here it is clear that the nanotube only and buffer only solutions do not appreciably degrade more than 6% of the RNA substrate, which in the RNaseA only control, was nearly 700 RFU, and is effectively the basal degradation rate of the relatively stable fluorescent substrate I've employed.

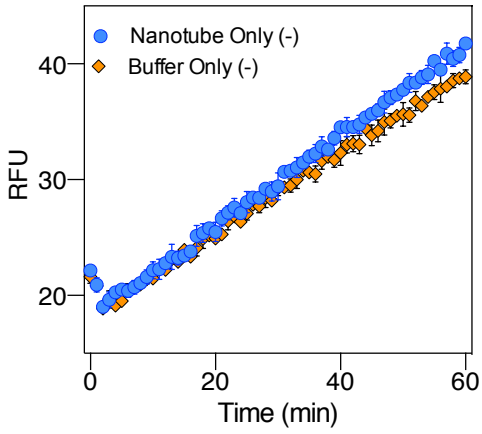

Figure 5.4: Relative fluorescence time-course of the nanotube only and buffer only controls.

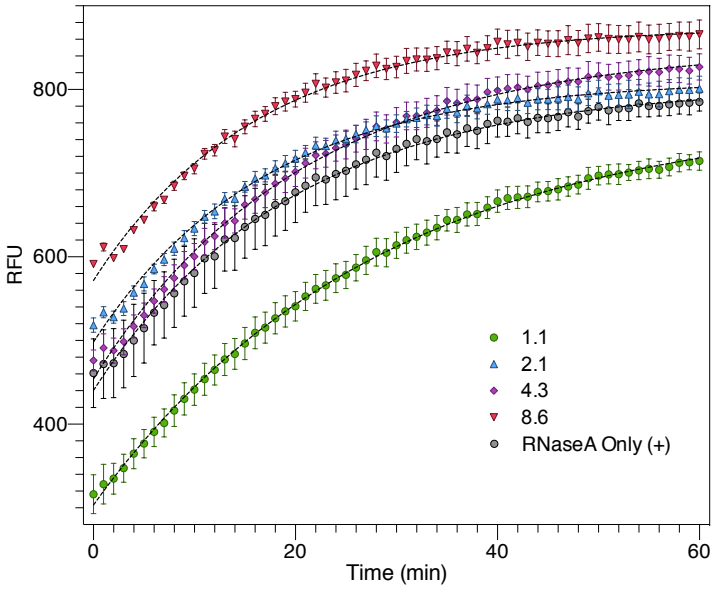

Figure 5.5: (Left) Fluorescently modified RNA was incubated for 1 hour with RNaseA-TiNT conjugates formed at different molar ratios RNaseA-to-TiO_2. The resulting fluorescent intensity is directly proportional to the number of fluorescently modified RNA cleaved by the RNaseA in solution. The samples were incubated for 1 hour at 37 °C with measurements taken every minute. The resulting measurements with fit to a first order kinetic model, as described in the text.

5.3.2.3 Enzyme Kinetics and Assembly Microstructure

In figure 5.5, I show the fluorescent intensity of the samples as a function of time. The measured intensity is directly proportional to the number of RNA cleaved. Consistent with previous studies, the degradation of RNA by RNaseA exhibits first order kinetics[12]. The characteristic time of this degradation, τ. is obtained by fitting the time dependence of the fluorescent intensity for the first 60 minutes, as seen in figure 5.5, to a first exponential growth model with characteristic timescale, τ:

$$I(t) = I_0 + (I_1 - I_0)\left(1 - \exp\left(\frac{t}{\tau}\right)\right) \tag{5.1}$$

	τ (min)		I_0		I_1	
ξ	τ	SE	I_0	SE	I_1	SE
1.1	28.00	0.92	303.42	5.95	773.00	10.63
2.1	16.89	0.41	498.21	4.99	811.34	3.58
4.3	20.57	0.64	454.17	6.76	850.88	6.79
8.6	16.11	0.45	571.75	5.74	874.74	3.82
RNaseA (+)	19.49	1.23	440.36	10.45	804.43	9.55

Table 5.1: Results of non-linear least squares fit of enzymatic activity time course, shown in figure 5.5, to equation (5.1), for different ξ.

the results of which are shown in table 5.1.

This timescale, τ, has a deeper physical meaning. τ is determined by the effective diffusivity, D_e, of the oligonucleotide through the immobilized protein layers[12, 272]. D_e is sensitive to the microstructure of the immobilized layer and will be decreased in layers which have either a lower porosity, ϕ_p , or an increased tortuosity, T .

Therefore, measurements of τ, which are dependent on D_e, serve to probe the microstructure of the immobilized layer, scaling as:

$$\tau \propto \frac{\mathrm{T}}{\phi_p} \tag{5.2}$$

As shown in figure 5.6 and table 5.1, τ for the multilayer adsorbed protein (ξ=1.1) is significantly larger than the protein-only control (p<0.001). In contrast, τ for the self-assembled sample occurring at ξ = 8.6 was slightly lower (p<0.05) than the protein-only control. The other self-assembled samples did not have a statistically significant difference from the protein-only control.

Interestingly, τ and relative enzymatic activity appears to be correlated. Compared to

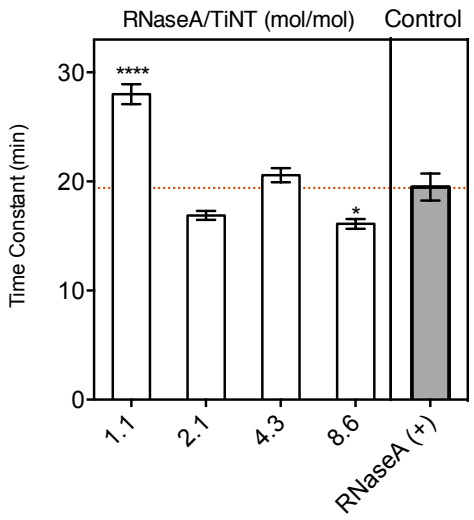

Figure 5.6: Enzymatic degradation reaction time constant, τ. Error bars show S.E.M; asterisks indicate statistical significance of relative enzymatic activities as compared to RNaseA control (*, p<0.05; ****, p<0.0001) S.E.M(n=3). Red line drawn at mean time constant of RNaseA only control (19.4 min).

the protein-only control, the relative activity was lower when τ was increased, enhanced when τ was decreased, and unchanged when τ was the same as the control. These findings suggest enzyme immobilized in the multilayer and self-assembled states have a different microstructure.

The relative activity is a function of the active lifetime of the enzyme and accessibility, while the reaction kinetics are an indicator of the diffusional resistance the substrate experiences. A more porous, or less tortuous immobilized layer would increase the enzyme accessibility and substrate diffusivity, resulting in enhanced activity and τ similar to the bulk protein. My measurements suggest that self assembly alters the microstructure of the immobilized multilayers, forming either a more porous or less tortuous network of immobilized proteins than is found in the multilayer state.

5.3.3 Cytoxicity

It is now well known that the many nanoscale materials have drastically different toxicological properties than their macroscopic counterparts[36, 72, 268, 273]. Here I briefly examine the whether titania nanotubes or conventional 32 nm anatase nanoparticles (TiNP) are cytotoxic to HeLa cells at different dosage levels.

In figure 5.7, I show the percentage of HeLa cells which died, compared to the nanomaterial-free controls, at different nanomaterial dosage levels. Here the cell density was varied, while the concentration of TiO_2 (moles/volume) was held constant. I performed a 2-way ANOVA on this data to examine whether the choice of nanomaterial or dosage had a statistically significant effect, the results of which are shown in table 5.2. I performed multiple comparison using Sidak's test.

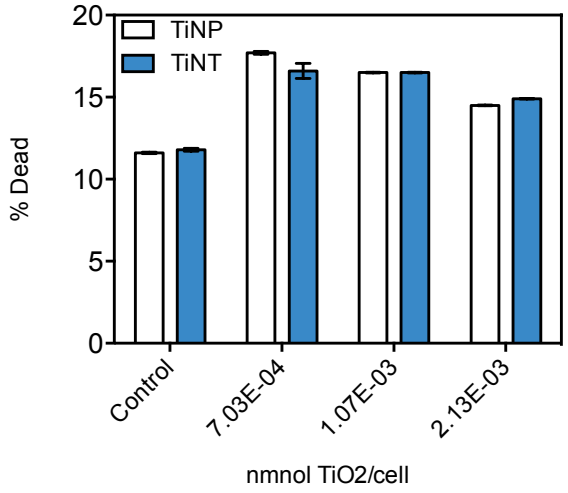

Figure 5.7: Cytotoxicity of titania nanotubes (Blue/Filled) and titania nanoparticles (unfilled) to HeLa cells as a function of dosage, nmol per cell. Error bars are S.E.M (n=3).

These results indicate that there is no statistically significant difference between the cytotoxicity of the nanotube and nanoparitcle (contributing less than 0.1% of the total variance). Although they individually do not differ, the cytotoxicity is dependent on the

Source of Variation	Degrees of Freedom	Sum of Squares	Mean Square
Nanomaterial	1.0	0.09375	0.09375
Dosage	3.0	107.1	35.70
Interaction	3.0	2.021	0.6738
Residual (error)	16.0	4.328	0.2705
Total	23.0	113.6	

Table 5.2: Results of 2-Way ANOVA examining whether the choice of nanomaterial or its dosage had a significant cytotoxic effect to HeLa cells.

dosage level of either nanomaterial, accounting for 94.33% of the total variance.

Previous studies have shown that anatase nanoparticles and nanotubes can be internalized by many cell lines. In particular, the cytotoxicity of TiO_2 nanoparticles has been extensively studied[36, 45, 75, 77, 79, 267, 273–276]. These studies have failed to reach a consensus on the exact source of cytotoxicity, but many different cellular responses have been observed, including: induction of chromosomal instability[275], pro-inflamatory response[240], and impairment of phagocytic function[79]. Although the exact source of cytotoxicity is beyond the scope of this dissertation, it is reasonable to think that the differences between the nanotube and nanoparticle could result from the significantly different surface reactivity[94], morphology[74], and possibly different mechanisms of internalization and locations with the cell.

5.4 Conclusions

The results presented in this chapter highlight the functionality of the self-assembled enzyme-nanotube hybrids and their use as novel biocatalysts and offer insight into the structure and morphology of these materials.

No oligomers of RNaseA or Ubiquitin were detected with denaturing gel electrophoresis (SDS-PAGE) experiments. Both the adsorbed and free protein were exclusively present as monomers. Covalent bonds are not cleaved by SDS-PAGE. If the protein were covalently bonded to each other (oligomers) but not the nanotube, we would expect to observe additional bands on the electropherogram. If the protein was oligomerized and covalently bound to the nanotube, we would not see any bands. This suggests that the protein is immobilized by a non-covalent mechanism. Furthermore, the band intensities also qualitatively agree with the observation of increased adsorption as higher ξ.

The enzymatic activity of RNaseA is slightly reduced when adsorbed in multilayers. However in the self-assembled state, where more enzyme is adsorbed, the activity is either the same or faster. Furthermore, the enzyme kinetics also appear to be either the same or enhances in the self-assembled state. This suggests that the enzyme's active site may be more accessible in the self-assembled state, as compared to the multilayer state. These findings give us insight into the microstructure of the self-assembled state. The increased effective diffusivity of the RNA probe molecule could occur if self-assembly either increases the porosity or decreased the tortuosity of the immobilized enzymes. An increase in microstructural order is consistent with previous observations of self-assembly[6, 277].

Both the nanotubes and nanoparticles were nominally cytotoxic to HeLa cells and exhibited a dose-dependent cytotoxic effect. Given the differing morphology of the nanotube and nanoparticle as well as their differing surface chemistries, it is likely that they are internalized differently with the cell and may differently affect the apoptotic pathway. Clearly a systematic investigation of the cytotoxicity and internalization pathways is necessary before any *in vivo* biomedical applications.

CHAPTER 6
DIFFERENTIAL SCANNING CALORIMETRY

6.1 Introduction

Many proteins and nucleic acids form complexes with other proteins or ligands. In fact, the fundamental function of biomolecules is dependent on its ability to associate and form macromolecular complexes with specific molecules or other partners. This association proceeds similarly to protein folding – where both specific secondary interactions and the dehydration of hydrophobic residues act as driving forces for assembly[56, 201]. However, unlike protein folding, complex formation reduces the system's total degrees of freedom, and complex formation is limited by the resulting loss of translational entropy[4].

These changes can be observed by calorimetric techniques. Differential scanning (micro)calorimetery is a technique for measuring the heat capacity of a sample as a function of temperature. Although traditionally DSC measurements were confined to examining solids, significant instrumental improvements and new techniques for controlling and measuring small heat flows have made DSC the technique of choice for easily examining the heat capacity of dilute solutions of small biomolecules[4, 278–283]. In this chapter, I briefly discuss the DSC instrument and theory of measurement. Subsequently, I review the thermodynamics of protein unfolding and provide a statistical-mechanics based framework for analyzing the thermal denaturation of proteins and other biomolecules.

6.2 DSC Instrumentation

Differential scanning microcalorimetry measures the heat capacity of a solution as a continuous function of temperature. In a typical differential measurement, the heat capacity of a sample cell, containing a dilute biomolecule solution in a given solvent, is measured relative to a reference cell, which contains only the solvent, at a constant pressure, as the temperature is continuously changed.

Measurements must be performed under dilute conditions where the proteins do not interact. The partial specific heat capacity of the protein (that is, the protein's heat capacity in the solute) is extremely small as compared to water and requires a highly precise and sensitive instrument to measure it.

To understand the sensitivity and precision needed for measurements, let us consider a back-of-the-envelope calculation of the calorimetric signal coming from a protein solution containing $3.3\,\mathrm{mg\,mL^{-1}}$ protein dissolved in water. For a differential measurement, the observed difference between the heat capacity of the reference cell filled with water and the $3.3\,\mathrm{mg\,mL^{-1}}$ protein solution solution will be:

$$\Delta C_p^{obsv} = C_p^{protein} m_{protein} - C_p^{water} \Delta m_{water} \tag{6.1}$$

where the mass of water the protein displaces is $\Delta m_{water} = m_{protein} \times \bar{v}_{protein}/\bar{v}_{water}$, $\bar{v}$ is the partial specific volume.

In my experiments the DSC sample volume is $300\,\mu\mathrm{L}$, so the total mass of protein in

the cell is$m_{protein}$=1 mg. Plugging in typical values of these constants[4] for the protein and water: $C_p^{protein}$=2 J K^{-1} g^{-1}, C_p^{water} = 4.2 J K^{-1} g^{-1}, $\bar{v}_{protein} = 0.73\,\mathrm{cm}^3/\mathrm{g}$, $\bar{v}_{water}$ =1 cm^3/g we find:

$$\Delta C_p^{obsv} = \left(2\frac{J}{\mathrm{gK}}\right)\left(10^{-3}\frac{g}{L}\right)\left(3\times10^{-8}L\right) - \left(4.2\frac{\mathrm{J}}{\mathrm{gK}}\right)\left(10^{-3}\mathrm{g}\times\frac{0.73}{1}\right) = -3.0\times10^{-3}\frac{\mathrm{J}}{\mathrm{K}}$$

However the heat capacity measured for the 300 µL of water is C_p^{water} × m_{water}=1.3 J K^{-1}. Quite amazingly, the heat capacity difference due to the protein is just 1/1000 that of the water's heat capacity. To make a measurement with a precision of 0.1%, we would require an instrument sensitive to changes on the order of of 1×10^{-6} J K^{-1}[4, 279, 280, 284]. In reality, modern differential scanning calorimeters can easily measure as small as 10 µg protein in a 300 µL cell, with 10 µJ K^{-1} sensitivity.

Traditionally, DSC instruments contain a reference and and sample cell which are heated in an adiabatic (or quasi-adiabatic) environment. The cells are heated with a constant power and the adiabatic jacket is controlled to closely follow the cell temperature. The system contains two feedback loops, one to maintain a near-zero temperature difference between the sample and reference cell as they are both heated at a constant power (power-compensation) and a second to ensure that the thermal adiabatic jacket closely follows the cell temperature and prevents heat flow between the environment and the sample (adiabatic control loop).

The temperature difference between each cell and the adiabatic jacket are measured by thermoelectric sensors. The thermoelectric sensor between the reference and sample cell produces a voltage proportional to the temperature difference. This voltage is used as the input to a feedback circuit which powers an auxiliary heating element, located in the sample cell. The feedback circuit is designed to reduce the temperature difference between the

sample and reference cell. The power needed to maintain a near-zero temperature difference between the two cells is recorded as a function of temperature. This technique is called a power-compensation technique and measures the additional power needed to keep the sample cell at the same temperature as the reference cell as they are both heated at a constant rate[4, 285]

This power can then be converted to the apparent molar excess heat capacity, C_p, using the temperature scan rate, dT/dt, molar concentration of the biomolecule, M, and the power supplied to the heater dQ_p/dt, where Q_p is the heat absorbed at a constant pressure[286]:

$$C_p = M^{-1} \frac{dQ_p}{dt} \left(\frac{dT}{dt} \right)^{-1} \tag{6.2}$$

In recent years nonadiabatic DSCs have become commercially available[4]. The nonadiabatic calorimetric block, shown in figure 6.1, contains two identical platinum capillary cells, one reference and one for the sample, which are connected together through a thermal shunt and contained with a thermally shielded chamber. The thermal shunt effectively fixes the operation volume of the calorimetry cells by shunting them to the thermal shield. In contrast to adiabatic DSC, non-adiabatic DSC controls the temperature outside of the cells through a series of Peltier elements and the thermal jacket leads the heating or cooling of the cell.

During a calorimetric experiment, the temperature of the calorimetric block (thermostat) is modulated to ensure that it is consistently larger than the cells. In this temperature-leading setup, heat flows to the cells from the heated calorimetric block and the cells follow the temperature of the heated surroundings. The temperature difference between the two reference and sample cells is monitored with bismuth telluride thermopiles[3]. The cells are

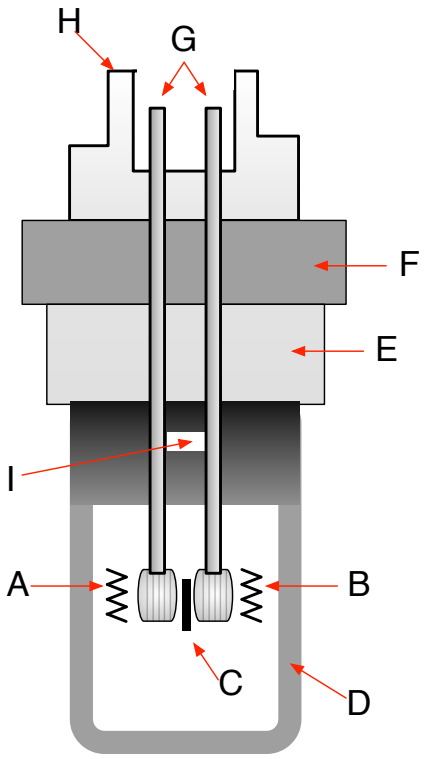

Figure 6.1: Schematic of non-adiabatic DSC. (A) Resistive heater for sample cell. (B) Resistive heater for reference cell. (C) Thermoelectric sensor to detect temperature difference between cells. (D) Thermal Shield. (E) Peltier elements (F) Peltier elements. (G) Sample inlet tubes and wound capillary cells at bottom. (H) Top of manifold containing manostat and pressure sensors. (I) Thermal shunt. Schematic drawn after Privalov[3, 4].

heated at a controlled rate, which is determined by the temperature shift between the cells and the calorimetric block.

This setup also enables the sample to be cooled. Both the sample and reference cell contain Peltier elements which are controlled by a computer to minimize the temperature difference between the two cells. The power difference between these two is recorded by the computer and used to convert to the molar heat capacity as described above. Furthermore, the Peltier elements can be heated appropriately to compensate for differences in the thermal properties of the two cells, determined using a calibration run prior to the experiments. These modifications significantly improve the stability, temperature control, and baseline[3, 4]. Current commercial instruments have a typical heating and cooling rate of 0.1 °C min^{-1} to

2.0 °C min^{-1} and have an accessible temperature range of −10 °C to 120 °C.

To avoid bubbles which could interfere with the signal, and to prevent the solvent from boiling, the cells are connected to a common manostat which can apply an excess pressure of 1 atm to 3 atm using a dry nitrogen supply. An excess pressure of 6 atm will increase the boiling temperature of water to approximately 120 °C[4].

In addition to the non-adiabatic design and manostat, additional improvements are found by utilizing a capillary cell, which permits the cells to be permanently placed in the calorimetric block and the volume to be fixed. The capillary cells generally consist of a narrow capillary wound into coils. This enables sample volumes (typically 300 µL) to be used and allows the cells to be easily reloaded using a pipette and removed using suction. The capillaries have a high surface to volume ratio which also reduces sample temperature gradients and enables faster scanning rates.

Another benefit is that capillary cells do not suffer from thermal gradients induced by fluid convection during heating, which ampules and cylindrical cells suffer from[279, 280, 285]. This is critical because the viscosity of a protein solution is strongly temperature dependent. As the viscosity changes during heating, fluid convection introduces temperature gradients which induce calorimetric artifacts[4].

6.3 Thermodynamics of Protein Unfolding

6.3.1 Equilibrium Two-State Transition

Let us first consider an ideal protein which can either be in the folded (native) state, N, or the unfolded state, U, schematically illustrated in figure 6.2. Furthermore, let us assume that this transition is spontaneous, reversible, and reaches equilibrium on timescales much shorter than any measurement we might make. In such a case, this transition is characterized by a temperature dependent equilibrium constant, K, and will proceed as:

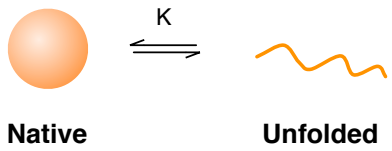

Figure 6.2: Schematic illustrating the two state transition of a protein in the native state (N) to an unfolded state (U), occurring with equilibrium constant K.

$$\mathrm{N} \overset{K}{\rightleftharpoons} \mathrm{U} \tag{6.3}$$

Assuming K displays a Arrhenius-like temperature dependence:

$$K = \exp\left(\frac{-\Delta G}{RT}\right) \tag{6.4}$$

where R is the gas constant, T the temperature, and ΔG the change in Gibb's free energy associated with the transition $\mathrm{N} \rightleftharpoons \mathrm{U}$. It follows that:

$$\Delta G = \Delta H - T\Delta S = -RT \ln K \tag{6.5}$$

where ΔH is the enthalpy change associated with the transition, and ΔS the entropy change. Solving for K:

$$\ln K = -\frac{\Delta H_{VH}}{RT} + \frac{\Delta S}{R} \tag{6.6}$$

For a two-state transition, the enthalpy change is related to the temperature-dependent rate constant and is designated the van't Hoff enthalpy, ΔH_{VH}. I have designated this above. Differentiating this equation with respect to T, we can derive a useful expression for the van't Hoff enthalpy in terms of measurable parameters[53]:

$$\frac{\partial (\ln K)}{\partial T} = (RT)^{-1} \frac{\partial \Delta H_{VH}}{\partial T} + (RT)^{-2} \Delta H_{VH} + R^{-1} \frac{\partial S}{\partial T} \tag{6.7}$$

At a fixed pressure, p, the temperature dependence of the enthalpy, which is found above, is called the heat capacity, C_p, and is specified by the Kirchoff relationship:

$$\Delta C_p = \left(\frac{\partial \Delta H}{\partial T} \right)_p \tag{6.8}$$

From the second law of dynamics:

$$\delta S = \frac{\delta H}{T} = \frac{C_p \delta T}{T} \tag{6.9}$$

we find:

$$\frac{\Delta C_p}{T} = \frac{\partial \Delta S}{\partial T} \tag{6.10}$$

Subsituting these into equation (6.7) we derive an expression which related the change in enthalpy for a two-state transition, the van't Hoff enthalpy, to the equilibrium constant of the transition :

$$\Delta H_{VH} = -RT^2 \frac{\partial \left(\ln K_{eq}\right)}{\partial T} \tag{6.11}$$

6.3.2 Thermodynamics of Protein Stability

In general, it is instructive to examine how the the Gibb's free energy of this unfolding transition varies with temperature. The heat capacity, ΔC_p shown in equation (6.8), provides a useful measure of how the enthalpy changes with temperature. Assuming that C_p is not a function of temperature, we can integrate equation (6.8), leading us to a general expression for the temperature dependence of ΔH:

$$\Delta H(T) = \Delta H(T_m) + \Delta C_p (T - T_m) \tag{6.12}$$

Here I have chosen to reference the system against the temperature where 50% of the protein has unfolded, which I indicate as T_m. Experimentally this corresponds to the midpoint of the endotherm resulting from thermal denaturation of a protein.

Relative to T_m the entropy change is

$$\Delta S(T) = \Delta S(T_m) = \Delta C_p \ln\left(\frac{T}{T_m}\right) \tag{6.13}$$

From equations (6.12) and (6.13) we can find the the Gibb's free energy:

$$\Delta G(T) = \Delta H(T) - T\Delta S(T) \tag{6.14a}$$

$$= \Delta H(T_m)\left(\frac{T_m - T}{T_m}\right) - (T_m - T)\Delta C_p + T\Delta C_p \ln\left(\frac{T_m}{T}\right) \tag{6.14b}$$

These equations present us with a thermodynamic basis for calorimetrically examining the stability of a monomeric protein, as a function of temperature, in terms of three parameters: T_m, $\Delta H(T_m)$, and ΔC_p.

In equation (6.14), ΔC_p controls the curvature, while ΔH controls the slope at a given temperature. The heat capacity of a globular protein is largely determined by its solvent-accessible surface area, decreasing with hydration of polar groups and increasing with the hydration of apolar groups. In general, the unfolded state of a globular protein has a higher heat capacity due to the increased exposure of the apolar residues[59], therefore $\Delta C_p > 0$ and the equation (6.14) will always be concave-down[4, 287]. With these constraints it is

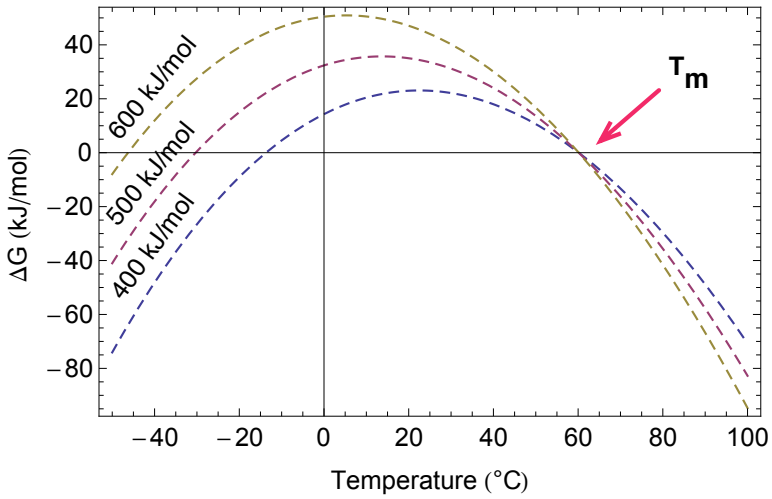

Figure 6.3: Simulation of the free energy of a two-state protein, $\Delta G(T)$ defined in equation (6.14), for three different unfolding enthalpies. Parameters for simulation were: ΔH = 400 kJ mol^{-1}, 500 kJ mol^{-1}, or 600 kJ mol^{-1}; ΔC_p = 10 kJ K^{-1} mol^{-1}, and T$_m$ = 60 °C, which is indicated in the figure.

evident from equation (6.14) that there will be two different temperatures were $\Delta G(T) = 0$, as seen in figure 6.3, where I have plotted $\Delta G(T)$ at three different ΔH.

While here we will focus on the denaturation due to heating (thermotropic denaturation), T$_m$, it is worthwhile to note that denaturing upon cooling, cold denaturation, is an active area of exploration[59, 214, 287, 288]. Thermotropic denaturation results from a concomitant increase in enthalpy and entropy resulting from heat adsorption by the protein. On the other hand, decreasing the temperature should do just the opposite and result in an increase in the order of the protein. However, remarkably the thermodynamics represented by equation (6.14) does hold true (at least for many globular proteins) and protein denaturation upon cooling has been observed[4]. Cold denaturation has extremely important implications for improving the storage and stability of biopharmaceticals, food, and to elucidating the mechanisms behind so called ”anti-freeze” proteins[270, 289, 290]. Although these temperatures are not always experimentally accessible, determining the cold and heat denaturation temperatures provides one of the most accurate means to determine heat capacity change upon unfolding, ΔC_p.

6.3.3 Partition Function of Protein Unfolding

Statistical mechanics provides a useful framework for examining protein structure and stability with calorimetric measurements. For an ensemble of protein states, the canonical partition function, Z is[284, 291]:

$$Z = \sum_{i=0}^{N} \exp\left(\frac{-\Delta G_i}{RT}\right) \tag{6.15}$$

where N is the number of accessible states, ΔG_i is the Gibb's free energy of the i state, R the gas constant, and T the temperature.

Letting $i = 0$ act as reference state against which all thermodynamic variables will be referenced, equation (6.15) becomes:

$$Z = 1 + \sum_{i=1}^{N} \exp\left(-\frac{\Delta G_i}{RT}\right) \tag{6.16}$$

The population of a given state, P_i is:

$$P_i = Z^{-1} \exp\left(\frac{-\Delta G_j}{RT}\right) \tag{6.17}$$

For a given measurable property, α, the average value will be:

$$\langle \alpha \rangle = \sum_{j=1}^{N} P_j \alpha_j \tag{6.18}$$

for instance, we can write the average excess enthalpy, $\langle \Delta H \rangle$, average excess entropy, $\langle \Delta S \rangle$, and average excess Gibb's free energy, $\langle \Delta G \rangle$:

$$\langle \Delta H \rangle = \sum_{j=1}^{N} P_j \Delta H_j = RT^2 \frac{\partial (\ln Z)}{\partial T} \tag{6.19a}$$

$$\langle \Delta S \rangle = \sum_{j=1}^{N} P_j \Delta S_j = RT \frac{\partial \ln Z}{\partial T} + R \ln Z \tag{6.19b}$$

$$\langle \Delta G \rangle = \sum_{j=1}^{N} P_j \Delta G_j = -RT \ln Z \tag{6.19c}$$

6.3.3.1 Partition Function of a Monomeric Protein Unfolding

We are now at a point where we can theoretically examine how a calorimetric experiment can investigate thermal denaturation of a protein. Let us consider again consider the thermotropic transition of a protein between the N and U states: N $\overset{K}{\rightleftharpoons}$ U. In this case, the partition function of the system, detailed in equation (6.15), reduces to:

$$Z = 1 + \exp\left(\frac{-\Delta G}{RT}\right) \tag{6.20}$$

Realizing that the second term on the right hand side of this equation is simply the equilibrium constant, K, shown in equation (6.4), equation (6.20) becomes $Z = 1 + K$,

where the equilibrium constant, K, is also the ratio of the equilibrium concentrations of the unfolded protein, [U], to the native protein, [N]:

$$K = \frac{[U]}{[N]} \tag{6.21}$$

The fractional populations of U and N are defined by equation (6.17), such that:

$$P_N = Z^{-1} = \frac{1}{1+K} \tag{6.22a}$$

$$P_U = Z^{-1}K = \frac{K}{1+K} \tag{6.22b}$$

Any measurement performed on this system will contain characteristic contributions from both the unfolded protein, α_U, and native protein, α_N, populations. Using equation (6.18), we can express these contributions in terms of the fractional occupancy of each state:

$$\langle \alpha \rangle = P_N \alpha_N + P_U \alpha_U \tag{6.23}$$

We are interested in experimentally examining how the protein unfolds upon heating. For the system indicated in equation (6.22) we can plot the progress curve, which tracks the fraction of protein unfolded in the sample. This plot is typically sigmoidal[287], as seen in figure 6.4. T_m occurs at the point where 50% of the protein is unfolded (P_U=0.5). Here the

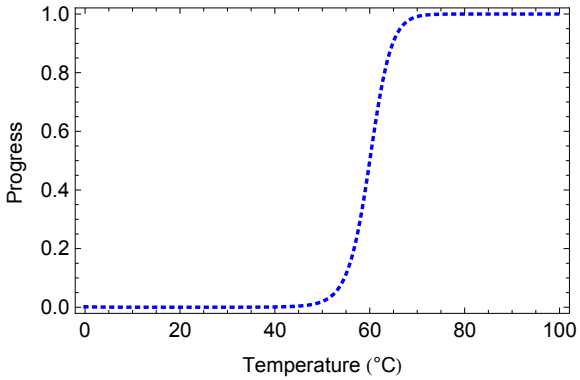

Figure 6.4: Simulation of progress curve for thermal denaturation of a protein, calculated from equation (6.22), with parameters ΔH = 400 kJ mol^{-1}, ΔC_p = 10 kJ K^{-1} mol^{-1}, and T$_m$ = 60 °C. The progress curve indicates the fraction of the population which is unfolded.

equilibrium constant, K =1. The width of this two-state transition is determined by the van't Hoff enthalpy, seen in equation equation (6.11).

6.3.4 Partition Function Analysis of Thermotropic Denaturation

Calorimetric measurements exploit the relationship between enthalpy and temperature, which are conjugate intensive and extensive variables. Experiments measure heat flow during thermally-induced transitions.

At constant pressure, the average heat capacity, $\langle C_p \rangle$, is defined as:

$$\langle C_p \rangle = \left(\frac{\partial H}{\partial T} \right)_p \tag{6.24}$$

expressing this in terms of the sums of the different states, it becomes:

$$\langle \Delta C_p \rangle = \sum_{j=1}^{N} \Delta H_j \left(\frac{\partial P_j}{\partial T} \right)_p + \sum_{j=1}^{N} P_j \Delta C_{p_j} \tag{6.25}$$

where the first term of equation (6.25) is the heat capacity of the transition $\langle \Delta C_p^{trans} \rangle$ responsible for the characteristic thermogram peak seen in figure 6.5A. The second term of equation (6.25) represents the difference between the heat capacity of the native protein, $C_{p,n}$, and unfolded protein, $C_{p,u}$, resulting in the baseline, $\langle \Delta C_p^{N \to U} \rangle$.

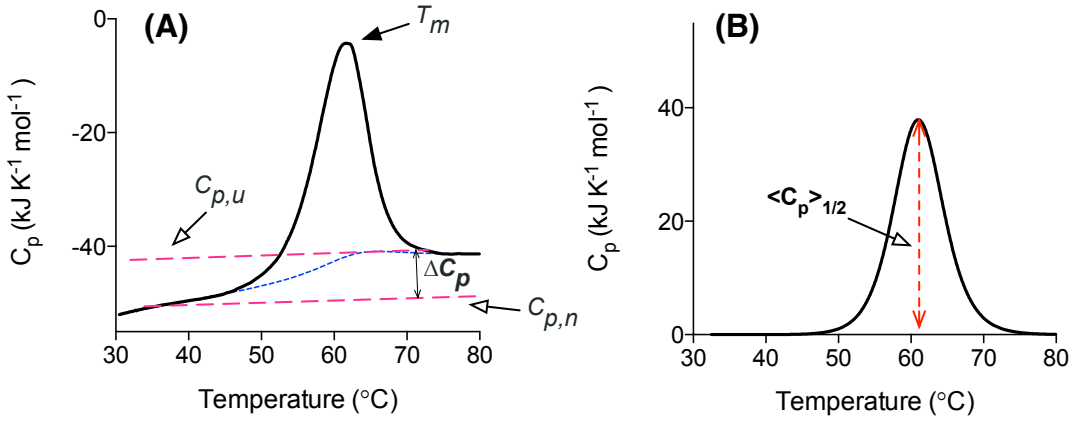

Figure 6.5: Experimental thermograms resulting from thermal denaturation of Ribonuclease A. **(A)** Molar heat capacity of RNaseA as a function of temperature. The protein has a different heat capacity in its native and unfolded states, a sigmoidal baseline (−) gradually connects the pre-transition heat capacity of native protein ($C_{p,n}$) and post-transition heat capacity of unfolded protein ($C_{p,u}$), the difference between these two is ΔC_p, the heat capacity change due to unfolding of the protein. The unfolding temperature (T_m) is the maxima of this curve. The heat capacity has not been offset although the instrumental baseline has been removed. **(B)** Removing the sigmoidal baseline provides a clearer picture of the two-state unfolding of the protein. The height of this peak provides us with, $\langle C_p \rangle_{1/2}$, the midpoint heat capacity of the baseline subtracted curve. This is used when calculating the van't Hoff enthalpy and is discussed in the text. The curve has been shifted to zero, thus providing the excess molar heat capacity due to protein unfolding.

The partition function analysis of the heat capacity curve provides a general formalism for analysis. It is particularly powerful because it is independent of the transition mechanism and the number of intermediate states. It is applicable for an equilibrium system in which the number of moles remains constant, and thus it is not directly applicable to oligomeric

systems[4, 291].

6.3.5 Simulation and Analysis of Two-State Thermotropic Transition

In this section I will simulate and examine the thermotropic denaturation of a simple two-state protein, using the formalism developed so far, and will use this to demonstrate how such a transition is observed and analyzed with DSC.

6.3.5.1 Excess Enthalpy

The signal measured with DSC reflects the heat needed to drive the transition. The observed enthalpy change, ΔH, contains contributions from all states of the the system. Relative to the native state of the protein, N, the excess enthalpy due to thermotropic protein unfolding, H_{excess}, is the product of the fractional population of unfolded protein, P_u, and the total enthalpy change relative to N, ΔH:

$$H_{excess} = P_u \Delta H \tag{6.26}$$

Relative to N, the heat capacity of this transition is calculated according to equation (6.24):

$$C_p = \left(\frac{\partial H_{excess}}{\partial T}\right)_p = P_u \left(\frac{\partial \Delta H}{\partial T}\right)_p + \Delta H \left(\frac{\partial P_u}{\partial T}\right)_p \tag{6.27}$$

As discussed in section 6.3.4, the first term in this equation represents the baseline contribution to the heat capacity resulting from the changing heat capacity of the solution, while the second term represents the temperature dependence of the excess enthalpy and represents the heat capacity change needed to drive the transition, C_p^{trans}(T). Using these equations, I simulate the temperature dependence of the excess enthalpy and the baseline contribution to the heat capacity in figure 6.6.

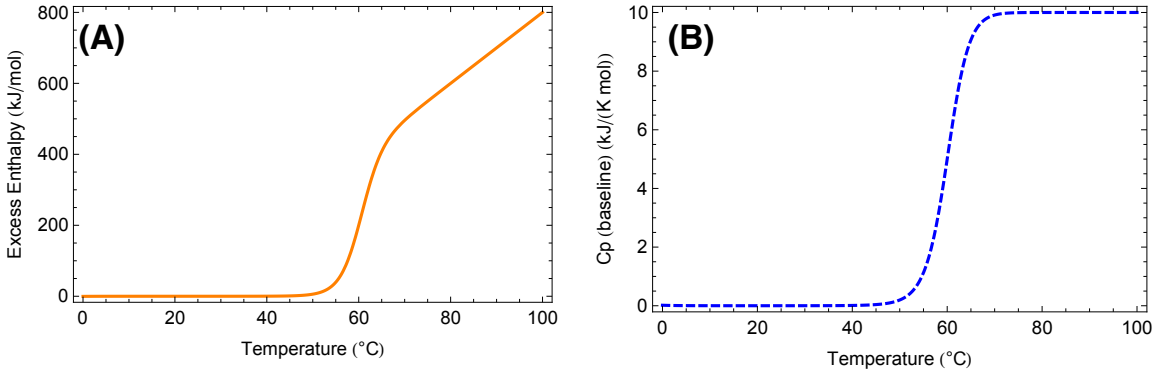

Figure 6.6: (A) Simulation of the temperature dependence of the excess enthalpy with parameters ΔH = 400 kJ mol^{-1}, ΔC_p = 10 kJ K^{-1} mol^{-1}, and T$_m$ = 60 °C and (B) Baseline contribution to heat capacity: P$_U$ $\left(\frac{\partial \Delta H}{\partial T}\right)$, simulated with the same parameters.

It is evident that we can determine the fractional occupancy of the unfolded protein as a function of temperature, P$_u$, by integrating C_p^{trans} from a temperature below the transition, T$_{pre}$, up to a given temperature, T:

$$P_u(T) = (\Delta H)^{-1} \int_{T_{pre}}^{T} C_p^{trans}(T) dT \tag{6.28}$$

This enables us to examine the progress of an thermotropic transition using DSC, as shown in figure 6.4. By integrating C_p^{trans} over the entire temperature range, we obtain the calorimetric enthalpy, H_{cal}:

$$\Delta H_{cal} = \int \Delta C_p^{trans}(T) dT \tag{6.29}$$

6.3.5.2 Evaluating DSC Measurements

Equation (6.27) provides the necessary foundation to analyze a basic thermotropic transition. The partial molar heat capacity of the protein, relative to the native state is easily obtained using DSC. In figure 6.7A, I simulate the endotherm resulting from two-state unfolding of a protein using equation (6.27). In an actual experiment, the heat flow measured with DSC would contain an instrumental background resulting from small thermal mismatches between the reference and sample cells. As will be discussed in chapter 7 this background is easily removed by subtracting the endotherm obtained when both cells are filled with the solvent used in the experiments.

It is clear from figure 6.7A the endotherm contains both the heat capacity change resulting from the enthalpy needed to drive the transition forward and a contribution due to the incremental increase in heat capacity as the fraction of protein unfolded increases. Prior to the endothermic transition the heat capacity remains constant, while after the transition the heat capacity is constant but is increased due to the larger heat capacity of unfolded protein as compared to native protein.

As seen in figure 6.7B, the heat capacity difference between the folded protein prior to the transition and the unfolded protein after the transition is connected with a progressively increasing baseline, which in experiments is typically well approximated by a sigmoidal function. Subtracting this baseline from the endotherm, as seen in figure 6.7C, reveals the endotherm representing the heat capacity change due to the thermotropic transition, shown

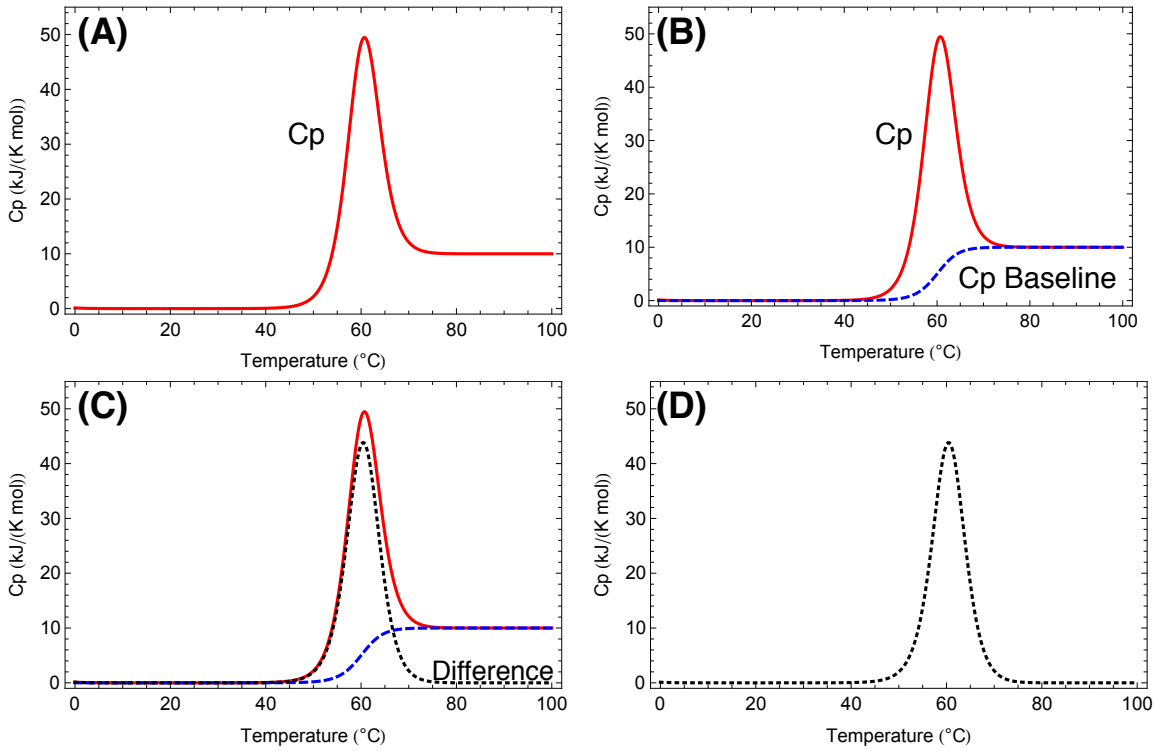

Figure 6.7: Simulations of DSC endotherm, baseline, and heat capacity change due to thermotropic unfolding of a protein. (A) Endotherm determined from DSC measurement. (B) Overlay of baseline from figure 6.6B. (C) The difference between the baseline and endotherm provides the (D) endotherm representing the heat capacity change due thermotropic unfolding. Simulation performed with same parameters as in previous figures: ΔH = 400 kJ mol^{-1}, ΔC_p = 10 kJ K^{-1} mol^{-1}, and T$_m$ = 60 °C.

by itself in figure 6.7D.

6.3.6 Analyzing DSC Experiments

Experimentally, a DSC determines the heat flow, Q, into the sample, in a given time. The experimental scan rate is precisely controlled by the instrument. Using these together, we can obtain the temperature dependent C$_p$(T) of the entire sample within the cell. The partial molar heat capacity of the protein can then be obtained by dividing C$_p$(T) by the protein's molecular weight. This is highlighted by experimental measurements of Ribonuclease A,

shown in figure 6.5A.

Accurate determination of thermal parameters from these experiments requires that the temperature dependence of the heat capacity before and after the transition be removed. Typically, the pre-transition baseline is linear with temperature, while the post-transition baseline frequently shows non-linear temperature dependence[287]. Fitting the baseline requires significant care and unfortunately is a highly variable source of error for most experiments.

In particular, endotherms containing multiple overlapping transitions or for which an insufficient range of data exists to fit can be extremely difficult to analyze using DSC. Techniques for examining these situations using deconvolution will be discussed in the subsequent section.

The importance of these baselines is clearly highlighted in 6.5. The change in heat capacity due to thermal denaturation of the protein is determined by examining the difference between the pre and post-transition baselines when extrapolated to T_m.

6.3.7 Deconvolution Analysis of DSC Thermograms

In 1978, Freire and Biltonen published a series of seminal papers in which they showed that the thermogram obtained with DSC provided enough information to calculate the partition function associated with folding or unfolding of a protein containing multiple intermediate states[292–294].

In general, the thermograms can be deconvoluted into n-independent two-state thermal

transitions. First the sigmoidal baseline representing the progressive change of the sample heat capacity as the protein unfolds, ΔC_p, is removed, as depicted in figure 6.5. It is assumed that the excess heat capacity changes observed in the baseline-subtracted thermogram (see figure 6.5B) contain only contributions from thermal transitions. The heat capacity for the transitions is:

$$C_p = \left(\frac{\partial H}{\partial T}\right)_p \tag{6.30}$$

The net enthalpy change of the transition, ΔH, is obtained over the entire transition, therefore at any given temperature, T, the enthalpy change, $H(T)$ should be related to the fraction of protein which have unfolded, $P_U(T)$:

$$H(T) = P_U(T)\Delta H \tag{6.31}$$

where

$$\alpha(T) = \frac{K(T)}{1 + K(T)} \tag{6.32}$$

where K(T) is the equilibrium constant:

$$K(T) = \exp\left(\frac{-\Delta H - T\left(\frac{\Delta H}{T_m}\right)}{RT}\right) \tag{6.33}$$

Determining the molar heat capacity requires the concentration of protein in solution to be known. However to account for discrepancies between the actual concentration and the one used in our calculations, I employ a scaling factor, A_w to scale the C_p in my fitting[4]. For a single transition, the heat capacity is fit by:

$$C_p(T) = A_w \frac{\partial H(T)}{\partial T} = A_w \frac{\Delta H^2 sech^2\left(\frac{\Delta H(T+T_m)}{2T_m(RT)}\right)}{4RT^2} \tag{6.34}$$

More generally, I can deconvolute a spectra into a series of n-independent transitions:

$$C_p^{met}(T) = \sum_{j=1}^{n} C_{p_j}(T) = \sum_{j=1}^{n} A_{w_j} \frac{\partial H_j(T)}{\partial T} \tag{6.35}$$

incidentally, this equation is simply the sum of the partial molar heat capacities of the different states, as seen in equation (6.25), with baseline reference state $C_{p,0}$ removed.

6.4 Conclusions

In this chapter, I have reviewed the thermodynamic basis for examining protein stability and protein-ligand interactions using DSC. In the next chapter, I utilize this information to examine the interaction between RNaseA and the nanotube.

CHAPTER 7

MICROCALORIMETRIC STUDIES OF RIBONUCLEASE A-TINT STRUCTURE AND FORMATION

7.1 Introduction

In chapters 3 and 4, I discussed the adsorption and apparent self-assembly of Ribonuclease A on Titania Nanotubes. Using denaturing gel electrophoresis, I showed that this occurred by a non-covalent mechanism. Although the proteins did not oligomerize, these findings do not exclude the possibility that the proteins undergo significant conformational change or that the proteins could exist in a distribution of conformational states.

Differential scanning calorimetry (DSC) is a powerful tool for experimentally examining protein stability. As detailed in chapter 6, the maximum of the protein's partial heat capacity (C_p^{max}), defined as the protein unfolding/melting transition temperature, T_m, serves as an excellent probe of protein stability and structural changes. On its most basic level, a decrease in T_m demonstrates a destabilization of the protein, while the converse suggests increasing stability[295]. These changes can result from specific and non-specific binding of other molecules to the protein, aggregation or oligomerization, or changes in protein's environment or structure. DSC serves as a direct means to investigate the protein-nanotube and protein-protein interactions resulting in the adsorption and assembly behavior observed in previous chapters.

In this chapter, I examine how the thermal denaturation of Ribonuclease A varies with ξ, the molar ratio of RNaseA-to-TiO_2. Analysis of the DSC endotherm allows me to determine the transition temperature, T_m and the excess heat capacity. Integrating the excess heat capacity curve, I determine the (calorimetric) enthalpy of unfolding the protein, ΔH_{cal}. In the case of protein complexes, such as multilayer adsorbed protein, the calorimetric enthalpy also includes the enthalpy of dissociation and thus affords direct determination of the enthalpy associated with forming the protein superstructures. Furthermore, I also determine the heat capacity change, ΔC_p associated with thermally denaturing the protein and dissociating any complexes by examining the change in the heat capacity of the baseline before and after the thermal transition.

The calorimetric enthalpy change associated with complexation offers insight into the energetic driving forces for this phenomenon, while the heat capacity change associated with complexation offers valuable information about the structural changes occurring during complex formation and changes in hydration[4].

In this chapter I provide a quantitative and qualitative examination of the interaction between the protein and nanotube and the assembly process using DSC. This is examined in three parts:

First, I investigate how the T_m varies with ξ. I show that the stability of the adsorbed protein increases with coverage. To further understand the endotherm, I investigate the cooperativity of the thermal denaturation by comparing the van't Hoff enthalpy and calorimetric enthalpy of the transition.

Based on these measurements, I subsequently deconvolute the endotherm into two protein populations – nanotube-associated protein and free protein – using the theory presented

in chapter 6.

Finally, I investigate if the assembled protein-nanotube hybrids depend on the volume-fraction of protein and nanotube or just ξ. I examine the endotherms and investigate how T_m, ΔC_p and the calorimetric enthalpy depend on volume fraction. I utilize these findings to examine the energetic driving forces for assembly and to investigate whether the assembled structure is kinetically determined.

7.2 Experiments

Experiments were performed similarly to chapter 3. Lyophilized, chromatographically-purified Bovine Pancreatic Ribonuclease A (RNaseA) was purchased from Sigma Aldrich, 1 M HEPES buffer (pH 7.2) was purchased from Fisher Scientific, both were used without further purification. For a given set of experiments, I freshly prepared 10 mM HEPES buffer from the 1 M stock using clean volumetric flasks, I then passed the buffer through a 0.10 µm PES membrane filter (Millipore) to remove any possible microbial contaminants or dust that could interfere with my experiments. Immediately prior to my experiments I weighed out lyophilized RNaseA on a calibrated Denver Instruments TP-114 analytical balance ($\pm$ 0.1 mg) within a low protein-binding Eppendorf microcentrifuge tube and subsequently added a known volume of the 10 mM HEPES buffer with a micropipette. In a typical experiment, the stock concentration was 2.5 ± 0.2 mg mL^{-1}. Samples were created identically to those for the experiments in chapters 3 and 4.

7.2.1 Differential Scanning Calorimetry

Differential scanning microcalorimetry (DSC) was performed on a TA Instruments nanoDSC, which employs a power-compensation technique to determine the heat flow. The nanoDSC contains two nearly–identical Hastelloy capillary cells with a nominal sample volume of 300 µL — one is a reference cell, the other contains the sample. Although the cells are carefully machined to be identical, an exact thermal match is impossible. Prior to performing any sample measurements, the instrument was thermocycled with degassed ddH_2O. This was used to calibrate the internal instrumental baseline due to the thermal mismatch between the cells. Samples were degassed, immediately prior to use, at 300 mmHg

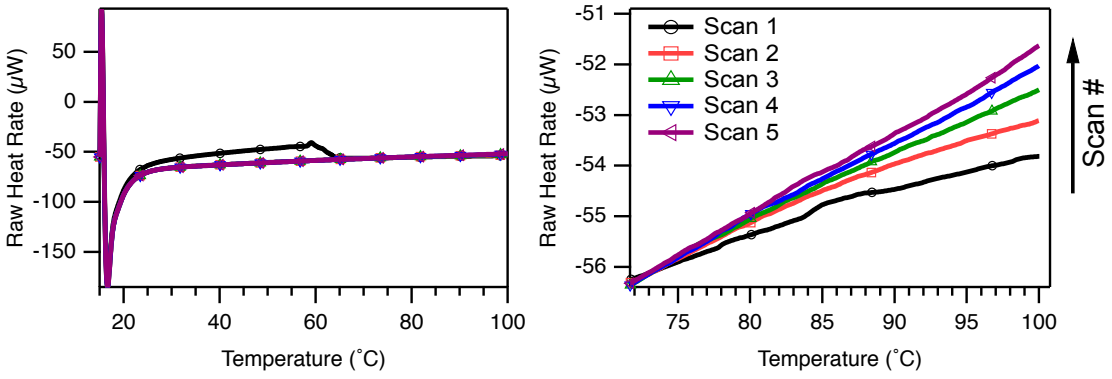

Figure 7.1: The NanoDSC shows remarkable baseline repeatability. (Left) Thermogram of first five scans of 10 mM HEPES highlights the instrumental baseline resulting from thermal differences between the reference and sample cells *(Right)* Enlarged plot of the same data, highlighting the stability of the baseline among scans.

for 12 min in a thermally regulated vacuum degassing unit kept at 25 °C. First, degassed 10 mM HEPES buffer was loaded into both the reference and sample cells. The DSC was thermocycled to condition the cells and repeated until the baseline repeatability was acceptably stable. The buffer baseline was then recorded for later subtraction; to ensure that the reference remained the same throughout the trials, the buffer was not exchanged from the reference cell and an additional thermogram of buffer was taken at the end of the trials. If the buffer was removed from the reference cell a new baseline was taken.

The baseline stability is extremely important. Cleaning the cells can change the surface wettability, which adds to the apparent thermal mismatch between the two cells. This is clearly shown in figure 7.1. Here, the cells were cleaned with 44 % formic acid and washed with ddH_2O immediately prior to use and then both the sample and reference cells were then filled with 10 mM HEPES and cycled between 15°C and 100°C to condition the cells.

It is evident that the instrumental baseline quickly begins to stabilize by the second scan. Among a series of experimental trials, the reference cell is not refilled and the sample cell is only cleaned by flushing through the sample buffer to remove contaminants. Samples were degassed immediately prior to use, as previously described, and loaded into the DSC at 25 °C via a micropipette and clean silicone tubing. The DSC was then pressurized with dry nitrogen to (3.00 $\pm$ 0.01) atm. In a typical experiment, the sample was then equilibrated at 15 °C at and scanned up to 80 °C at 1 °C min^{-1}. The sample was equilibrated at 80 °C for 10 min and then scanned down to 15 °C at -1 °C min^{-1}.

7.3 Results and Discussion

Figure 7.2 shows the DSC endotherms of the RNaseA-TiNT samples as a function of ξ, the molar ratio of RNaseA-to-TiO_2, as they were heated from 20 °C to 80 °C. The endotherm contains contributions from both the adsorbed and free protein populations. The buffer-only contribution to the heat capacity has been subtracted. Using the known protein concentration in sample and the volume of sample cell, the spectra have been normalized and are presented in terms of the apparent excess molar heat capacity.

Without the nanotube, the unfolding transition of free RNaseA occurs at 61.36 °C, this

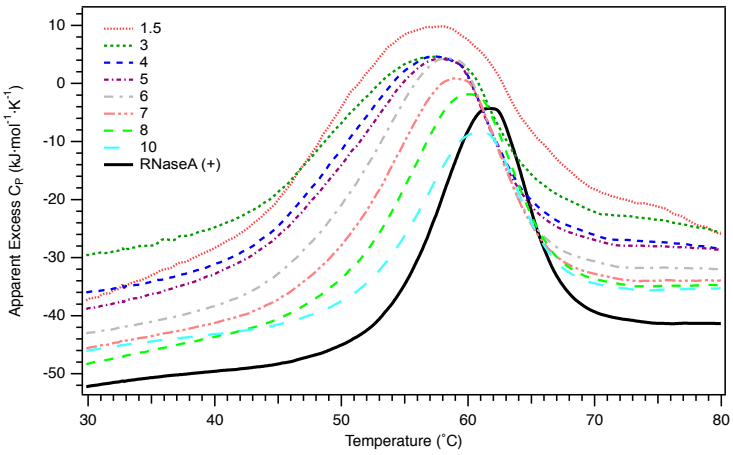

Figure 7.2: Baseline-subtracted, DSC thermograms of TiNT (9.39 µM in 10 mM HEPES, pH 7.2) in the presence of increasing concentrations of RNaseA. Measurements were performed using a scan rate of 1 °C min^{-1} at 3 atm against a reference cell containing only buffer. The apparent excess C_p of the RNaseA-TiNT samples as a function of the molar ratio of RNaseA-to-TiO_2, ξ, shows that the unfolding temperature, T_m, increases with ξ.

is consistent with published values[200, 285, 295, 296]. Here the RNaseA control shown in figure 7.2 was mixed at ambient temperature for the same time span as the experimental samples. Over this temperature range, the nanotube does not undergo any discernible thermal transitions.

As seen in figure 7.2 the presence of the nanotube has a marked effect on the thermal denaturation of RNaseA. The resulting endotherms are broader than the protein control, which has half-width at half-max of (4.35 ± 0.04) °C. For instance, at $\xi = 1.5$ the HWHM has nearly doubled to (8.54 ± 0.07) °C. The broadening is a sign of multiple populations or change in the cooperatively unfolding domain size, while the shift in T_m is indicative of structural destabilization. In the following two sections I will examine each of these aspects independently.

7.3.1 Endotherm T_m Shifts With ξ

Here I examine the maxima of of heat capacity curve, which conventionally is referred to as the the protein's unfolding temperature (T_m)[281, 295], as previously illustrated in figure 6.5.

In all samples, the T_m was always less than that of the free protein. At the lowest protein-to-nanotube ratio shown in this figure, ξ=1.5, the T_m, 56.78 °C, is 5.5 °C lower than that of the free protein. At higher ξ the T_m is significantly less depressed, for instance at ξ=10, the T_m is only 0.69 °C lower than that of the free protein.

In figure 7.3, I plot the relative change in the unfolding temperature, $\Delta T/T_m = (T_m - T_{m_0})/T_m$, where T_m is the unfolding temperature of the sample and T_{m_0} is the unfolding temperature of the protein control, as a function of ξ. With increasing protein concentration (reflected here by increasing ξ) the relative difference between the sample and the protein control diminishes.

The slope of this curve above and below ξ=2 differs by an order of magnitude, changing from 0.075 ± 0.016 per ξ below $\xi = 2$, to 0.0094 ± 0.0008 per ξ above ξ^*=2. Since the concentration of TiO_2 was held at 9.39 µM among all of these samples, I can express this change in more physically reasonable units: below ξ=2, the temperature changes by (0.383 ± 0.007) °C/µmol RNaseA. While above ξ=2, the temperature changes by (0.056 ± 0.005) °C/µmol RNaseA.

The initial reduction in T_m observed when the nanotube is introduced suggests that the nanotube may have a destabilizing effect on adsorbed protein. This change could result if the nanotube preferentially bound to the unfolded form of protein[285].

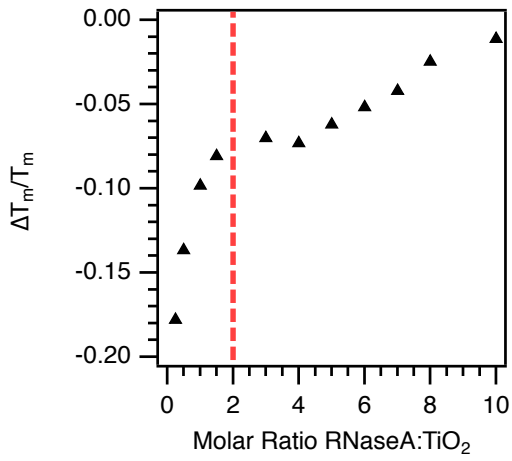

Figure 7.3: The relative shift of the unfolding temperature associated with the RNaseA-TiNT interaction plotted versus the molar ratio . The dashed red line is drawn to indicate the critical aggregation concentration, ξ^* determined in chapter 4.

The temperature shift in figure 7.3 is plotted as a function of the molar ratio of protein to TiO_2, ξ, and therefore the highest concentration of nanotube per protein occurs at the lowest ξ. If the protein does bind to the nanotube and denature, we would expect the largest change to be at the lowest ξ. As shown in the appendix of this chapter, the T_m shift should be proportional to the nanotube concentration and the binding affinity of the ligand (nanotube surface site) to the unfolded protein (U), $K_{L,U}$, [285]:

$$\frac{\Delta T}{T_m} = -\frac{RT_{m_0}}{\Delta H_{unf,0}} \ln\left(1 + \frac{[L]}{K_{L,U}}\right) \tag{7.1}$$

It is evident from equation (7.1) that the temperature shift is strongly dependent on both the concentration of binding sites on the nanotube, [L], and the affinity of the unfolded protein for the nanotube, $K_{L,U}$.

Each nanotube contains multiple surface sites which can interact with the protein. In equation (7.1), the ligand concentration, [L], describes the number of surface sites rather

than the number of nanotubes. Below monolayer coverage, this equation could serve as a rough approximation of the behavior. However, once these surface sites are all occupied, the interaction will be dominated by the affinity of the free protein for the denatured, surface-adsorbed protein, U. Under conditions where protein multilayers form, the linked equilibria become increasingly complicated[21–23].

7.3.1.1 Relationship Between ΔT_m and Surface Coverage

The samples for DSC were prepared identically to those used in my adsorption measurements in chapter 3. In figure 7.4, I plot the relative change in the unfolding temperature, $\Delta T/T_m$, shown in figure 7.3, alongside the quantitative adsorption measurements discussed in chapter 3, versus the log(ξ). Geometric monolayer adsorption of RNaseA on the nanotube corresponds to $\approx$0.48 µmol RNaseA/m^2, under these experimental conditions. The surface coverage will exceed monolayer coverage above $\xi \approx 0.1$. Therefore the temperature shift for the first DSC sample $\xi = .25$ actually represents a weighted average of the thermal denaturation of a series of different protein macrostates: (i) surface adsorbed protein (ii) multilayer adsorbed protein and (iii) unbound free protein. Unfortunately the protein concentration below $\xi = .2$ is too small to be measured reliably with DSC at these volume fractions. Although clearly the presence of the nanotube does destabilize the protein, it is difficult to conclusively state what occurs in the first layer.

As the amount of protein adsorbed increases, the relative temperature also increases. If the temperature shift were solely due to denaturation of the protein monolayer, the temperature shift should be linearly proportional to the protein concentration over the entire range of measurements. We would either observe two different peaks in the endotherm, corresponding to the separate denaturation of the free protein and the adsorbed protein,

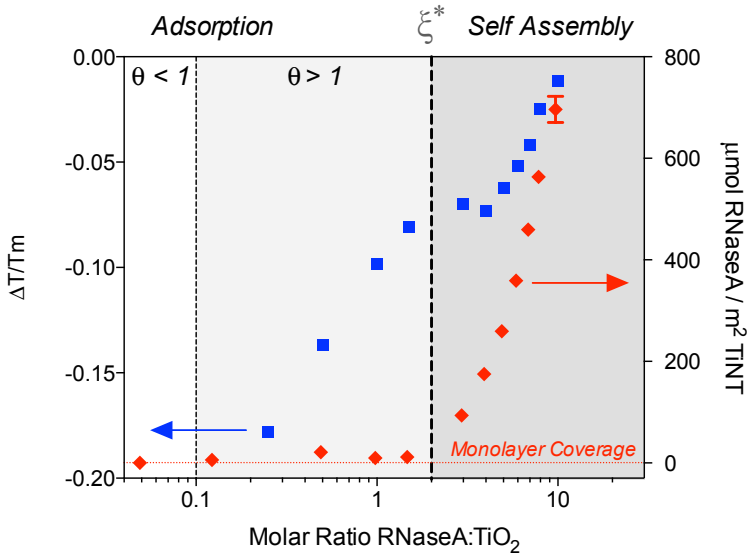

Figure 7.4: Lin-log plot of the relative T_m shift (left axis, ■) and the adsorbed RNaseA coverage (right axis, ♦) as a function of ξ. Both trials had identical nanotube concentrations and volume fractions. The theoretical monolayer adsorption capacity, 0.48 µmol RNaseA/m^2 TiO_2, is indicated by the red horizontal line. The thin vertical line at $\xi \approx 0.1$ is drawn to indicate the shift from monolayer ($\theta < 1$) to multilayer ($\theta > 1$) coverage. The critical concentration for self-assembly, ξ^* is indicated by the thick dashed vertical line at $\xi = 2$. These three regimes are shaded differently as well.

or if they overlapped, a single broadened peak[285]. However, the temperature shift is not linearly proportional to the protein concentration over the entire range of measurements, rather it contains two distinct two distinct linear regimes. Furthermore, the drastic change in the slope of this curve at the critical aggregation concentration, $\xi = 2$, further evidences a change in the system's behavior likely corresponding to the self-assembly and overall structural transition that occurs here.

The increasing transition temperature suggests that although the layers of protein near the surface of the nanotube may be significantly unfolded, protein bound in successive multilayers and in the self-assembled state retain most of their initial structure. These findings are consistent the enzymatic activity measurements discussed in chapter 5, in which I found that the activity of the multilayer-adsorbed protein was reduced, while in the self-assembled state, the enzymatic activity was fully retained or increased. Together, these results support

a model in which the self-assembled state retains the structure and site-accessibility of a large percentage of the associated protein.

7.3.2 Size of the Cooperatively Unfolding Domain

It is clear from the thermograms in figure 7.2, that the unfolding transition is significantly broadened upon introduction of the nanotube. The RNaseA-only control, shown in figures 6.5 and 7.2, has a HWHM of (4.35 $\pm$ 0.04) °C and CU = 1.07 $\pm$ 0.03. In contrast, at $\xi = 1.5$ the HWHM has nearly doubled to (8.54 $\pm$ 0.07) °C and a CU = 0.51 $\pm$ 0.03. This broadening could result if the unfolding process was not two-state or if the protein unfolded through a series of intermediate states[285].

Typically, small globular proteins will completely denature over a narrow temperature range. This produces a sharp endotherm with a half width at half-max (HWHM) of typically 4 °C to 6 °C[53]. The narrow peak suggests a highly cooperative transition between the completely folded and unfolded states and a general lack of intermediate states[288]. Under physiological conditions, the thermal denaturation of RNaseA is well represented by a simple, first-order, two-state transition between functional native state, N , and the unfolded state, U[279]. For such a reaction, the enthalpy change can be determined from the van't Hoff equation, which relates the enthalpy and the temperature dependent equilibrium constant, K_{eq} , as detailed in chapter 6.

In general, for a one-step transition between two states containing n units, $N_n \rightleftharpoons nU$ the van't Hoff enthalpy is well approximated by[279]:

$$\Delta H_{VH} = \frac{(1+\sqrt{n})^2 R T_{1/2}^2 \left(\langle C_p \rangle_{1/2} - \frac{\Delta C_p^{N \to U} \sqrt{n}}{1+\sqrt{n}} \right)}{\Delta H_{cal}} \tag{7.2}$$

where $\langle C_p \rangle_{1/2}$ is the heat capacity at T_m, measured relative to the extrapolated heat capacity of the native protein pre-transition baseline at T_m[4, 279, 285], $\Delta C_p^{N \to U}$ is the change in heat capacity between the pre-transition and post-transition baselines, and n is the number of molecules involved in the transition[279].

In contrast, the calorimetric enthalpy, ΔH_{cal} is calculated by integrating under the measured heat capacity curve, as seen in equation (6.29) and is done so without any assumption of how the protein unfolds or the nature of its transition[4].

Comparing these two different measurements of enthalpy can provide useful information about the nature of the observed transition and the size of the cooperatively unfolding domain. The ratio between the van't Hoff and calorimetric enthalpies is defined as the cooperativity unit (CU) :

$$\text{CU} = \frac{\Delta H_{VH}}{\Delta H_{cal}} \tag{7.3}$$

The ratio should be unity if the stoichiometry assumed in this transition is correct, the reaction is reversible, and if the reaction is truly a two-state reaction[4, 53, 295].

When the cooperative domain is the entire molecule, as seen in Figure 7.5A, $\Delta H_{VH} = \Delta H_{cal}$ (CU $= 1$). In the case of a protein which contains multiple unfolding domains the thermogram , $\Delta H_{VH} > \Delta H_{cal}$ (CU < 1), and the thermogram will be broader, as illustrated in figure 7.5B. This is an indicator that the domain size is smaller than assumed

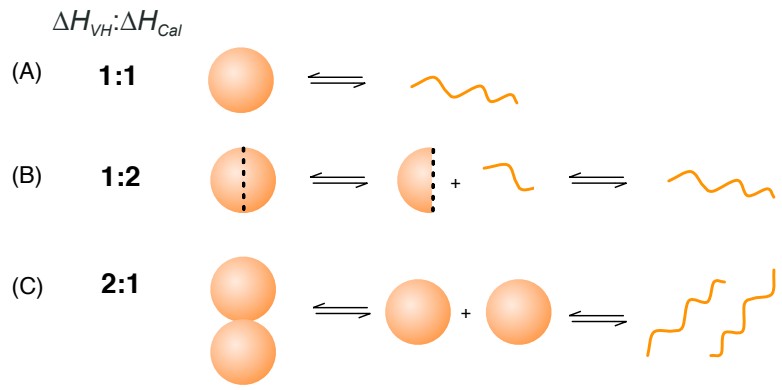

Figure 7.5: Illustration showing the relationship between the calorimetric and van't Hoff enthalpies for different sizes of cooperative domains. (A) Cooperative unfolding of a monomer (CU=1). (B) Monomer which unfolds in two domains ($\frac{1}{2}$). (C) Unfolding of dimer into cooperatively unfolding monomers domains (CU=2).

or the stoichiometry is larger. Finally, as shown in figure 7.5C, When the cooperative domain is larger than the molecule the thermogram will be narrower, in this case $\Delta H_{VH} < \Delta H_{cal}$ (CU < 1). This could indicate oligomerization or increased intermolecular association[285].

Figure 7.6 shows the calculated CU and the relative temperature shift as a function of ξ. Below $xi = 8$, CU < 1, as ξ is increase, the CU appears to steadily increase towards CU = 1. Above $\xi = 8$, CU >1, however there is no clear trend to this increase. Native RNaseA has a CU ≈ 1[53, 292, 293, 296, 297], the values of CU < 1 suggests that the nanotube could cause the protein to unfold in two separate stages or this could result from the presence of a significant number of intermediate states. Such deviations would indicate dramatic structural changes to the protein. Previous calorimetric studies of covalently-immobilized RNaseA have observed similarly decreased CU[296]. Here the authors argued that the covalently-immobilized RNaseA could unfold in two separate domains, although limited experimental evidence exists to confirm this assertion.

Because the calculation of ΔH_{VH} relies on a single point, the uncertainty is large. Furthermore, while ΔH_{cal} is a direct measurement of enthalpy, it is also very sensitive to the experimental baseline and requires the protein concentration to be accurately and precisely

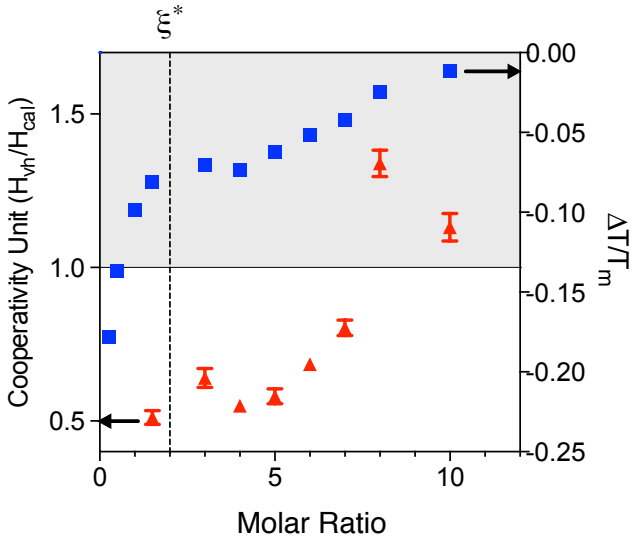

Figure 7.6: The size of the cooperatively unfolding domain is indicated by the ratio of the van't Hoff and calorimetric enthalpies (left axis). The relative temperature depression is also shown. A line at $\xi = 2$ is drawn to guide the eyes. The shaded region, drawn for CU > 1, indicates the region where the cooperative unfolding domain is larger than the monomer.

known[298]. Thus the ratio of ΔH_{VH} to ΔH_{cal} does not necessarily provide an accurate measure of the nature of the transition[299]. Incidentally, these deviations have effects on understanding the energetics of the transition as well. Empirical results have shown that a more accurate prediction of the transition enthalpy is often found by employing a weighted average of the ΔH_{VH} and ΔH_{cal}[299], which is affected less by errors in the baseline and presence of intermediate states. The presence of multiple populations is better handled by deconvolution of the resulting endotherms into multiple populations. This is examined in the subsequent section.

7.3.3 Deconvolution Analysis

The nanotube-bound protein and free protein were not separated for the DSC measurements and the resulting thermograms should contain contributions from both the nanotube-

associated proteins and the unbound protein in solution. It is plausible that the thermogram is actually made up of a series of different overlapping thermal transitions which are not independently resolvable. I deconvolved the spectra in two components, as described in chapter 6 (see section 6.3.7).

Although in my sample the nanotube-associated protein likely exists in a variety of different conformational states, these minor differences may not be easy to resolve. Rather than risk over-parameterizing this system, I opted to examine the thermograms using only two populations and assumed that the heterogeneity of either population would affect the the width of the transition.

The thermograms in figure 7.2 were deconvoluted in two different ways - in the first, all fitting parameters were varied, while in the second T_{m_2} was fixed at the T_m of the protein control. In both cases, deconvolution analysis of the excess heat capacity shows two very different overlapping populations. The best-fit T_m values for the unconstrained fitting and constrained fitting are shown in figure 7.7A and figure 7.7B, respectively.

Assuming that the protein is destabilized by the nanotube we should expect that the higher temperature transition, T_{m_2}, corresponds to the unbound protein or protein with very minor structural changes, while the lower temperature transition, T_{m_1}, corresponds to the population of nanotube-associated protein. As seen in figure 7.7A, the lower temperature peak, T_{m_1}, increases with ξ, increasing from 53.24 °C at $\xi = 1.5$ to 58.27 °C at ξ=10. This peak emerges when the nanotubes interact with the protein, suggesting that the protein near the nanotube surface is destabilized by the interaction.

At $\xi = 1.5$, the higher temperature peak, T_{m_2}, is 59.94 °C; this is slightly lower than the unfolding transition temperature of the protein. T_{m_2} decreases with increasing ξ until $\xi = 5$.

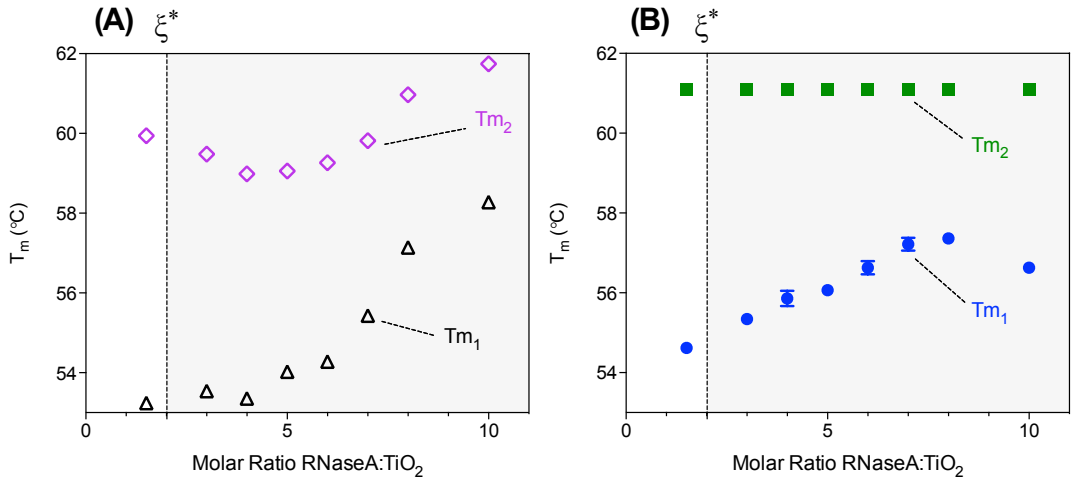

Figure 7.7: Plots of the best fit T_m values obtained by deconvoluting the RNaseA-TiNT thermograms into two independent, overlapping two-state transitions, using equation (6.35). In (A) all fitting parameters were free. In (B) the higher temperature, T_{m_2} was fixed to the approximate T_m of the free protein, 61.1 °C, and all other fitting parameters were free. The dashed line indicates CAC, and the shaded region indicates region where $\xi > \xi^*$. Fitting parameter error bars represent the 95% confidence interval, which were determined using Monte Carlo simulations of fitting (n=100).

Subsequently it increases. If this peak in fact represents the free protein in solution it would suggest that the unadsorbed protein has been structurally modified at lower ξ. Soon after the system has self-assembled, this temperature begins to increase. Another possibility is that T_{m_2} represented a population-weighted average of protein which has undergone limited conformational change with the free, native protein.

If the unadsorbed protein is unaffected by the nanotube it should have the same T_m as the free protein control. Therefore I performed a second series of deconvolutions in which I fixed T_{m_2} to 61.1 °C. This temperature is the T_m obtained by fitting the protein-only control with a single two-state model. As seen in figure 7.7B similarly to the unconstrained deconvolution, T_{m_1} also increases with ξ, increasing from 54.62 °C at $\xi = 1.5$ to 57.36 °C at $\xi = 8$. The constrained model poorly fit the samples at $\xi = 4$ and $\xi = 10$ and was unable to adequately replicate the thermograms. This could be due the baseline subtraction or processing of the data, unintended aggregation of the protein, or the presence of other

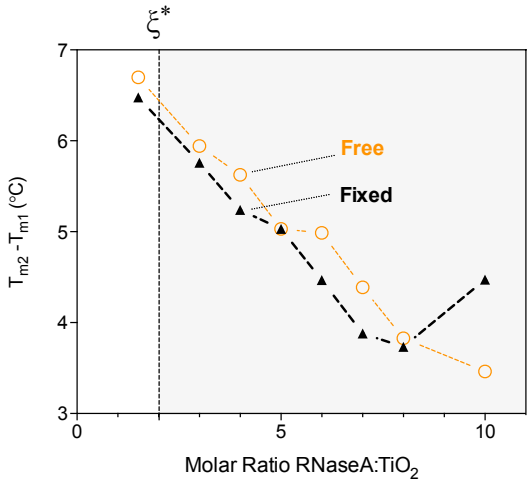

Figure 7.8: The difference between T_{m_2} and T_{m_1} for both the free and constrained fitting models versus ξ. Line drawn to guide the eyes.

protein intermediate states in the sample. However, regardless of these two points, it is clear that T_{m_1} increases significantly with ξ when T_{m_2} is fixed. In both fittings, the difference between T_{m_1} and T_{m_2} decreased with increasing ξ, as seen in figure 7.8.

7.3.4 Relative Populations of Bound and Free Protein

As discussed in chapter 3, at a fixed nanotube concentration, the amount of protein bound (the surface coverage) increases with ξ. The nonlinear nature of the adsorption isotherm has an additional consequence. As ξ is increased, a much larger percentage of the protein in the sample is adsorbed. This shift in the relative populations of the bound and free protein is particularly remarkable. As seen in figure 7.9, both fittings show a strong dependence between T_{m_1} and ξ. This increase in temperature occurs as the protein population shifts from being dominantly free to primary adsorbed and the contribution of the adsorbed protein population also increases. Both the midpoint temperature, $T_{m_{1/2}}$, from the thermogram and the lower temperature obtained from deconvolution, T_{m_1}, increase with ξ. This suggests

that the protein adsorbed at higher ξ is actually more stable than protein adsorbed at lower ξ. This supports a model in which protein adsorbed further away from the nanotube surface experiences significantly less conformational change than protein closer to the surface.

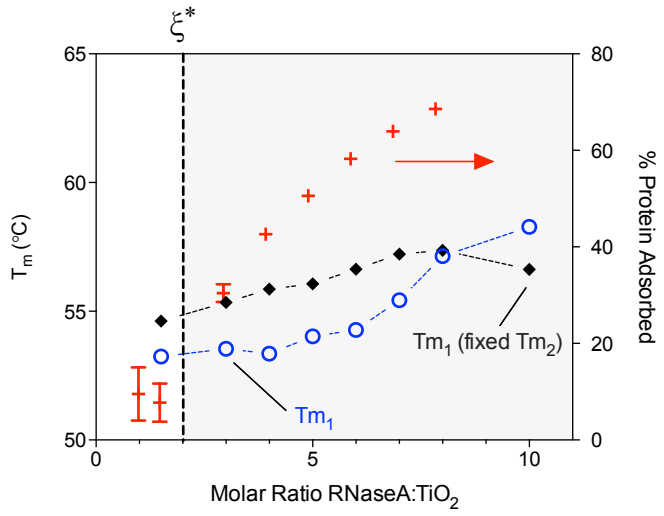

Figure 7.9: Comparison of the fitted values ofT_{m_1} when T_{m_2} was allowed to vary (○) and when it was fixed at the free protein T_m (⧫). The percentage of the protein which was adsorbed at a given ξ, determined from quantitative adsorption experiments detailed in chapter 3 is shown on the right axis (+).

7.3.4.1 Relative Enthalpic Contributions

The enthalpic fitting parameter in my deconvolutions, as seen in equation (6.35), is representative of the van't Hoff enthalpy. Sharp, highly cooperative transitions, fit with equation (6.35) will have a small scaling parameter, A_w, and large enthalpy, ΔH. To directly compare the enthalpic contributions of these different transitions to the observed thermogram, it is necessary to examine the the product of these two parameters, the scaled enthalpy: $A_w \times \Delta H$.

Assuming the thermogram is well fit by equation (6.35), the sum of these scaled enthalpies should equal the total calorimetric enthalpy:

$$\Delta H_{cal} \approx \sum_{j=1}^{n} A_w \Delta H \tag{7.4}$$

From this we can determine the scaled contribution of a given transition to the calorimetric enthalpy and examine the relative enthalpic contributions of the different components. In figure 7.10 I compare the relative enthalpic contributions of the T_{m_1} and T_{m_2} transitions obtained in the free and constrained deconvolution. Alongside each I have plotted either the percentage of protein in the sample which is adsorbed or unadsorbed, determined from quantitative adsorption measurements in chapter 3.

The relative enthalpic contributions resulting from the free and constrained deconvolutions differ significantly. In the free-parameter deconvolution, the relative contributions of T_{m_1} and T_{m_2} transitions do not vary significantly as ξ increases – the average value ($\pm$ SD) of T_{m_1} is (56.34 $\pm$ 4.58) °C. In contrast, the relative contribution of T_{m_1} decreases with ξ. Including the potentially anomalous fittings at $\xi = 4$ and $\xi = 10$, it has an average value ($\pm$ SD) of (71.91 $\pm$ 21.91) °C. With these two points removed, the average ($\pm$ SD) increases to (82.02 $\pm$ 11.95) °C. It is clear that the lower temperature peak, which I have argued is the adsorbed protein population, dominantly contributes to the enthalpy of this population in both fittings, although significantly more so in the constrained model.

There is no clear correlation between the relative enthalpic contribution of either peak in either model with the increasing percentage of protein adsorbed. Furthermore, the enthalpic contribution in the fixed model appears to decrease as more protein is adsorbed and contributes much more significantly when less protein is adsorbed. This would suggest that either the fixed model is inappropriate to characterize the transition, the transitions are underparameterized (i.e. it may need additional peaks to represent the variety of unfolded populations), or the transition may not in fact be two-state.

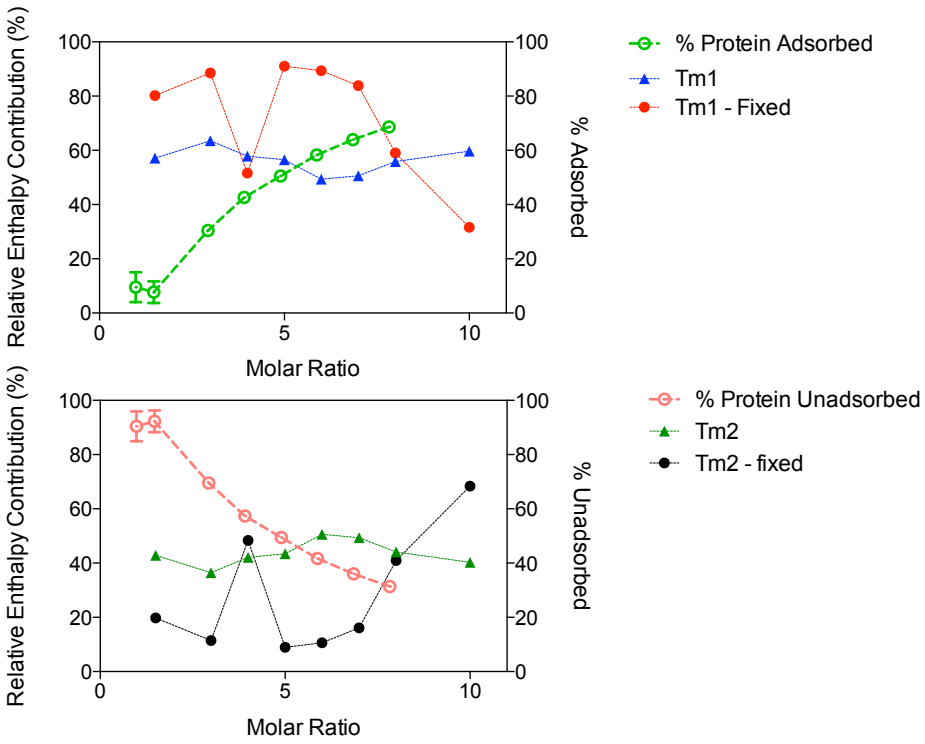

Figure 7.10: Comparison of the relative enthalpic contributions of the (Top) T_{m_1} and (Bottom) T_{m_2} transitions, determined by the deconvolution analysis described in the text, to the calorimetric enthalpy when T_{m_2} was free and when it was constrained to 61.1 °C. The percentage of the protein which was (Top) adsorbed or (Bottom) unadsorbed at a given ξ, determined from quantitative adsorption experiments detailed in chapter 3, is shown on the right axis

While the deconvolution does help us to understand how changes in the different protein populations (adsorbed and free) could contribute to the overall increase in T_m observed in the thermograms, without additional evidence of the role or identity of these peaks, the deconvolution can only offer a qualitative understanding of this phenomenon.

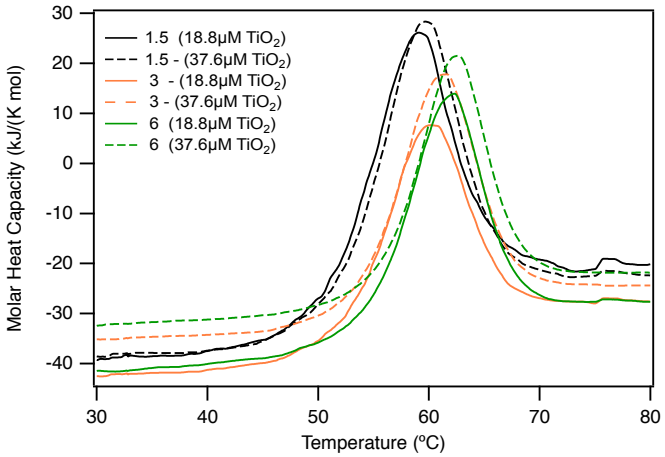

Figure 7.11: Examining the effect of doubling the protein and nanotube concentration at three different ξ. Shown are raw thermograms of RNaseA-TiNT samples' heat capacity (buffer and nanotube contribution subtracted) at three different values of ξ

7.3.5 Effect of Protein and Nanotube Volume Fraction

7.3.5.1 Effect on Unfolding Temperature

In previous sections the nanotube concentration was fixed and the protein concentration varied. To further investigate the stoichiometry and process of assembly I performed additional experiments at two different nanotube concentrations and at different molar ratios of RNaseA:TiNT, ξ.

In figures 7.11 and 7.12, I examine the effect of doubling the protein and nanotube concentration at three different values of ξ. The baseline contribution of the nanotube and buffer were removed from the thermograms by subtracting the thermogram of the appropriate nanotube-only controls in the same HEPES buffer.

Similarly to my previous measurements, I observe a small temperature decrease at the lowest ξ, resulting form the interaction between the protein and nanotube. For a fixed

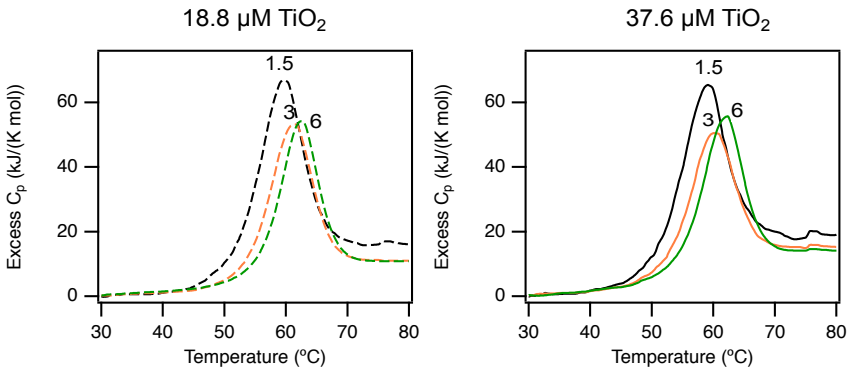

Figure 7.12: Examining the effect of doubling the nanotube concentration from 18.8 µM to 37.6 µM TiO_2 on the resulting thermogram. The endotherms are labeled with the corresponding molar ratio of protein to nanotube, ξ. All curves have been shifted to C_p=0 at T=30 °C to enable comparison.

nanotube concentration, T_m increases with protein concentration. At fixed ξ, the relative temperature change decreased when the concentration of nanotube and protein were doubled, as seen in figure 7.13. At $\xi = 6$ the T_m is actually greater than the protein control. This is in contrast to the measurement at $\xi = 6$ shown in figure 7.3.

The volume fraction dependence suggests that the structure of the multilayer coated nanotubes and self-assembled protein-nanotube hybrids is different. At higher volume fractions but identical molar ratios, T_m is larger, indicating either a smaller degree of structural perturbation or that the protein multilayers and self-assembled hybrids have a different three-dimensional structure.

There is another intriguing explanation. A volume fraction dependence could occur if there was a kinetically limited step in assembly. Double the volume fraction increases the collision rate between protein and the nanotube as well as between free and adsorbed proteins. When an isolated protein adsorbs onto the nanotube surface it will undergo a series of orientational and structural relaxations, spreading at the interface to minimize the hydration of hydrophobic residues on the protein surface. These relaxations are hindered

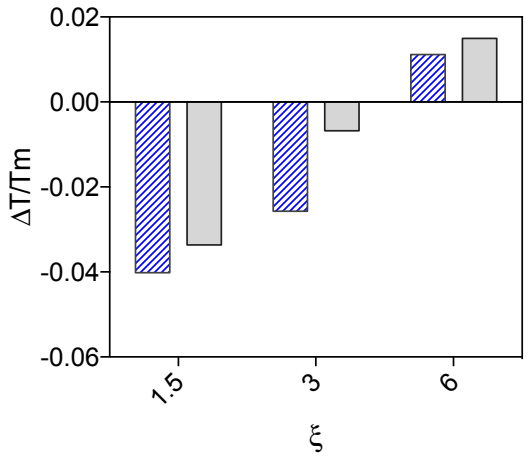

Figure 7.13: Examining the effect of doubling the nanotube volume fraction on the relative shift of T_m. Here the relative change in temperature of RNaseA-TiNT samples is plotted versus the molar ratio of RNaseA:TiO_2 for samples containing either 18.8 µM TiO_2 (blue) 37.6 µM TiO_2 (grey) .

by neighboring adsorbed proteins. At increased bulk protein concentrations an adsorbed protein will remain isolated on the nanotube surface for less time. This will both limit the structural relaxation and will also change the packing of the protein on the interface. Under these conditions it is favorable for the ellipsoidal protein to be oriented with its longer axis perpendicular to the surface which will result a denser surface packing[40, 42, 202]. These findings suggest that it may also be possible to tune the structure and morphology of the assembled protein-nanotube hybrids by varying the volume fractions during assembly.

7.3.5.2 Heat Capacity Change

The partial molar heat capacity of a globular protein significantly increases upon denaturation. Well below the onset of thermal denaturation, the heat capacity largely reflects the difference in heat capacity between the protein and solvent which is displaced. For most globular proteins, the partial molar heat capacity prior to this transition will increase linearly with temperature[53]. The unfolded globular protein will typically have higher partial molar

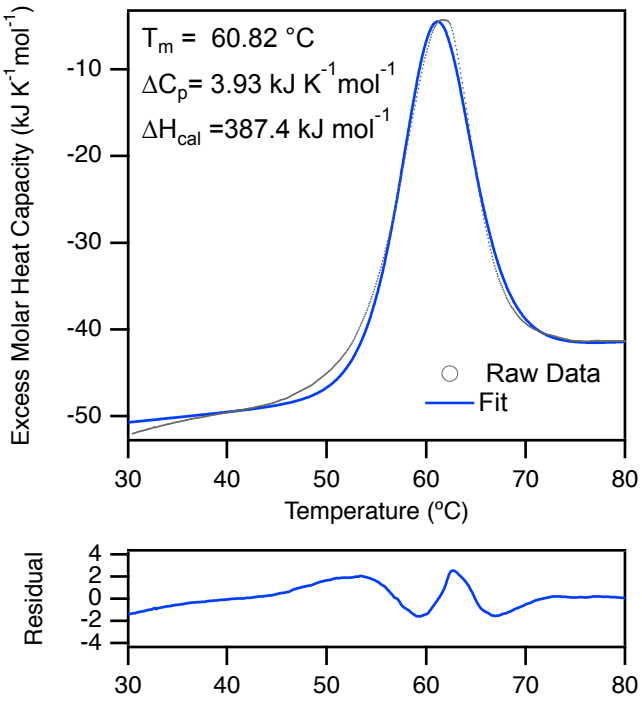

Figure 7.14: Excess molar heat capacity of Ribonuclease A control and fit to equation (6.25). The residuals of the fit are shown below. The S.D. around the fit is 1.09. The best fit parameters ($\pm$ 95% C.I. determined from Monte Carlo simulations (n=100)) are: T_m =(60.822 $\pm$ 0.041) °C; ΔC_p=(3.934 $\pm$ 0.178) kJ K^{-1} mol^{-1}; ΔH_{cal}= (387.412 $\pm$ 1.412) kJ mol^{-1}.

heat capacity, this is primarily attributed to disruption of the hydrogen bonding structure of interfacial water and significantly increased exposure of hydrophobic protein residues[300].

The heat capacity change associated with thermally denaturing the protein, ΔC_p, can be estimated by extrapolating the pre-transition and post-transition baselines to T_m and examining their difference. Assuming complete denaturation at the end point, alterations to this difference could reflect changes to the native protein conformation, solvent exposure, or other environmental conditions. In the absence of the nanotube the RNaseA control had ΔC_p = (3.934 $\pm$ 0.178) kJ K^{-1} mol^{-1}, as seen in figure 7.14. These results are in line with other experimental measurements, which typically range from 3 to 6 kJ K^{-1} mol^{-1}[53, 214, 279, 285, 287, 296, 297, 300, 301].

The change in heat capacity, ΔC_p, associated with thermal denaturation offers us insight into the structure and environment of the protein in the multilayer adsorbed and self-assembled states. The measured heat capacity change contains contributions from the different combinations of protein (p), nanotube (n), and the solvent (s) interactions:

$$\Delta C_p = \Delta C_p^{p-p} + \Delta C_p^{p-s} + \Delta C_p^{s-s} + \Delta C_p^{n-s} + \Delta C_p^{p-n} \tag{7.5}$$

Only a fraction of the protein in my measurements are in direct contact with the nanotube, and ΔC_p^{p-n} will only make a fractional contribution. As such, we can consider the total heat capacity change to be the combination of the protein-protein interaction and a combination of different changes in hydration:

$$\Delta C_p = \Delta C_p^{p-p} + \Delta C_p^{hydration} \tag{7.6}$$

In figure 7.15 I examine $\Delta\Delta C_p$, the difference between ΔC_p of the RNaseA in the presence of TiNT (after removing the contribution of the nanotube to the sample heat capacity) and ΔC_p of the RNaseA without TiNT. $\Delta\Delta C_p$ is positive for all values of ξ, indicating that $\Delta C_p^{Complex} > \Delta C_p^{RNaseA}$. Increases in ΔC_p could be the result of increased hydrogen bonding between the adsorbed proteins as well as dehydration or shielding of apolar (hydrophobic) residues, which occupy approximately 40% of the external area of the protein[59, 297, 302]. This is consistent with my hypothesis that multilayer adsorption occurs as a result of non-covalent interactions, as discussed in chapter 5.

A small reduction in ΔC_p occurs when going from the multilayer-adsorbed state to the self assembled state ($\xi > \xi^*$), although ΔC_p is still larger than that of the protein control.

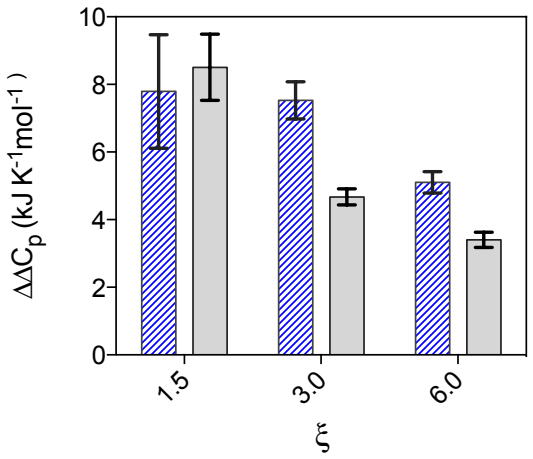

Figure 7.15: Examining the effect of the nanotube volume fraction on the change in molar heat capacity associated with unfolding the protein. $\Delta\Delta C_p$ is the difference between the apparent molar excess heat capacity change associated with denaturing the protein in the presence of the TiNT, $\Delta C_p^{Complex}$, and the apparent molar excess heat capacity change associated with denaturing the protein by itself, ΔC_p^{RNaseA}. $\Delta\Delta C_p$ is plotted versus the molar ratio of RNaseA:TiO_2 for samples containing either 18.8 µM TiO_2 (blue) 37.6 µM TiO_2 (grey). The error bars on $\Delta\Delta C_p$ represent the propagated uncertainty in the extrapolated values of ΔC_p.

This suggests that self-assembly results in a reduction in protein-protein hydrogen bonding or that more of the protein hydrophobic surface is exposed in the self-assembled state. Based on the increased accessibility of the protein in the self-assembled state, suggested by my enzymatic activity measurements in chapter 5, this decrease in ΔC_p likely results from the hydration of a small number of apolar residues associated with self-assembly.

Similarly to T_m, ΔC_p also appears to have a volume fraction dependence. However it is unclear why I observe a reduction in ΔC_p for the self-assembled state at higher volume fractions. Although these preliminary measurements do highlight the volume-fraction dependence on the assembled product, it is unclear what the exact physical changes are. These measurements could result if the self-assembled product at higher volume fractions was more porous and thus more apolar residues were hydrated or if there were changes to the internal structure of the proteins. It would be intriguing to examine the enzyme kinetics under these different conditions and see if the enzymes were more or less accessible.

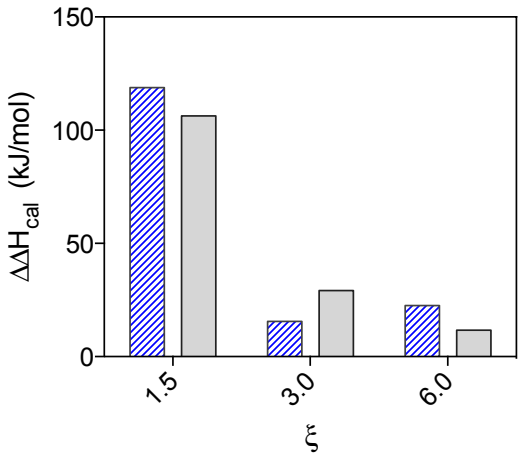

Figure 7.16: Examining the effect of the nanotube volume fraction on the calorimetric enthalpy of unfolding the protein. Here the difference between the calorimetric enthalpy of the RNaseA-TiNT samples and the protein control are plotted versus the molar ratio of RNaseA:TiO_2, ξ, for samples containing either 18.8 µM TiO_2 (blue) 37.6 µM or TiO_2 (grey).

7.3.5.3 Enthalpy of Complex Formation

These measurements also allow us to examine the enthalpy change associated with forming the different protein-nanotube hybrids. Similarly to the heat capacity change, the enthalpy change also contains contributions from the protein-protein interactions, protein-solvent interactions, and the solvent-solvent interactions. Examining the difference between the protein-only control and the protein-nanotube hybrids (after removing the nanotube contribution) allows us to examine the enthalpy associated with multilayer adsorption and self-assembly.

In figure 7.16 I plot $\Delta\Delta H_{cal}^{Complex-RNaseA}$, the difference between the the calorimetric enthalpy of unfolding, ΔH_{cal}, of the protein-nanotube samples shown in figure 7.11, and the protein control (see figure 7.14). Remarkably, both multilayer adsorption and self-assembly have a larger enthalpy than the protein by itself, increasing by 118.85 kJ mol^{-1} for the sample with 18.8 µM TiO_2 and 106.35 kJ mol^{-1} for the sample with 37.6 µM TiO_2, respectively. However there is a dramatic difference between the enthalpy of the multilayer adsorbed

state at $\xi = 1.5$ and the self-assembled states at $\xi = 3.0$ and $\xi = 6.0$.

These measurements show that it is very enthalpically unfavorable for the protein to form multilayers on the nanotube. Self-assembly decreases the enthalpy, but the enthalpy is still larger than the protein-control. For either of these processes to be energetically favorable, the increased enthalpy must be offset by a concomitant increase in entropy.

These measurements suggest that the multilayer adsorption occurs due to a large increase in entropy. Self-assembly of the multilayer-coated nanotubes significantly decreases the enthalpy, although it is unclear whether this also results in an entropic increase. Although a more ordered structure is formed, most self-assembly processes are entropically favored. This can occur when self-assembly results in the dehydration of hydrophobic species, which releases interfacial water near hydrophobic residues. The released water has a significantly larger translational entropy[6, 31, 59, 302].

7.4 Conclusions

In this chapter I employed differential scanning calorimetry to investigate the thermodynamics of multilayer adsorption and self-assembly. For a fixed nanotube volume fraction, at low ξ, where the largest percentage of protein examined could interact with the nanotube surface directly, I observe a significant decrease in the thermal denaturation temperature of the protein. However as the protein concentration (and adsorbed coverage) increases, the temperature steadily increases. The rate at which the temperature increases with protein concentration differs dramatically between the multilayer-adsorbed and self-assembled states. Below $\xi = 2$, the temperature changes at $(0.383 \pm 0.007)\,^{\circ}\mathrm{C}/\mu\mathrm{mol}$ RNaseA, while above

$\xi = 2$ the temperature increases much more slowly, at $(0.056 \pm 0.005)\,^{\circ}$C/μmol RNaseA. I examined the relative enthalpic contributions and temperature change of bound and free protein by deconvolution analysis, which only yielded qualitative results in support of two different populations.

Finally and most interestingly, I examined the effect of increasing the protein and nanotube volume fraction on the enthalpy, heat capacity change, and temperature. These results suggest that increasing the rate of collisions between the nanotube and protein may result in a lesser degree of conformational change and may produce multilayer-adsorbed and self-assembled hybrids with different microstructures.They also highlight the role of entropy in forming these assemblies. Multilayer adsorption was accompanied by a large increase in the calorimetric enthalpy; for this to be energetically favorable, it suggests that it must be accompanied also by a large increase in the entropy.

These findings suggest that it may be possible to tune the resulting structure by changing the volume fractions. At the same time, it would also be interesting to examine the effect of introducing non-adsorbing polymers to act as a depletion or crowding agent. This could induce entropically driven assembly[18, 215, 244, 303, 304]. Entropically driven phase transitions or complex coercevation are promising routes for assembly of anisotropic objects and also one where many interesting questions (and possibly new phenomena) exist.

CHAPTER 8
CONCLUSIONS

In this dissertation, I developed an inorganic nanomaterial which templates the assembly of micron-sized functional biomolecule structures. I demonstrated that titania nanotubes with a high density of unterminated undercoordinated Ti surface sites are able to immobilize extraordinarily large quantities of biomolecules, over 1000 times above monolayer coverage, while other forms of TiO_2 nanomaterials do not show such properties.

Broadly, I showed that biomolecule immobilization and assembly on titania nanotubes occurs in two different stages. First, at low biomolecule-to-TiO_2 molar ratios, biomolecule immobilization takes place up to approximately 55 layers of coverage. The coverage then remains constant until a critical biomolecule-to-TiO_2 molar ratio is reached. Upon reaching this critical ratio, the system self assembles into large aggregates, above which any subsequently added biomolecules incorporate into the existing self-assembled aggregates. For Ribonuclease A (RNaseA), self assembly occurs at an RNaseA-to-TiO_2 molar ratio of 2 and was observed in independent experiments employing dynamic light scattering, adsorption measurements, microcalorimetry, and electron microscopy. The self-assembled product is micron-sized, immobilizing as much as 920 g/g RNaseA/TiO_2. Moreover, such self-assembled aggregates completely retain or even enhance the enzymatic activity.

Although the protein did not oligomerize, it is possible that adsorption on the nanotube surface could significantly alter the protein conformation, however the retention and enhancement of enzymatic activity at high molar ratios, as well as the coverage-dependent

increase in the thermal stability of the protein, indicated by DSC, suggest that conformation of protein bound far from the nanotube surface is minimally perturbed.

Multilayer protein adsorption and the self-assembly of proteins into larger biomaterials were only observed on the undercoordinated anatatase-(001) like surface of titania nanotubes. Neither the hydroxylated anatase-(001) surface or the more common anatase (101) surface templated larger protein assemblies. The mechanistic details of how the nanotube modifies protein-protein interactions remains to be determined, but appear to be correlated to either the hydration properties of the nanotube's surface or the exposure of undercoordinated metal groups.

Amino-acid specificity for the nanotube surface is an important factor which would be opportune for both experimental and theoretical studies. For instance, simulations show that amino acids adsorb differently on the anatase (101) and (001) crystal faces[177]. Experimental studies in vacuum have shown that the backbone carboxyl groups of amino acids will attach to 5-fold coordinated Ti groups by replacing a basic hydroxyl Ti site[305]. The clean crystallographic anatase (001) surface has an incredibly high surface energy (0.90 J/m^2), as compared to the (101) surfaces (0.44 J/m^2)[124], and with the exception of the nanotube, the undercoordated surface will be instantly hydroxylated. However in vaucum the anatase (001) surface does display remarkably high affinity for histidine residues.

The affinity of histidine residues for metal oxides is well known and forms the basis of metal ion affinity chromatography and metal-chelate chromatography. In traditional embodiments, transition metal ions, frequently 4-fold coordinated Ti are immobilized to a polymeric resin[306]. Proteins with exposed histidine, cysteine, or tryptophan residues have higher affinity for the undercoordinated transition metal sites and will be preferentially adsorbed, forming a metal-ligand complex with the Ti site. Varying the solution conditions,

such as pH, ionic strength, or buffer composition, will vary the binding strength or affinity of a given residue and can also be used to remove the protein at a later time.

The high density of undercoordinated Ti sites on the nanotube and the high surface area could offer significant improvements in the capture, separation, and purification of specific proteins and overcome many of the problems with existing metal-ion affinity chromatographies. Using the nanotube as a chromatographic resin or incorporating it into other chromatographic resins, could offer significant improvements in many areas of proteomics.

In addition to the amino acid specificity, it is well known transition metal ions and in particular the nanotube have very high affinities for phosphonate groups[203, 307], catechols, and other phenols[176]. There is significant interest in studying post-transitional modifications of proteins, particularly phosphorylation. However purification of sufficient quantities of phosphorylated peptides for mass spectrometry has so far been extremely difficult and there is an immediate need for significant improvements in the capture and enrichment of phosphopeptides from trypic digested protein samples[76, 226, 227, 306, 308–314]. It would be interesting to investigate the use of the nanotube as a chromatographic resin for a variety of different functional groups, but in particular, to examine its applications in phosphoproteomic purifications.

On a more fundamental level, the volume-fraction dependence of the heat capacity, calorimetric enthalpy, and unfolding temperature, suggests that I may be observing a non-equilibrium assembly process or that there is a kinetically limiting step. There are a number of ways to study this. For instance, kinetic processes can be investigated using isothermal titration calorimetry. This technique measures the heat necessary to maintain a constant temperature while the composition is changed. When the nanotube and protein are combined, it would be interesting to examine the time needed before the system returns to equilibrium

and to examine how enthalpy changes as a function of time[315–318].

Using DSC, one could examine the endotherms of the protein-nanotube conjugates at different scanning rates and volume fractions. A scanning-rate dependence of the endotherm shape or calorimetric enthalpy could indicate irreversible denaturation or kinetically limited steps. DSC has been previously used to investigate many different process involving protein denaturation, aggregation, or the presence of intermediate states[4, 279, 319–321]. Distortions to the endotherm due to rate-limiting or irreversible steps would enable the development of a more detailed model of the assembly process and a deeper understanding of the possible different steps involved. For activated processes, the rate dependence of the enthotherm can yield information about the activation energy[319].

My findings highlight the importance of nanomaterial surface chemistry. Specifically, the surface of the titania nanotube contains a very high density of unterminated undercoordinated Ti sites, which are stable against hydroxylation due to the bond strain imposed by the nanotube's curvature. When the nanotube's curvature is removed, such as in the case of nanosheets or nanotiles, the high energy undercoordinated surface Ti sites are instantly terminated by hydroxylation, restoring sixfold coordination. These materials can only immobilize biomolecules up to monolayer coverage.

Here I have demonstrated that undercoordinated transition metal sites may play a critical role in biomolecule immobilization or the templating of larger biomolecule structures. Maintaining enzymatic activity and achieving high immobilization capacities have both been major obstacles for enzyme immobilization. My results suggest that increasing the density of unterminated undercoordinated transition metal surface sites, either synthetically or by careful control of defect chemistry, could prove to be a fruitful strategy for creating novel enzyme immobilization substrates and may act as an enabling technology for creating

protein-based biomaterials or enzyme biocatalysts.

APPENDIX A

PROTOCOL FOR SYNTHESIZING TINT AND DERIVED STRUCTURES

Chemical	**Manufacturer**	**Product No.**
Anatase TiO_2 Nanoparticles (32 nm APS Power)	Alfa Aesar	39953
Sodium Hydroxide Pellets	Fisher Scientific	S320
1M HEPES Buffer (pH 7.3)	Fisher Scientific	BP299-100
Distilled Deionized H_2O	Generated On Site	
Hydrochloric Acid (36.5-38%)	Fisher Scientific	A114C-212

Supplies or Instruments	**Manufacturer**	**Product No.**
Teflon Lined Autoclave	Custom-machined	N/A
Multitube Vortexer	Fisher Scientific	02-215-452
Disposable Vacuum Filter Flask (0.22 um PES)	Millipore	SCGPS01RE
Borosilicate Crystallization Dish	Corning	3140-90
Gravity Convention Oven (Fisher IsoTEMP 500)	Fisher Scientific	13246516GAQ
Vacuum Oven	Yamato	ADP21
Vacuum Pump	Fisher Scientific	13-880-14
Ultrasonic Cleaner (low power, 40kHz)	Branson	M1800
Fixed angle centrifuge	Eppendorf	5702
Parafilm M	Pechiney/Fisher Sci.	PM996
Ball Milling Chamber Assembly	BioSpec	11007900-101
50 mL grinding chamber	BioSpec	110803-50SS
350 mL grinding chamber	BioSpec	1107910
0.1 mm Zirconia/Silica Beads	BioSpec	11079101z
pH Meter or Paper	Misc	Misc
Micropipettes	Misc	Misc
Centrifuge Tubes and other disposable containers	Misc	Misc

(A) Hydrothermal synthesis of Unshortened (Long) Titania Nanotubes Timing: 3d

1. Preheat gravity box oven to 130 °C
2. Prepare a 10 M solution of Sodium Hydroxide within the Teflon autoclave liner (reaction vessel) by dissolving 160 g NaOH in distilled deionized water (400 mL). This is highly exothermic; allow the solution to cool to near ambient temperature.

3. Slowly add 4.00 g of Anatase Nanoparticles to aqueous NaOH. Gently mix with Teflon stir rod to disperse nanoparticles in NaOH. Resulting suspension should appear milky.
4. Cover Teflon autoclave liner with Teflon top. Place this assembly within the stainless steel autoclave.
5. Hand-tighten the threaded stainless steel autoclave top onto the stainless steel autoclave. This maintains hydrostatic pressure during synthesis. Lid does not need to be extremely tight and does not apply physical pressure on the Teflon reaction vessel.
6. Place sealed autoclave into gravity convection oven and heat it at 130 °C for 72 hours.

(B) Dispersing Reaction Product Timing: 0.5 - 1.0 d

7. Remove sealed autoclave from oven. Allow autoclave to cool to room temperature (typically 8 hours). Then gently unscrew the stainless steel lid and remove Teflon reaction vessel.
8. Most of reaction product will appear as caked sediment. Remove excess supernatant water (which will be nearly clear) from reaction vessel, taking care to leave some water near bottom so as not to remove the reaction product.
9. Pour out caked reaction product and remaining water into a 300 mL Pyrex crystallization dish or beaker.
10. Using a clean glass rod, scrape any remaining reaction product from the Teflon reaction vessel.
11. Use a ceramic pestle to pulverize the reaction product and solution contained in the crystallization dish. This process should be continued until the reaction product is broken up into small pieces with a diameter no greater than a few millimeters (3 mm max).

12. Cover the crystallization dish with Parafilm and use a rubber band to further seal the Parafilm against the crystallization dish.
13. Sonicate crystallization dish continuously for 45 minutes in an ultrasonic cleaner/bath (we use an ultrasonic cleaner without temperature control, for example a Branson M1800, frequency is 40 kHz, $\approx$ 80 W power typically.)
14. Remove Parafilm from crystallization dish and empty contents into a clean beaker.

(C) Washing Nanotubes Timing: 0.5 - 1.0 d

15. Distribute the contents of the beaker into 15 mL conical centrifuge tubes.
16. Centrifuge 4 to 5 minutes at 3.8k rpm (2000g)
17. Nanotubes will be pelleted, remove supernatant and record its pH.
18. Fill the centrifuge tubes with desired washing solution: To produce acid washed nanotubes: Wash with 0.1 M HCl To produce water washed nanotubes: ddH_20 only.
19. Place centrifuge tubes in multitube vortexer (we currently use Fisher 02-215-452) for 10 minutes without pulsing using the highest-powered setting.
20. Repeat Steps 16 - 19 until pH level of supernatant reaches desired level (typically pH 6, but could be 5-8)
21. Once desired pH has been reached, vortex briefly to disperse and pool all centrifuge tubes into a HDPE container. If dry nanotubes are desired, the nanotubes can be dried within the vacuum oven overnight at 50 °C, the resulting pellet broken up into a mortar and pestle. Alternatively, the solution can be placed on a flat glass plate within the box oven (typically done at 50 °C) overnight, the resulting white film should be scraped off with a razor blade.

22. Verify reaction product structure using XRD, SEM, and TEM. The surface chemistry can be characterized with solid state ^{1}H NMR by examining the presence and acidity of surface hydroxyl groups of the dried material and when the surface is hydrated in a water-vapor saturated atmosphere.

(D) Production of Shortened Titania Nanotube by Wet Ball Milling Timing: 2 - 3 hr

The nanotubes produced in the previous section have a typical length of 1 μm to 3 μm and do not form a stable dispersion in aqueous solution. Here we shorten the nanotubes to a typical length of 100 nm to 200 nm (typically we find lengths between 30 nm to 400 nm) to form dispersion.

In this method we utilize a wet ball milling method to produce shortened nanotubes. We utilize a Hamilton Beach 908 Blender motor (Biospec Products #11007900-101) and either a (A) 50 mL polypropylene grinding chamber that contains a Teflon blade (Biospec #110803-50SS) (B) 350 mL polypropylene grinding chamber that contains a Teflon blade (Biospec #1107910).

(i) Small Chamber (50 mL)

23. Add 30 g of 0.1 mm diameter Zirconia/Silica beads (Biospec #11079101z) (also referred to as grinding media) to the 50 mL grinding chamber (Biospec #110803-15SS).
24. Add 200 mg of LTiNT to the grinding chamber, either by weighing out the dry nanotubes or by using an appropriate volume of the nanotube stock solution if you know the concentration. The amount does not have to be exact, but roughly 150 mg to

400 mg is good.

25. The total liquid working volume in the grinding chamber should be approximately 50 mL. Use ddH_2O to make up the remaining volume if needed. Do not overfill beyond 50 mL or you will risk damaging the chamber. Hand tighten the cap onto the grinding chamber.

26. The grinding chamber should be kept cold during grinding. Do not exceed 100 °C. Place the grinding chamber within an ice-water filled outer shell and place the assembly into an ice bath.

27. Proceed to Step #32

(ii) Large Chamber (350 mL)

28. Add 250 g of 0.1 mm diameter Zirconia/Silica beads (Biospec #11079101z) (also referred to as grinding media) to the 350 mL grinding chamber (Biospec #1107910).

29. Add 400 mg of LTiNT to the grinding chamber, either by weighing out the dry nanotubes or by using an appropriate volume of the nanotube stock solution if you know the concentration. The amount does not have to be exact, but roughly 400 mg to 500 mg is good.

30. The total liquid working volume in the grinding chamber should be approximately 200 mL. Use ddH_2O to make up the remaining volume if needed. Do not overfill beyond 200 mL or you will risk damaging the chamber. The large chamber assembles differently from the 50 mL chamber. Place the separate Teflon rotor assembly onto the chamber and thread the grinding chamber's outer ice bath shell onto the chamber to seal the assembly. Now invert the assembly and place it on the blender.

31. The grinding chamber should be kept cold during grinding. Do not exceed 100 °C. Fill the outer ice bath shell with ice and water. If desired, a salt-water bath can be

used to further lower the temperature.

32. Grind for 30 - 45 minutes, changing the ice baths as needed to ensure that the temperature does not exceed 100 °C.

33. The grinding media will quickly sediment. Remove the supernatant solution and if needed, briefly centrifuge to verify all grinding media has been removed.

34. Remove any larger nanotube aggregates or contaminants by filtering the resulting material using either a syringe or vacuum membrane filter (0.22 µm).

35. Examine the material using TEM, SEM, and XRD, and DLS, to verify structure and size.

36. Determine mass concentration of nanotubes in solution using TGA or a comparable technique to determine the nanotube concentration.

37. Dilute the short nanotubes you've produced in the buffer of your choice. For the experiments in the manuscript, it was diluted 10x within 10 mM HEPES buffer (pH 7.2 - 7.3)

APPENDIX B
DYNAMIC LIGHT SCATTERING

DLS relies on the fact that when photons scatter off a system of freely diffusing particles, the instantaneous scattering intensity at a given time, t, $I(q,t)$, will fluctuate about its mean, $I(q)$, due to Brownian motion, on the order of q^{-1}, where, $q \equiv |\vec{q}| = \frac{4\pi n}{\lambda}\sin\frac{\theta}{2}$, is the wavevector.

The correlation time of these fluctuations, τ, should be larger for slower diffusing particles. Thus the temporal correlation between the intensity at two different times, $I(q,t')$ and $I(q,t'')$ will deviate sooner for faster diffusing particles, and can be quantified by calculating the time autocorrelation function (ACF) of the instantaneous intensity[247, 322]:

$$\langle I(q,0)I(q,t)\rangle \equiv \lim_{t'\to\infty}\frac{1}{t'}\int_0^{t'} I(q,t'')I(q,t''+t)dt'' \tag{B.1}$$

At times much longer than the correlation time, $t \gg \tau$, the values of $I(q,0)$ and $I(q,t)$ are independent, and $\langle I(q,0)I(q,t)\rangle$ will decay to the square mean, $\langle I(q,0)\rangle^2$.

I performed all of my measurements using a Malvern Zetasizer Nano ZS. This system contains a vertically polarized HeNe laser with wavelength, λ=633 nm and the measurements were performed at a fixed angle, θ=173°. This system employs a heterodyne measurement technique in which the scattered light is mixed with light from the incident beam and the beat frequency is measured. The mixed signal is incident on a photodetector and

fed into a hardware auto-correlator[247]. From this, we can determine the normalized ACF of the scattered electric field, $g^{(1)}_{VV}(q,t)$:

$$g^{(1)}(q,t) = \frac{\langle \vec{E}^*(t) \cdot \vec{E}(0) \rangle}{\langle |\vec{E}(0)| \rangle^2} \tag{B.2}$$

The Siegert relationship[247, 248], $g^2(t) = 1 + [g^{(1)}(t)]^2$, can be used to relate the ACF of the scattered electric field, $g^{(1)}(t)$, to the ACF of the intensity, $g^2(q,t)$, where

$$g^{(2)}(q,t) = \frac{\langle I(0)I(t) \rangle}{\langle I(0) \rangle^2} \tag{B.3}$$

B.1 Apparent diffusion coefficient

For a monodisperse system of spherical, non-interacting particles, $g^{(1)}(q,t)$, decays exponentially with a rate, Γ, as $g^{(1)}_{VV}(q,t) \propto exp\,(-\Gamma t)$. Where the decay rate, Γ, is related to the apparent diffusion coefficient, D_p, as $\Gamma = D_p q^2$. For spherical particles, D_p will correspond to the center-of-mass translational diffusion, D_T.

From the Stokes-Einstein relationship, we can express the translational diffusion coefficient, D_T, in terms of a frictional coefficient, f_T (representing hydrodynamic resistance for anisotropic objects), the temperature, T, and the Boltzmann constant, k_B:

$$D_T = \frac{k_B T}{f_T} \tag{B.4}$$

and for freely-diffusing spherical particles, the hydrodynamic radius will be found by:

$$R_H = \frac{k_B T}{6\pi\eta_0 D_T} \tag{B.5}$$

where η_0 is the viscosity.

B.2 Correlation function for monodisperse rods

This situation is considerably more complicated for objects with anisotropic geometries or optical anisotropy. The optical anisotropy is manifested by an orientation dependent polarizability, while the geometric anisotropy is manifested by an orientationally dependent diffusion constant and q-dependent coupling of translational and rotational diffusion. For clarity, the following discussion treats these two anisotropies differently.

B.2.1 Optical anisotropy

The polarizability tensor, $\underset{\approx}{\alpha}$ for an axially-symmetric scatterer contains contributions along three principle axes:

$$\underset{\approx}{\alpha} = \begin{pmatrix} \alpha_\perp & 0 & 0 \\ 0 & \alpha_\perp & 0 \\ 0 & 0 & \alpha_\parallel \end{pmatrix} \tag{B.6}$$

where the subscripts $\perp$ and $\parallel$ indicate the polarizability perpendicular and parallel to the axis of rotation, respectively.

Defining the isotropic contribution to the polarizability, α, and anisotropic contribution to the polarizability, β:

$$\alpha = \frac{\alpha_{\parallel} + 2\alpha_{\perp}}{3} \tag{B.7}$$

$$\beta = (\alpha_{\parallel} - \alpha_{\perp}) \tag{B.8}$$

the ACF can be expressed as[323]:

$$g_{VV}^{(1)}(q,t) = AN\left(\alpha^2 + \frac{4}{45}\beta^2 e^{(-6D_R)t}\right) e^{(-q^2 D_T)t} e^{(-i\omega_0)} \tag{B.9}$$

where D_R is the rotational diffusion coefficient, D_T the translational diffusion coefficient, A an amplitude, N a number of scattering particles in the scattering volume.

Equation (B.9) contains three different decay modes: an isotropic contribution (with an amplitude related to α^2), an anisotropic contribution (with amplitude related to β^2), and a fast decay mode, $e^{(-i\omega_0)t}$. The fast decaying term, $e^{(-i\omega_0)t}$ will decay much faster than the other terms and is dropped for the remainder of our discussion.

The isotropic decay mode contains only contributions from translational diffusion and will decay with time constant $\tau_1 = (q^2 D_T)^{-1}$, while the anisotropic contribution will decay with a time constant $\tau_2 = (6D_R + q^2 D_T)^{-1}$. If the anisotropic contribution is significant, the apparent diffusion coefficient I obtain by fitting the ACF will contain contributions from

both translational and rotational diffusion. Without additional experiments, described, later in this discussion, it is difficult to temporally separate out these contributions and determine the apparent hydrodynamic size increase from these measurements.

When $\alpha \gg \beta$, the translational-only (isotropic) decay mode will dominate. I can estimate the relative values of α and β by considering the scattering coefficient, per fractional volume, of an ellipsoidal particle [324]. The scattering coefficient, μ_s, per fractional volume will be:

$$\frac{\mu_s}{NV_p} = \frac{8\pi V_p}{9\lambda}\left(\epsilon_m^2\left(\epsilon_2^2 + (\epsilon_1 - \epsilon_m)^2\right)\right)F \tag{B.10}$$

where N is the particle number density, V_p is the ellipsoid volume, λ is the wavelength of the laser, ϵ_M the dielectric constant of the surrounding solution, ϵ_1 is the real component of the particle's dielectric constant, ϵ_2 is the imaginary component of the particle's dielectric constant and F is a geometric factor defined over the different principle axis:

$$F = \sum_{i=1}^{3}\left(L_i^2\left(\epsilon_2^2 + \left(\epsilon_1 + \epsilon_m\left(\frac{1-L_i}{L_i}\right)\right)^2\right)\right)^{-1} \tag{B.11}$$

where the axis-dependent geometric factors, L_i are defined in terms of a parameter, e, which is determined by the particle's aspect ratio, R:

$$e = \left(1 - R^{-2}\right)^{1/2} \tag{B.12}$$

The contribution of the the parallel (semi-major axis), L_1, is:

$$L_1 = \left(\frac{1-e^2}{e^2}\right)\left((2e)^{-1} ln\left(\frac{1+e}{1-e}\right) - 1\right) \tag{B.13}$$

and the perpendicular axis (semi-minor axis) contribution, L_2 and L_3 are:

$$L_2 = L_3 = \frac{1-L_1}{2} \tag{B.14}$$

To first order, the effect of the anisotropic polarizability, can be estimated by noting that $\alpha_{\parallel} \propto F_1$ and $\alpha_{\perp} \propto F_2$. For anatase[124], $\epsilon_1 \approx (2.56)^2\epsilon_0$ and $\epsilon_2 \approx 0$. The solvent, water, has $\epsilon_m \approx (1.33)^2\epsilon_0$, where ϵ_0 is the permittivity of free space. For nanotubes with a length of 100 nm and diameter of 12 nm, the ratio of F_1, the parallel contribution, to F_2, the perpendicular contribution, is:

$$\frac{F_1}{F_2} \approx \frac{0.259}{0.061} = 4.25 \tag{B.15}$$

therefore the relative contributions of α and β shown in equations (B.7) and (B.8) will be:

$$\alpha \approx 2.08 \tag{B.16}$$

$$\beta \approx 3.25 \tag{B.17}$$

From equation (B.9), it is evident that we will can ignore the anisotropic polarizability in the case that $\alpha^2 \gg \frac{4}{45}\beta^2$. Based on the estimates I show above the the ratio of these two terms is:

$$\frac{\alpha^2}{\frac{4}{45}\beta^2} \approx 4.59 \tag{B.18}$$

Based on these estimates, it is not clear that these terms can be readily separated, nor could the rotational contribution be effectively ignored unless $q^2 D_T \gg 6D_R$. This results from the geometrical anisotropy, and will be consisered below.

B.2.2 Effect of geometric anisotropy

A rod will have two different translational diffusion constants, one for translation parallel to the symmetry axis, $D_T^{\parallel}$, and one for translational perpendicular to the symmetry axis, $D_T^{\perp}$[253]. The rotational diffusion will also exhibit anisotropy and will have a contribution for end-over-end tumbling of the rod, $D_R^{\perp}$, which corresponds to rotation around a perpendicular axis, as well as rotational diffusion about a parallel axis, $D_R^{\parallel}$. This is further complicated by coupling of the rod's translational diffusion to its rotational diffusion.

Translational diffusion will always be observed in my measurements, but the contribution of rotational diffusion will depend on the rod length, L, and scattering vector, q. For a heterodyne measurement, the normalized electric-field ACF of optically isotropic, monodisperse, rod-like particles, contains two different decay modes[247]:

$$g_{VV}^{(1)}(q,t) = S_0(qL)e^{\left(-q^2 D_T\right)t} + S_1(qL)e^{-\left(q^2 D_T + 6D_R\right)t} \tag{B.19}$$

where D_T is the isotropically averaged translational diffusion coefficient, defined by $D_T =$

$\frac{1}{3}\left(D_T^{\parallel} + 2D_T^{\perp}\right)$ and D_R is the effective rotational diffusion coefficient. S_0 and S_1 are the amplitudes of the two different decay modes and depend on the wavevector, q, and the length of the rods, L[247, 258]. The first term in equation (B.19) is due to purely translational processes, while the second term corresponds to a mixture of translational and rotational diffusion. This equation is valid for $qL < 8$ (an excellent discussion of this can be found in §8.7 of Berne and Pecora[247].)

For $qL < 3$, the translational-rotational coupling is weak and equation (B.19) will be dominated by the translational-only mode and $g^1(q,t)$ will decorrelate at a rate of $\Gamma_{slow} \approx q^2 D_T$. In my measurements, this condition is satisfied when L < 120 nm (typically 75 nm< $L_{nanotube}$ < 100 nm).

For $qL > 3$, $g^{(1)}(q,t)$ contains contributions from both Γ_{slow} and $\Gamma_{fast} = (q^2 D_T + 6D_R)$. Thus the effects of rotational diffusion cannot be neglected for $qL > 3$ unless $D_T q^2 \ll 6D_R$. Under these conditions the temporal separation between the fast and slow decay modes is significant and it is possible to effectively resolve the translational diffusion.

A number of models have been developed to estimate the diffusion constants for different geometries and aspect ratios[247, 249, 251, 253]. Using the Hydrosub software developed by Ortega and de la Torre[253], I estimate that 100 nm long, 12 nm wide nanotubes have D_T ≈1.04 × 10^{-7} cm^2 s^{-1} and D_R ≈ 3.11 × 10^4 s^{-1}. For q =2.5 × 10^{-2} nm^{-1}, leading to a ratio $6D_R/\left(q^2 D_T\right)$ ≈28.64. Modeling this as a prolate ellipsoid, these values are both slightly larger, D_T ≈1.22 × 10^{-7} cm^2 s^{-1} and D_R ≈ 4.94 × 10^4 s^{-1} and thus $6D_R/\left(q^2 D_T\right)$ ≈38.87.

TEM and SEM imaging suggest that protein adsorbed to the nanotube forms a prolate

ellipsoid. As a limiting case, I consider a prolate ellipsoid which is 100 nm long and 40 nm wide (this corresponds to a 14 nm thick layer of protein), $D_T \approx 7.4 \times 10^{-8}\,\mathrm{cm^2\,s^{-1}}$ and $D_R \approx 6.36 \times 10^3\,\mathrm{s^{-1}}$, resulting in $6D_R/\left(q^2 D_T\right) \approx 8.25$. In both of these cases, $qL < 3$, and rotational diffusion does not significantly contribute to $g^{(1)}$. More realistically, the nanotube's length also increases with protein adsorption. Subsequently, $6D_R/\left(q^2 D_T\right)$ decreases. For a nanotube with a 14 nm protein layer, doubling the nanotube's length to 200 nm ($qL \approx 5$), $6D_R/\left(q^2 D_T\right) \approx 4.71$.

A depolarized dynamic light scattering experiment could be used to remove the purely translational relaxation mode that is shown in equation (B.19). In such an experiment, the incident radiation is vertically polarized and the only the horizontally polarized component is measured. The measured correlation function, $g^{(1)}_{VH}$, will only contain the second term of equation (B.19) corresponding to the translational relaxation. D_T and D_R can be determined by plotting the decay rate, Γ versus q^2, D_T will be the slope of the curve and D_R the intercept.

However, the instrument I had access did not allow for depolarized measurements nor could I vary q, therefore it is not possible to directly extract the parameters in equation (B.19) from my measurements.

The apparent diffusion coefficient I obtain by fitting my autocorrelation function therefore may contain contributions from both rotation and translational diffusion. These contributions will vary as the aspect ratio or anisotropy changes. Therefore the proportionality between the physical size increase and apparent hydrodynamic radius increase may vary over different length scales and aspect ratios. In the absence of more detailed information about the aggregate morphology or measurements at a variety of q, it is not possible to conclusively determine how increases in the apparent hydrodynamic size correspond to

aggregate growth. It is only possible to use these measurements to examine whether the size has increased, it is not possible to state how much it has actually increased.

B.3 Analyzing DLS data

The apparent diffusion coefficient, is extracted using the the method of cumulants[136, 247] in which the logarithm of the correlation function is expanded as a power series:

$$\ln\left[g^{(1)}(q,\tau)\right] = \sum_{n=1}^{\infty} K_n(q)\frac{(-\tau)^n}{n!} \tag{B.20}$$

The first cumulant K_1:

$$K_1(q) = \lim_{\tau\to 0}\frac{d(ln[g^{(1)}(q,\tau)])}{d\tau} \tag{B.21}$$

is used to define the mean diffusion coefficient:

$$\langle D\rangle = \frac{K_1(q)}{q^2} \tag{B.22}$$

More practically, for a given q, we can extract the mean diffusion coefficient, called the harmonic mean diffusion coefficient,by a simple polynomial fit of the first two cumulants. Therefore I fit $ln[g^{(1)}(\tau)]$ to:

$$ln[g^{(1)}(\tau)] = a + b\tau + c\tau^2 \tag{B.23}$$

where the coefficient b is the harmonic mean diameter (the first cumulant) and the coefficient c is related to the polydispersity of the population and τ is the correlation time.

Using equations (B.5), (B.22) and (B.23) we can extract the apparent mean hydrodynamic size of the population, referred to as the Z_{avg} diameter.

Although the analysis of data with a single decay rate, $\Gamma_i = q^2 D_i$, is relatively straightforward, the correlation function of my system (assuming it obey's Gaussian statistics)[249], will be represented by a sum of different decay modes[247]:

$$\langle I(q,0)I(q,t)\rangle = \left(\sum_{i=1}^{\mathrm{N}} A_i \exp(-\Gamma_i t)\right)^2 + constant \tag{B.24}$$

Taking the Laplace transform this can be represented as a continuous distribution of decay rates, A(Γ)[247, 322]:

$$\langle I(q,0)I(q,t)\rangle = \left(\int_0^\infty A(\Gamma)\exp(-\Gamma t)d\Gamma\right)^2 + B \tag{B.25}$$

The actual details of solving this problem are nontrivial. This equation is a Fredholm integral equation of the first kind, and it is unfortunately an ill-posed problem[247, 284]. This integral equation can be best solved by a regularization technique, which involves substituting a similar but well-posed problem to solve for the distribution of decay modes. For

my measurements, this is implemented in the Malvern Software using the CONTIN[325] algorithm.

APPENDIX C

PROTEIN UNFOLDING COUPLED TO LIGAND BINDING

Assuming a basic equilibria between the denatured form of the protein, U, and the nanotube (ligand), L:

$$\mathrm{U} + \mathrm{L} \rightleftharpoons \mathrm{UL} \tag{C.1}$$

with an affinity $K_{L,U} = \frac{[U][L]}{[UL]}$, where the letter L indicates a ligand (the nanotube) and U the unfolded form of the protein, the unfolding equilibrium constant K_{unf} will be:

$$K_{unf} = \frac{[U] + [UL]}{[N]} = K_0 \left(1 + \frac{[L]}{K_{L,U}}\right) \approx \frac{K_0[L]}{K_{L,U}} \tag{C.2}$$

where N indicates the native form of the protein and K_0 indicates the unfolding constant for denaturation in the absence of the nanotube, $K_0 = \frac{[U]}{[N]}$:

$$\mathrm{N} \rightleftharpoons \mathrm{U} \tag{C.3}$$

the free energy of unfolding will therefore be:

$$\Delta G_{unf} = -RT \ln\left(K_{unf}\right) = \Delta G_{unf,0} - RT \ln\left([L]\right) \tag{C.4}$$

where $\Delta G_{unf,0}$ is the free energy of unfolding the protein in the absence of the nanotube. $\Delta G_{unf} = 0$ at the midpoint of the thermal unfolding transition, T_m. The heat capacity of RNaseA, ΔC_p, is essentially constant over the temperature range we are examining[53]. In the absence of the nanotube, the Gibb's free energy change at a given temperature is[4, 285]:

$$\Delta G_{unf,0} = \Delta H_{unf,0} \left(1 - \frac{T}{T_{m_0}}\right) \tag{C.5}$$

where $\Delta H_{unf,0}$ is the enthalpy change of this transition and T_{m_0} is the midpoint of the transition. From this we can derive an expression of the change in unfolding temperature, $\Delta T = T_m - T_{m_0}$:

$$\frac{\Delta T}{T_m} = -\frac{RT_{m_0}}{\Delta H_{unf,0}} \ln\left(1 + \frac{[L]}{K_{L,U}}\right) \tag{C.6}$$

REFERENCES

[1] Marek Kosmulski. *Surface Charging and Points of Zero Charge*. CRC Press, September 2010.

[2] M Horn, C F Schwerdtfeger, and E P Meagher. Refinement of the structure of anatase at several temperatures. *Zeitschrift Fur Kristallographie*, 136(3-4):273–281, 1972.

[3] G Privalov, V Kavina, E Freire, and P L Privalov. Precise scanning calorimeter for studying thermal properties of biological macromolecules in dilute solution. *Analytical Biochemistry*, 232(1):79–85, November 1995.

[4] P L Privalov. *Microcalorimetry of Macromolecules: The Physical Basis of Biological Structures*. Wiley series in protein and peptide science. Wiley, Hoboken, N.J, 2012.

[5] Gregory F Payne, Eunkyoung Kim, Yi Cheng, Hsuan-Chen Wu, Reza Ghodssi, Gary W Rubloff, Srinivasa R Raghavan, James N Culver, and William E Bentley. Accessing biology's toolbox for the mesoscale biofabrication of soft matter. *Soft Matter*, pages 6019–6032, 2013.

[6] Barry W Ninham and Pierandrea Lo Nostro. *Molecular Forces and Self Assembly*. In Colloid, Nano Sciences and Biology. Cambridge University Press, Cambridge; New York, April 2010.

[7] Ofer O Idan and Henry H Hess. Diffusive transport phenomena in artificial enzyme cascades on scaffolds. *Nature Nanotechnology*, 7(12):769–770, December 2012.

[8] E R Stadtman and P B Chock. Superiority of interconvertible enzyme cascades in metabolic regulation: analysis of monocyclic systems. *Proceedings Of The National Academy Of Sciences Of The United States Of America-physical Sciences*, 74:2761–2765, 1977.

[9] O I Wilner, Y Weizmann, R Gill, and O Lioubashevski. Enzyme cascades activated on topologically programmed DNA scaffolds. *Nature Nanotechnology*, 4:249–254, 2009.

[10] M Maskos and R H Stauber. *3.319. Characterization of Nanoparticles in Biological Environments*. Elsevier Ltd., 2011.

[11] Yang Y Liu, Juanjuan J Du, Ming M Yan, Mo Yin MY Lau, Jay J Hu, Hui H Han,

Otto O OO Yang, Sheng S Liang, Wei W Wei, Hui H Wang, Jianmin J Li, Xinyuan X Zhu, Linqi L Shi, Wei W Chen, Cheng C Ji, and Yunfeng Y Lu. Biomimetic enzyme nanocomplexes and their use as antidotes and preventive measures for alcohol intoxication. *Nature Nanotechnology*, 8(3):187–192, March 2013.

[12] Linqiu Cao. *Carrier-bound Immobilized Enzymes*. Principles, Application and Design. Wiley-VCH, May 2006.

[13] M.; Aranda P. Ruiz-Hitzky, E.; Darder. An introduction to bio-nanohybrid materials. In K.; Lvov Y.M.; Ruiz-Hitzky, E.; Ariga, editor, *Bio-inorganic Hybrid Nanomaterials*, chapter An Introduction to Bio-nanohybrid Materials, pages 1–40. Wiley, November 2008.

[14] Yen-Ting Lai, Neil P King, and Todd O Yeates. Principles for designing ordered protein assemblies. *Trends in Cell Biology*, pages 1–9, September 2012.

[15] Carla Thomas, Matthew Glassman, and Bradley Olsen. Solid-state nanostructured materials from self-assembly of a globular protein-polymer diblock copolymer. *Acs Nano*, 5(7):5697–5707, July 2011.

[16] Jungbae Kim, Jay W Grate, and Ping Wang. Nanostructures for enzyme stabilization. *Chemical Engineering Science*, 61(3):1017–1026, February 2006.

[17] Richard P Sear. Protein crystals and charged surfaces: Interactions and heterogeneous nucleation. *Physical Review E*, 67(6):061907, 2003.

[18] Huan-Xiang Zhou, Germán Rivas, and Allen P Minton. Macromolecular Crowding and Confinement: Biochemical, Biophysical, and Potential Physiological Consequences. *Annual Review Of Biophysics*, 37(1):375–397, June 2008.

[19] Ameya U Borwankar, Aileen K Dinin, Joshua R Laber, April Twu, Brian K Wilson, Jennifer A Maynard, Thomas M Truskett, and Keith P Johnston. Tunable equilibrium nanocluster dispersions at high protein concentrations. *Soft Matter*, 2013.

[20] John D Chodera and David L Mobley. Entropy-enthalpy compensation: Role and ramifications in biomolecular ligand recognition and design. *Annual Review Of Biophysics*, 42:121–142, January 2013.

[21] S J Gill. Thermodynamics of ligand-binding to proteins. *Pure and Applied Chemistry*, 61:1009–1020, 1989.

[22] J J Wyman. The cybernetics of biological macromolecules. *Biophysical Chemistry*,

14(2):135–146, October 1981.

[23] J J Wyman. A group of thermodynamic potentials applicable to ligand binding by a polyfunctional macromolecule. *Proceedings Of The National Academy Of Sciences Of The United States Of America-physical Sciences*, 72(4):1464–1468, April 1975.

[24] Scott Banta, Ian R Wheeldon, and Mark Blenner. Protein engineering in the development of functional hydrogels. *Annual Review Of Biomedical Engineering*, 12(1):167–186, August 2010.

[25] Pamela Torres-Salas, Alberto del Monte-Martinez, Bessy Cutiño-Avila, Barbara Rodriguez-Colinas, Miguel Alcalde, Antonio O Ballesteros, and Francisco J Plou. Immobilized Biocatalysts: Novel Approaches and Tools for Binding Enzymes to Supports. *Advanced Materials*, 23(44):5275–5282, August 2011.

[26] Zhao Huang, Taha Salim, Autumn Brawley, Jan Patterson, Kathleen S Matthews, and Sarah E Bondos. Functionalization and Patterning of Protein-Based Materials Using Active Ultrabithorax Chimeras. *Advanced Functional Materials*, 21(14):2633–2640, April 2011.

[27] Xiao Hu, Peggy Cebe, Anthony S Weiss, Fiorenzo Omenetto, and David L Kaplan. Protein-based composite materials. *Mater. Today*, 15(5):208–215, May 2012.

[28] U T Bornscheuer, G W Huisman, R J Kazlauskas, S Lutz, J C Moore, and K Robins. Engineering the third wave of biocatalysis. *Nature*, 485(7397):185–194, May 2012.

[29] Yan Zhang, Jingyan Zhang, Xuelei Huang, Xuejiao Zhou, Haixia Wu, and Shouwu Guo. Assembly of Graphene Oxide-Enzyme Conjugates through Hydrophobic Interaction. *Small*, 8(1):154–159, October 2011.

[30] Wen Shang, Joseph H Nuffer, Jonathan S Dordick, and Richard W Siegel. Unfolding of ribonuclease A on silica nanoparticle surfaces. *Nano Letters*, 7(7):1991–1995, July 2007.

[31] Willem Norde, Jos Buijs, and Hans Lyklema. Adsorption of globular proteins. In J Lyklema, editor, *Fundamentals of Interface and Colloid Science*, volume 5, chapter Adsorption of Globular Proteins, pages 1–59. Elsevier, 2005.

[32] Martin M Lundqvist, Ingmar I Sethson, and Bengt-Harald BH Jonsson. Protein adsorption onto silica nanoparticles: conformational changes depend on the particles' curvature and the protein stability. *Langmuir*, 20(24):10639–10647, November 2004.

[33] Valeria Puddu and Carole C Perry. Peptide adsorption on silica nanoparticles: evidence of hydrophobic interactions. *Acs Nano*, 6(7):6356–6363, July 2012.

[34] Alexey A Vertegel, Richard W Siegel, and Jonathan S Dordick. Silica nanoparticle size influences the structure and enzymatic activity of adsorbed lysozyme. *Langmuir*, 20(16):6800–6807, August 2004.

[35] Roger A Sheldon. Enzyme immobilization: the quest for optimum performance. *Advanced Synthesis & Catalysis*, 349(8):1289–1307, 2007.

[36] Francesco Turci, Elena Ghibaudi, Massimiliano Colonna, Barbara Boscolo, Ivana Fenoglio, and Bice Fubini. An integrated approach to the study of the interaction between proteins and nanoparticles. *Langmuir*, 26(11):8336–8346, June 2010.

[37] Avelino Corma, Vicente Fornes, and Fernando Rey. Delaminated zeolites: an efficient support for enzymes. *Advanced Materials*, 14(1):71–74, 2002.

[38] Hongfei Jia, Guangyu Zhu, and Ping Wang. Catalytic behaviors of enzymes attached to nanoparticles: the effect of particle mobility. *Biotechnology and Bioengineering*, 84(4):406–414, November 2003.

[39] Prashanth P Asuri, Shyam Sundhar Bale, Ravindra C Pangule, Dhiral A Shah, Ravi S Kane, and Jonathan S Dordick. Structure, function, and stability of enzymes covalently attached to single-walled carbon nanotubes. *Langmuir*, 23(24):12318–12321, November 2007.

[40] Michael Rabe, Dorinel Verdes, and Stefan Seeger. Understanding protein adsorption phenomena at solid surfaces. *Advances in Colloid and Interface Science*, 162(1-2):87–106, February 2011.

[41] Wei Wang, Wei Wang, Christopher John Roberts, and Christopher John Roberts. *Aggregation of therapeutic proteins*. Wiley, Hoboken, N.J., 2010.

[42] J J Ramsden. Puzzles and paradoxes in protein adsorption. *Chemical Society Reviews*, 24(1):73–78, 1995.

[43] S Noinville and M Revault. *Conformations of proteins adsorbed at liquid-solid interfaces*, pages 119–150. Springer, 2006.

[44] P M Claesson, E Blomberg, J C Fröberg, T Nylander, and T Arnebrant. Protein interactions at solid surfaces. *Advances in Colloid and Interface Science*, 57:161–227, 1995.

[45] Andre E Nel, Lutz Mädler, Darrell Velegol, Tian Xia, Eric M V Hoek, Ponisseril Somasundaran, Fred Klaessig, Vince Castranova, and Mike Thompson. Understanding biophysicochemical interactions at the nano–bio interface. *Nature Materials*, 8(7):543–557, June 2009.

[46] A N Asanov, L J DeLucas, P B Oldham, and W W Wilson. Interfacial aggregation of bovine serum albumin related to crystallization conditions studied by total internal reflection fluorescence. *Journal Of Colloid and Interface Science*, 196(1):62–73, December 1997.

[47] Ian W Hamley. Amyloid formation: Interface influence. *Nature*, 2(9):707–708, September 2010.

[48] Jeremy Pronchik, Jeremy Pronchik, Xianglan He, Xianglan He, Jason T Giurleo, Jason T Giurleo, David S Talaga, and David S Talaga. In Vitro Formation of Amyloid from α-Synuclein Is Dominated by Reactions at Hydrophobic Interfaces. *Journal Of The American Chemical Society*, 132(28):9797–9803, July 2010.

[49] A Krishnan, P Cha, A. Liu, D Allara, and E Vogler. Interfacial energetics of blood plasma and serum adsorption to a hydrophobic self-assembled monolayer surface. *Biomaterials*, 27(17):3187–3194, June 2006.

[50] W Norde and J Lyklema. The adsorption of human plasma albumin and bovine pancreas ribonuclease at negatively charged polystyrene surfaces: I. Adsorption isotherms. Effects of charge, ionic strength, and temperature. *Journal Of Colloid and Interface Science*, 66(2):257–265, 1978.

[51] A Krishnan, Y H Liu, P Cha, D Allara, and E A Vogler. Interfacial energetics of globular-blood protein adsorption to a hydrophobic interface from aqueous-buffer solution. *Journal Of The Royal Society Interface*, 3(7):283–301, April 2006.

[52] K K Nakanishi, T T Sakiyama, and K K Imamura. On the adsorption of proteins on solid surfaces, a common but very complicated phenomenon. *Journal Of Bioscience and Bioengineering*, 91(3):233–244, January 2001.

[53] Peter L Privalov and Anatoly I Dragan. Microcalorimetry of biological macromolecules. *Biophysical Chemistry*, 126(1-3):16–24, March 2007.

[54] Jean-Pierre Changeux. Allostery and the Monod-Wyman-Changeux Model After 50 Years. *Annual Review Of Biophysics*, 41(1):103–133, June 2012.

[55] Tom A Waigh. *Applied Biophysics*. Wiley, November 2007.

[56] Kenneth P Murphy. *Protein Structure, Stability, and Folding*. Springer, 2001.

[57] Voichita M Dadarlat and Carol Beth Post. Adhesive-cohesive model for protein compressibility: an alternative perspective on stability. *Proceedings Of The National Academy Of Sciences Of The United States Of America-physical Sciences*, 100(25):14778–14783, December 2003.

[58] Carel J van Oss. *Interfacial Forces in Aqueous Media, Second Edition*. CRC Press, May 2006.

[59] Ninad V Prabhu and Kim A Sharp. Heat Capacity in Proteins. *Annual Review Of Physical Chemistry*, 56(1):521–548, May 2005.

[60] G G Belfort and C S CS Lee. Attractive and repulsive interactions between and within adsorbed ribonuclease A layers. *Proceedings Of The National Academy Of Sciences Of The United States Of America-physical Sciences*, 88(20):9146–9150, October 1991.

[61] Martin Malmsten. *Biopolymers at Interfaces, Second Edition*. CRC Press, January 2010.

[62] W Norde, Jose M Sanchez-Ruiz, and J Lyklema. Thermodynamics of Protein Adsorption - Theory with Special Reference to the Adsorption of Human-Plasma Albumin and Bovine Pancreas Ribonuclease at Polystyrene Surfaces. *Journal Of Colloid and Interface Science*, 71(2):350–366, 1979.

[63] E A Vogler. Structure and reactivity of water at biomaterial surfaces. *Advances in Colloid and Interface Science*, 74:69–117, February 1998.

[64] P Tengvall. 4.406 - Protein Interactions with Biomaterials. In Editor-in-Chief Paul Ducheyne, editor, *Comprehensive Biomaterials*, pages 63–73. Elsevier, Oxford, 2011.

[65] Andrea Gessner, Antje Lieske, Bernd R Paulke, and Rainer H Müller. Influence of surface charge density on protein adsorption on polymeric nanoparticles: analysis by two-dimensional electrophoresis. *European Journal Of Pharmaceutics and Biopharmaceutics*, 54(2):165–170, September 2002.

[66] M Lundqvist, J Stigler, G Elia, I Lynch, T Cedervall, and K A Dawson. Nanoparticle size and surface properties determine the protein corona with possible implications for biological impacts. *Proceedings Of The National Academy Of Sciences Of The United States Of America-physical Sciences*, 105(38):14265–14270, 2008.

[67] Martin Malmsten and NetLibrary Inc.,. *Biopolymers at interfaces*. M. Dekker, New York, 1998.

[68] Susan M Daly, Todd M Przybycien, and Robert D Tilton. Coverage-Dependent Orientation of Lysozyme Adsorbed on Silica. *Langmuir*, 19(9):3848–3857, April 2003.

[69] Iseult Lynch and Kenneth A Dawson. Protein-nanoparticle interactions. *Nano Today*, 3(1-2):40–47, February 2008.

[70] E Perevedentseva, P J Cai, Y C Chiu, and C L Cheng. Characterizing Protein Activities on the Lysozyme and Nanodiamond Complex Prepared for Bio Applications. *Langmuir*, 27(3):1085–1091, February 2011.

[71] Sumanth N Jamadagni, Sumanth N Jamadagni, Rahul Godawat, Rahul Godawat, Jonathan S Dordick, Jonathan S Dordick, Shekhar Garde, and Shekhar Garde. How Interfaces Affect Hydrophobically Driven Polymer Folding âĂă. *Journal Of Physical Chemistry B*, 113(13):4093–4101, April 2009.

[72] Carl D CD Walkey and Warren C W WC Chan. Understanding and controlling the interaction of nanomaterials with proteins in a physiological environment. *Chemical Society Reviews*, 41(7):2780–2799, April 2012.

[73] Jukka Sund, E Karatan, Harri Alenius, P Watnick, Minnamari Vippola, Kai Savolainen, and Anne Puustinen. Proteomic Characterization of Engineered Nanomaterial–Protein Interactions in Relation to Surface Reactivity. *Acs Nano*, 5(6):4300–4309, June 2011.

[74] Arnaud A Magrez, Lenke L Horváth, Rita R Smajda, Valérie V Salicio, Nathalie N Pasquier, László L Forró, and Beat B Schwaller. Cellular toxicity of TiO_2-based nanofilaments. *Acs Nano*, 3(8):2274–2280, August 2009.

[75] Wan-Kyu Oh, Sojin Kim, Moonjung Choi, Chanhoi Kim, Yoon Seon Jeong, Bo-Ram Cho, Ji-Sook Hahn, and Jyongsik Jang. Cellular uptake, cytotoxicity, and innate immune response of silica and titania hollow nanoparticles based on size and surface functionality. *Acs Nano*, 4(9):5301–5313, 2010.

[76] Sweccha Joshi, Indrajit Ghosh, Suman Pokhrel, Lutz Mädler, and Werner M Nau. Interactions of amino acids and polypeptides with metal oxide nanoparticles probed by fluorescent indicator adsorption and displacement. *Acs Nano*, 6(6):5668–5679, June 2012.

[77] Mrinmoy De, Partha S Ghosh, and Vincent M Rotello. Applications of Nanoparticles in Biology. *Advanced Materials*, 20(22):4225–4241, 2008.

[78] Silvia H De Paoli SH Lacerda, Jung Jin JJ Park, Curt C Meuse, Denis D Pristinski, Matthew L ML Becker, Alamgir A Karim, and Jack F JF Douglas. Interaction of gold nanoparticles with common human blood proteins. *Acs Nano*, 4(1):365–379, January 2010.

[79] Anton A Shemetov, Igor Nabiev, and Alyona Sukhanova. Molecular interaction of proteins and peptides with nanoparticles. *Acs Nano*, 6(6):4585–4602, June 2012.

[80] Aihua A Liu, Mingdeng M Wei, Itaru I Honma, and Haoshen H Zhou. Direct electrochemistry of myoglobin in titanate nanotubes film. *Analytical Chemistry*, 77(24):8068–8074, December 2005.

[81] Peng Si, Shujiang Ding, Jun Yuan, Xiong Wen David Lou, and Dong-Hwan Kim. Hierarchically structured one-dimensional TiO_2 for protein immobilization, direct electrochemistry, and mediator-free glucose sensing. *Acs Nano*, 5(9):7617–7626, September 2011.

[82] Soumyananda Chakraborti, Tanaya Chatterjee, Prachi Joshi, Asim Poddar, Bhabatarak Bhattacharyya, Surinder P Singh, Vinay Gupta, and Pinak Chakrabarti. Structure and Activity of Lysozyme on Binding to ZnO Nanoparticles. *Langmuir*, 26:3506–3513, December 2009.

[83] Zhou J Deng, Gysell Mortimer, Tara Schiller, Anthony Musumeci, Darren Martin, and Rodney F Minchin. Differential plasma protein binding to metal oxide nanoparticles. *Zoom Lenses Iii*, 20(45):455101, November 2009.

[84] A B Faia-Torres, T Goren, M Textor, and M Pla-Roca. *4.413. Patterned Biointerfaces*. Elsevier Ltd., 2011.

[85] Jennifer E Gagner, Marimar D Lopez, Jonathan S Dordick, and Richard W Siegel. Effect of gold nanoparticle morphology on adsorbed protein structure and function. *Biomaterials*, 32(29):7241–7252, October 2011.

[86] Binghui Wang, Peng Wu, Robert A Yokel, and Eric A Grulke. Influence of surface charge on lysozyme adsorption to ceria nanoparticles. *Applied Surface Science*, 258(14):5332–5341, May 2012.

[87] Claudio Melis, Alessandro Mattoni, and Luciano Colombo. Atomistic Investigation of Poly(3-hexylthiophene) Adhesion on Nanostructured Titania. *Journal Of Physical*

Chemistry C, 114(8):3401–3406, March 2010.

[88] S Reiß, H Krumm, A Niklewski, V Staemmler, and Ch Wöll. The adsorption of acenes on rutile TiO[sub 2](110): A multi-technique investigation. *Journal Of Chemical Physics*, 116(17):7704, 2002.

[89] Selver S Ahmed and Stephanie L SL Wunder. Effect of high surface curvature on the main phase transition of supported phospholipid bilayers on SiO_2 nanoparticles. *Langmuir*, 25(6):3682–3691, April 2009.

[90] Frédéric A Denis, Antoine Pallandre, Bernard Nysten, Alain M Jonas, and Christine C Dupont-Gillain. Alignment and assembly of adsorbed collagen molecules induced by anisotropic chemical nanopatterns. *Small*, 1(10):984–991, October 2005.

[91] Celaletdin Ergun, Huinan Liu, John W Halloran, and Thomas J Webster. Increased osteoblast adhesion on nanograined hydroxyapatite and tricalcium phosphate containing calcium titanate. *Journal Of Biomedical Materials Research Part A*, 80(4):990–997, March 2007.

[92] Komkrit Suttiponparnit, Jingkun Jiang, Manoranjan Sahu, Sirikalaya Suvachittanont, Tawatchai Charinpanitkul, and Pratim Biswas. Role of surface area, primary particle size, and crystal phase on titanium dioxide nanoparticle dispersion properties. *Nanoscale Research Letters*, 6(1):27, 2011.

[93] Z V Saponjic, N M Dimitrijevic, D M Tiede, A J Goshe, X Zuo, L X Chen, A S Barnard, P Zapol, L Curtiss, and T Rajh. Shaping Nanometer-Scale Architecture Through Surface Chemistry. *Advanced Materials*, 17(8):965–971, April 2005.

[94] Ivana Fenoglio, Bice Fubini, Elena M Ghibaudi, and Francesco Turci. Multiple aspects of the interaction of biomacromolecules with inorganic surfaces. *Advanced Drug Delivery Reviews*, 63(13):1186–1209, October 2011.

[95] Kim E Sapsford, Katherine M Tyner, Benita J Dair, Jeffrey R Deschamps, and Igor L Medintz. Analyzing nanomaterial bioconjugates: a review of current and emerging purification and characterization techniques. *Analytical Chemistry*, 83(12):4453–4488, June 2011.

[96] George D Panagiotou, Theano Petsi, Kyriakos Bourikas, Christos S Garoufalis, Athanassios Tsevis, Nikos Spanos, Christos Kordulis, and Alexis Lycourghiotis. Mapping the surface (hydr)oxo-groups of titanium oxide and its interface with an aqueous solution: the state of the art and a new approach. *Advances in Colloid and Interface Science*, 142(1-2):20–42, October 2008.

[97] Stina Lindman, Iseult Lynch, Eva Thulin, Hanna Nilsson, Kenneth A Dawson, and Sara Linse. Systematic investigation of the thermodynamics of HSA adsorption to N-iso-propylacrylamide/N-tert-butylacrylamide copolymer nanoparticles. Effects of particle size and hydrophobicity. *Nano Letters*, 7(4):914–920, April 2007.

[98] C F CF Schmidt, R M RM Zimmermann, and H E HE Gaub. Multilayer adsorption of lysozyme on a hydrophobic substrate. *Biophysical Journal*, 57(3):12–12, March 1990.

[99] Mrinmoy De, Mrinmoy De, Oscar R Miranda, Oscar R Miranda, Subinoy Rana, Subinoy Rana, Vincent M Rotello, and Vincent M Rotello. Size and geometry dependent protein–nanoparticle self-assembly. *Chemical Communications*, (16):2157, 2009.

[100] T Cedervall, I Lynch, S Lindman, T Berggård, E Thulin, H Nilsson, K A Dawson, and S Linse. Understanding the nanoparticle–protein corona using methods to quantify exchange rates and affinities of proteins for nanoparticles. *Proceedings Of The National Academy Of Sciences Of The United States Of America-physical Sciences*, 104(7):2050–2055, 2007.

[101] Eric N EN Salgado, Robert J RJ Radford, and F Akif FA Tezcan. Metal-directed protein self-assembly. *Accounts Of Chemical Research*, 43(5):661–672, May 2010.

[102] Eric N EN Salgado, Richard A RA Lewis, Jasmin J Faraone-Mennella, and F Akif FA Tezcan. Metal-mediated self-assembly of protein superstructures: influence of secondary interactions on protein oligomerization and aggregation. *Journal Of The American Chemical Society*, 130(19):6082–6084, May 2008.

[103] Eric N EN Salgado, Xavier I XI Ambroggio, Jeffrey D JD Brodin, Richard A RA Lewis, Brian B Kuhlman, and F Akif FA Tezcan. Metal templated design of protein interfaces. *Proceedings Of The National Academy Of Sciences Of The United States Of America-physical Sciences*, 107(5):1827–1832, February 2010.

[104] S J Archibald and R Smith. *3.22 Protein-Binding Metal Complexes: Noncovalent and Coordinative Interactions*. Elsevier Ltd., 2013.

[105] Stephen Mann. Self-assembly and transformation of hybrid nano-objects and nanostructures under equilibrium and non-equilibrium conditions. *Nature Materials*, 8(10):781–792, September 2009.

[106] Sara Linse, Celia Cabaleiro-Lago, Wei-Feng Xue, Iseult Lynch, Stina Lindman, Eva Thulin, Sheena E Radford, and Kenneth A Dawson. Nucleation of protein fibrillation by nanoparticles. *Proceedings Of The National Academy Of Sciences Of The United*

States Of America-physical Sciences, 104(21):8691–8696, May 2007.

[107] Zhi-You ZY Zhou, Na N Tian, Jun-Tao JT Li, Ian I Broadwell, and Shi-Gang SG Sun. Nanomaterials of high surface energy with exceptional properties in catalysis and energy storage. *Chemical Society Reviews*, 40(7):4167–4185, July 2011.

[108] Manish Sethi, Dennis B Pacardo, and Marc R Knecht. Biological Surface Effects of Metallic Nanomaterials for Applications in Assembly and Catalysis. *Langmuir*, pages 15121–15134, March 2010.

[109] Daniel F DF Moyano and Vincent M VM Rotello. Nano meets biology: structure and function at the nanoparticle interface. *Langmuir*, 27(17):10376–10385, September 2011.

[110] Lily Peng, Adam D Mendelsohn, Thomas J LaTempa, Sorachon Yoriya, Craig A Grimes, and Tejal A Desai. Long-Term Small Molecule and Protein Elution from TiO 2Nanotubes. *Nano Letters*, 9(5):1932–1936, May 2009.

[111] Gregory Mogilevsky, Qiang Chen, Harsha Kulkarni, Alfred Kleinhammes, William M Mullins, and Yue Wu. Layered Nanostructures of Delaminated Anatase: Nanosheets and Nanotubes. *Journal Of Physical Chemistry C*, 112(9):3239–3246, March 2008.

[112] Gregory Mogilevsky, Qiang Chen, Alfred Kleinhammes, and Yue Wu. The structure of multilayered titania nanotubes based on delaminated anatase. *Chemical Physics Letters*, 460(4-6):517–520, July 2008.

[113] Qiang Chen, Gregory Mogilevsky, George W Wagner, Jacob Forstater, Alfred Kleinhammes, and Yue Wu. Active anatase (001)-like surface of hydrothermally synthesized titania nanotubes. *Chemical Physics Letters*, 482(1):134–138, 2009.

[114] P R Connelly, P R Connelly, J A Thomson, J A Thomson, M J Fitzgibbon, M J Fitzgibbon, F J Bruzzese, and F J Bruzzese. Probing hydration contributions to the thermodynamics of ligand binding by proteins. Enthalpy and heat capacity changes of tacrolimus and rapamycin binding to FK506 binding protein in D2O and H2O. *Water Relationships in Foods*, 32(21):5583–5590, June 1993.

[115] M Gerstein and C Chothia. Packing at the protein-water interface. *Proceedings Of The National Academy Of Sciences Of The United States Of America-physical Sciences*, 93(19):10167–10172, September 1996.

[116] K B Wong, T H Yu, and C H Chan. *3.2 Energetics of Protein Folding*. Elsevier Ltd., February 2012.

[117] J N Israelachvili. *Intermolecular and Surface Forces*. Intermolecular and Surface Forces. Elsevier Science, Burlington, MA, 3rd edition, 2011.

[118] Ian D Morrison and Sydney Ross. *Colloidal Dispersions*. Suspensions, Emulsions, and Foams. Wiley-Interscience, March 2002.

[119] T W Hutchens and T T Yip. Protein interactions with surface-immobilized metal ions: structure-dependent variations in affinity and binding capacity with temperature and urea concentration. *Journal Of Inorganic Biochemistry*, 42(2):105–118, 1991.

[120] Xiguang X Han, Qin Q Kuang, Mingshang M Jin, Zhaoxiong Z Xie, and Lansun L Zheng. Synthesis of titania nanosheets with a high percentage of exposed (001) facets and related photocatalytic properties. *Journal Of The American Chemical Society*, 131(9):3152–3153, March 2009.

[121] Robin Jon Hawes Clark. *The chemistry of titanium and vanadium.* An introduction to the chemistry of the early transition elements. Elsevier, Amsterdam, 1968.

[122] 21CFR72.3575: Listing of Color Additives Exempt from Certification . 1(73.3575):384, April 2012.

[123] A A Fujishima and K K Honda. Electrochemical photolysis of water at a semiconductor electrode. *Nature*, 238(5358):37–38, July 1972.

[124] Ulrike Diebold. The surface science of titanium dioxide. *Surface Science Reports*, 48(5):53–229, 2003.

[125] A Vittadini, A Selloni, F P Rotzinger, and M Grätzel. Structure and Energetics of Water Adsorbed at TiO_2 Anatase (101) and (001) Surfaces. *Physical Review Letters*, 81(14):2954–2957, October 1998.

[126] Maurizio Casarin, Andrea Vittadini, and Annabella Selloni. First principles study of hydrated/hydroxylated TiO_2 nanolayers: from isolated sheets to stacks and tubes. *Acs Nano*, 3(2):317–324, February 2009.

[127] Dmitry V Bavykin, Marina Carravetta, Alexander N Kulak, and Frank C Walsh. Application of Magic-Angle Spinning NMR to Examine the Nature of Protons in Titanate Nanotubes. *Chemistry Of Materials*, 22(8):2458–2465, April 2010.

[128] Robert Menzel, Andre Duerrbeck, Emanuela Liberti, Hin Chun Yau, David McComb, and Milo S P Shaffer. Determining the Morphology and Photocatalytic Activity of Two-Dimensional Anatase Nanoplatelets Using Reagent Stoichiometry. *Chemistry*

Of Materials, 25(10):2137–2145, May 2013.

[129] Dimitry V Bavykin and Frank C Walsh. *Titanate and Titania Nanotubes*. Synthesis, Properties and Applications. Royal Society of Chemistry, 2010.

[130] Edson Roberto Leite and Caue Ribeiro. Trends and Perspectives in Nanoparticles Synthesis. In *Crystallization and growth of colloidal nanocrystals*, pages 83–92. Springer New York, New York, NY, October 2011.

[131] Dmitry V Bavykin, Alexander N Kulak, and Frank C Walsh. Control over the hierarchical structure of titanate nanotube agglomerates. *Langmuir*, 27(9):5644–5649, May 2011.

[132] C N R Rao, Achim M ller, and Anthony K Cheetham. *Nanomaterials Chemistry*. Recent Developments and New Directions. John Wiley & Sons, September 2007.

[133] D V Bavykin, J M Friedrich, and F C Walsh. Protonated Titanates and TiO_2 Nanostructured Materials: Synthesis, Properties, and Applications. *Advanced Materials*, 18(21):2807–2824, November 2006.

[134] Johan Buitenhuis, Jan K G Dhont, and Henk N W Lekkerkerker. Static and Dynamic Light Scattering by Concentrated Colloidal Suspensions of Polydisperse Sterically Stabilized Boehmite Rods. *The Journal of Physical Chemistry C*, 27(25):7267–7277, November 2001.

[135] Philippe Knauth and Joop Schoonman. *Nanocrystalline Metals and Oxides*. Selected Properties and Applications. Springer, January 2002.

[136] Robert J Hunter. *Foundations of Colloid Science*. Oxford University Press, Oxford; New York, 2nd edition, 2001.

[137] Hans-J rgen Butt and Michael Kappl. *Surface and Interfacial Forces*. John Wiley & Sons, December 2009.

[138] Hans-J rgen Butt, Karlheinz Graf, and Michael Kappl. *Physics and Chemistry of Interfaces*. John Wiley & Sons, March 2006.

[139] Hiroyuki Ohshima. *Biophysical Chemistry of Biointerfaces*. Wiley, May 2010.

[140] G Lagaly and I Dekany. *Colloid Clay Science*, volume 5. Elsevier Ltd., 2 edition, 2013.

[141] Rongjun Pan and Kongyong Liew. Isoelectric Point of Nanoaprticles. In Klaus D Sattler, editor, *Handbook of Nanophysics*. CRC Press, Boca Raton, September 2010.

[142] R Aveyard, B P Binks, and J H Clint. Emulsions stabilised solely by colloidal particles. *Advances in Colloid and Interface Science*, 100:503–546, 2003.

[143] B P Binks. Particles as surfactants—similarities and differences. *Current Opinion in Colloid & Interface Science*, 7(1):21–41, 2002.

[144] Laurier L Schramm. *Emulsions, Foams, and Suspensions*. John Wiley & Sons, May 2006.

[145] Xue-Qing XQ Gong and Annabella A Selloni. Reactivity of anatase TiO(2) nanoparticles: the role of the minority (001) surface. *Journal Of Physical Chemistry B*, 109(42):19560–19562, October 2005.

[146] Klaus D Sattler. *Handbook of Nanophysics*, volume 2 of *Nanoparticles and Quantum Dots*. CRC Press, Boca Raton, 1 edition, September 2010.

[147] Guangshe G Li, Liping L Li, Juliana J Boerio-Goates, and Brian F BF Woodfield. High purity anatase TiO(2) nanocrystals: near room-temperature synthesis, grain growth kinetics, and surface hydration chemistry. *Journal Of The American Chemical Society*, 127(24):8659–8666, June 2005.

[148] Xiao Hua Yang, Zhen Li, Gang Liu, Jun Xing, Chenghua Sun, Hua Gui Yang, and Chunzhong Li. Ultra-thin anatase TiO_2 nanosheets dominated with 001 facets: thickness-controlled synthesis, growth mechanism and water-splitting properties. *Crystengcomm*, 13(5):1378, 2011.

[149] J R Rustad. Molecular Models of Surface Relaxation, Hydroxylation, and Surface Charging at Oxide-Water Interfaces. *Reviews in Mineralogy and Geochemistry*, 42(1):169–198, January 2001.

[150] Dénes Szieberth, Anna Maria Ferrari, Yves Noel, and Matteo Ferrabone. Ab initio modeling of TiO_2 nanotubes. *Nanoscale*, 2(1):81–89, January 2010.

[151] Michel Posternak, Alfonso Baldereschi, and Bernard Delley. Dissociation of Water on Anatase TiO_2 Nanoparticles: the Role of Undercoordinated Ti Atoms at Edges. *Journal Of Physical Chemistry C*, 113(36):15862–15867, September 2009.

[152] Javier Soria, Jesus Sanz, Isabel Sobrados, Juan M Coronado, A Javier Maira, Maria D Hernandez-Alonso, and Fernando Fresno. FTIR and NMR Study of the Ad-

sorbed Water on Nanocrystalline Anatase. *Journal Of Physical Chemistry C*, 111(28):10590–10596, July 2007.

[153] J L G Fierro. *Metal Oxides*. Chemistry and Applications. CRC Press, December 2010.

[154] S Koppen and W Langel. Adsorption of small organic molecules on anatase and rutile surfaces: a theoretical study. *Physical Chemistry Chemical Physics*, 10(14):1907–1915, 2008.

[155] Yunbin Y He, Antonio A Tilocca, Olga O Dulub, Annabella A Selloni, and Ulrike U Diebold. Local ordering and electronic signatures of submonolayer water on anatase TiO_2(101). *Nature Materials*, 8(7):585–589, July 2009.

[156] Xue-Qing Gong, Annabella Selloni, Matthias Batzill, and Ulrike Diebold. Steps on anatase TiO_2(101). *Nature Materials*, 5(8):665–670, August 2006.

[157] Hua Gui HG Yang, Cheng Hua CH Sun, Shi Zhang SZ Qiao, Jin J Zou, Gang G Liu, Sean Campbell SC Smith, Hui Ming HM Cheng, and Gao Qing GQ Lu. Anatase TiO_2 single crystals with a large percentage of reactive facets. *Nature*, 453(7195):638–641, May 2008.

[158] Sencer Selçuk and Annabella Selloni. Surface Structure and Reactivity of Anatase TiO 2Crystals with Dominant 001 Facets. *Journal Of Physical Chemistry C*, 117(12):6358–6362, March 2013.

[159] Francesca Nunzi and Filippo De Angelis. DFT Investigations of Formic Acid Adsorption on Single-Wall TiO_2 Nanotubes: Effect of the Surface Curvature. *Journal Of Physical Chemistry C*, 115(5):2179–2186, February 2011.

[160] Masato Sumita, Chunping Hu, and Yoshitaka Tateyama. Interface Water on TiO_2 Anatase (101) and (001) Surfaces: First-Principles Study with TiO 2Slabs Dipped in Bulk Water. *Journal Of Physical Chemistry C*, 114(43):18529–18537, November 2010.

[161] Anna M Ferrari, M Lessio, D Szieberth, and L Maschio. On the Stability of Dititanate Nanotubes: A Density Functional Theory Study. *Journal Of Physical Chemistry C*, 114(49):21219–21225, 2010.

[162] A Vittadini, A Selloni, F P Rotzinger, and M Grätzel. Formic Acid Adsorption on Dry and Hydrated TiO 2Anatase (101) Surfaces by DFT Calculations. *Journal Of Physical Chemistry B*, 104(6):1300–1306, February 2000.

[163] Chenghua Sun, Li-Min Liu, Annabella Selloni, Gao Qing Max Lu, and Sean C Smith. Titania-water interactions: a review of theoretical studies. *Journal Of Materials Chemistry*, 20(46):10319–10334, 2010.

[164] Chuan-yi Wang, Henning Groenzin, and Mary Jane Shultz. Comparative Study of Acetic Acid, Methanol, and Water Adsorbed on Anatase TiO_2 Probed by Sum Frequency Generation Spectroscopy. *Journal Of The American Chemical Society*, 127(27):9736–9744, July 2005.

[165] Andrew G Thomas and Karen L Syres. Adsorption of organic molecules on rutile TiO_2 and anatase TiO_2 single crystal surfaces. *Chemical Society Reviews*, 41(11):4207–4217, June 2012.

[166] Michele Lazzeri and Annabella Selloni. Stress-Driven Reconstruction of an Oxide Surface: The Anatase TiO_2(001)-(1 ÃŮ 4) Surface. *Physical Review Letters*, 87(26):266105, December 2001.

[167] Melinda J Duer. *Solid State NMR Spectroscopy*. Principles and Applications. John Wiley & Sons, April 2008.

[168] Duncan W Bruce, Dermot O'Hare, and Richard I Walton. *Local Structural Characterisation*. Inorganic Materials Series. John Wiley & Sons, July 2013.

[169] Melinda J Duer. *Introduction to Solid-State NMR Spectroscopy*. Wiley-Blackwell, 2004.

[170] Michael Hunger and Eike Brunner. NMR spectroscopy. pages 201–293, 2004.

[171] E Brunner. Solid state NMR—a powerful tool for the investigation of surface hydroxyl groups in zeolites and their interactions with adsorbed probe molecules. *Journal Of Molecular Structure*, 355(1):61–85, 1995.

[172] Mark Crocker, Ruud H M Herold, Antonio E Wilson, Munro Mackay, Cees A Emeis, and Alda M Hoogendoorn. 1H NMR spectroscopy of titania. Chemical shift assignments for hydroxy groups in crystalline and amorphous forms of TiO_2. *J Chem Soc Faraday Trans*, 92(15):2791–2798, 1996.

[173] J H De Boer. *The dynamical character of adsorption*. Clarendon Press, Oxford, 2 edition, 1968.

[174] A Y Nosaka, T Fujiwara, H Yagi, H Akutsu, and Y Nosaka. Characteristics of water adsorbed on TiO_2 photocatalytic systems with increasing temperature as studied by

solid-state 1H NMR spectroscopy. *Journal Of Physical Chemistry B*, 108(26):9121–9125, 2004.

[175] Tijana Rajh, Zoran Saponjic, Jianqin Liu, Nada M Dimitrijevic, Norbert F Scherer, Manuel Vega-Arroyo, Peter Zapol, Larry A Curtiss, and Marion C Thurnauer. Charge Transfer Across the Nanocrystalline-DNA Interface: Probing DNA Recognition. *Nano Letters*, 4(6):1017–1023, June 2004.

[176] Qiang Chen, Yuanyuan Jia, Shubin Liu, Gregory Mogilevsky, Alfred Kleinhammes, and Yue Wu. Molecules Immobilization in Titania Nanotubes: A Solid-State NMR and Computational Chemistry Study. *Journal Of Physical Chemistry C*, 112(44):17331–17335, November 2008.

[177] Susan Köppen, Oliver Bronkalla, and Walter Langel. Adsorption Configurations and Energies of Amino Acids on Anatase and Rutile Surfaces. *Journal Of Physical Chemistry C*, 112(35):13600–13606, September 2008.

[178] Y Jia, A Kleinhammes, and H Kulkarni. Synthesis and characterization of TiO_2 nanotube/hydroquinone hybrid structure. *Journal Of Nanoscience and Nanotechnology*, 2007.

[179] Michael R MR Duff and Challa V CV Kumar. Protein-solid interactions: important role of solvent, ions, temperature, and buffer in protein binding to alpha-Zr(IV) phosphate. *Langmuir*, 25(21):12635–12643, November 2009.

[180] Erwin A Vogler. Protein adsorption in three dimensions. *Biomaterials*, 33(5):1201–1237, February 2012.

[181] F Hook, M Rodahl, B Kasemo, and P Brzezinski. Structural changes in hemoglobin during adsorption to solid surfaces: Effects of pH, ionic strength, and ligand binding. *Proceedings Of The National Academy Of Sciences Of The United States Of America-physical Sciences*, 95(21):12271–12276, October 1998.

[182] MarÄśÌĄa Tirado-Miranda, MarÄśÌĄa Tirado-Miranda, Artur Schmitt, Artur Schmitt, José Callejas-Fernández, José Callejas-Fernández, Antonio Fernández-Barbero, and Antonio Fernández-Barbero. Aggregation of protein-coated colloidal particles: Interaction energy, cluster morphology, and aggregation kinetics. *Journal Of Chemical Physics*, 119(17):9251, 2003.

[183] Karina Kubiak-Ossowska, Karina Kubiak-Ossowska, Paul A Mulheran, and Paul A Mulheran. Protein Diffusion and Long-Term Adsorption States at Charged Solid Surfaces. *Langmuir*, 28(44):15577–15585, November 2012.

[184] Ariane Proteau, Nicole Welsch, Rong Shi, Alisa L Becker, Miroslaw Cygler, Joachim Dzubiella, and Matthias Ballauff. Core–shell microgels as "smart" carriers for enzymes. *Soft Matter*, 8(5):1428, 2012.

[185] Nicole Welsch, Nicole Welsch, Joachim Dzubiella, Joachim Dzubiella, Alexandra Graebert, Alexandra Graebert, Matthias Ballauff, and Matthias Ballauff. Protein binding to soft polymeric layers: a quantitative study by fluorescence spectroscopy. *Soft Matter*, 8(48):12043, 2012.

[186] María Tirado-Miranda, Artur Schmitt, José Callejas-Fernández, and Antonio Fernández-Barbero. The aggregation behaviour of protein-coated particles: a light scattering study. *European Biophysics Journal*, 32(2):128–136, April 2003.

[187] Alisa L Becker, Alisa L Becker, Nicole Welsch, Nicole Welsch, Christian Schneider, Christian Schneider, Matthias Ballauff, and Matthias Ballauff. Adsorption of RNase A on Cationic Polyelectrolyte Brushes: A Study by Isothermal Titration Calorimetry. *Biomacromolecules*, 12(11):3936–3944, November 2011.

[188] N Podhipleux, V Krisdhasima, and J McGuire. Molecular charge effects on protein behavior at hydrophobic and hydrophilic solid surfaces. *Food Hydrocolloids*, 1996.

[189] A Gessner, R Waicz, A Lieske, B R Paulke, K Mäder, and R H Müller. Nanoparticles with decreasing surface hydrophobicities: influence on plasma protein adsorption. *International Journal Of Pharmaceutics*, 196(2):245–249, March 2000.

[190] Jędrzej Szymański, Jędrzej Szymański, Ewa Poboży, Ewa Poboży, Marek Trojanowicz, Marek Trojanowicz, Agnieszka Wilk, Agnieszka Wilk, Piotr Garstecki, Piotr Garstecki, Robert Hołyst, and Robert Hołyst. Net Charge and Electrophoretic Mobility of Lysozyme Charge Ladders in Solutions of Nonionic Surfactant. *Journal Of Physical Chemistry B*, 111(19):5503–5510, May 2007.

[191] E Córdova, J Gao, and G M Whitesides. Noncovalent polycationic coatings for capillaries in capillary electrophoresis of proteins. *Analytical Chemistry*, 69(7):1370–1379, April 1997.

[192] Xiuli Dong, Xiuli Dong, Qi Wang, Qi Wang, Tao Wu, Tao Wu, Haihua Pan, and Haihua Pan. Understanding Adsorption-Desorption Dynamics of BMP-2 on Hydroxyapatite (001) Surface. *Biophysical Journal*, 93(3):750–759, August 2007.

[193] T Arai and W Norde. The behavior of some model proteins at solid-liquid interfaces 1. Adsorption from single protein solutions. *Colloids and Surfaces*, 51:1–15, 1990.

[194] Karina Kubiak-Ossowska, Karina Kubiak-Ossowska, Paul A Mulheran, and Paul A Mulheran. Mechanism of Hen Egg White Lysozyme Adsorption on a Charged Solid Surface. *Langmuir*, 26(20):15954–15965, October 2010.

[195] Jian R Lu, Jian R Lu, Marcus J Swann, Marcus J Swann, Louise L Peel, Louise L Peel, Neville J Freeman, and Neville J Freeman. Lysozyme Adsorption Studies at the Silica/Water Interface Using Dual Polarization Interferometry. *Langmuir*, 20(5):1827–1832, March 2004.

[196] Tamer Al Kayal, Tamer Al Kayal, Silvia Nappini, Silvia Nappini, Edda Russo, Edda Russo, Debora Berti, Debora Berti, Monica Bucciantini, Monica Bucciantini, Massimo Stefani, Massimo Stefani, Piero Baglioni, and Piero Baglioni. Lysozyme interaction with negatively charged lipid bilayers: protein aggregation and membrane fusion. *Soft Matter*, 8(16):4524, 2012.

[197] Silvia Milani, Silvia Milani, Francesca Baldelli Bombelli, Francesca Baldelli Bombelli, Andrzej S Pitek, Andrzej S Pitek, Kenneth A Dawson, Kenneth A Dawson, Joachim Rädler, and Joachim Rädler. Reversible versusIrreversible Binding of Transferrin to Polystyrene Nanoparticles: Soft and Hard Corona. *Acs Nano*, 6(3):2532–2541, March 2012.

[198] S R Sousa, S R Sousa, P Moradas-Ferreira, P Moradas-Ferreira, B Saramago, B Saramago, L Viseu Melo, L Viseu Melo, M A Barbosa, and M A Barbosa. Human Serum Albumin Adsorption on TiO 2from Single Protein Solutions and from Plasma. *Langmuir*, 20(22):9745–9754, October 2004.

[199] Christopher M Wijmans and Eric Dickinson. Brownian dynamics simulation of a bonded network of reversibly adsorbed particles: Towards a model of protein adsorbed layers. *Physical Chemistry Chemical Physics*, 1(9):2141–2147, 1999.

[200] Ronald T Raines. Ribonuclease A. *Chemical Reviews*, 98(3):1045–1066, May 1998.

[201] James D Gunton, Andrey Shiryayev, and Daniel L Pagan. *Protein Condensation*. Kinetic Pathways to Crystallization and Disease. Cambridge University Press, September 2007.

[202] József Tóth. *Adsorption*, volume 107 of *Theory, Modeling, and Analysis*. CRC Press, May 2002.

[203] George W Wagner, Qiang Chen, and Yue Wu. Reactions of VX, GD, and HD with Nanotubular Titania. *Journal Of Physical Chemistry C*, 112(31):11901–11906, August 2008.

[204] T V Chalikian, M Totrov, R Abagyan, and K J Breslauer. The hydration of globular proteins as derived from volume and compressibility measurements: cross correlating thermodynamic and structural data. *Journal Of Molecular Biology*, 260(4):588–603, July 1996.

[205] S Vijay-Kumar, C E Bugg, K D Wilkinson, and W J Cook. Three-dimensional structure of ubiquitin at 2.8 A resolution. *Proceedings Of The National Academy Of Sciences Of The United States Of America-physical Sciences*, 1985.

[206] Martin Malmsten. *Biopolymers at interfaces / edited by Martin Malmsten*. Marcel Dekker, New York, 2nd edition, 2003.

[207] Richard B McClurg and Charles F Zukoski. The Electrostatic Interaction of Rigid, Globular Proteins with Arbitrary Charge Distributions. *Journal Of Colloid and Interface Science*, 208(2):529–542, December 1998.

[208] Gary L Hunter and Eric R Weeks. The physics of the colloidal glass transition. *Reports On Progress in Physics*, 75(6):066501, May 2012.

[209] Shannon E Hill, Joshua Robinson, Garrett Matthews, and Martin Muschol. Amyloid Protofibrils of Lysozyme Nucleate and Grow Via Oligomer Fusion. *Biophysical Journal*, 96(9):3781–3790, May 2009.

[210] Jeremy D Schmit, Kingshuk Ghosh, and Ken Dill. What Drives Amyloid Molecules To Assemble into Oligomers and Fibrils? *Biophysical Journal*, 100(2):450–458, January 2011.

[211] Alisa L Becker, A Stradner, Nicole Welsch, H Sedgwick, Christian Schneider, F Cardinaux, Matthias Ballauff, W C K Poon, S U Egelhaaf, and P Schurtenberger. Equilibrium cluster formation in concentrated protein solutions and colloids. *Nature*, 432(7016):492–495, 2004.

[212] Marek M Grzelczak, Jan J Vermant, Eric M EM Furst, and Luis M LM Liz-Marzán. Directed self-assembly of nanoparticles. *Acs Nano*, 4(7):3591–3605, July 2010.

[213] C R Iacovella, A S Keys, and S C Glotzer. Self-assembly of soft-matter quasicrystals and their approximants. *Proceedings Of The National Academy Of Sciences Of The United States Of America-physical Sciences*, 108(52):20935–20940, December 2011.

[214] T A Klink, K J Woycechowsky, K M Taylor, and R T Raines. Contribution of disulfide bonds to the conformational stability and catalytic activity of ribonuclease A. *European Journal Of Biochemistry*, 267(2):566–572, January 2000.

[215] Jan Groenewold, Jan Groenewold, Willem K Kegel, and Willem K Kegel. Anomalously Large Equilibrium Clusters of Colloids. *Journal Of Physical Chemistry B*, 105(47):11702–11709, November 2001.

[216] V Gopalakrishnan and C Zukoski. Microstructure of equilibrium fluid clusters in colloid-polymer suspensions. *Physical Review E*, 75(2):021406, February 2007.

[217] Per Linse and Håkan Wennerström. Adsorption versus aggregation. Particles and surface of the same material. *Soft Matter*, 8(8):2486–2493, 2012.

[218] D T Kim, H W Blanch, and C J Radke. Direct imaging of lysozyme adsorption onto mica by atomic force microscopy. *Langmuir*, 18(15):5841–5850, 2002.

[219] A Bentaleb, V Ball, Y Haikel, J C Voegel, and P Schaaf. Kinetics of the homogeneous exchange of lysozyme adsorbed on a titanium oxide surface. *Langmuir*, 13(4):729–735, 1997.

[220] Beatriz M Brena and Francisco Batista-Viera. Methods in Biotechnology. In Jose M Guisan, editor, *Immobilization of Enzymes and Cells*, pages 15–30. Humana Press, Totowa, 2006.

[221] I Lundström and H Elwing. Simple kinetic models for protein exchange reactions on solid surfaces. *Journal Of Colloid and Interface Science*, 136(1):68–84, 1990.

[222] Ananthakrishnan Sethuraman, Ananthakrishnan Sethuraman, Ganesh Vedantham, Ganesh Vedantham, Taiji Imoto, Taiji Imoto, Todd Przybycien, Todd Przybycien, Georges Belfort, and Georges Belfort. *Protein unfolding at interfaces: Slow dynamics of α-helix to β-sheet transition*, volume 56, pages 669–678. June 2004.

[223] T Arnebrant, T Arnebrant, M C Wahlgren, and M C Wahlgren. Protein surfactant interactions at solid surfaces. *Xenobiotics and Food-producing Animals*, 602:239–254, 1995.

[224] Gurvinder Singh, Vipul Gohri, Saju Pillai, Ayyoob Arpanaei, Morten Foss, and Peter Kingshott. Large-area protein patterns generated by ordered binary colloidal assemblies as templates. *Acs Nano*, 5(5):3542–3551, May 2011.

[225] Peter A Kralchevsky, Krassimir D Danov, and Nikolai D Denkov. Chemical physics of colloid systems and interfaces. In *Handbook of Applied Surface and Colloid Chemistry*, volume 2, chapter Chemical Physics of Colloidal Systems and Interfaces. CRC Press LLS: Boca Raton, 2009.

[226] Muhammad Najam-ul Haq, Fahmida Jabeen, Dilshad Hussain, Adeela Saeed, Syed Ghulam Musharraf, Christian W Huck, and Günther K Bonn. Versatile nanocomposites in phosphoproteomics: A review. *Analytica Chimica Acta*, 747:7–18, October 2012.

[227] Shih-Shin Liang, Honest Makamba, Shang-Yu Huang, and Shu-Hui Chen. Nano-titanium dioxide composites for the enrichment of phosphopeptides. *Journal Of Chromatography A*, 1116(1-2):38–45, May 2006.

[228] N A Kotov. Inorganic Nanoparticles as Protein Mimics. *Science*, 330(6001):188–189, October 2010.

[229] Sung Tae Kim, Krishnendu Saha, Chaekyu Kim, and Vincent M Rotello. The Role of Surface Functionality in Determining Nanoparticle Cytotoxicity. *Accounts Of Chemical Research*, page 130107091843000, January 2013.

[230] R M Vallant, M Rainer, M NAJAM-UL-HAQ, R Bakry, C Petter, N Heigl, G K Bonn, and C W Huck. *Biosensing Using Nanomaterials*, chapter Nanostructured Affinity Surfaces for MALDI-TOF-MS–Based Protein Profiling and Biomarker Discovery, page 421. Wiley-Interscience, 2009.

[231] Atsushi Hirano, Atsushi Hirano, Yutaka Maeda, Yutaka Maeda, Xiaofei Yuan, Xiaofei Yuan, Ryuuichi Ueki, Ryuuichi Ueki, Yosuke Miyazawa, Yosuke Miyazawa, Jun-ichi Fujita, Jun-ichi Fujita, Takeshi Akasaka, Takeshi Akasaka, Kentaro Shiraki, and Kentaro Shiraki. Controlled Dispersion and Purification of Protein-Carbon Nanotube Conjugates Using Guanidine Hydrochloride. *Chem – Eur J*, 16(40):12221–12228, September 2010.

[232] Nina Kovalchuk, Nina Kovalchuk, Victor Starov, Victor Starov, Paul Langston, Paul Langston, Nidal Hilal, and Nidal Hilal. Formation of stable clusters in colloidal suspensions. *Advances in Colloid and Interface Science*, 147-148(C):144–154, March 2009.

[233] Rachel M Greer, Brittni A Scruggs, R Alan May, and Bert D Chandler. Patterning High Surface Area Silica with Lysozyme: Adsorption Kinetics, Fluorescence Quenching, and Protein Readsorption Studies To Evaluate the Templated Surface. *Langmuir*, 25(12):7161–7168, June 2009.

[234] Atsushi A Hirano, Ken K Uda, Yutaka Y Maeda, Takeshi T Akasaka, and Kentaro K Shiraki. One-dimensional protein-based nanoparticles induce lipid bilayer disruption: carbon nanotube conjugates and amyloid fibrils. *Langmuir*, 26(22):17256–17259, November 2010.

[235] Julia S Gebauer, Julia S Gebauer, Marcelina Malissek, Marcelina Malissek, Sonja Simon, Sonja Simon, Shirley K Knauer, Shirley K Knauer, Michael Maskos, Michael Maskos, Roland H Stauber, Roland H Stauber, Wolfgang Peukert, Wolfgang Peukert, Lennart Treuel, and Lennart Treuel. Impact of the Nanoparticle–Protein Corona on Colloidal Stability and Protein Structure. *Langmuir*, 28(25):9673–9679, June 2012.

[236] Mandeep Singh Bakshi, Mandeep Singh Bakshi, Harpreet Kaur, Harpreet Kaur, Tarlok Singh Banipal, Tarlok Singh Banipal, Narpinder Singh, Narpinder Singh, Gurinder Kaur, and Gurinder Kaur. Biomineralization of Gold Nanoparticles by Lysozyme and Cytochrome c and Their Applications in Protein Film Formation. *Langmuir*, 26(16):13535–13544, August 2010.

[237] Andrea Bellova, Andrea Bellova, Eva Bystrenova, Eva Bystrenova, Martina Koneracka, Martina Koneracka, Peter Kopcansky, Peter Kopcansky, Francesco Valle, Francesco Valle, Natalia Tomasovicova, Natalia Tomasovicova, Milan Timko, Milan Timko, Jaroslava Bagelova, Jaroslava Bagelova, Fabio Biscarini, Fabio Biscarini, Zuzana Gazova, and Zuzana Gazova. Effect of Fe 3O 4magnetic nanoparticles on lysozyme amyloid aggregation. *Zoom Lenses Iii*, 21(6):065103, January 2010.

[238] Bhuvnesh Bharti, Bhuvnesh Bharti, Jens Meissner, Jens Meissner, Gerhard H Findenegg, and Gerhard H Findenegg. Aggregation of Silica Nanoparticles Directed by Adsorption of Lysozyme. *Langmuir*, 27(16):9823–9833, August 2011.

[239] Li Fei and Sarah Perrett. Effect of Nanoparticles on Protein Folding and Fibrillogenesis. *International Journal Of Molecular Sciences*, 10(2):646–655, February 2009.

[240] Zhou J Deng, Mingtao Liang, Michael Monteiro, Istvan Toth, and Rodney F Minchin. Nanoparticle-induced unfolding of fibrinogen promotes Mac-1 receptor activation and inflammation. *Nature Nanotechnology*, 6(1):39–44, 2010.

[241] Dongmao Zhang, Oara Neumann, Hui Wang, Virany M Yuwono, Aoune Barhoumi, Michael Perham, Jeffrey D Hartgerink, Pernilla Wittung-Stafshede, and Naomi J Halas. Gold nanoparticles can induce the formation of protein-based aggregates at physiological pH. *Nano Letters*, 9(2):666–671, February 2009.

[242] Smita Raghava, Smita Raghava, Pradeep K Singh, Pradeep K Singh, A Ranga Rao, A Ranga Rao, V Dutta, V Dutta, Munishwar N Gupta, and Munishwar N Gupta. Nanoparticles of unmodified titanium dioxide facilitate protein refolding. *Journal Of Materials Chemistry*, 19(18):2830, 2009.

[243] Martin Lundqvist, Ingmar Sethson, and Bengt-Harald Jonsson. Transient Interaction with Nanoparticles "Freezes" a Protein in an Ensemble of Metastable Near-Native

Conformations âĂă. *Water Relationships in Foods*, 44(30):10093–10099, August 2005.

[244] R John Ellis and Allen P Minton. Protein aggregation in crowded environments. *Biological Chemistry*, 387(5):485–497, 2006.

[245] Allen P Minton and Allen P Minton. Models for Excluded Volume Interaction between an Unfolded Protein and Rigid Macromolecular Cosolutes: Macromolecular Crowding and Protein Stability Revisited. *Biophysical Journal*, 88(2):971–985, February 2005.

[246] Maria M Holmberg and Xiaolin X Hou. Competitive protein adsorption–multilayer adsorption and surface induced protein aggregation. *Langmuir*, 25(4):2081–2089, February 2009.

[247] Bruce J Berne and Robert Pecora. *Dynamic Light Scattering : With Applications to Chemistry, Biology, and Physics*. Wiley, New York, 1976.

[248] K S Schmitz. *An Introduction to Dynamic Light Scattering by Macromolecules*. Academic Press, Boston, 1990.

[249] M A Tracy and R Pecora. Dynamics of Rigid and Semirigid Rodlike Polymers. *Annual Review Of Physical Chemistry*, 43(1):525–557, October 1992.

[250] M A Castanho, W Brown, and M J Prieto. Rod-like cholesterol micelles in aqueous solution studied using polarized and depolarized dynamic light scattering. *Biophysical Journal*, 63(6):1455–1461, December 1992.

[251] S Broersma. Rotational diffusion constant of a cylindrical particle. *Journal Of Chemical Physics*, 32:1626, 1960.

[252] Seymour H. Koenig. Brownian motion of an ellipsoid. a correction to perrin's results. *Biopolymers*, 14:2421–2423, 1975.

[253] A Ortega and J G de la Torre. Hydrodynamic properties of rodlike and disklike particles in dilute solution. *Journal Of Chemical Physics*, 119:9914, 2003.

[254] J García de la Torre, S Navarro, and MC Lopez Martinez. HYDRO: a computer program for the prediction of hydrodynamic properties of macromolecules. *Biophysical Journal*, 1994.

[255] José García de la Torre and Victor A Bloomfield. Hydrodynamic properties of com-

plex, rigid, biological macromolecules: theory and applications. *Quarterly Reviews Of Biophysics*, 14(01):81, March 2009.

[256] J GarcÄśa de la Torre. Hydration from hydrodynamics. General considerations and applications of bead modelling to globular proteins. *Biophysical Chemistry*, 2001.

[257] B Carrasco and J García de la Torre. Hydrodynamic properties of rigid particles: comparison of different modeling and computational procedures. *Biophysical Journal*, 76:3044–3057, 1999.

[258] Martin Hoffmann, Claudia S Wagner, Ludger Harnau, and Alexander Wittemann. 3D Brownian Diffusion of Submicron-Sized Particle Clusters. *Acs Nano*, 3(10):3326–3334, October 2009.

[259] Jacob N Israelachvili, D John Mitchell, and Barry W Ninham. Theory of self-assembly of hydrocarbon amphiphiles into micelles and bilayers. *Journal of the Chemical Society, Faraday Transactions 2*, 72:1525, 1976.

[260] J N Israelachvili, D J Mitchell, and B W Ninham. Theory of self-assembly of lipid bilayers and vesicles. *Biochimica Et Biophysica Acta*, 470(2):185–201, October 1977.

[261] Samuel Safran. *Statistical Thermodynamics of Surfaces, Interfaces, and Membranes*. Frontiers in physics. Westview Press, 2003.

[262] William M Gelbart, Avinoam Ben-Shaul, William E McMullen, and Andrew Masters. Micellar growth due to interaggregate interactions. *Journal Of Physical Chemistry C*, 88(5):861–866, 1984.

[263] Yu Kang, Xin Li, Yaoquan Tu, Qi Wang, and Hans Ågren. On the Mechanism of Protein Adsorption onto Hydroxylated and Nonhydroxylated TiO 2Surfaces. *Journal Of Physical Chemistry C*, 114(34):14496–14502, September 2010.

[264] A Lomakin, D S Chung, G B Benedek, D A Kirschner, and D B Teplow. On the nucleation and growth of amyloid beta-protein fibrils: detection of nuclei and quantitation of rate constants. *Proceedings Of The National Academy Of Sciences Of The United States Of America-physical Sciences*, 93(3):1125–1129, 1996.

[265] A Lomakin, D B Teplow, D A Kirschner, and G B Benedek. Kinetic theory of fibrillogenesis of amyloid beta-protein. *Proceedings Of The National Academy Of Sciences Of The United States Of America-physical Sciences*, 94(15):7942–7947, July 1997.

[266] Dorota Walczyk, Francesca Baldelli Bombelli, Marco P Monopoli, Iseult Lynch, and Kenneth A Dawson. What the Cell "Sees" in Bionanoscience. *Journal Of The American Chemical Society*, 132(16):5761–5768, April 2010.

[267] Xin-Rui Xia, Xin-Rui Xia, Nancy A Monteiro-Riviere, Nancy A Monteiro-Riviere, Jim E Riviere, and Jim E Riviere. An index for characterization of nanomaterials in biological systems. *Nature Nanotechnology*, advance online publication, 2010.

[268] David B Warheit. Debunking Some Misconceptions about Nanotoxicology. *Nano Letters*, 10(12):4777–4782, December 2010.

[269] Monica Bucciantini, Monica Bucciantini, Elisa Giannoni, Elisa Giannoni, Fabrizio Chiti, Fabrizio Chiti, Fabiana Baroni, Fabiana Baroni, Lucia Formigli, Lucia Formigli, Jesus Zurdo, Jesus Zurdo, Niccolo Taddei, Niccolo Taddei, Giampietro Ramponi, Giampietro Ramponi, Christopher M Dobson, Christopher M Dobson, Massimo Stefani, and Massimo Stefani. Inherent toxicity of aggregates implies a common mechanism for protein misfolding diseases. *Nature*, 416(6880):507–511, 2002.

[270] Christopher J Roberts Wei Wang, editor. *Aggregation of Therapeutic Proteins*. Wiley, 2010.

[271] Celia Cabaleiro-Lago, Fiona Quinlan-Pluck, Iseult Lynch, Kenneth A Dawson, and Sara Linse. Dual effect of amino modified polystyrene nanoparticles on amyloid β protein fibrillation. *ACS Chem Neurosci*, 1(4):279–287, April 2010.

[272] F A L Dullien. *Porous Media: Fluid Transport and Pore Structure*. Academic Press, 2 edition, 1992.

[273] Brian C Schanen, Ajay S Karakoti, Sudipta Seal, Donald R Drake, III, William L Warren, and William T Self. Exposure to Titanium Dioxide Nanomaterials Provokes Inflammation of an in VitroHuman Immune Construct. *Acs Nano*, 3(9):2523–2532, September 2009.

[274] Robert Landsiedel, Robert Landsiedel, Lan Ma-Hock, Lan Ma-Hock, Alexandra Kroll, Alexandra Kroll, Daniela Hahn, Daniela Hahn, Jürgen Schnekenburger, Jürgen Schnekenburger, Karin Wiench, Karin Wiench, Wendel Wohlleben, and Wendel Wohlleben. Testing Metal-Oxide Nanomaterials for Human Safety. *Advanced Materials*, 22(24):2601–2627, May 2010.

[275] Hans Arora, Caroline Doty, Ye Yuan, John Boyle, Katarina Petras, Bryan Rabatic, Tatjana Paunesku, and Gayle Woloschak. Titanium dioxide nanocomposites. In

Challa S S R Kumar, editor, *Nanomaterials for the Life Sciences Vol.8: Nanocomposites*. Wiley Online Library, 2010.

[276] Alex Weir, Alex Weir, Paul Westerhoff, Paul Westerhoff, Lars Fabricius, Lars Fabricius, Kiril Hristovski, Kiril Hristovski, Natalie von Goetz, and Natalie von Goetz. Titanium Dioxide Nanoparticles in Food and Personal Care Products. *Environmental Science & Technology*, 46(4):2242–2250, February 2012.

[277] Helmut Cölfen and Stephen Mann. Higher-Order Organization by Mesoscale Self-Assembly and Transformation of Hybrid Nanostructures. *Angew Chem, Int Ed*, 42(21):2350–2365, May 2003.

[278] George P Privalov and Peter L Privalov. Problems and prospects in microcalorimetry of biological macromolecules. *Vitamins and Coenzymes*, 323:31–62, August 2013.

[279] Jörg Rösgen and Hans-Jürgen Hinz. Theory and practice of DSC measurements on proteins. In *Handbook of Thermal Analysis and Calorimetry*, volume 4, pages 63–108. Elsevier, 1999.

[280] John E Ladbury and Michael L Doyle. *Biocalorimetry 2*. Applications of Calorimetry in the Biological Sciences. John Wiley & Sons, July 2005.

[281] Pooria Gill, Tahereh Tohidi Moghadam, and Bijan Ranjbar. Differential scanning calorimetry techniques: applications in biology and nanoscience. *J Biomol Tech*, 21(4):167–193, December 2010.

[282] Viktoriya Kholodenko and Ernesto Freire. A simple method to measure the absolute heat capacity of proteins. *Analytical Biochemistry*, 270(2):336–338, 1999.

[283] Gilles Bruylants, Johan Wouters, and Catherine Michaux. Differential scanning calorimetry in life science: thermodynamics, stability, molecular recognition and application in drug design. *Current Medicinal Chemistry*, 12(17):2011–2020, 2005.

[284] Joseph Zaccai Igor N Serdyuk, Nathan R Zaccai. *Methods in Molecular Biophysics: Structure, Dynamics, Function*. Cambridge University Press, February 2007.

[285] Alan Cooper, Margaret A Nutley, and Abdul Wadood. Differential scanning microcalorimetry. In Stephen E Harding and Babur Z Chowdhry, editors, *Protein-Ligand Interactions: Hydrodynamics and Calorimetry*, pages 287–318. Oxford University Press, New York, 2001.

[286] J. E. Ladbury and B. Z. Chowdhry, editors. *Biocalorimetry : applications of calorime-*

try in the biological sciences. Wiley, 1998.

[287] John W Shriver. *Protein Structure, Stability, and Interactions*. Humana Press, November 2010.

[288] Christopher M Johnson. Archives of Biochemistry and Biophysics. *Archives Of Biochemistry and Biophysics*, 531(1-2):100–109, March 2013.

[289] Carmine Ercole, Jorge Pedro López-Alonso, Josep Font, Marc Ribó, Maria Vilanova, Delia Picone, and Douglas V Laurents. Crowding agents and osmolytes provide insight into the formation and dissociation of RNase A oligomers. *Archives Of Biochemistry and Biophysics*, 506(2):123–129, February 2011.

[290] A B Siemer, K Y Huang, and A E McDermott. Protein–ice interaction of an antifreeze protein observed with solid-state NMR. *Proceedings Of The National Academy Of Sciences Of The United States Of America-physical Sciences*, 107(41):17580–17585, 2010.

[291] E Freire, W W van Osdol, O L Mayorga, and J M Sanchez-Ruiz. Calorimetrically determined dynamics of complex unfolding transitions in proteins. *Annual Review Of Biophysics and Biophysical Chemistry*, 19(1):159–188, 1990.

[292] Ernesto Freire and Rodney L Biltonen. Statistical mechanical deconvolution of thermal transitions in macromolecules. I. Theory and application to homogeneous systems. *Biopolymers*, 17(2):463–479, 1978.

[293] Ernesto Freire and Rodney L Biltonen. Statistical mechanical deconvolution of thermal transitions in macromolecules. II. General treatment of cooperative phenomena. *Biopolymers*, 17(2):481–496, 1978.

[294] Ernesto Freire and Rodney L Biltonen. Statistical mechanical deconvolution of thermal transitions in macromolecules. III. Application to doubleâĂŘstranded to singleâĂŘstranded transitions of nucleic acids. *Biopolymers*, 17(2):497–510, 1978.

[295] J. E. Ladbury and M L Doyle, editors. *Biocalorimetry 2: applications of calorimetry in the biological sciences*. Wiley, 2005.

[296] G Rialdi and E Battistel. Decoupling of melting domains in immobilized ribonuclease A. *Proteins: Structure, Function, and Bioinformatics*, 19(2):120–131, June 1994.

[297] C N Pace, G R Grimsley, S T Thomas, and G I Makhatadze. Heat capacity change for ribonuclease A folding. *Protein science : a publication of the Protein Society*,

8(7):1500–1504, July 1999.

[298] E E Freire. Statistical thermodynamic analysis of differential scanning calorimetry data: structural deconvolution of heat capacity function of proteins. *Vitamins and Coenzymes*, 240:502–530, January 1994.

[299] Donald T Haynie. Analysis of Differential Scanning Calorimetric Data. In J. E. Ladbury and B. Z. Chowdhry, editors, *Biocalorimetry*, pages 183–205. Wiley, Chichester; New York, 1998.

[300] T Y TY Tsong, R P RP Hearn, D P DP Wrathall, and J M JM Sturtevant. A calorimetric study of thermally induced conformational transitions of ribonuclease A and certain of its derivatives. *Water Relationships in Foods*, 9(13):2666–2677, June 1970.

[301] Peter L Privalov. Thermodynamic problems in structural molecular biology. *Pure and Applied Chemistry*, 79(8):1445–1462, 2007.

[302] J M Sturtevant. Heat capacity and entropy changes in processes involving proteins. *Proceedings Of The National Academy Of Sciences Of The United States Of America-physical Sciences*, 74(6):2236–2240, June 1977.

[303] M Adams, Z Dogic, S L Keller, and S Fraden. Entropically driven microphase transitions in mixtures of colloidal rods and spheres. *Nature*, 393(6683):349–352, 1998.

[304] Edward Barry and Zvonimir Dogic. Entropy driven self-assembly of nonamphiphilic colloidal membranes. *Proceedings Of The National Academy Of Sciences Of The United States Of America-physical Sciences*, 107(23):10348–10353, June 2010.

[305] Martin Schmidt and Samuel G Steinemann. XPS studies of amino acids adsorbed on titanium dioxide surfaces. *Fresenius J Anal Chem*, 341(5-6):412–415, 1991.

[306] Tine E Thingholm, Thomas J D Jørgensen, Ole N Jensen, and Martin R Larsen. Highly selective enrichment of phosphorylated peptides using titanium dioxide. *Nature Protocols*, 1(4):1929–1935, November 2006.

[307] Houjiang Zhou, Mingliang Ye, Jing Dong, Eleonora Corradini, Alba Cristobal, Albert J R Heck, Hanfa Zou, and Shabaz Mohammed. Robust phosphoproteome enrichment using monodisperse microsphere–based immobilized titanium (IV) ion affinity chromatography. *Nature Protocols*, 8(3):461–480, February 2013.

[308] Thomas Eickner, Stefan Mikkat, Peter Lorenz, Martin Sklorz, Ralf Zimmermann,

Hans-Jürgen Thiesen, and Michael Glocker. EJMS Protocol: Systematic studies on TiO_2-based phosphopeptide enrichment procedures upon in-solution and in-gel digestions of proteins. Are there readily applicable protocols suitable for MALDI-MS-based phosphopeptide stability estimations? *European Journal Of Mass Spectrometry*, 17(5):507, 2011.

[309] Martin R Larsen, Tine E Thingholm, Ole N Jensen, Peter Roepstorff, and Thomas J D Jørgensen. Highly selective enrichment of phosphorylated peptides from peptide mixtures using titanium dioxide microcolumns. *Molecular & Cellular Proteomics*, 4(7):873–886, July 2005.

[310] Federico F Torta, Matteo M Fusi, Carlo S CS Casari, Andrea Li AL Bassi, and Angela A Bachi. Nanostructured TiO_2 thin films for phosphoproteomics studies with MALDI mass spectrometry. *Methods in Molecular Biology*, 790:173–181, January 2011.

[311] P A Connor and A J McQuillan. Phosphate Adsorption onto TiO_2 from Aqueous Solutions: An in Situ Internal Reflection Infrared Spectroscopic Study. *Langmuir*, 15(8):2916–2921, April 1999.

[312] Zhenda Lu, Jicheng Duan, Le He, Yongxing Hu, and Yadong Yin. Mesoporous TiO_2 Nanocrystal Clusters for Selective Enrichment of Phosphopeptides. *Analytical Chemistry*, 82(17):7249–7258, September 2010.

[313] Bochra Bejaoui Kefi, Latifa Latrous El Atrache, Hafedh Kochkar, and Abdelhamid Ghorbel. TiO_2 nanotubes as solid-phase extraction adsorbent for the determination of polycyclic aromatic hydrocarbons in environmental water samples. *Journal Of Environmental Sciences*, 23(5):860–867, January 2011.

[314] Tine E Thingholm and Martin R Larsen. The use of titanium dioxide micro-columns to selectively isolate phosphopeptides from proteolytic digests. *Methods in Molecular Biology*, 527:57–66– xi, 2009.

[315] Neil A Demarse, Neil A Demarse, Colette F Quinn, Colette F Quinn, Dennis L Eggett, Dennis L Eggett, Donald J Russell, Donald J Russell, Lee D Hansen, and Lee D Hansen. Calibration of nanowatt isothermal titration calorimeters with overflow reaction vessels. *Analytical Biochemistry*, 417(2):247–255, October 2011.

[316] Matthew W Freyer, Matthew W Freyer, Edwin A Lewis, and Edwin A Lewis. Isothermal titration calorimetry: experimental design, data analysis, and probing macromolecule/ligand binding and kinetic interactions. *Zebrafish:2nd Edition Genetics Genomics and Informatics*, 84:79–113, 2008.

[317] Adrian Velazquez-Campoy, Stephanie A Leavitt, and Ernesto Freire. Characterization of protein-protein interactions by isothermal titration calorimetry. *Methods in Molecular Biology*, 261:35–54, 2004.

[318] Matthew J Todd and Javier Gomez. Enzyme Kinetics Determined Using Calorimetry: A General Assay for Enzyme Activity? *Analytical Biochemistry*, 296(2):179–187, September 2001.

[319] Jose M Sanchez-Ruiz. Lumry-Eyring. *Biophysical Journal*, 61(4):921–935, April 1992.

[320] R Lumry. On the interpretation of data from isothermal processes. *Vitamins and Coenzymes*, 259:628–720, 1995.

[321] Travis T Waldron and Kenneth P Murphy. Stabilization of Proteins by Ligand Binding: Application to Drug Screening and Determination of Unfolding Energetics âĂă. *Water Relationships in Foods*, 42(17):5058–5064, May 2003.

[322] Michael Rubinstein and Ralph H Colby. *Polymer Physics*. Oxford University Press, USA, 2003.

[323] Charles Sidney Johnson and Don A Gabriel. *Laser Light Scattering*. Courier Dover Publications, 1994.

[324] Amy L Oldenburg, Matthew N Hansen, Alexander Wei, and Stephen A Boppart. Backscattering albedo contrast in OCT using plasmon-resonant gold nanorods. In James G Fujimoto, Joseph A Izatt, and Valery V Tuchin, editors, *Biomedical Optics (BiOS) 2007*, pages 64291Z–64291Z–8. SPIE, February 2007.

[325] Stephen W Provencher. A constrained regularization method for inverting data represented by linear algebraic or integral equations. *Computer Physics Communications*, 27(3):213–227, September 1982.